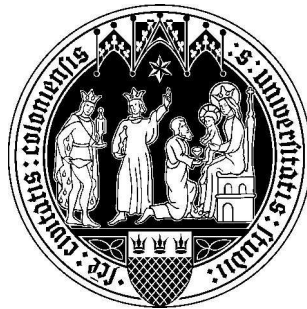


Multi-frequency study of relativistic jets in active galactic nuclei

Inaugural-Dissertation

zur
Erlangung des Doktorgrades
der Mathematisch-Naturwissenschaftlichen Fakultät
der Universität zu Köln



vorgelegt von

Kirill V. Sokolovsky
aus Moskau, Russland

Köln 2010

Berichtersteller:

Prof. Dr. Andreas Eckart
Prof. Dr. J. Anton Zensus

Tag der mündlichen Prüfung: 01.02.2011

Contents

1	Introduction	1
1.1	Multi-band approach as a powerful tool to probe physical processes in AGN jets	2
1.2	Parsec-scale study of AGN radio jets with VLBI	5
1.2.1	Jets aligned with the line of sight	5
1.2.2	Misaligned jets	7
1.3	Radiation from a homogeneous uniform synchrotron source and how it applies to jets	8
1.3.1	Synchrotron radiation along the line of sight	10
1.3.2	Synchrotron radiation of a spherical source	11
1.4	Outline of this work	12
2	Constraining the magnetic field strength and particle energy spectrum in AGN jets with multi-frequency VLBI observations	14
2.1	A CLEAN component-based method of spatially resolved spectrum reconstruction	15
2.1.1	VLBI imaging with CLEAN algorithm	15
2.1.2	Description of the spectrum reconstruction method	16
2.1.3	Discussion of the method	18
2.2	Magnetic field in the parsec-scale core regions of bright γ -ray blazars	18
2.2.1	Introduction	19
2.2.2	Observations and data reduction	21
2.2.3	Results	23
2.2.4	Discussion	47
2.3	Magnetic field in the parsec-scale core regions of high core shift radio sources	48
2.4	Chapter summary	50
3	Individual blazars across the electromagnetic spectrum	51
3.1	VLBI radio behavior of 3C 454.3 during its 2008 activity period	52
3.2	Multifrequency VLBA view of BL Lacertae during the <i>Fermi</i> campaign	60
3.2.1	General properties	60
3.2.2	Results of 5–43 GHz VLBA observations	61
3.3	Multiwavelength observations of PKS 1510–089	63
3.3.1	General properties	64
3.3.2	VLBA observations of PKS 1510–089	64
3.3.3	Quasi-simultaneous SED of PKS 1510–089	66
3.4	VLBA view of TeV blazars Mrk 421 and Mrk 501	69

3.5	Chapter summary	71
4	A VLBA survey of the core shift effect in AGN jets	72
4.1	Introduction	72
4.2	VLBA observations	73
4.2.1	Sample selection	73
4.2.2	VLBA observation setup	74
4.2.3	Data calibration and imaging	75
4.3	Discussion	101
4.3.1	Core position as a function of frequency	101
4.3.2	Fitting results assuming synchrotron self-absorption opacity	103
4.3.3	Comparison with previous 2.3/8.6 GHz measurements	104
4.4	Chapter summary	105
5	The quest for young radio sources seen edge-on	106
5.1	A sample of GHz-peaked spectrum sources selected with RATAN-600: spectral and variability properties	107
5.1.1	General remarks	107
5.1.2	Observational data and sample selection	108
5.1.3	Spectral properties	109
5.1.4	Variability	111
5.1.5	Summary of the sample properties	113
5.2	Parsec-scale properties of the RATAN-600 GPS sources derived from 2.3 and 8.6 GHz VLBI surveys	118
5.2.1	Morphological classification	118
5.2.2	VLBI-scale compactness	120
5.2.3	Magnetic field in the dominating source components	121
5.2.4	Summary	122
5.3	A VLBI selected sample of Compact Symmetric Object candidates and frequency dependent position of hotspots	123
5.3.1	Introduction	123
5.3.2	The VLBI-selected sample of CSO candidates and its basic characteristics	124
5.3.3	Properties of the dominating parsec-scale components	126
5.3.4	Frequency dependent component position	127
5.3.5	Summary	129
5.4	γ -ray counterparts of candidate young radio sources seen edge-on	138
5.5	Chapter summary	138
6	Conclusions	140

List of Figures

1.1	Scheme of a radio-loud AGN. Note that relative sizes are not to scale and shapes of many structures (like the Broad Line Region – BLR and Narrow Line Region – NLR) are very uncertain. The “blazar zone” is likely a small section of the inner jet, presumably located inside or just outside the BLR. The “blazar zone” is responsible for relativistically-beamed, highly variable emission at NIR and optical bands and at high energies.	2
1.2	The observed Spectral Energy Distribution (SED) of a quasar-type blazar compared to a model. See Fig. 3.13 and Section 3.3 for a detailed discussion.	4
1.3	Scheme of a blazar jet. Note that mm-band core is located upstream (closer to central engine) than cm-band core due to the “core shift” effect. At any given frequency, sections of the jet upstream from the core corresponding to this frequency are hidden from sight by opacity. The “blazar zone”, site of the NIR, optical and high-energy emission, is located upstream from the mm-band core. Shocks traveling the jet could potentially also be responsible for a fraction of high-energy emission.	6
1.4	Scheme of a Compact Symmetric Object (CSO) – a miniature radio source contained entirely within the Narrow Line Region (NLR) of its host galaxy.	8
1.5	Theoretical spectrum of a uniform synchrotron source (Section 1.3.1) plotted in spectral (F_ν , 1.5a) and SED (νF_ν , 1.5b) coordinates.	9
2.1	Maps of the best-fit synchrotron spectrum (Fig. 2.2) parameters and the estimated magnetic field strength derived from nine images (1.4–15.4 GHz range) of the source 1458+718 convolved with the same Gaussian beam. From this example it is clear why convolution with a Gaussian beam makes VLBI images unsuitable for magnetic field estimation. The convolved images have large areas of artificial low flux surrounding each area where the actual flux is detected (see the distribution of the peak intensity at Fig. 2.1b). These artificial low-flux areas (where there should be no flux at all) result in very high estimated values of B_\perp (Fig. 2.1a) around each spot with actual detected flux (and, therefore, a valid estimation of B_\perp). The peak frequency (Fig 2.1c) and power index of the electron energy distribution (Fig 2.1d) do not change much across the area and the effect of their changes is negligible compared to the effect of convolution. We note that only pixels where spectral turnover was detected (i.e. the spectrum in such pixel significantly deviates from a power law) are shown on the images.	19

2.2	Spectrum of a single pixel (red points) in Fig. 2.1 compared to a power law (green line) and synchrotron spectrum (blue curve) fit. The synchrotron model clearly provides better fit to the data. Spatial distributions of the best-fit parameters of the synchrotron model: peak intensity S_{peak} , peak frequency ν_{peak} and electron energy distribution index p ($p = 1 - 2\alpha$, $S_{\nu} \propto \nu^{\alpha}$) are presented on Fig 2.1b, 2.1c and 2.1d respectively.	20
2.3	Spectrum of the core and naturally weighted CLEAN images of the γ -ray bright blazars observed with the VLBA between 4.6 and 43.2 GHz. The lowest contour value ‘clev’ is chosen at four times the rms noise, the peak brightness is given by ‘max’. The contour levels increase by factors of two. The dashed contours indicate negative brightness. The half power beam width is shown in the bottom left corner of the images in grey. An epoch of observation is shown in the bottom right corner.	26
2.4	VLBA spectra of core regions of 1510–089 (a) and OJ 248 (b). The former spectrum is flat while the latter one shows a prominent synchrotron self-absorption peak. The green line is a power law fit. The blue curve is a homogeneous synchrotron source model.	46
3.1	Total intensity VLBA images of 3C 454.3 at 43.2 GHz at four epochs covered by our multifrequency observations. Image details: 3.1a – peak 24.6 Jy/beam, first contour 0.030 Jy/beam; 3.1b – peak 23.4 Jy/beam, first contour 0.030 Jy/beam; 3.1c – peak 21.7 Jy/beam, first contour 0.015 Jy/beam; 3.1d – peak 15.6 Jy/beam, first contour 0.020 Jy/beam. Contours are a factor of 4 apart in all cases. The beam is plotted in the lower left corner of each image. Green circles represent Gaussian components used to model the 43.2 GHz brightness distribution of the source.	53
3.2	Total intensity VLBA image at 4.6 GHz. The first contour is 0.002 Jy/beam, factor = 4. The beam is shown in the lower left corner of the image.	55
3.3	Spectral index map constructed by fitting a power law to observations at three frequencies: 8.1, 8.4 and 15.4 GHz. Contours represent total intensity at 8.4 GHz. Contour map peak = 6.442 Jy/beam, first contour 0.1% of the peak. Beam FWHM = 2.12×1.05 mas at PA = $-4^{\circ}64$	56
3.4	Lightcurve of the 43 GHz core of 3C 454.3 (marked “C00”) and the first jet component “C01” about 0.15 mas away from the core.	57
3.5	Size of the first jet component (C01) and the core (C00) as a function of time.	57
3.6	Separation of the component “C01” from the core (“C00”) of 3C 454.3 as a function of time. The blue line represents the least square fit to the data.	58
3.7	Position Angle (PA) of the component C01 with respect to the core.	58
3.8	Core spectrum of 3C 454.3.	59
3.9	Inner jet of BL Lacertae as observed by the VLBA on September 02, 2008. Images at different frequencies are shifted by 8 mas in relative Right Ascension. For the 15.4, 23.8 and 43.2 GHz image map peaks are 1.69, 1.52, 1.32 Jy/beam, first contours are 1.70, 3.00, 5.00 mJy/beam respectively. The contour levels are increased by a factor of 3. Beam size (natural weighting) for each frequency is indicated by the cross to the left of the corresponding image.	62

3.10	Spectral index map ($F_\nu \sim \nu^{-\alpha}$, α is shown in color) of BL Lacertae constructed using VLBA observations at 4.6, 5.0, 8.1 and 8.4 GHz. The overlaid contours represent total intensity at 8.4 GHz (the peak intensity is 1.75 Jy/beam, the first contour is 0.70 mJy/beam, the beam size is 1.57×1.22 mas at PA = $10^\circ.4$). The spectral index map was smoothed by a median filter with radius equal to the indicated beam size. The map shows an optically thin jet with $\alpha \sim 0.7$ and the self-absorbed core region ($\alpha < 0.0$). A 2D cross-correlation technique using the optically thin part of the jet was employed to align images at different frequencies allowing reliable extraction of the spectral information. The spectral steepening towards the jet edges visible on the spectral index map occurs on the angular scale comparable to the beam size and is likely an effect of the uneven uv -coverage at different frequencies.	63
3.11	Stokes I CLEAN images of PKS 1510–089 observed by VLBA on 2009 April 9, at 15, 24, and 43 GHz. The lowest contour and peak intensity are 0.7 mJy/beam and 1.47 Jy/beam (15 GHz), 0.7 mJy/beam and 1.56 Jy/beam (24 GHz), 2 mJy/beam and 1.85 Jy/beam (43 GHz). Contours are plotted with a step $\times 4$. Natural weighting of visibility data is used, HPBW beam size is shown in the lower left corner. Angular size of 1 mas corresponds to 5 pc.	65
3.12	Spectral index α ($F(\nu) \propto \nu^\alpha$) map between 15.4 and 23.8 GHz (shown in color) of PKS 1510–089 as observed by the VLBA on 2009 April 9. The overlaid contours represent total intensity at 15.4 GHz (see Figure 3.11 for details). The spectral index map was smoothed by a median filter with a 0.6 mas radius.	67
3.13	Quasi-simultaneous SED of PKS 1510–089 from Sokolovsky et al. (2010a) constructed using observations with the VLBA, <i>Swift</i> , <i>Fermi</i> /LAT, NOT, SMA and the 2.1 m telescope Guillermo Haro. The violet curve (a) represents the combined SED model: green curve (b) is the synchrotron component, red (c) is the SSC component, blue (d) is the accretion disk and brown (e) represents EC scattering of the disk radiation (see also Table 3.3).	68
3.14	The VLBA spectrum of Mrk 501: 3.14a — integrated parsec-scale spectrum, 3.14b — core spectrum.	71
4.1	Naturally weighted CLEAN images of the observed sources between 1.4 and 15 GHz. The lowest contour value ‘clev’ is chosen at four times the rms noise, the peak brightness is given by ‘max’. The contour levels increase by factors of two. The dashed contours indicate negative brightness. The beam’s full width at half maximum (FWHM) is shown in the bottom left corner of the images in grey. An epoch of observation is shown in the bottom right corner. Red and blue spots indicate the positions and sizes (FWHM) of Gaussian model components for the core and the jet features respectively.	78
4.2	Separation of the core from a reference optically-thin jet component as a function of frequency. The curve represents the best-fit function $r_c(\nu) = a + b\nu^{-1/k}$, the coefficient $k = 1$ was fixed during the fitting. The best-fit parameters are presented in Table 4.4.	98
4.2	continued...	99

4.3	Distribution of the observed difference in distance between the core and reference component measured at two sub-bands of X , C , S and L band.	100
4.4	Distribution of the k parameter in the core position as a function of frequency fit: $r_c(\nu) \propto \nu^{-1/k}$. The mean value is $k = 0.98 \pm 0.11$ while the median is 0.89. One discrepant measurement on the histogram corresponds to the source 0952+179 where the value of k is not well constrained: $k = 2.7 \pm 1.7$	102
4.5	Core shift ratio versus X band core flux density ratio. The core shift ratio is defined to be greater than unity, i.e., for each pair of measurements, the larger value of the shift is in the numerator of the ratio. The one source (not shown in this plot) which exhibited a large core shift change without a major change in flux density is W Com (1219+285); it has a core shift ratio of 3.67 ± 0.36 and core flux ratio of 1.19 ± 0.08	104
5.1	Radio spectra of 3 out of 60 newly identified GPS source candidates. Variability index as a function of frequency is presented in the panels under the spectra plots. Black points correspond to RATAN-600 data, grey points represent data collected from the literature.	110
5.2	Combined spectra of all selected 226 GPS candidates normalized by peak flux density and peak frequency values. Filled circles represent the observed spectra binned and shifted along the vertical axis. The solid line is a normalized and shifted theoretical spectrum of a homogeneous synchrotron emitting cloud with self-absorption and power index $\gamma = 2.54$ of the electron energy distribution.	111
5.3	Peak frequency distribution for GPS quasars, galaxies and unidentified radio sources (empty fields).	112
5.4	Distribution of variability index ν for the model non-variable sources measured with the relative accuracy of 5, 8 and 10% respectively.	113
5.5	Distribution of the observed variability index ν_{11} at 11 GHz for GPS quasars, galaxies and unidentified radio sources (empty fields) in our sample.	114
5.6	Redshift distribution of GPS galaxies and GPS quasars from the sample.	119
5.7	Relation between the variability index at 11 GHz ν_{11} and the high-frequency spectral index α_1 for galaxies (G), quasars (Q) and unidentified radio sources (R). The line is a least square fit to the data: $a_1 \approx 1.08(\pm 0.02) \nu_{11} - 0.90(\pm 0.002)$	120
5.8	Distributions of 2.3–8.6 GHz spectral indices of VLBI components of CSO candidates.	120
5.9	PKS 1555–140 – new GPS galaxy with CSO morphology at $z = 0.097$. Red points on the panel (b) denote RATAN-600 observations, green points represent literature data.	121
5.10	Observed peak frequency distribution for GPS sources with different optical identification and parsec-scale radio structure.	121
5.11	“Compactness index” for sources from the RATAN-600 GPS sample (a) and from the complete sample of flat spectrum sources (b).	122
5.12	Distribution of estimated $\log_{10} B$ (G) for sources with different morphological types. Filled bars - sources with known redshift. Empty bars - sources with unknown redshift.	123

5.13	Dual-frequency simultaneous 2 and 8 GHz naturally weighted CLEAN images. The lowest contour value ‘clev’ is chosen at four times the rms level, the peak brightness is given by ‘max’ (Jy/beam). The contour levels increase by factors of two. The dashed contours indicate negative flux. The beam is shown in the bottom left corner of the images. An epoch of observation is shown in the bottom right corner. Light blue and orange spots indicate Gaussian model components 1 and 2 respectively.	125
------	--	-----

List of Tables

1.1	Dimensionless parameters of the spherical synchrotron source model	12
2.1	A sample of γ -ray bright blazars observed with the VLBA	22
2.2	IF central frequencies	22
2.3	Amplitude corrections for the BK150 VLBA experiment	23
2.4	Comparison of the emission region parameters estimated from the VLBA data and SED modeling	47
2.5	Estimated physical parameters of parsec-scale cores of the “high core shift sample” sources	49
3.1	Parameters of the core and jet components of 3C 454.3 at 43.2 GHz	54
3.2	VLBA flux measurements of 3C 454.3	59
3.3	PKS 1510–089 SED model parameters from Sokolovsky et al. (2010a)	66
3.4	VLBA flux measurements of Mrk 421 and Mrk 501	70
4.1	The high core shift source sample observed with the VLBA	74
4.2	IF central frequencies	75
4.3	Amplitude corrections for the BK134 VLBA experiment	99
4.4	Core distance from the reference jet component as a function of frequency: fit results ($r = a + b/\nu$)	103
5.1	RATAN–600 sample of GPS sources	114
5.2	List of CSO candidates selected from VCS and RDV surveys	132

Acknowledgements

I am deeply grateful to Dr. Yuri Kovalev for giving me the opportunity to work on the interesting projects described in the thesis and for his continuous support and advice. I would like to thank Dr. Andrei Lobanov for sharing his deep understanding of AGN physics and VLBI technique. Dr. Alexander Pushkarev, Frank Schinzel, Dr. Tuomas Savolainen, Dr. Ru-Sen Lu, Dr. Marios Karouzos, Dr. Emmanouil Angelakis, Dr. Eduardo Ros, Dr. Richard Porcas, Dr. Thomas Krichbaum, Dr. Matthias Kadler, Dr. Lars Fuhrmann, Dr. Nicola Marchili and many other current and past members of the MPIfR's VLBI group were always available for an interesting and helpful discussion both about science and life, thank you very much for that! I would like to thank referees Prof. Dr. Andreas Eckart and Prof. Dr. J. Anton Zensus, who agreed to review the thesis. I am especially grateful to Prof. Dr. J. Anton Zensus for the opportunity to work in the VLBI group of the MPIfR – this was a very interesting and educative experience for me. Special thanks to Gabi Breuer, and Simone Pott for all their help, which made my life in Bonn easier. Finally, I would like to thank the Fermi/LAT AGN group for the good collaboration and for the opportunity to work with the top specialists in γ -ray and blazar astronomy. My work on the thesis has been supported by the International Max Planck Research School (IMPRS) for Astronomy and Astrophysics at the Universities of Bonn and Cologne.

Abstract

The thesis at hand presents the results of multi-frequency Very Long Baseline Interferometry (VLBI) observations of jets associated with active galactic nuclei. The results are discussed in the context of broad-band jet emission models and used to constrain physical properties of the parsec-scale core – inner part of the jet which is likely related to the observed high-energy emission. The analysis of the frequency-dependent core position shift supports interpretation of the parsec-core as the integral part of the jet; the observed core position is determined by opacity. Synchrotron self-absorption is found to be the dominating opacity mechanism in the observed sources. A comparison between radio sources possessing jets aligned closely to the line of sight with those aligned at large angles to it supports the idea that the bright extragalactic γ -ray sources are associated with jets affected by relativistic beaming.

Zusammenfassung

Die hier vorliegende Dissertation präsentiert die Ergebnisse von Multifrequenz Very Long Baseline Interferometry (VLBI) Beobachtungen von Jets aktiver galaktischer Kerne (AGN). Die Ergebnisse werden im Zusammenhang mit breitbandigen Jet Emissionsmodellen diskutiert und werden dafür benutzt die physikalischen Eigenschaften des Kerns auf Parsec Skalen, d.h. der innere Teil des Jets welcher sehr wahrscheinlich mit beobachteter hochenergetischen Strahlung zusammenhängt, einzugrenzen. Die Auswertung der frequenzabhängigen Positionsverschiebung des Kerns auf Grund von Opazität unterstützt die Interpretation des Kerns auf Parsec Skalen als einen wesentlichen Bestandteil des Jets. Die Synchrotron-Selbstabsorption wurde als der dominierende Mechanismus der frequenzabhängigen Opazität in den beobachteten Quellen identifiziert. Ein Vergleich zwischen Radioquellen mit Jets entlang der Sichtlinie mit jenen unter grossen Winkeln zur Sichtlinie untermauert die Annahme das helle extragalaktische und Gammastrahlung emittierende Quellen mit Jets verknüpft werden die relativistische Beaming zeigen.

Chapter 1

Introduction

Active Galactic Nuclei (AGN) are small regions in centers of some galaxies which emit powerful electromagnetic radiation, often outshining stars, gas, and dust which make up the host galaxy. If AGN emission dominates the galaxy emission all over the electromagnetic spectrum, such object is known as the “quasar”. The energy source powering AGN is believed to be accretion of gas onto a supermassive black hole. This is a very efficient energy release process potentially able to extract a large fraction (maybe 10% or more) of the rest energy of the infalling matter (mc^2). The released energy makes AGN visible from cosmological distances. Accretion of matter onto a compact object (such as a black hole, neutron star, young stellar object and, possibly, a white dwarf) is often associated with production of collimated bipolar outflows known as jets. Jets carry a fraction of infalling matter (and its angular momentum) away from a central object. It is likely that despite the striking visual similarity of jets produced by stars, stellar-mass and supermassive black holes, different physical mechanisms are responsible for jet production and evolution in these systems. In the case of accretion onto a supermassive black hole, the produced jets are extreme, with matter in such jets moving with relativistic speed.

While it is widely accepted that accretion onto a supermassive black hole powers AGN, the mechanisms which convert the energy of infalling gas into the extreme electromagnetic radiation we observe are not well understood. An AGN is a complex system consisting of the central (possibly rotating) supermassive black hole, infalling matter in a form of an inner accretion disk, dusty torus (which is further away from the central object and is thus cooler), and clouds of gas orbiting the black hole, as well as outflowing matter (which moves away from the central black hole) in a form of collimated relativistic jets, and possibly slower, not well collimated outflow. A simplified scheme of a radio-loud AGN is presented on Fig. 1.1. Magnetic fields are likely to play a significant role in the dynamics of inner accretion disk and the process of launching the relativistic jet. Components of this system radiate through a number of mechanisms according to their physical condition, and radiation of one component influences physical conditions in other components (radiation of the accretion disk ionizes the surrounding gas clouds, photons produced by ionized gas clouds are up-scattered to high energies by relativistic electrons in the jet). Details of these processes are yet unclear. Different accretion rate and its total duration, viewing angle, presence or absence and relative importance of different structural components may be the reasons why AGN phenomenon appear in so many different forms. While it is believed that most galaxies contain a supermassive black hole in their center, only a small fraction of them appear

as AGN, and even smaller fraction of them produce bright radio-emitting jets.

This work is concentrated on radio loud AGN in which relativistic jets are most prominent. In some of them (the so-called “blazars”), the relativistic jet dominates not only radio, but also optical emission. Blazars are also powerful high-energy emitters, the property which is likely to be directly related to the presence of a relativistic jet. In this work we highlight some observational properties of AGN jets and, whenever possible, try to provide physical interpretation of the observed phenomena. A more detailed outline of this work may be found in Section 1.4.

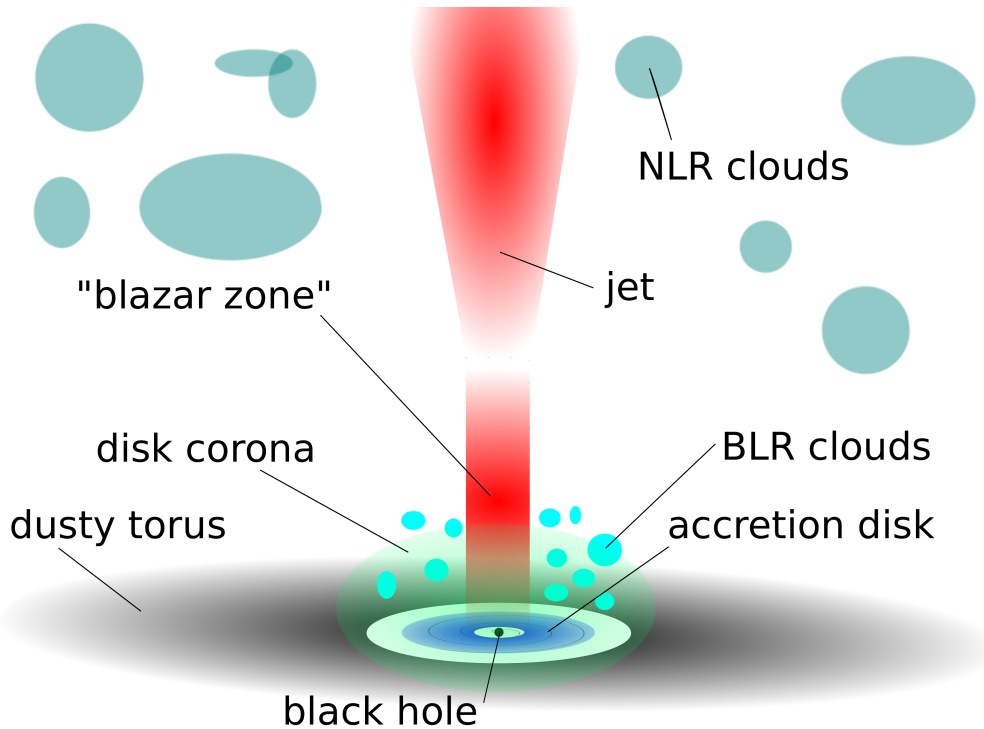


Figure 1.1: Scheme of a radio-loud AGN. Note that relative sizes are not to scale and shapes of many structures (like the Broad Line Region – BLR and Narrow Line Region – NLR) are very uncertain. The “blazar zone” is likely a small section of the inner jet, presumably located inside or just outside the BLR. The “blazar zone” is responsible for relativistically-beamed, highly variable emission at NIR and optical bands and at high energies.

1.1 Multi-band approach as a powerful tool to probe physical processes in AGN jets

It is not clear why only about 10% of AGN are radio loud. The formation of a radio emitting jet may be related to conditions in the near black hole (e.g., Hujerit et al. 2003; Narayan 2005) environment, the magnetic field strength, or the black hole spin (Blandford & Payne 1982; Blandford & Znajek 1977; Wilson & Colbert 1995). It is likely that radio-quiet AGNs are just scaled-down (in terms of jet power) versions of radio-loud AGNs (e.g., Falcke 2001; Kellermann et al. 1994). Alternatively it has been

suggested that the origin of weak radio emission observed from radio-quiet AGNs may be different from the one in radio-loud AGNs (e.g., Ishibashi & Courvoisier 2010).

The observed spectrum, high brightness temperature and significant polarization of radio emission from AGN jets clearly indicates that it has a non-thermal origin. The most likely mechanism behind the observed jet radio emission is the synchrotron radiation (e.g., Ginzburg & Syrovatskii 1965; Kardashev et al. 1962; Krolik 1999; Marscher 2009). The major open physical questions regarding AGN jets are related to their launching, energy dissipation and origin of the Spectral Energy Distribution (SED) components.

The relative positions of principal structures making up a radio-loud AGN are presented in Fig. 1.1. Such AGN will be observed as a blazar if viewed along (or close to) the jet axis. If viewed from a large angle to the jet axis, it will be observed as a radio galaxy or a steep-spectrum quasar.

Blazars are a class of AGN which includes Flat-Spectrum Radio Quasars (FSRQ) and BL Lacertae-type objects. One of the most remarkable things about blazars is their ability to radiate across the entire electromagnetic spectrum: from radio to GeV and TeV γ -rays (e.g., Marscher 2006a, 2009). This emission is believed to be produced by a relativistic jet pointing roughly towards the observer. The SED of a blazar, in $\nu\text{-}\nu F_\nu$ representation, has two broad components: one peaking between far-IR and X-ray wavelengths and the other peaking at γ -rays (Fig. 1.2). For recent reviews of the blazar emission mechanisms and energetics one may consult Boettcher (2010); Celotti & Ghisellini (2008); Ghisellini & Tavecchio (2009). The radio to UV (sometimes up to X-ray) emission of blazars is believed to be dominated by synchrotron radiation of relativistic electrons while radiation at higher energies could be due to the inverse Compton scattering of synchrotron photons emitted by the electrons themselves (the synchrotron self-Compton process, SSC, Ghisellini & Maraschi 1989; Jones et al. 1974) and/or photons from external sources (External Compton, EC, Dermer & Schlickeiser 2002; Sikora et al. 1994). The sources of the external seed photons for the EC process include accretion disc, broad line region (BLR) clouds, warm dust, and the cosmic microwave background (CMB), with their relative contribution varying for different blazars.

Despite the wide acceptance of the picture outlined above, the exact location, geometry and physical properties of the regions responsible for blazar emission (the “blazar zone”) at different bands remain a controversial issue. It is critical to identify the location of γ -ray emitting regions in order to distinguish between SSC and EC models and determine the origin of seed photons for the EC process. Moreover, the blazar phenomenon can be explained in the framework of the hadronic models, where the relativistic protons in the jet are the primary accelerated particles, emitting γ -ray radiation by means of photo-pair and photo-pion production and synchrotron radiation (see Mücke & Protheroe 2001; Mücke et al. 2003 for reviews on hadronic models).

Blazar emission is variable in flux and polarization on timescales from minutes to decades and longer. Shock-in-jet (Hughes et al. 1985; Marscher 1996; Marscher & Gear 1985), colliding relativistic plasma shells (Guetta et al. 2004), lighthouse effect (Camenzind & Krockenberger 1992), MHD-instabilities (Sikora et al. 2005) or variations of the jet orientation caused by the orbital motion in a binary black hole system (e.g., Begelman et al. 1980; Valtonen et al. 2008; Villata & Raiteri 1999) are some of the models that attempt to explain blazar variability at different time scales. Although the exact physical processes at play are unclear, the study of the temporal behavior of the SED is important (Angelakis et al. 2009) since different mechanisms predict different variability patterns (e.g., Böttcher 2002).

Flux variability in blazars and AGN in general is often discussed in terms of “flares”,

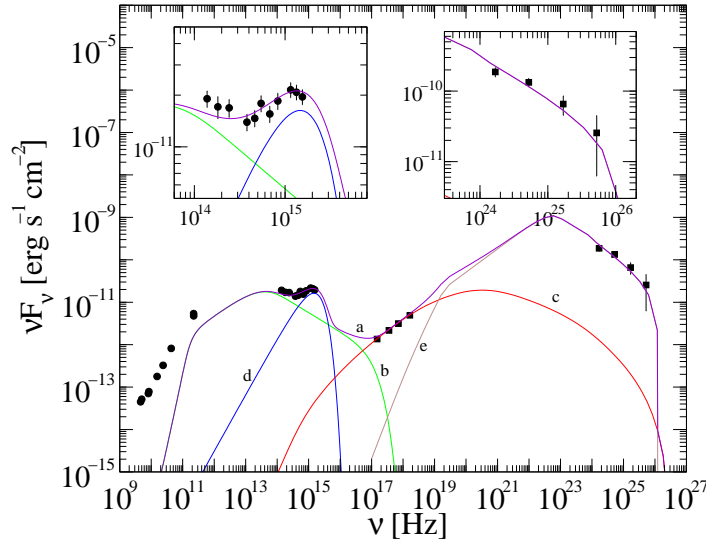


Figure 1.2: The observed Spectral Energy Distribution (SED) of a quasar-type blazar compared to a model. See Fig. 3.13 and Section 3.3 for a detailed discussion.

however such terminology may be misleading. While it is often possible to visually identify individual flares in an AGN lightcurve (e.g, Hovatta et al. 2008) it is not clear if these flares actually represent a sudden and catastrophic change in the source properties (such as a dwarf nova flare associated with the phase transition in its accretion disc). On the contrary, it is quite possible that “flaring state” is the natural state for an AGN. AGN variability may be caused by a process which continuously produces flares with varying amplitudes and time scales.

There is a substantial amount of evidence (Lobanov 2010a) for relativistic jets contributing to generation of non-thermal continuum in the optical (Arshakian et al. 2010; Jorstad et al. 2010; León-Tavares et al. 2010), X-ray (Chatterjee et al. 2009; D’Arcangelo et al. 2007; Marscher et al. 2008; Soldi et al. 2008; Unwin et al. 1997)), γ -ray at MeV–GeV (Jorstad et al. 2010; Marscher et al. 2010b; Otterbein et al. 1998; Savolainen et al. 2010) and TeV (Acciari et al. 2009a; Charlot et al. 2006; Piner & Edwards 2004) energies. Spatial localization of production sites of variable non-thermal continuum emission in AGN jets is crucial for understanding the mechanism for release and transport of energy in active galaxies.

It is natural to try to unlock blazar secrets by studying the relation between their radiation in different bands. Comparison of variability properties at two or more frequencies may provide information about the size (through the shortest observed variability timescale) and relative position (correlated variability and timelags) of the corresponding radiating regions. If a quasi-simultaneous SED of a blazar has been obtained – it may be modeled. Depending on specific SED model, it may potentially provide information about physical conditions in the blazar emission zone, properties of the BLR and/or dusty torus or accretion disk around the black hole as well as the black hole mass. A number of dedicated observing campaigns has been conducted aiming to study correlation between blazar variability at different bands and reconstruction and modeling of blazar SED at high and low luminosity states (Abdo et al. 2010f; Acciari et al. 2009c; Bach et al. 2006; Vercellone et al. 2010; Villata et al. 2009 are just a few recent examples). It is widely accepted, that multi-wavelength studies of variable

γ -ray blazars are crucial in addressing the questions about the high-energy emission processes and the mechanisms that convert the flow energy to the internal energy of the particle population (e.g., Abdo et al. 2010a; Marscher et al. 2008). However, until very recently difficulties in organizing observational campaigns have limited detailed studies to only a handful of individual AGN. The wide range of variability and often contradictory time lag behavior seen among wave-bands in this limited, heterogeneous sample underscores the need to obtain data on a wider range of objects.

Radio-loud AGNs and especially blazars are by far the most numerous and most luminous class of extragalactic γ -ray sources (Abdo et al. 2009; Giroletti et al. 2010; Hartman et al. 1999; Kovalev 2009). This implies that there should be an intimate relation between the appearance of bright radio jet and the production of γ -rays (Bloom 2008; Marscher 2006b; Salamon & Stecker 1994). However, the presence of a direct correlation between the total radio and γ -ray flux of blazars remains doubtful (Max-Moerbeck et al. 2009; Muecke et al. 1997). The main reason is that high-quality simultaneous observations at both bands are needed on a time scale of years which will cover many episodes of blazar flaring activity. Since the launch of *Fermi* Gamma-ray Space Telescope in June 2008 such observations in γ -ray band finally became routinely possible. A number of ongoing ground-based blazar radio flux monitoring programs are collecting data which may be useful for γ -ray—radio correlation studies (Aller et al. 2010; Angelakis et al. 2010; Kovalev & Kovalev 2006; Richards et al. 2010; Teräsranta et al. 2003).

Blazar variability behavior at radio band and its relation to blazar emission in other bands is further complicated by emission from the extended radio jet which cannot be spatially resolved by single-dish radio instruments. This problem can be attacked with the technique of the Very Long Baseline Interferometry (VLBI) discussed in the next section.

1.2 Parsec-scale study of AGN radio jets with VLBI

1.2.1 Jets aligned with the line of sight

Radio observations with Very Long Baseline Interferometry (VLBI) provide the highest resolution view of parsec-scale AGN jets (e.g., Lobanov 2010a; Zensus 1997; Zensus et al. 2006). Parsec-scale structure of most radio sources (blazars) which are bright and compact enough to be detected with VLBI is dominated by a bright, unresolved or barely-resolved feature called the core. The core has a flat or inverted radio spectrum, characteristic of optically-thick synchrotron emission (Section 1.3). The exact physical nature of the structure which we observe as a parsec-scale core is still being debated (Marscher 2008; Section 4.1), however the available evidence currently favor its interpretation as a continuous Blandford & Konigl (1979) type jet with smooth gradients of physical properties along it. The observed position of the core at a given frequency is identified with the surface at which the optical depth $\tau_\nu \approx 1$ (photosphere) in the continuous jet. The observed position, $r_c(\nu)$, of the core depends on the frequency of observation, ν , so that $r_c(\nu) \propto \nu^{-1/k}$ (this is so-called “core shift” effect, Fig. 1.3). If the dominating absorption mechanism in the core is synchrotron self-absorbed and there is an equipartition between particle and magnetic field energy in it, the power index $k = 1$ (Blandford & Konigl 1979). The core shift can be used for determining basic physical properties of the ultra-compact region of the jet and the surrounding absorbing material (Lobanov 1998b). A detailed discussion of this effect may be found in Chapter 4.

A steep spectrum jet (often transversely unresolved) is usually found extending from the core. Its spectral shape is characteristic for optically-thin synchrotron emission and results in jet being more pronounced at lower frequencies. An examples of such structure may be found in Fig. 2.3.

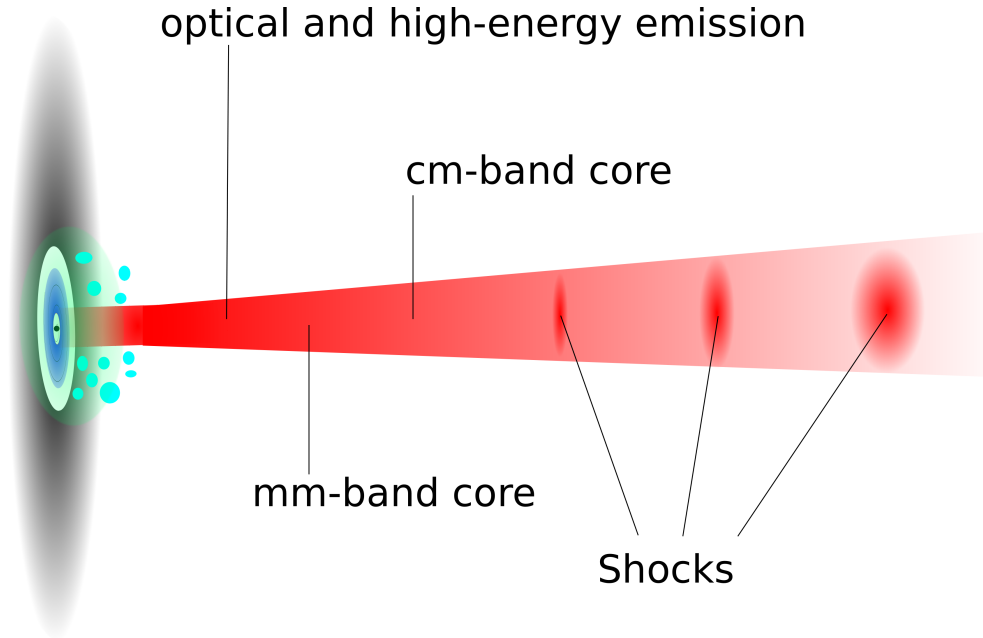


Figure 1.3: Scheme of a blazar jet. Note that mm-band core is located upstream (closer to central engine) than cm-band core due to the “core shift” effect. At any given frequency, sections of the jet upstream from the core corresponding to this frequency are hidden from sight by opacity. The “blazar zone”, site of the NIR, optical and high-energy emission, is located upstream from the mm-band core. Shocks traveling the jet could potentially also be responsible for a fraction of high-energy emission.

Bright features known as “components” often appear over a continuous jet flow (Fig. 4.1). Due to a limited dynamic range of VLBI observations, many jets appear as a series of discrete components while the underlying flow emission is too weak to be detected. Jet components are usually associated with shock waves propagating through the jet (Blandford & Konigl 1979; Marscher 2009). Components often display apparent superluminal motion (see Fig. 3.6 for an example). Alternatively, components may signify regions in a continuous bent jet which are more aligned with the line of sight (and are thus brighter due to higher relativistic beaming) than nearby jet regions. The bending of a jet may occur due to flow instabilities or motion of the jet foot-point (e.g., Lobanov 2010b; Lobanov & Zensus 2001). Components resulting from a difference in angle to the line of sight (and therefore beaming) between sections of a continuous flow are not expected to show superluminal motion. It is possible that both components related to shocks and components related to jet bending may be found in real extragalactic jets.

Multi-epoch VLBI observations provide the only direct evidence for relativistic motion in AGN jets. Observations of jet kinematics are important to estimate total jet power, study the jet structure and geometry and how they change with time. Such observations may also constrain the jet acceleration mechanism (Königl 2007). The relation between changes in parsec-scale jet and flux density and polarization changes

observed at other wavelength are still an open question and an interesting topic of research. If a sufficiently long VLBI time baseline is obtained, it is, in principle, possible to probe poorly known aspects of AGN outflows, including dynamical accelerations and instabilities, precession, collimation, and jet magnetic field stability. A number of multi-epoch VLBI monitoring programs aimed for investigating these and other questions are currently in place (Lister et al. 2009; Marscher et al. 2009; Ojha et al. 2010; Pushkarev & Kovalev 2008).

Multi-frequency VLBI observations provide constrains on SED models of blazars and therefore may be especially useful in the framework of a multi-wavelength campaign which samples the SED and its variability with time (Savolainen et al. 2008; Sokolovsky et al. 2010a). Participation of a VLBI array in a long-term multi-frequency campaign also provides a unique opportunity to study the relation between changes in the parsec scale jet structure, polarization and the overall SED of the source. The relation between the γ -ray flares and the activity in the parsec-scale radio jet has been suggested by a number of authors (Jorstad et al. 2001; Lähteenmäki & Valtaoja 2003; Marscher et al. 2010b).

1.2.2 Misaligned jets

The core – jet type structure associated with blazars is not the only option of how an AGN jet may look like on VLBI images. Approximately 7% of radio galaxies in complete, flux-limited samples display parsec-scale jets and lobe emission on both sides of a central engine (Taylor et al. 2000, 1996 and references therein). Two-sided jets are detected with VLBI in bright radio galaxies such as Cyg A (Bach et al. 2005, 2008) and NGC 1052 (Kadler et al. 2004). The so-called Compact Symmetric Objects (CSO; Readhead et al. 1996a; Wilkinson et al. 1994) also show emission on both sides of an active galactic nucleus (see Section 5.3). These objects are like radio galaxies in miniature, with hotspots and mini-lobes (not jets) usually dominating their parsec-scale radio emission (Fig. 1.4). Due to this obvious similarity of structure between CSO and large-scale radio galaxies it was suggested (Phillips & Mutel 1982) that they are young radio sources which would evolve into large radio sources.

Alternatively, Carvalho (1994, 1998) have suggested that CSOs are not small by virtue of youth, but rather are frustrated jets impeded by a dense interstellar medium. With this model, the derived ages of the sources range from 10^6 to 10^7 yr. The random orientations of CSOs test the unified schemes of AGNs that require an obscuring torus of gas and dust surrounding the central engine. The angle that the line of sight of the observer makes with this torus determines which features are seen (Antonucci 1993; Urry & Padovani 1995). CSOs often exhibit very broad HI absorption lines (Gupta et al. 2006; Peck et al. 2000; Pihlström et al. 2003; Taylor et al. 1999) and free-free absorption (Peck et al. 1999), providing evidence for the existence of this circumnuclear torus. H_2O megamasers also provide clues to circumnuclear tori in nearby AGNs (Lo 2005 and references therein). CSOs typically exhibit very low polarization (Gugliucci et al. 2007), if any, because of the large Faraday rotation measures induced by ionized gas associated with the torus (Gugliucci et al. 2005).

Kinematic ages can be obtained by measuring the separation speed between hot spots over time or the proper motion of a hot spot or jet component with respect to the core (Gugliucci et al. 2007). The measurement of a kinematic age for the CSO 0710+439 by Owsianik & Conway (1998) of just 1100 ± 100 yr lent strong support to the theory that CSOs are small by virtue of their youth and not because of confinement. The overall CSO age distribution seems to be disproportionately stacked toward the

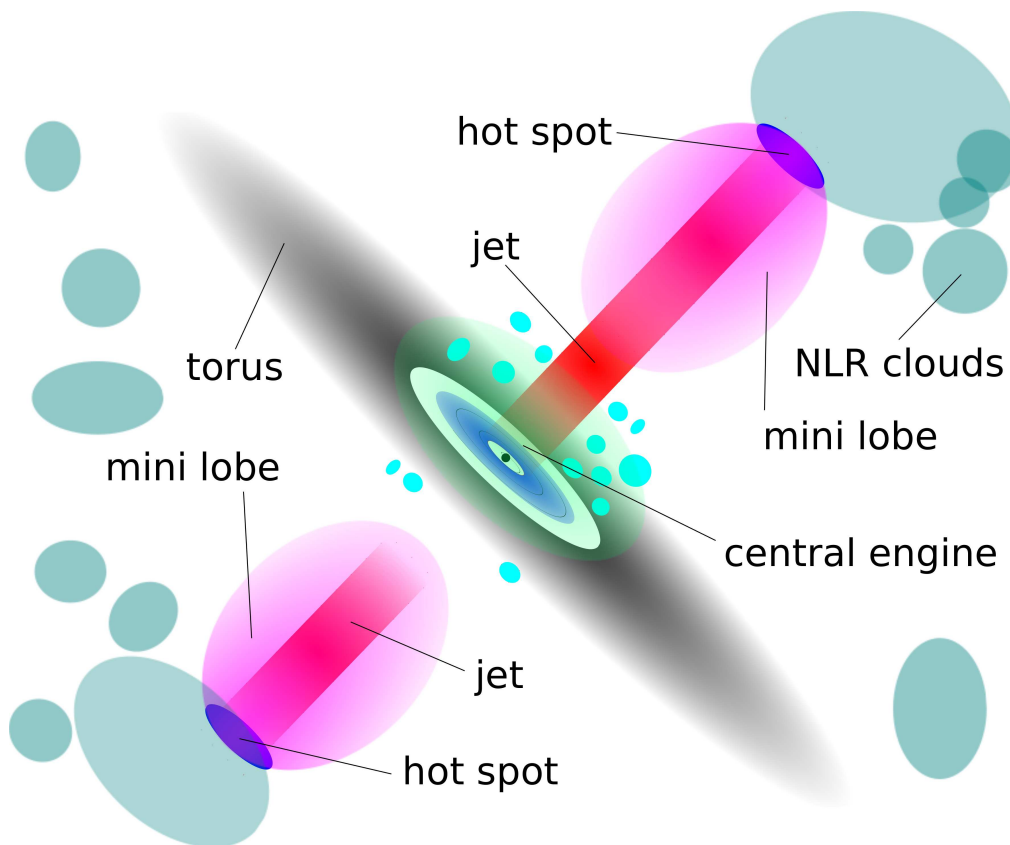


Figure 1.4: Scheme of a Compact Symmetric Object (CSO) – a miniature radio source contained entirely within the Narrow Line Region (NLR) of its host galaxy.

younger ages (Gugliucci et al. 2007). Possible explanations are that there is a selection effect against older CSOs, that the jet activity tends to die off after a certain period of time, or that CSOs have periods of deactivation and reactivation (Tingay et al. 2003). It is important to construct representative samples of CSOs which go down to low fluxes and are sensitive to symmetric objects of medium sizes in order to investigate these possibilities in detail.

Many CSOs exhibit a distinctive shape of the single-dish radio spectrum with peak at frequencies from a few hundred megahertz up to a few gigahertz (e.g., Polatidis & Conway 2003). Radio sources with such spectral shape are known as Compact Steep-Spectrum (CSS) and Gigahertz Peaked-Spectrum (GPS) sources (O’Dea 1998; see Section 5.1). Sensitive multi-frequency VLBI observations are required to demonstrate symmetric structure on the parsec scale (Taylor et al. 2000). In particular, not all GPS radio galaxies belong to the CSO class (Section 5.2).

1.3 Radiation from a homogeneous uniform synchrotron source and how it applies to jets

While a real relativistic jet is a complex structure, a small section of it (such as an individual jet component) may be approximately treated as a uniform cloud of magnetized plasma. The plasma is presumed to be leptonic with a power law particle energy dis-

tribution. The theory of synchrotron radiation from such cloud is well developed (see Sections 1.3.1, 1.3.2 and references therein).

The most notable spectral feature of a uniform synchrotron cloud is a peak, resulting from synchrotron self-absorption at lower frequencies. Fig. 1.5 shows the theoretical spectrum of a uniform synchrotron emitting cloud. The spectrum is plotted in the usual spectral (F_ν , Fig. 1.5a) and SED (νF_ν , Fig. 1.5b) representation. The optically thick part of this spectrum is characterized by a power law shape with the spectral index $\alpha = 5/2$ ($F_\nu \propto \nu^\alpha$). The optically thin part of the spectrum also has a power law shape and is characterized by a spectral index $\alpha = (1 - p)/2$. Here p is the index in the particle energy distribution $N(E) \propto E^{-p}$. The abundance of celestial radio sources which spectra are characterized by a power law with $\alpha < 0$ strongly supports the adopted assumption about the power law particle energy distribution.

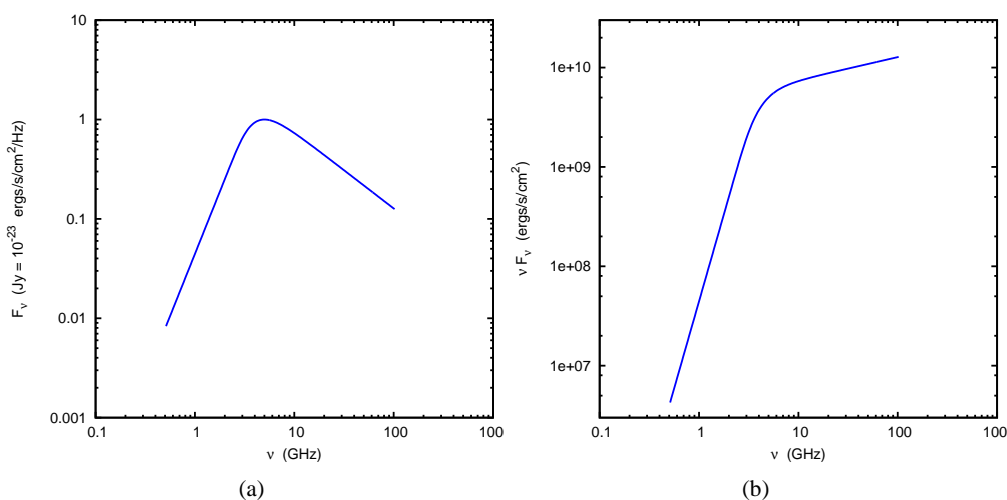


Figure 1.5: Theoretical spectrum of a uniform synchrotron source (Section 1.3.1) plotted in spectral (F_ν , 1.5a) and SED (νF_ν , 1.5b) coordinates.

Flat spectra of compact cores require an explanation. The flat radio spectrum is usually explained as a result of emission from an inhomogeneous source. There are two most favored paradigms which suggest how such an inhomogeneous radio source near the base of an AGN jet may look like. The first one suggest that what we observe as a parsec-scale core is a surface at which the optical depth $\tau_\nu \approx 1$ (photosphere) in a continuous jet flow with gradually changing physical properties (Blandford & Konigl 1979). The other explanation, known as the “cosmic conspiracy”, suggests that the observed flat spectrum results from a series of distinct bright components which have spectral peaks at different frequencies (e.g., Marscher 1980).

In practice, spectrum of a parsec-scale core is not always flat. The spectral turnover caused by synchrotron self-absorption can often be identified if observations in a sufficiently wide frequency range are available (Chapter 2). It is unclear however, how such spectral turnover should be understood in the light of different interpretations of the core spectrum origin described above. The spectral turnover and physical parameters derived from its properties may correspond to a distinct component in the jet which has the lowest turnover frequency but is still too close to other components upstream to be spatially resolved from them. The next component downstream will be larger and will have even lower turnover frequency, however it will be spatially resolved and

will not contribute to the spectrum of the collection of components which we see as the core. Alternatively, the turnover may correspond to a section in a continuous jet (Blandford & Konigl 1979; Konigl 1981) where its properties suddenly change due to some disruption, and the lack of emission at lower frequencies from this jet region (due to opacity in it) is no longer fully compensated by optically thin emission from other regions downstream.

The self absorption turnover in the core spectrum carries information about the region near the downstream end of the structure which we observe as the core. However, even if the spectral turnover is detected, the spectrum of the core region usually deviates significantly from the theoretical spectrum of a homogeneous source due to contribution of emission from nearby regions. Sometimes, the spectral turnover may be detected in a jet component spatially separated from the core (Savolainen et al. 2008; Sokolovsky et al. 2010b). Spectrum of such component is usually much closer to the spectrum of a uniform source. This provides an opportunity to accurately determine physical conditions in such component.

Sections 1.3.1 and 1.3.2 will describe the relation between the observed parameters of synchrotron self-absorption peak in the spectrum and the physical parameters of the emitting plasma cloud.

1.3.1 Synchrotron radiation along the line of sight

Following Pacholczyk (1970), we consider a uniform cloud of relativistic electrons in the external uniform magnetic field with component B_{\perp} perpendicular to the line of sight. We assume that the electron energy distribution is described by a power law within a certain energy range:

$$N(E) = N_0 E^{-p}, \quad E_{\min} < E < E_{\max},$$

where N_0 and p are constants. For this case, we can write the radiation transfer equation

$$\frac{dI_{\nu}}{ds} = -\kappa_{\nu} I_{\nu} + j_{\nu},$$

where I_{ν} is the specific intensity of synchrotron radiation at the frequency ν , ds is the differential element of path length, j_{ν} is the emission coefficient (emissivity), κ_{ν} is the absorption (extinction) coefficient. If j_{ν} and κ_{ν} are constant along the line of sight, the solution of the radiation transfer equation is

$$I_{\nu} = \int_0^L j_{\nu} e^{-\int_0^s \kappa_{\nu} ds} ds = \frac{j_{\nu}}{\kappa_{\nu}} (1 - e^{-\kappa_{\nu} L}),$$

where L is the size of the electron cloud along the line of sight, and $\kappa_{\nu} L = \tau_{\nu}$ is the optical depth.

According to Pacholczyk (1970), this solution can be written in the form:

$$I_{\nu} = S(\nu_1) J\left(\frac{\nu}{\nu_1}, p\right), \quad (1.1)$$

where

$$\nu_1 = 2c_1 (N_0 L c_6(p))^{2/(p+4)} B_{\perp}^{(p+2)/(p+4)}, \quad (1.2)$$

$$S(\nu_1) = \frac{c_5(p)}{c_6(p)} B_{\perp}^{-1/2} \frac{\nu_1^{5/2}}{2c_1}, \quad (1.3)$$

$$\begin{aligned}
J(z, p) &= z^{5/2}(1 - \exp[-z^{-(p+4)/2}]), \\
c_1 &= \frac{3e}{4\pi m_e^3 c^5} = 6.27 \times 10^{18}, \\
c_3 &= \frac{\sqrt{3}}{4\pi} \frac{e^3}{m_e c^2} = 1.87 \times 10^{-23}, \\
c_5(p) &= \frac{1}{4} c_3 \Gamma\left(\frac{3p-1}{12}\right) \Gamma\left(\frac{3p+7}{12}\right) \left(\frac{p+7/3}{p+1}\right), \\
c_6(p) &= \frac{1}{32} \left(\frac{c}{c_1}\right)^2 c_3 \left(p + \frac{10}{3}\right) \Gamma\left(\frac{3p+2}{12}\right) \Gamma\left(\frac{3p+10}{12}\right),
\end{aligned}$$

where e is the electron charge, m_e is the electron mass, and c is the speed of light in vacuum.

The power law index p of the electron energy distribution may be found from the spectral index α ($F_\nu \propto \nu^\alpha$) in the optically thin part of the spectrum: $p = 1 - 2\alpha$. The optical depth τ_m corresponding to the observed spectral peak frequency ν_m may be found from equation $\exp[\tau_m] = 1 + \frac{p+4}{5}\tau_m$.

The frequency ν_1 corresponding to $\tau_{\nu_1} = 1$ may be found from ν_m , p and τ_m : $\nu_1 = \tau_m^{2/(p+4)} \nu_m$.

From equations (1.1), (1.2) and (1.3), we can derive the perpendicular component of the magnetic field:

$$B_\perp = \left(\frac{c_5(p)}{c_6(p)} \frac{J\left(\frac{\nu}{\nu_1}, p\right)}{I_\nu} \right)^2 \left(\frac{\nu_1}{2c_1} \right)^5. \quad (1.4)$$

Note, that if the size of an emitting region is smaller than the angular resolution, only a *lower limit* on the intensity and, correspondingly, an *upper limit* on the magnetic field B_\perp can be derived.

Gould (1979) has correctly pointed out that the spectrum of a uniform ‘‘slab’’ described here would be different from the spectrum of a uniform spherical cloud. The reason is that in a uniform spherical cloud, while local medium properties (such as the particle density and magnetic field strength) may be constant across all the volume of the cloud, the optical depth of a spherical cloud would be different along different lines of sight. However, there is no reason to believe that the spherical cloud may approximate a section of a real extragalactic jet any better than the slab – this is a very crude approximation anyway. Unfortunately, a more accurate model cannot be developed without detailed information about the emitting region geometry which is currently not available.

1.3.2 Synchrotron radiation of a spherical source

In Section 1.3.1 we have briefly described how intensity of synchrotron radiation is related to the magnetic field strength B in the emitting plasma. In practice however from interpretation of VLBI data one obtains total flux of a jet component and estimation of its size. For this kind of data a convenient formalism has been provided by Marscher (1983) who computed the total synchrotron flux from a spherical synchrotron emitting cloud.

The model of Marscher (1983) assumes a spherical cloud of plasma with a uniform (in strength, but disordered in direction) magnetic field B and an isotropic, power-law particle energy (E) distribution:

$$N(E) = N_0 E^{2\alpha-1} \quad (\gamma_1 mc^2 < E < \gamma_2 mc^2)$$

where α is an observed spectral index in the optically thin part of the spectrum¹. In the framework of this model, the magnetic field strength can be derived (Marscher 1983) as:

$$B = 10^{-5} b(\alpha) \theta^4 v_m^5 S_m^{-2} \frac{\delta}{1+z}$$

where B is in G, v_m is the peak frequency in GHz, S_m is the flux density in Jy *extrapolated from the optically thin part of the spectrum*, $\delta = \frac{1}{\gamma(1-\beta \cos \psi)}$ is a Doppler factor, $\beta = \frac{v}{c}$, $\gamma = \frac{1}{\sqrt{1-\beta^2}}$, ψ is an angle between the cloud velocity v and the line of sight, z – source redshift. θ is the angular diameter of the cloud in milliarcseconds. Note, that according to Marscher (1983) it is not appropriate to use FWHM of the best-fit Gaussian component to determine θ in the above formula since it is substantially less than the diameter of a spherical component which could be used to reproduce the data. For a partially resolved component the substitution $\theta = 1.8 \cdot \text{FWHM}$ is reasonably accurate (Marscher 1983).

Table 1.1: Dimensionless parameters of the spherical synchrotron source model

α	b	n
0.25	1.8	7.9
0.50	3.2	0.27
0.75	3.6	0.012
1.00	3.8	0.00059

Adapted from Marscher (1983).

Normalization constant in the particle energy distribution (Marscher 1983):

$$N_0 = n(\alpha) D_{Gpc}^{-1} \theta^{4\alpha-7} v_m^{4\alpha-5} S_m^{3-2\alpha} (1+z)^{2(3-\alpha)} \delta^{2(\alpha-3)}$$

$n(\alpha)$ and $b(\alpha)$ are dimensionless parameters listed in Table 1.1, D_{Gpc} is the luminosity distance in Gigaparsecs.

1.4 Outline of this work

- In Chapter 2 we propose a recipe for estimating the magnetic field strength in AGN jets on the basis of simultaneous multi-frequency VLBI data. The method is applied to VLBA observations of 38 bright extragalactic radio sources.
- Chapter 3 describes individual sources in a context of multi-wavelength blazar observing campaigns associated with the *Fermi* Gamma-ray Space Telescope (FGST). The VLBA data are used to put additional constraints on Spectral Energy Distribution (SED) models.

¹ $F_\nu \propto \nu^\alpha$

- Chapter 4 presents observational results of a multi-frequency VLBA program to observe twenty sources showing large frequency-dependent displacement of the parsec-scale core position (the “core shift” effect). It is shown that synchrotron self-absorption is the dominating opacity mechanism responsible for the observed effect.
- In Chapter 5 we describe an effort to identify promising candidate young radio-loud AGN on the basis of multi-frequency single-dish and VLBI data. Some of these sources may be intrinsically similar to blazars, but not aligned with the line of sight. We compare the high-energy emitting properties of the selected young radio source candidates with those of blazars.
- The results of this work are summarized in Chapter 6.

Throughout this work, we adopt a Λ CDM cosmology, with the following values for the cosmological parameters: $H_0 = 0.71$, $\Omega_m = 0.27$, and $\Omega_\Lambda = 0.73$ (Komatsu et al. 2009).

Chapter 2

Constraining the magnetic field strength and particle energy spectrum in AGN jets with multi-frequency VLBI observations

The spatially resolved broad-band radio spectroscopy with Very Long Baseline Interferometry (VLBI) is one of the few methods that can probe the physical conditions inside blazar jets. Detection of the synchrotron self-absorption turnover in the spectrum of a radio jet feature combined with an estimation of its size provides an opportunity to estimate the magnetic field strength in it by applying simple synchrotron theory. However, reconstruction of a broad-band radio spectrum from VLBI data is challenging due to differences in uv -coverage and sensitivity at high and low frequencies and problems with multifrequency VLBI image alignment. The applicability of the simple theory of a uniform synchrotron source to real radio sources also remains an open question.

Single-zone synchrotron self-Compton and external Compton models are widely used to explain broad-band Spectral Energy Distributions (SEDs) of blazars from infrared to gamma-rays. These models bear obvious similarities to the homogeneous synchrotron cloud model which is often applied to explain radio emission from individual components of parsec-scale radio jets. The parsec-scale core, typically the brightest, highly variable and the most compact feature at the apparent base of a blazar radio jet, could be the source of high-energy emission. We report on ongoing work to test this hypothesis by means of simultaneous multi-frequency VLBA observations. These observations allow one to obtain the emitting region size and spectrum which, in turn, provide us with estimates of magnetic field strength and particle energy spectrum in the radio emitting region.

We describe a method which allows one to reconstruct spatially resolved spectra from simultaneous multifrequency VLBI observations. These spectra can be used to constrain the magnetic field strength in the regions of the source where synchrotron self-absorption peak is detected. The method is applied to a number of sources observed with the VLBA.

First results of the work described in this chapter were presented in Sokolovsky et al. (2010a,b).

2.1 A CLEAN component-based method of spatially resolved spectrum reconstruction

This section will present a method of recovering spatially resolved spectra from multifrequency VLBI data. However, before proceeding to the description of the method which will be given in Section 2.1.2, Section 2.1.1 will present a short introduction to the standard single-frequency VLBI image reconstruction technique.

2.1.1 VLBI imaging with CLEAN algorithm

An astronomical interferometer is a device that measures the interference (or attributes associated with the interference) of radiation from astronomical sources. The interferometer consist of a number of elements (telescopes) and a device which combines signals from individual elements (correlator). “Aperture synthesis” or “synthesis imaging” is a type of interferometry that mixes signals from a collection of telescopes to produce images having the same angular resolution as an instrument the size of the entire collection. Aperture synthesis is possible only if both the amplitude and the phase of the incoming signal is measured by each telescope. This may be achieved by correlating signals received by two telescopes using two channels: in the first channel the signals are combined as-is (cosine channel) and in the second channel signals are combined after introducing a 90° phase shift into one of the signals (sine channel; Porcas 2008). Naturally, the phase shift may be introduced only in a sufficiently narrow band. A wide-band signal recorded at each telescope is divided into many individual sub-bands at the stage of correlation. The complex value measured by an interferometer capable of aperture synthesis is known as the “complex visibility” (Thompson 1999).

Most aperture synthesis interferometers use the rotation of the Earth to increase the number of different baselines included in an observation. However, even with the aid of Earth rotation, the complex visibility is measured on a limited number of baselines forming an irregular pattern on the uv -plane (the plane at right angles to the center of the observed field). The finite extent of the uv -plane coverage and gaps in the coverage (areas where no visibility measurements are available) will produce artifacts (sidelobes) in an image obtained by Fourier transform of measured complex visibilities. Sidelobes from bright features in the image will severely limit the image dynamic range obscuring fainter features and making such image essentially useless (Briggs et al. 1999). Therefore, a more sophisticated image reconstruction technique is needed which will incorporate a priori knowledge about some properties of the reconstructed image to overcome the problem of the uneven uv -coverage.

The CLEAN algorithm proposed by Högbom (1974) allows one to reconstruct an image with suppressed sidelobes by approximating the real source structure with a number of point sources (δ -functions commonly referred to as “CLEAN components”) in an otherwise empty field of view (Cornwell et al. 1999). An iterative approach is employed to find the positions and strengths of these point sources. The initial image is used to identify the brightest spot and the model point source is placed in the position of the spot. The flux of the point source is chosen to be only a fraction $\gamma < 1$ (called the “loop gain”) of the flux associated with the spot on the initial image to improve

stability of the algorithm. The estimated contribution of this point source (together with associated sidelobes) is subtracted from the initial image. Then, the search for the brightest peak on the residual image is conducted and the new model component is placed in its position. The procedure is repeated until no significant peaks remain in the residual image. The final resulting image, known as the CLEAN image, is the sum of all these point source components (CLEAN components) convolved with a restoring beam (usually of Gaussian shape) plus the residual image (which was left after subtracting all point source components). The convolution with the Gaussian beam is needed to smooth-out fine details of the CLEAN model which are not constrained by actual measurements (baselines that would constrain them are larger than maximum covered uv -radius) and, therefore are arbitrary. Addition of the residual image is needed to indicate the remaining noise level. Therefore, both convolution with the Gaussian beam (which has no sidelobes but still has long wings) and addition of the residual map serve one purpose to convert the non-unique CLEAN model approximating the data to an image which is reasonably well constrained and can be interpreted. The resulting image should be a good approximation of the real brightness distribution of the source convolved with the restored beam down to a level indicated by the residual image noise.

2.1.2 Description of the spectrum reconstruction method

Synchrotron self-absorption turnover frequency and flux density provide an estimate of magnetic field strength in the jet (e.g., Lobanov & Zensus 1998; Section 1.3) making spectrum reconstruction from VLBI data desirable. One way to extract a spectrum of a particular region in the jet from multifrequency VLBI dataset is to model the jet structure (in image or visibility plane) at each frequency with a number of two dimensional (2D) Gaussian components and then visually cross-identify the components between frequencies. In many cases, such identification in a wide frequency range is indeed possible (Chapter 4) and this method is widely used (e.g., Savolainen et al. 2008). If a jet component shows the spectral turnover caused by synchrotron self-absorption, the magnetic field strength in it may be estimated using formulas presented in Section 1.3.2. However, this method has a few obvious disadvantages: *(i)* it relies on the assumption that the brightness distribution of a jet component may be represented reasonably accurate with a Gaussian fit, *(ii)* component identification between frequency is labor-intensive and *(iii)* somewhat subjective (since different models may represent the observational data equally well).

To overcome the inherent limitations of the Gaussian component-based method and test how they may affect analysis results, we have developed an alternative method based on automatic identification of CLEAN-components (δ -functions) across frequencies within a certain jet region. This method allows to construct a source image with a spectrum associated with each image pixel. First we give a detailed description of the proposed procedure and then repeat the description in a more condensed form.

As a preliminary step for the spectral reconstruction with this CLEAN component-based method, VLBI images obtained at different frequencies need to be aligned. This can be achieved using 2D cross-correlation technique or by modeling the source structure with Gaussian components and their cross-identification. Note, that in the latter case, there is still an advantage over the use of Gaussian model parameters for spectral determination since only a single bright, optically thin component needs to be identified across all frequencies for the relative image shifts to be determined. At frequencies above 5 GHz where the frequency dependent core shift effect is small (Chapter 4) it is often possible to use the position of the optically thick core for image alignment. For a

discussion of VLBI image alignment techniques see also Section 4.2.2. After the shifts between images at different frequencies are determined, they are applied to the images and the corresponding CLEAN models.

In order to reconstruct the radio spectrum in a given pixel of a shifted image, the sum of CLEAN components around this pixel is used. The CLEAN components are summed inside the radius $R = \Theta(\text{lowest frequency})/3$ at each frequency, where $\Theta(\text{lowest frequency})$ is the half-power beam width at the lowest observing frequency of a multifrequency dataset. A reasonable cut-off needs to be chosen for the total flux of the CLEAN components summed within the radius R . The radius R should be comparable to the angular resolution at the chosen flux cut-off. For the value of $R = \Theta(\text{lowest frequency})/3$ used here we set the cut-off value at the signal to noise ratio $\text{SNR} = 10$. Note also that, naturally, the estimated magnetic field strength values in two nearby pixels will be dependent on each other (since the same CLEAN component may contribute to the flux assigned to both pixels) if the distance between the two pixels is less than R . A median filter with the radius R may be applied to smooth the resulting map. The median filtering may instead be applied later to the resulting magnetic field strength map. Such filtering is justified since no spatial information on the size scale less than R is expected to be recoverable with this spectrum reconstruction method.

If the spectral turnover is detected in a given pixel, the magnetic field strength in this pixel may be constrained using the formulas from Section 1.3.1. The intensity of the synchrotron radiation I_ν needs to be estimated to use the results of Section 1.3.1. It may be estimated simply as the total flux assigned to a given pixel divided by $2\pi R$, where R is defined above. The problem with such estimation is that if the actual size of the emitting region (even in one direction) is smaller than R , the resulting value will be only a lower limit on the radiation intensity and, therefore, only an upper limit on the magnetic field strength may be determined using it.

Below we repeat the description of the proposed method step-by-step.

1. Observations at each frequency (which were conducted simultaneously) need to be reduced independently following the standard procedure of CLEAN'ing and self-calibration (hybrid mapping).
2. Shifts between the resulting images should be determined (through model fitting or 2D cross-correlation technique, see also the discussion in Chapter 4) and applied to the images and CLEAN models.
3. "Unconvolved images" should be reconstructed from the CLEAN model at each frequency by summing all the CLEAN components within a given radius R determined by the angular resolution at the lowest observing frequency. The pixel size of such image may be chosen arbitrary, however it makes sense to choose the pixel size equal to or smaller than R . The pixel size should be the same for each frequency. A flux cut-off should be applied to these images in order to avoid areas with low flux which spatial origin cannot be constrained to an area smaller than R .
4. Since the models at all frequencies are spatially aligned and the pixel size is the same at each frequency, the spectrum at each pixel may be determined. Only pixels where the spectral turnover is detected are kept for future analysis.
5. The spectrum in each pixel should be fitted with the uniform synchrotron source model (Section 1.3.1). The model will provide an estimate of the magnetic field

strength in the pixel from the parameters of the fitted spectrum and the value R . The estimated magnetic field strength value should be treated as an upper limit unless it is known from a separate analysis that the spatially extent of the source in this pixel is greater than R .

2.1.3 Discussion of the method

While being relatively free of the disadvantage of the Gaussian component-based method mentioned above, the CLEAN component-based method has two important disadvantages of its own. First, within the method, there is no way to distinguish between the resolved and unresolved jet regions. For unresolved regions only a lower limit on the intensity of synchrotron radiation and, therefore only an upper limit on the magnetic field strength can be determined (Section 1.3.1). Second, the angular resolution associated with the reconstructed spectrum is determined by the resolution at the lowest observing frequency. Unfortunately, for a typical multifrequency VLBA observation, the regions where spectral turnover is detected are not spatially resolved at low frequencies. Therefore, in the majority of cases, only an upper limit on the magnetic field strength can be determined. On the other hand, for the Gaussian component-based method it is possible to achieve “super-resolution” at lower frequencies by applying additional constraints on the model (such as fixing the number and relative positions of the model components) using information obtained at higher frequencies where angular resolution is better (Savolainen et al. 2008).

Finally, it should be noted, that it is not possible to use the convolved CLEAN images directly (even if the images are convolved with the same beam) to obtain spectra suitable for magnetic field strength estimation. The reason can be understood from Fig. 2.1. Convolution of the actual brightness distribution of the source (which is approximated by the CLEAN model) with a Gaussian produces large areas of artificial low flux surrounding each area where the actual flux is detected and signified by CLEAN component(s) placed in that area. These artificial low-flux areas (where there should be no flux at all) result in very high estimated values of B_{\perp} (Fig. 2.1a) around each spot with actual detected flux (and, therefore, a reasonable estimation of B_{\perp}). Therefore, only values in the center of the Fig. 2.1a where $B_{\perp} < 10$ G may be considered as reasonable upper limits on the magnetic field strength. The impossibility to distinguish areas with real flux from areas with a flux value assigned due to the convolution makes the use of convolved images for magnetic field distribution reconstruction impractical. The procedure of CLEAN-components summation within a certain radius can be considered an equivalent to the convolution of the CLEAN model with a box-shaped beam instead of the Gaussian-shaped beam.

2.2 Magnetic field in the parsec-scale core regions of bright γ -ray blazars

This section will describe application of the spectrum reconstruction method presented in Section 2.1 to a sample of 20 γ -ray bright blazars observed with the Very Long Baseline Array (VLBA) at seven frequencies in the range 4.6–43.2 GHz during the first year of the *Fermi* γ -ray observatory mission.

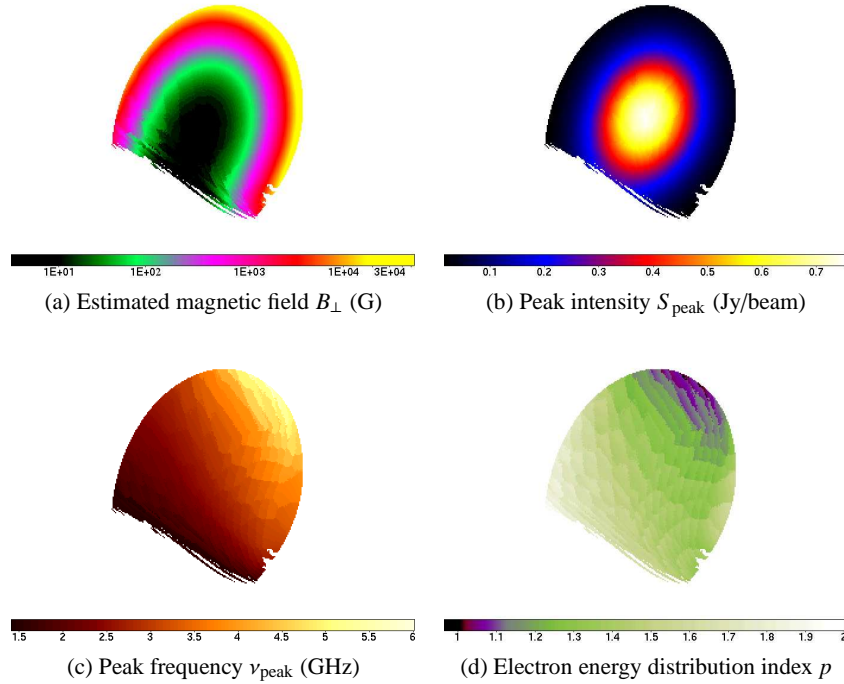


Figure 2.1: Maps of the best-fit synchrotron spectrum (Fig. 2.2) parameters and the estimated magnetic field strength derived from nine images (1.4–15.4 GHz range) of the source 1458+718 convolved with the same Gaussian beam. From this example it is clear why convolution with a Gaussian beam makes VLBI images unsuitable for magnetic field estimation. The convolved images have large areas of artificial low flux surrounding each area where the actual flux is detected (see the distribution of the peak intensity at Fig. 2.1b). These artificial low-flux areas (where there should be no flux at all) result in very high estimated values of B_{\perp} (Fig. 2.1a) around each spot with actual detected flux (and, therefore, a valid estimation of B_{\perp}). The peak frequency (Fig 2.1c) and power index of the electron energy distribution (Fig 2.1d) do not change much across the area and the effect of their changes is negligible compared to the effect of convolution. We note that only pixels where spectral turnover was detected (i.e. the spectrum in such pixel significantly deviates from a power law) are shown on the images.

2.2.1 Introduction

Blazars are active galactic nuclei characterized by highly variable non-thermal continuum emission across the electromagnetic spectrum (Section 1.1, Marscher (2006a, 2009)). Their radio to UV (sometimes – X-ray) emission is believed to be dominated by synchrotron radiation of relativistic electrons while radiation at higher energies could be due to the inverse Compton scattering of synchrotron photons emitted by the electrons themselves (the synchrotron self-Compton process, SSC, Ghisellini & Maraschi 1989; Jones et al. 1974) and photons from external sources (External Compton, EC, Dermer & Schlickeiser 2002; Sikora et al. 1994). The sources of the external seed photons for the EC process include the accretion disc, broad line region (BLR) clouds, warm dust and the cosmic microwave background (CMB), with their relative contribution varying for different blazars.

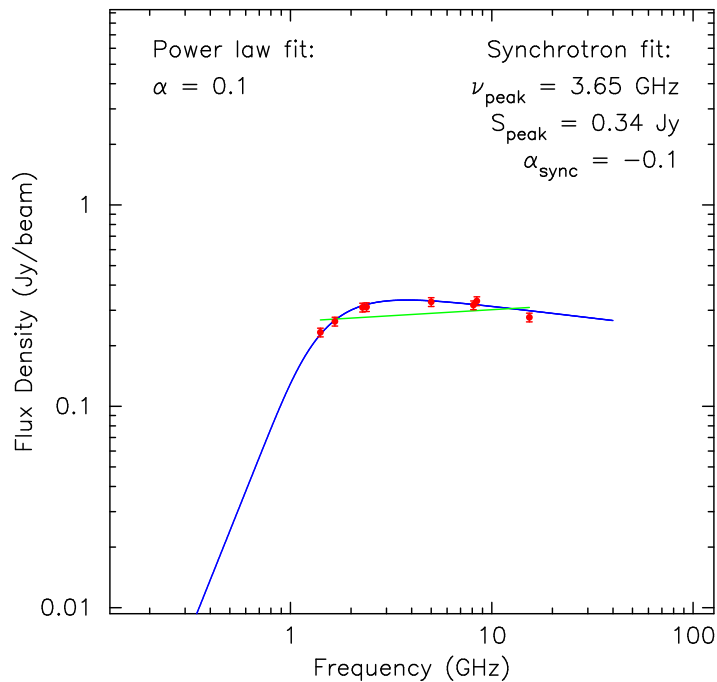


Figure 2.2: Spectrum of a single pixel (red points) in Fig. 2.1 compared to a power law (green line) and synchrotron spectrum (blue curve) fit. The synchrotron model clearly provides better fit to the data. Spatial distributions of the best-fit parameters of the synchrotron model: peak intensity S_{peak} , peak frequency ν_{peak} and electron energy distribution index p ($p = 1 - 2\alpha$, $S_{\nu} \propto \nu^{\alpha}$) are presented on Fig 2.1b, 2.1c and 2.1d respectively.

Despite the wide acceptance of the picture outlined above, the exact location, geometry and physical properties of the regions responsible for blazar emission at different bands remain largely unknown. Considerable success has been achieved by single-zone models (assuming a single spherical relativistically moving blob of magnetized plasma which emits synchrotron radiation and interacts with an ambient photon field) in explaining blazar emission from IR to γ -ray energies (among the many recent examples: Abdo et al. 2010a; Finke & Dermer 2010 and the references in Table 2.4). For additional discussion of the blazar emission see Section 1.1.

The Large Area Telescope (LAT; Atwood et al. 2009) on board the *Fermi* γ -ray observatory, launched on 2008 June 11, provides a wealth of new information about high-energy radiation of blazars. It is believed that this high-energy emission is intimately connected with the emission at lower energies (radio – optical) through the process of inverse Compton scattering. Very Long Baseline Interferometry (VLBI), with its spectacular angular resolution, provides the most detailed view of inner regions of blazars (Zensus 1997). In most cases, VLBI observations reveal one-sided relativistically beamed parsec-scale jets originating in a bright, compact region called the “core”.

The spatially resolved broad-band spectroscopy is one of the few methods that can probe the physical conditions inside blazar jets. Despite the great potential of this method, its applications are still relatively rare (see Savolainen et al. 2008 and references therein), owing to difficulties in implementing it and interpreting results obtained (Lobanov 1998a). In addition, multifrequency VLBI observations require

large amounts of observing time and most VLBI arrays lack technical capability to perform simultaneous multifrequency observations.

A significant fraction of blazar radio emission is known to originate at the extended parsec-scale jet and cannot be accounted for in the framework of a single-zone model. However, emission from individual jet components resolved with the Very Long Baseline Interferometry (VLBI) can usually be well described by a single uniform synchrotron source model (Marscher 1983, 2009; Pacholczyk 1970; Section 1.3). It is tempting to identify one of the jet components resolved by VLBI with the zone responsible for the emission at higher frequencies (Marscher 2006b; Unwin et al. 1994).

We utilize the NRAO's¹ Very Long Baseline Array (VLBA; Napier 1994) which has the unique capability to conduct observations quasi-simultaneously at many frequencies needed to constrain physical conditions in the regions where blazar radio emission originates. We reconstruct radio spectra of parsec-scale features in jets of selected γ -ray bright blazars and compare them with the simple homogeneous synchrotron source model, which allows us to derive information about the magnetic field strength and particle energy distribution.

2.2.2 Observations and data reduction

VLBA observation setup

Twenty blazars that were expected to be bright γ -ray emitters, prior to the launch of *Fermi* Gamma-ray Space Telescope were observed with the VLBA during eleven 7–14 h long dedicated sessions in September 2008 – June 2009. The list of the observed sources is presented in Table 2.1. Each source was observed simultaneously using C , X , K_u , K , and Q band receivers (according to the Institute of Electrical and Electronics Engineers or IEEE nomenclature, see Table 2.2) in the 4.6–43.2 GHz range. At each band four 8 MHz-wide frequency channels (IFs, Table 2.2) were recorded in both right and left circular polarizations with 2-bit sampling and a total aggregate bit rate of 128 Mbits/sec (6 sessions) or 256 Mbits/sec (5 sessions). The higher aggregation bit rate was used for faint sources. The correlation of the data was performed at the VLBA Array Operation Center in Socorro, NM, USA, with an averaging time of 2 seconds. Data in C and X bands were divided in two sub-bands (two IFs in each sub-band) centered at 4.6, 5.0, 8.1, and 8.4 GHz. K_u , K , and Q bands were not divided into sub-bands in order to achieve image sensitivity similar to lower frequencies in a comparable integration time; all four IFs were stacked together around 15.4, 23.8, and 43.2 GHz respectively. The central frequencies of the sub-bands were chosen in such a way that at least one sub-band in each band is centered at a frequency for which antenna gain curve measurements are available. A special procedure was applied to ensure accurate amplitude calibration of all sub-bands (the procedure is described in Section 4.2.3).

VLBA data calibration and imaging

The initial calibration was conducted in *AIPS* (Greisen 2003) following the standard VLBA calibration procedure involving a priori amplitude calibration with measured antenna gain curves and system temperatures, phase calibration using the phase-cal signal injected during observations and fringe fitting. The fringe fitting was performed by the task *FRING*. A separate solution for the group delay and phase rate was made

¹The National Radio Astronomy Observatory: <http://www.nrao.edu/>

Table 2.1: A sample of γ -ray bright blazars observed with the VLBA

Name	Alias	R.A. (J2000)	Dec. (J2000)	z	Optical class	VLBA epoch
0235+164		02:38:38.930107	+16:36:59.27449	0.940	QSO	A: 2008-09-02
0528+134		05:30:56.416749	+13:31:55.14944	2.07	QSO	C: 2008-10-02
0716+714		07:21:53.448480	+71:20:36.36341	0.31 ^a	BL Lac	G: 2009-02-05
0827+243	OJ 248	08:30:52.086195	+24:10:59.82027	0.939	QSO	H: 2009-04-09
0851+202	OJ 287	08:54:48.874931	+20:06:30.64077	0.306	BL Lac	F: 2009-02-02
1101+384	Mrk 421	11:04:27.313945	+38:12:31.79895	0.031	BL Lac	I: 2009-04-22
1219+285	W Comae	12:21:31.690524	+28:13:58.50011	0.161 ^b	BL Lac	J: 2009-05-14
1226+023	3C 273	12:29:06.699731	+02:03:08.59795	0.158	QSO	G: 2009-02-05
1253-055	3C 279	12:56:11.166556	-05:47:21.52491	0.538	QSO	F: 2009-02-02
1406-076		14:08:56.481198	-07:52:26.66661	1.493	QSO	I: 2009-04-22
1510-089		15:12:50.532927	-09:05:59.82980	0.360	QSO	H: 2009-04-09
1622-297		16:26:06.020840	-29:51:26.97132	0.815	QSO	K: 2009-06-01
1633+383	4C 38.41	16:35:15.492974	+38:08:04.50043	1.807	QSO	L: 2009-06-20
1652+398	Mrk 501	16:53:52.216683	+39:45:36.60879	0.033	BL Lac	J: 2009-05-14
1730-130	NRAO 530	17:33:02.705786	-13:04:49.54839	0.902	QSO	L: 2009-06-20
1959+650		19:59:59.852086	+65:08:54.65262	0.047	BL Lac	D: 2008-10-23
2155-304		21:58:52.065130	-30:13:32.11833	0.116	BL Lac	B: 2008-09-05
2200+420	BL Lacertae	22:02:43.291371	+42:16:39.97985	0.069	BL Lac	A: 2008-09-02
2251+158	3C 454.3	22:53:57.747940	+16:08:53.56075	0.859	QSO	C: 2008-10-02
2344+514		23:47:04.836815	+51:42:17.88146	0.044	BL Lac	D: 2008-10-23

Column designation: Col. 1 – IAU source name (B1950), Col. 2 – commonly used source name, Col. 3 and 4 – VLBI position, for details see http://astrogeo.org/vlbi/solutions/rfc_2010c/ and Beasley et al. (2002); Fomalont et al. (2003); Kovalev et al. (2007); Petrov et al. (2009, 2005, 2006, 2008), Col. 5 and 6 – redshift and optical class from Véron-Cetty & Véron (2010), Col. 7 – one-letter epoch code and the corresponding date of multi-frequency VLBA observations reported in this work.

^a Photometric redshift obtained by Nilsson et al. (2008).

^b Photometric redshift, see Finke et al. (2008).

for each frequency channel (IF). As the final step of calibration, bandpass corrections were applied utilizing the task *BPASS*.

Table 2.2: IF central frequencies

IEEE Band	IF	Frequency (MHz)
<i>C</i>	1	4604.49
<i>C</i>	2	4612.49
<i>C</i>	3	4999.49
<i>C</i>	4	5007.49
<i>X</i>	1	8104.49
<i>X</i>	2	8112.49
<i>X</i>	3	8425.49
<i>X</i>	4	8433.49
<i>K_u</i>	1	15353.49
<i>K_u</i>	2	15361.49
<i>K_u</i>	3	15369.49
<i>K_u</i>	4	15377.49
<i>K</i>	1	23792.49
<i>K</i>	2	23800.49
<i>K</i>	3	23808.49
<i>K</i>	4	23816.49
<i>Q</i>	1	43205.49
<i>Q</i>	2	43213.49
<i>Q</i>	3	43221.49
<i>Q</i>	4	43229.49

Column designation: Col. 1 – Radio band name according to the IEEE radar band nomenclature, Col. 2 – number of the frequency channel (IF), Col. 3 – central frequency of the frequency channel (IF).

The sources were imaged independently in each band, using the CLEAN algorithm

(Högbom 1974) implemented in the *Difmap* software (Shepherd 1997). Global amplitude corrections for left and right circular polarization for each IF at each antenna were determined by comparing the total intensity CLEAN model obtained with the initially calibrated data (again using *Difmap*). The amplitude corrections obtained were averaged over all the sources observed in the experiment. The significant amplitude correction factors which were found are listed in Table 2.3. These amplitude corrections were introduced into the dataset using the *AIPS* task *CLCOR*. After that *C* and *X* band data were split into two sub-bands as described above and final total intensity imaging for each sub-band was conducted independently using *Difmap*. The resulting accuracy of the amplitude calibration is expected to be $\sim 5\%$ at *C*, *X*, and K_u bands and $\sim 10\%$ at *K* and *Q* bands.

2.2.3 Results

Parsec-scale radio emission of all the observed sources (Table 2.4) is dominated by a bright unresolved core (the apparent origin of the jet (Fig. 2.3), see a discussion by Marscher 2008, see also Chapter 4). The radio spectra in the parsec-scale core regions of the observed blazars have diverse properties. Most of them are nearly flat, with signs of curvature at lower frequencies, which we interpret as synchrotron self-absorption. Cores in four sources (0716+714, OJ 287, 1622–297, and 3C 454.3) show inverted spectra which are slightly curved. The core spectrum of only one source (1510–089) can be adequately described by a simple power law in the whole 4.6–43.2 GHz frequency range. Fig. 2.4 compares core radio spectra of 1510–089 and OJ 248. In the following, we focus on sources that show a well defined spectral turnover, and thus can be used to determine the physical conditions in the emitting plasma.

Table 2.3: Amplitude corrections for the BK150 VLBA experiment

Ant.	Band	IF	Epoch	Polarization	Corr.
BR	<i>C</i>	1	A, B, C, D	R	1.10
BR	<i>C</i>	2	A, B, C, D	R	1.11
MK	<i>C</i>	1	A, B, C, D	R	1.22
MK	<i>C</i>	2	A, B, C, D	R	1.18
BR	<i>C</i>	1	F, G, H, I	R	1.11
BR	<i>C</i>	2	F, G, H, I	R	1.11
HN	<i>C</i>	1	F	R	1.16
HN	<i>C</i>	2	F	R	1.15
HN	<i>C</i>	3	F	R	1.22
HN	<i>C</i>	4	F	R	1.22
HN	<i>C</i>	1	G	R	1.09
HN	<i>C</i>	2	G	R	1.08
HN	<i>C</i>	3	G	R	1.14
HN	<i>C</i>	4	G	R	1.14
KP	<i>C</i>	1	H	R	1.10
KP	<i>C</i>	2	H	R	1.09
KP	<i>C</i>	1	I	R	1.10
KP	<i>C</i>	2	I	R	1.10
BR	<i>C</i>	1–2	J, K, L	R	1.09
KP	<i>C</i>	1–2	J, K, L	R	1.08
KP	<i>C</i>	1	A, B, C, D	L	1.11
KP	<i>C</i>	2	A, B, C, D	L	1.14
KP	<i>C</i>	1	F, G, H, I	L	1.12
KP	<i>C</i>	2	F, G, H, I	L	1.14
HN	<i>C</i>	1	F	L	1.18
HN	<i>C</i>	2	F	L	1.22
HN	<i>C</i>	3	F	L	1.21
HN	<i>C</i>	4	F	L	1.15
HN	<i>C</i>	1	G	L	1.10
HN	<i>C</i>	2	G	L	1.14
HN	<i>C</i>	3	G	L	1.13

HN	C	4	G	L	1.07
KP	C	1	J, K, L	L	1.10
KP	C	2	J, K, L	L	1.14
KP	X	1	A, B, C, D	R	0.89
KP	X	2	A, B, C, D	R	0.90
KP	X	1	F, G, H, I	R	0.89
KP	X	2	F, G, H, I	R	0.90
HN	X	1	F	R	1.24
HN	X	2	F	R	1.22
HN	X	3	F	R	1.26
HN	X	4	F	R	1.25
HN	X	4	I	R	1.11
HN	X	1	G	R	1.15
HN	X	2	G	R	1.13
HN	X	3	G	R	1.15
HN	X	4	G	R	1.15
KP	X	1	J, K, L	R	0.89
KP	X	2	J, K, L	R	0.90
OV	X	1	A, B, C, D	L	1.07
SC	X	1	A, B, C, D	L	1.07
HN	X	1	F	L	1.26
HN	X	2	F	L	1.29
HN	X	3	F	L	1.20
HN	X	4	F	L	1.16
HN	X	1	G	L	1.16
HN	X	2	G	L	1.19
HN	X	3	G	L	1.13
HN	X	4	G	L	1.08
HN	K_u	1	F	R	1.20
HN	K_u	2	F	R	1.16
HN	K_u	3	F	R	1.20
HN	K_u	4	F	R	1.20
HN	K_u	1	G	R	1.17
HN	K_u	2	G	R	1.14
HN	K_u	3	G	R	1.16
HN	K_u	4	G	R	1.16
LA	K_u	3	J, K, L	R	1.05
BR	K_u	4	F, G, H, I	R, L	0.94
BR	K_u	4	J, K, L	R, L	0.95
SC	K_u	1	F, G, H, I	L	1.07
HN	K_u	1	F	L	1.24
HN	K_u	2	F	L	1.24
HN	K_u	3	F	L	1.22
HN	K_u	4	F	L	1.16
HN	K_u	1	G	L	1.20
HN	K_u	2	G	L	1.20
HN	K_u	3	G	L	1.18
HN	K_u	4	G	L	1.12
SC	K_u	1	J, K, L	L	1.06
BR	K	1	A, B, C	R	1.13
BR	K	2	A, B, C	R	1.09
SC	K	1-4	A	R	1.14
HN	K	1-4	B	R	1.20
BR	K	1	D	R	0.95
BR	K	2	D	R	0.92
BR	K	3	D	R	0.88
BR	K	4	D	R	0.87
BR	K	3	F	R	0.91
BR	K	4	F	R	0.89
BR	K	3	G	R	0.90
BR	K	4	G	R	0.88
BR	K	1	H	R	0.93
BR	K	2	H	R	0.90
BR	K	3	H	R	0.88
BR	K	4	H	R	0.87
HN	K	1	F	R	1.20
HN	K	2	F	R	1.22
HN	K	3	F	R	1.26

HN	K	4	F	R	1.26
HN	K	1	G	R	1.25
HN	K	2	G	R	1.26
HN	K	3	G	R	1.31
HN	K	4	G	R	1.29
BR	K	1-4	K	R	1.20
BR	K	1-4	L	R	1.13
NL	K	1-4	L	R	1.16
SC	K	1-4	H	R, L	1.11
HN	K	1-4	I	R, L	1.10
SC	K	1-4	A	L	1.14
HN	K	1-4	B	L	1.20
BR	K	1	D	L	0.95
BR	K	2	D	L	0.96
BR	K	3	D	L	0.93
BR	K	4	D	L	0.89
BR	K	1	H	L	0.87
BR	K	2	H	L	0.88
BR	K	3	H	L	0.84
BR	K	4	H	L	0.80
BR	K	1	I	L	0.88
BR	K	2	I	L	0.90
BR	K	3	I	L	0.86
BR	K	4	I	L	0.83
HN	K	1	F	L	1.22
HN	K	2	F	L	1.28
HN	K	3	F	L	1.30
HN	K	4	F	L	1.22
HN	K	1	G	L	1.24
HN	K	2	G	L	1.31
HN	K	3	G	L	1.31
HN	K	4	G	L	1.23
NL	K	1-4	L	L	1.12
SC	K	3	L	L	0.90
FD	Q	1-4	A, B, C, D	R	0.835
NL	Q	1-4	A	R	1.18
NL	Q	1-4	B	R	1.11
SC	Q	1-4	B	R	1.14
BR	Q	1-4	D	R	1.10
FD	Q	1	F	R	1.15
HN	Q	1	F	R	1.26
HN	Q	2	F	R	1.25
HN	Q	3	F	R	1.28
HN	Q	4	F	R	1.29
HN	Q	1	G	R	1.56
HN	Q	2	G	R	1.55
HN	Q	3	G	R	1.58
HN	Q	4	G	R	1.61
NL	Q	1-4	L	R, L	1.40
NL	Q	1-4	A	L	1.18
NL	Q	1-4	B	L	1.11
SC	Q	1-4	B	L	1.14
BR	Q	1-4	D	L	1.10
HN	Q	1	F	L	1.34
HN	Q	2	F	L	1.35
HN	Q	3	F	L	1.36
HN	Q	4	F	L	1.30
HN	Q	1	G	L	1.68
HN	Q	2	G	L	1.67
HN	Q	3	G	L	1.67
HN	Q	4	G	L	1.61
OV	Q	1-4	K	L	0.92

Column designation: Col. 1 – Antenna name, Col. 2 – radio band name, Col. 3 – number of the frequency channel (IF), Col. 4 – epoch to which the amplitude correction was applied (date corresponding to an epoch name may be found in Table 2.1), Col. 5 – polarization (right or left circular), Col. 6 – amplitude correction coefficient.

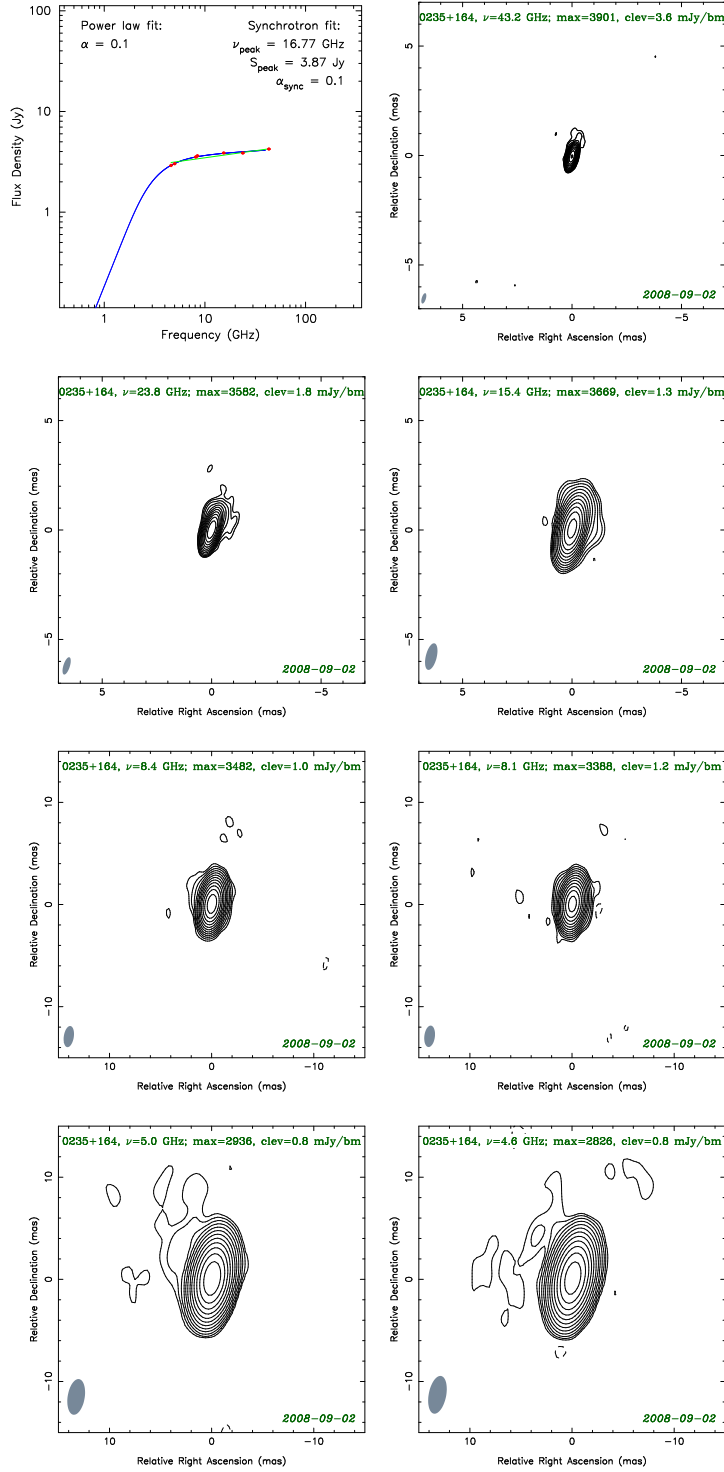


Figure 2.3: Spectrum of the core and naturally weighted CLEAN images of the γ -ray bright blazars observed with the VLBA between 4.6 and 43.2 GHz. The lowest contour value ‘clev’ is chosen at four times the rms noise, the peak brightness is given by ‘max’. The contour levels increase by factors of two. The dashed contours indicate negative brightness. The half power beam width is shown in the bottom left corner of the images in grey. An epoch of observation is shown in the bottom right corner.

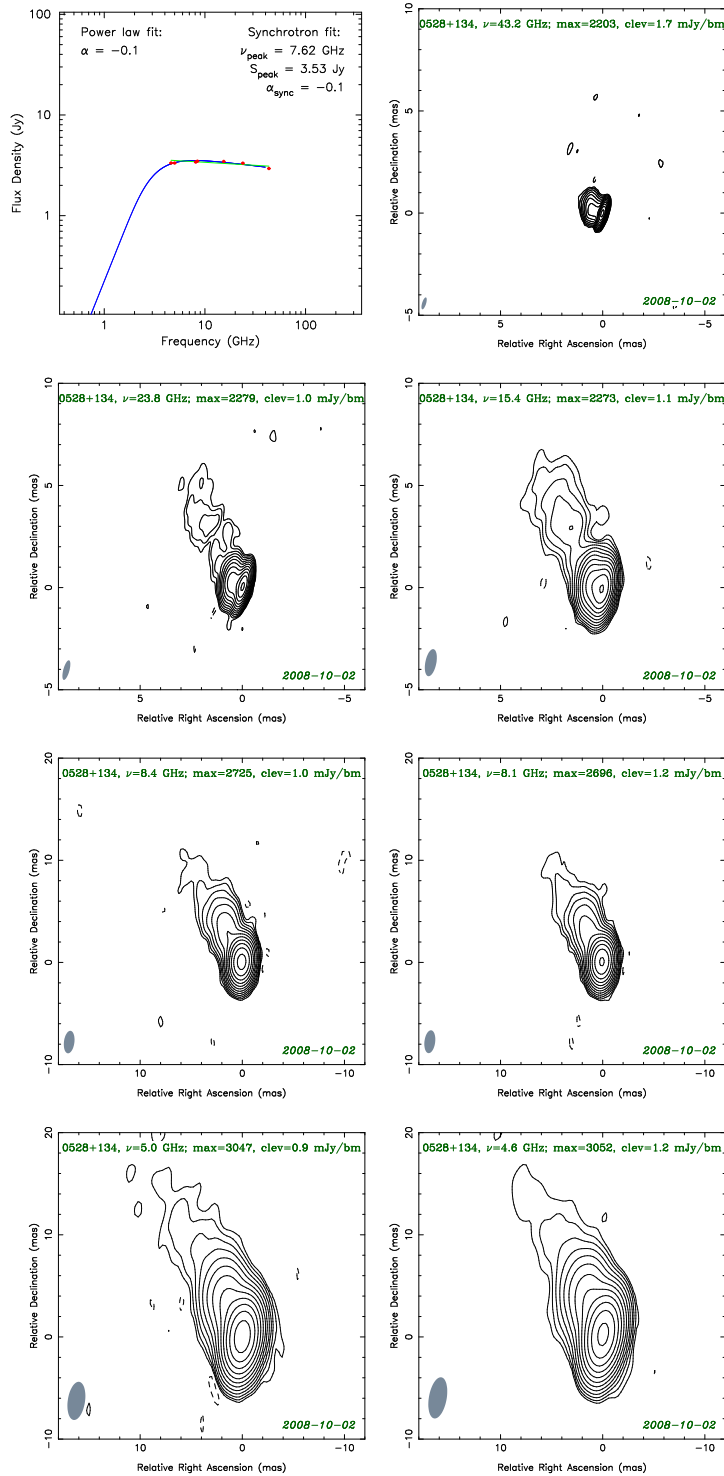


Figure 4.1 continued...

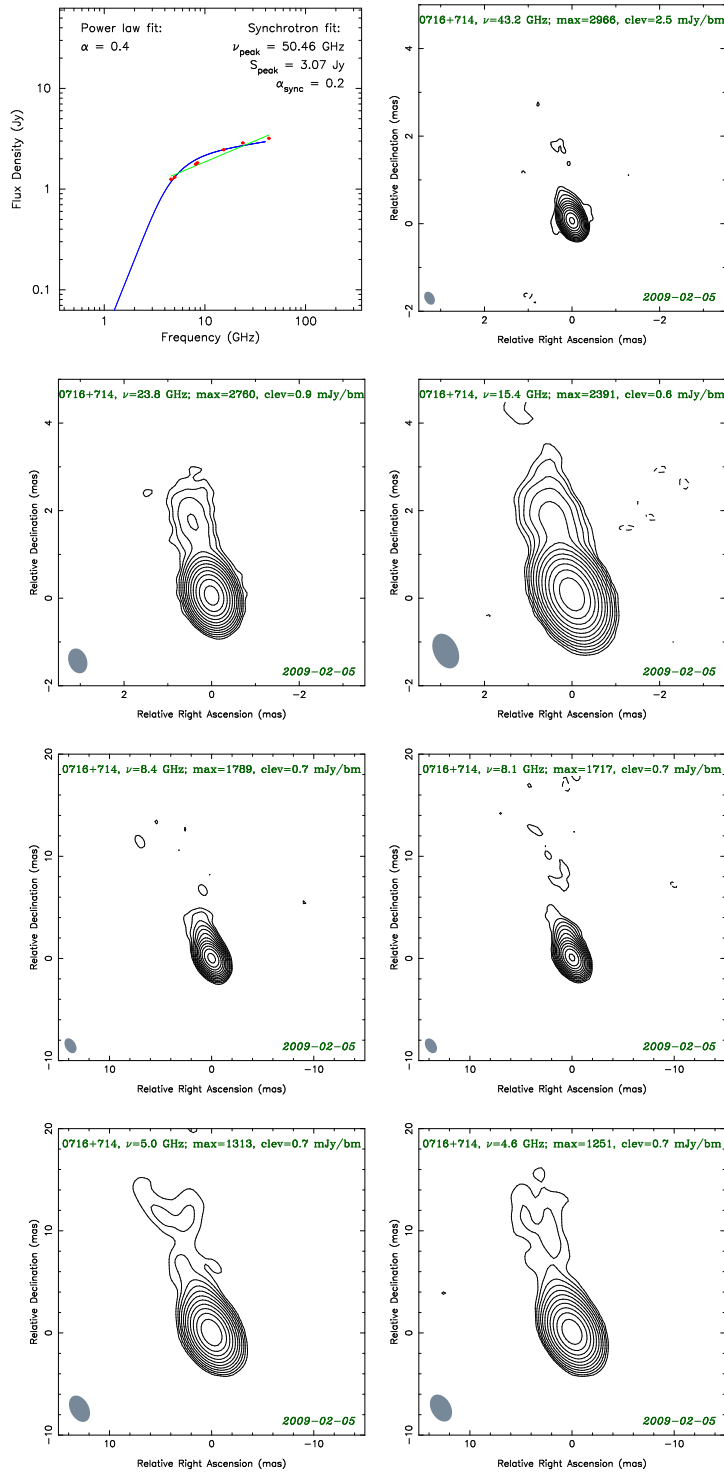


Figure 4.1 continued...

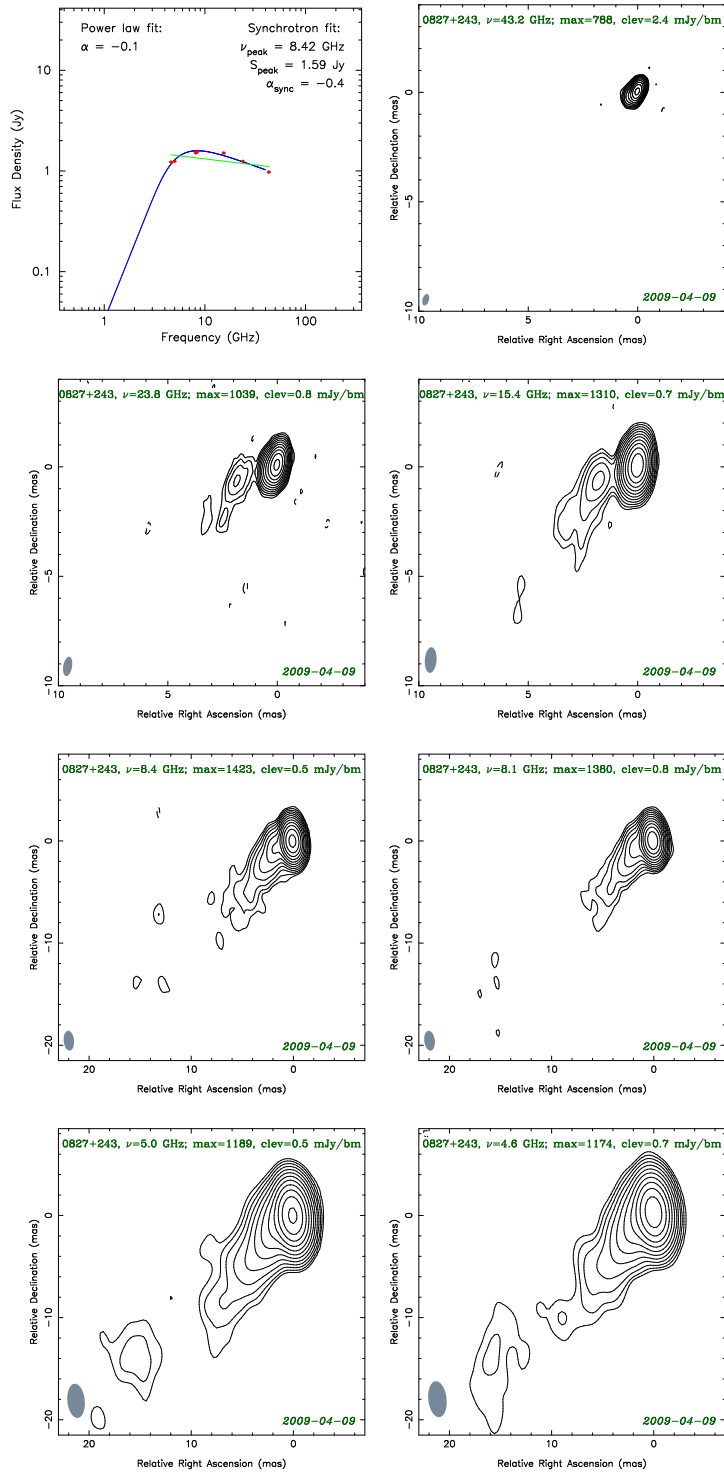


Figure 4.1 continued...

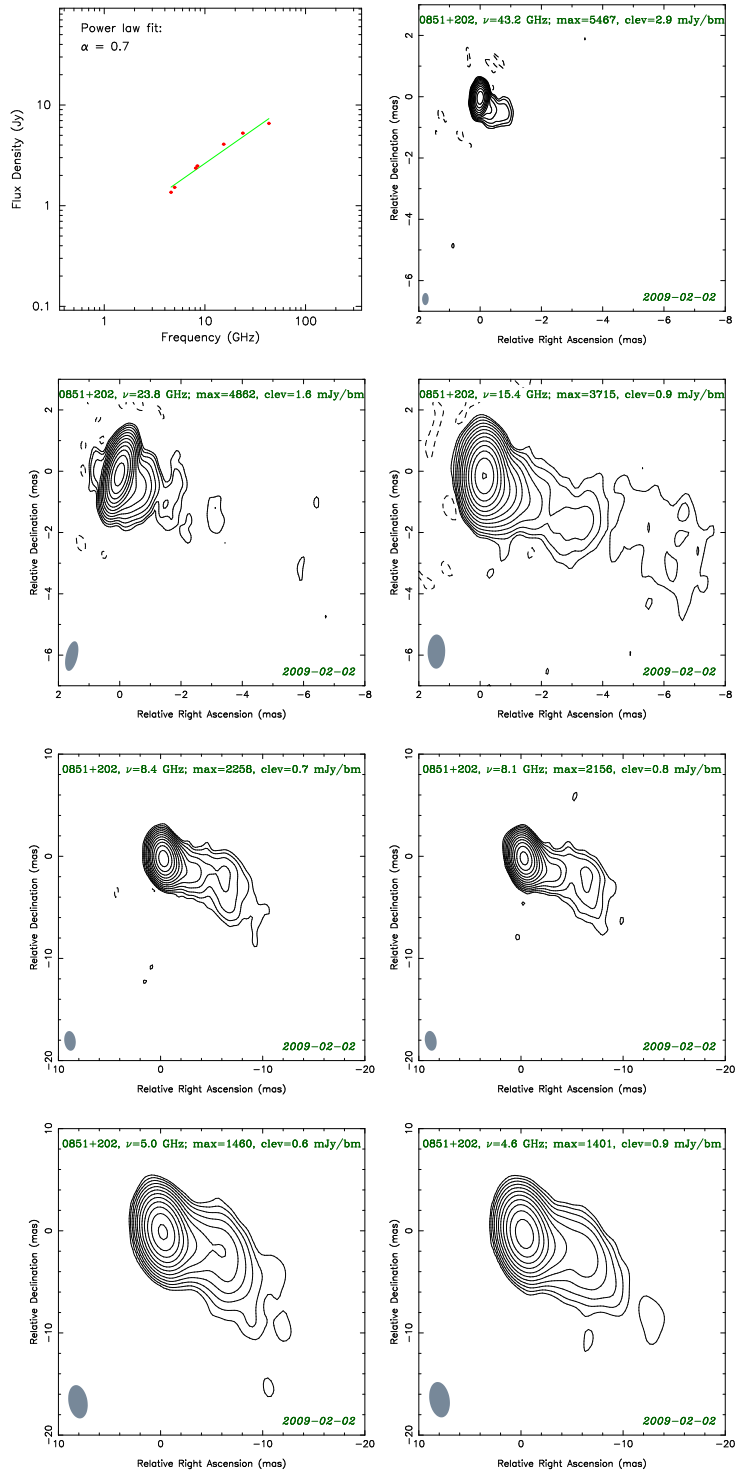


Figure 4.1 continued...

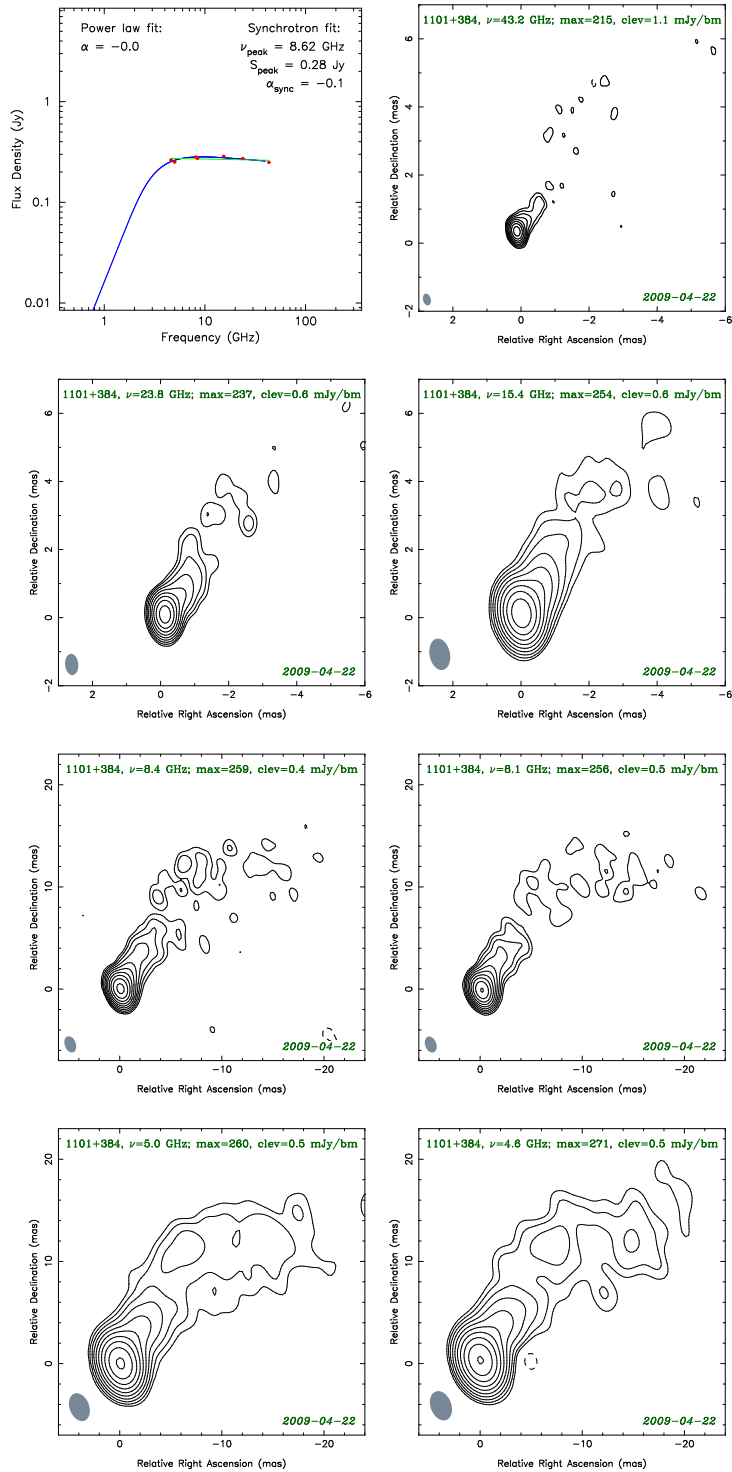


Figure 4.1 continued...

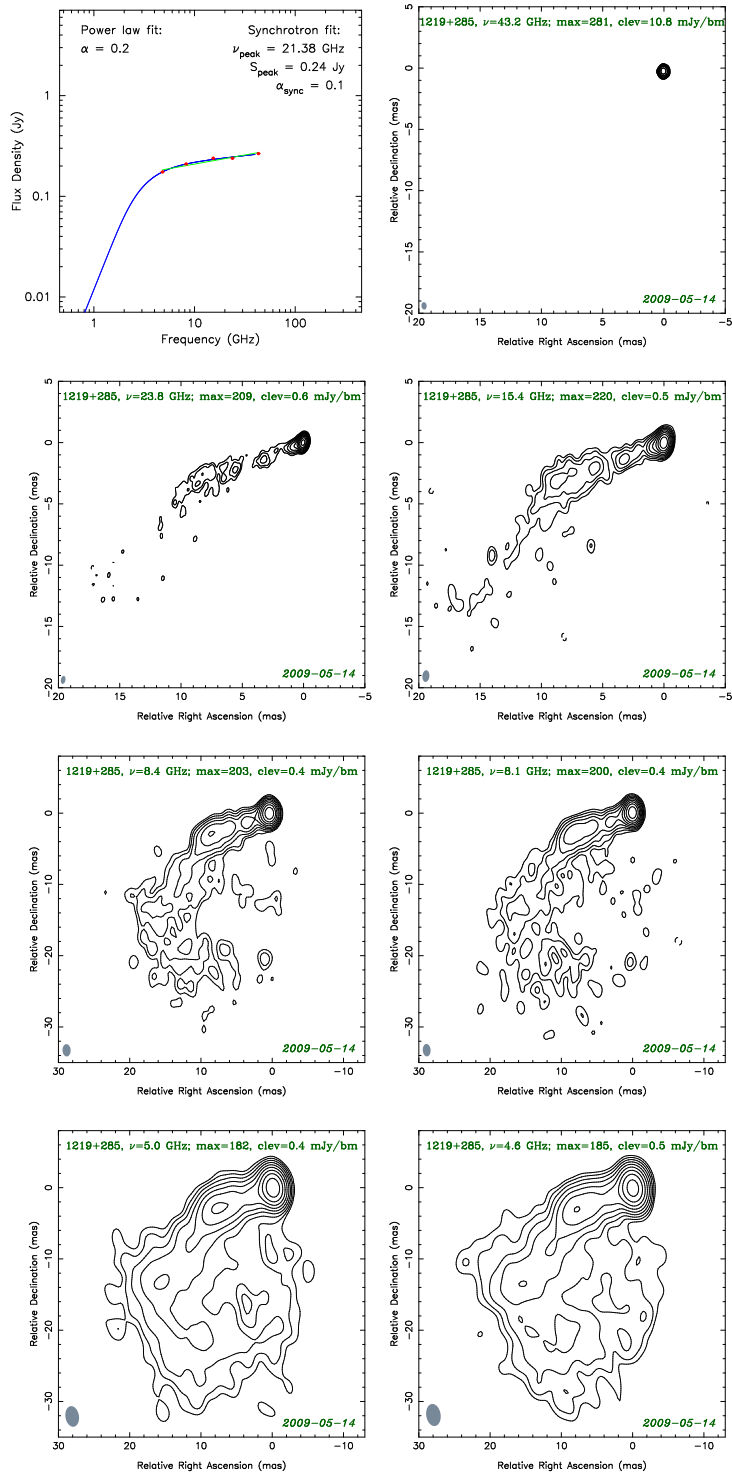


Figure 4.1 continued...

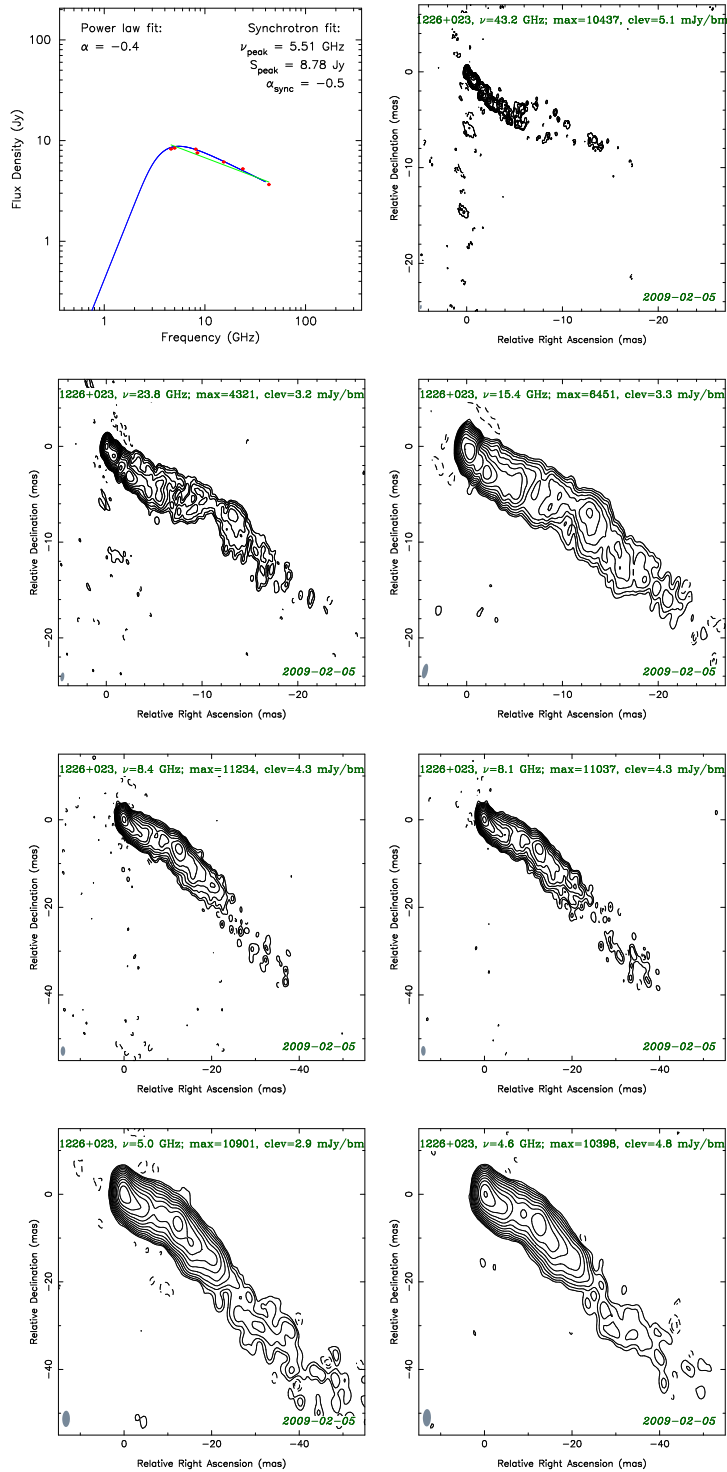


Figure 4.1 continued...

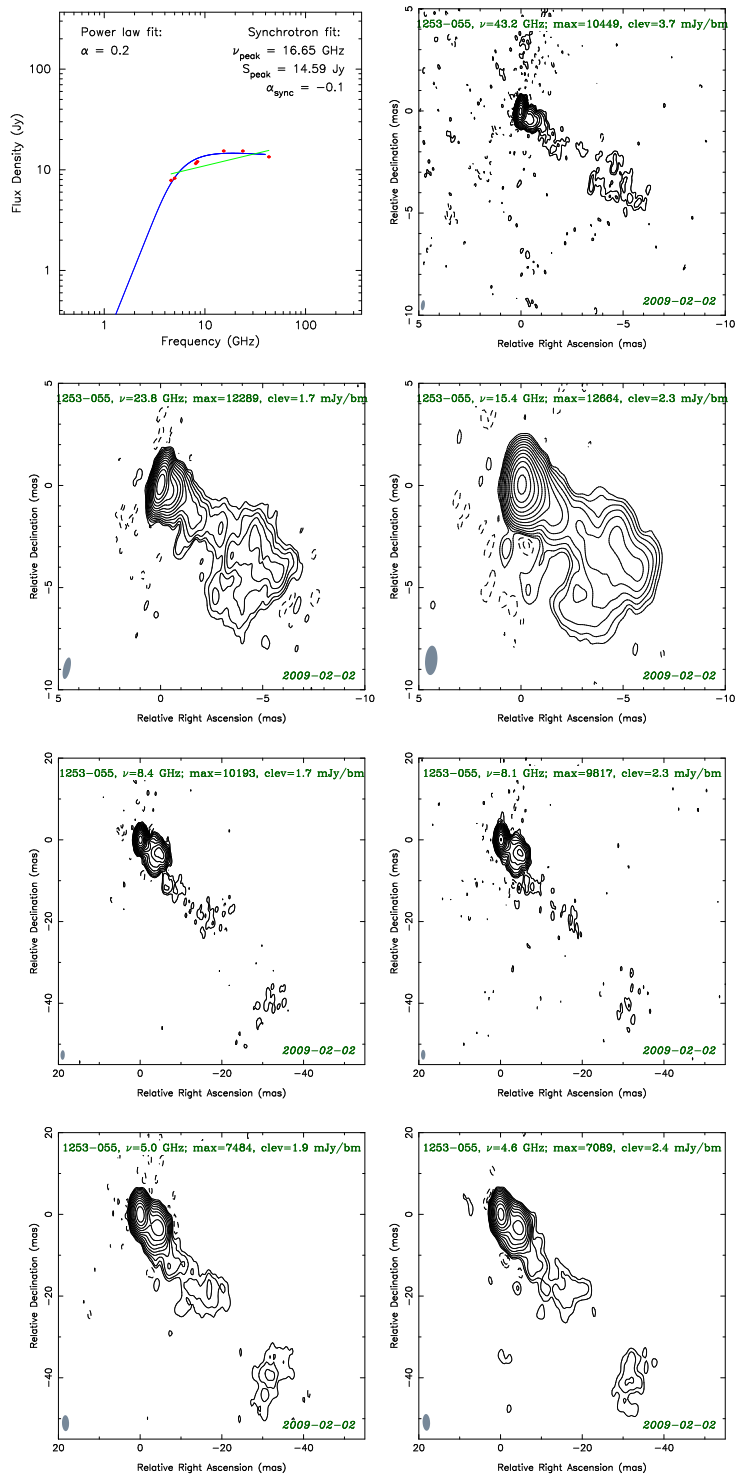


Figure 4.1 continued...

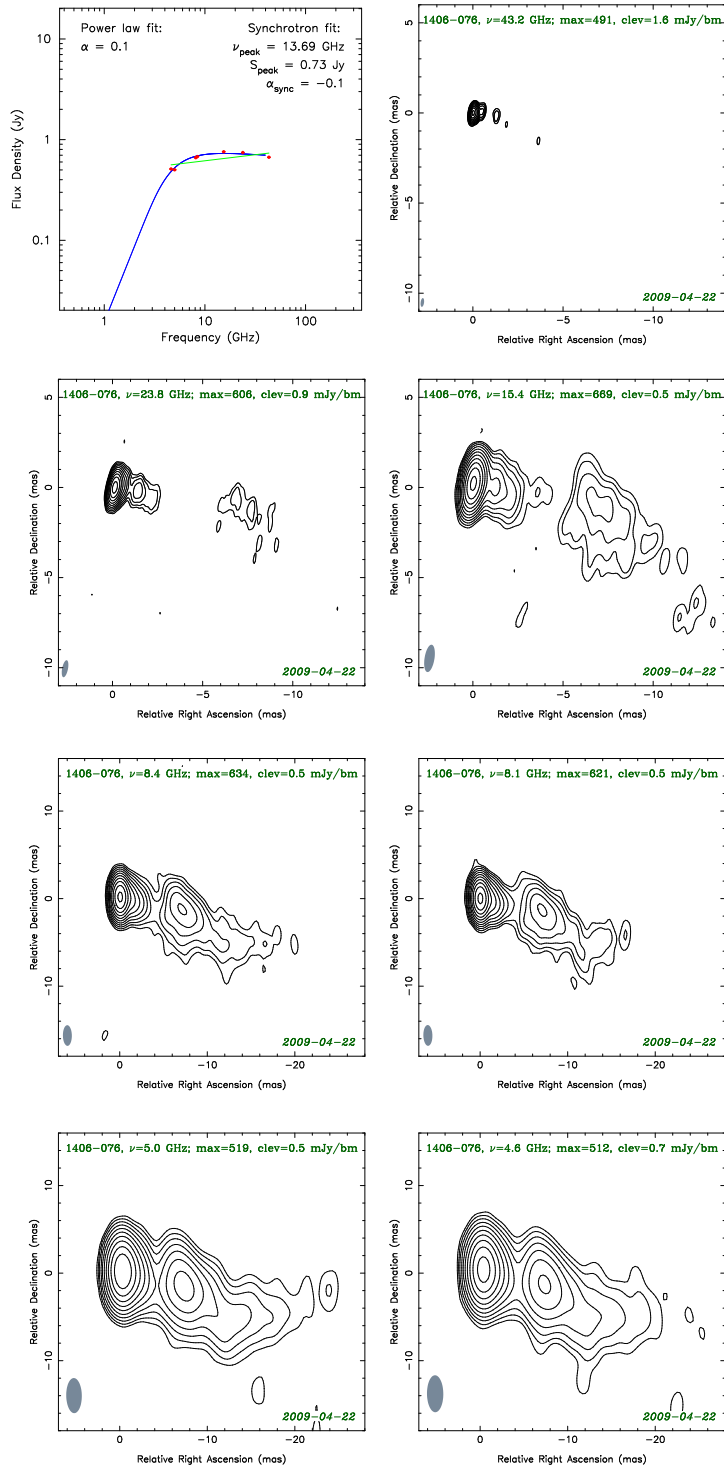


Figure 4.1 continued...

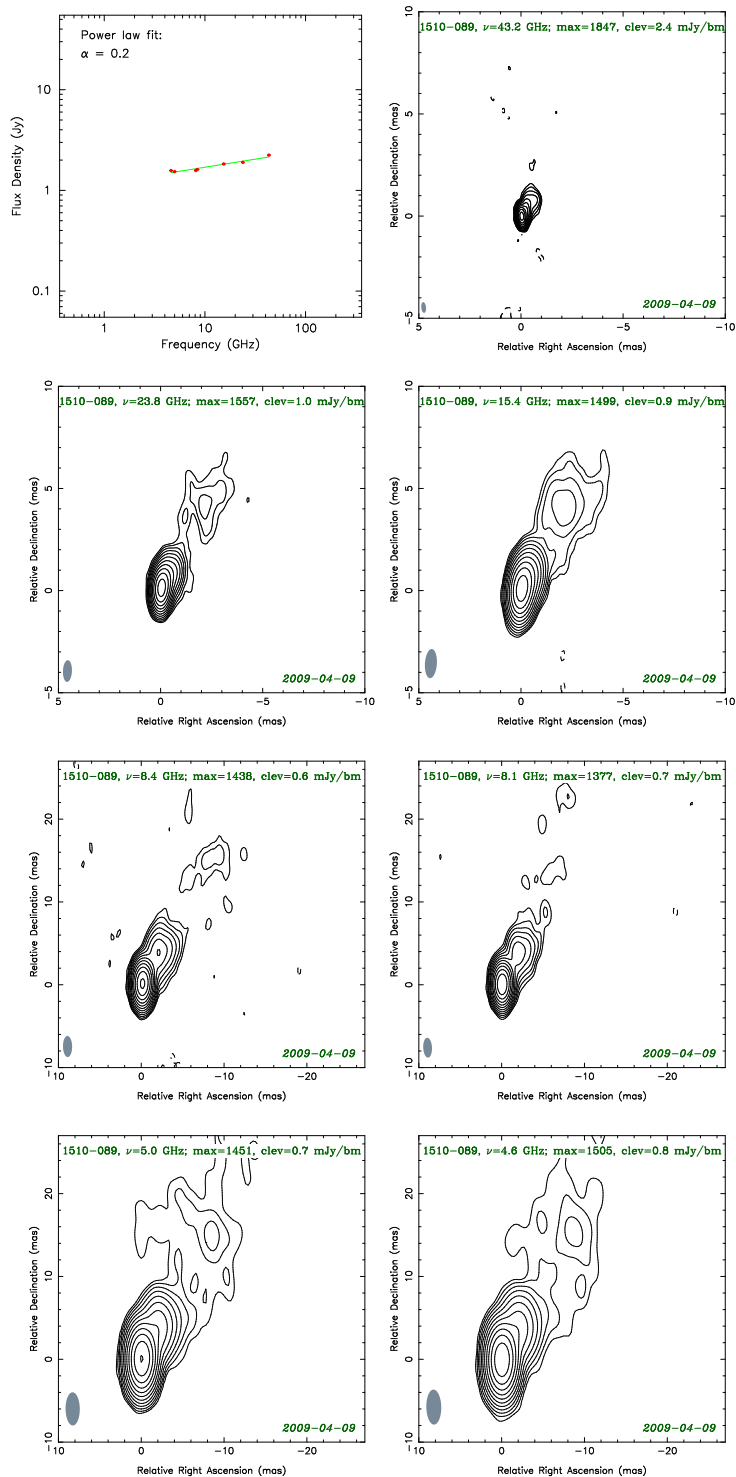


Figure 4.1 continued...

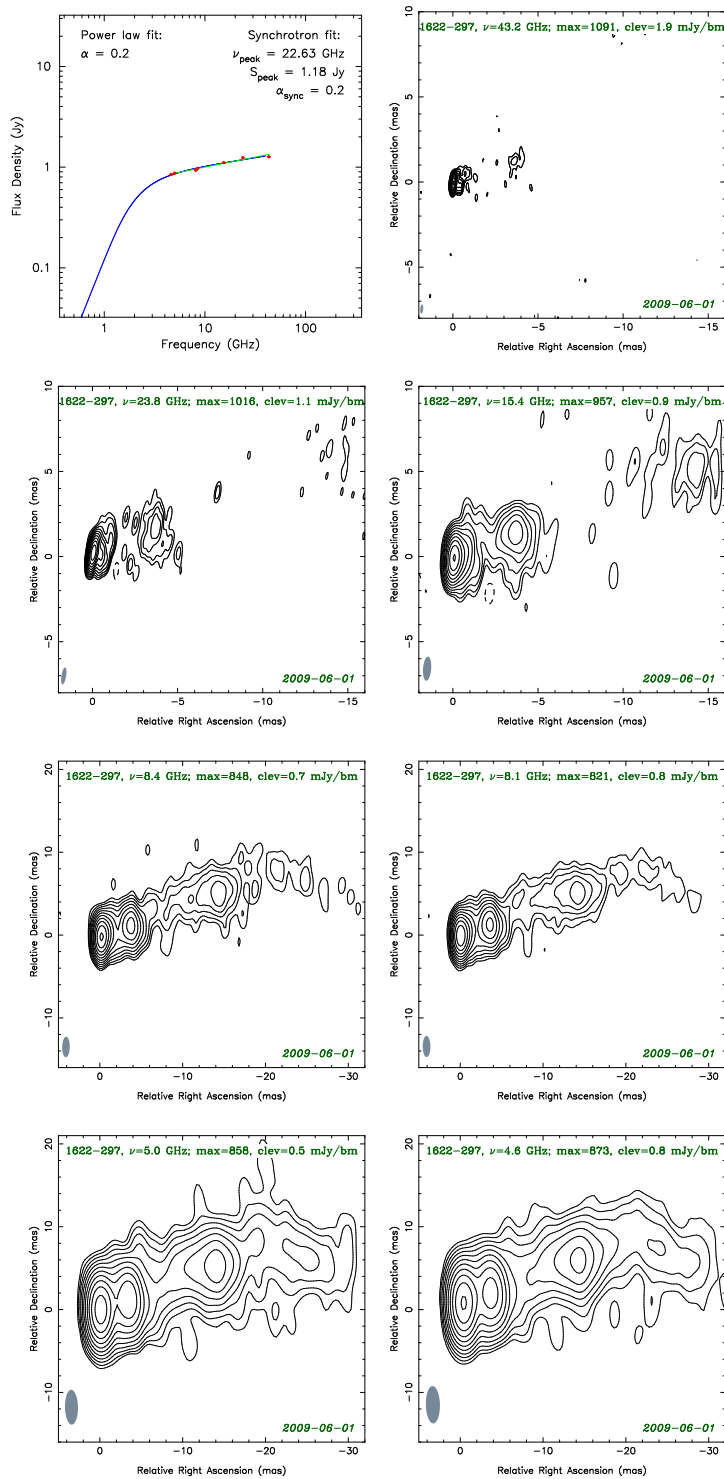


Figure 4.1 continued...

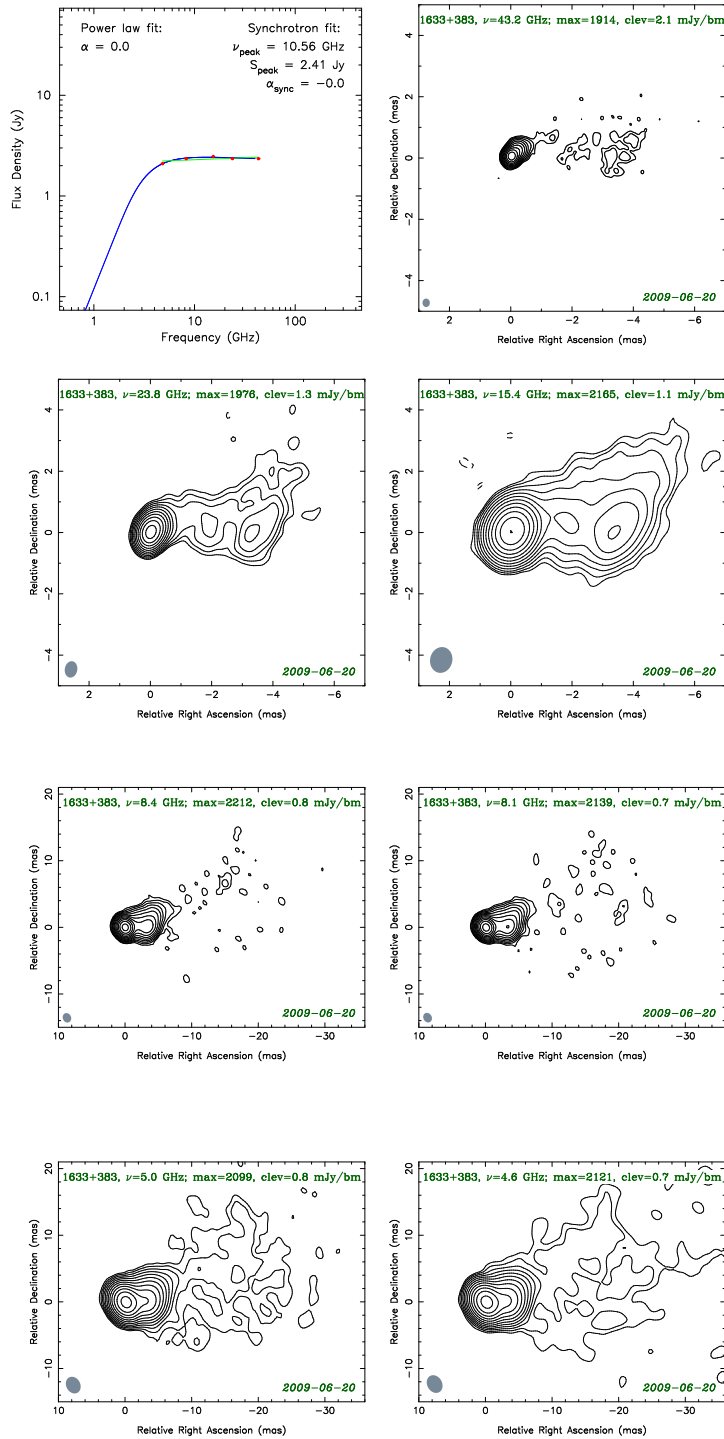


Figure 4.1 continued...

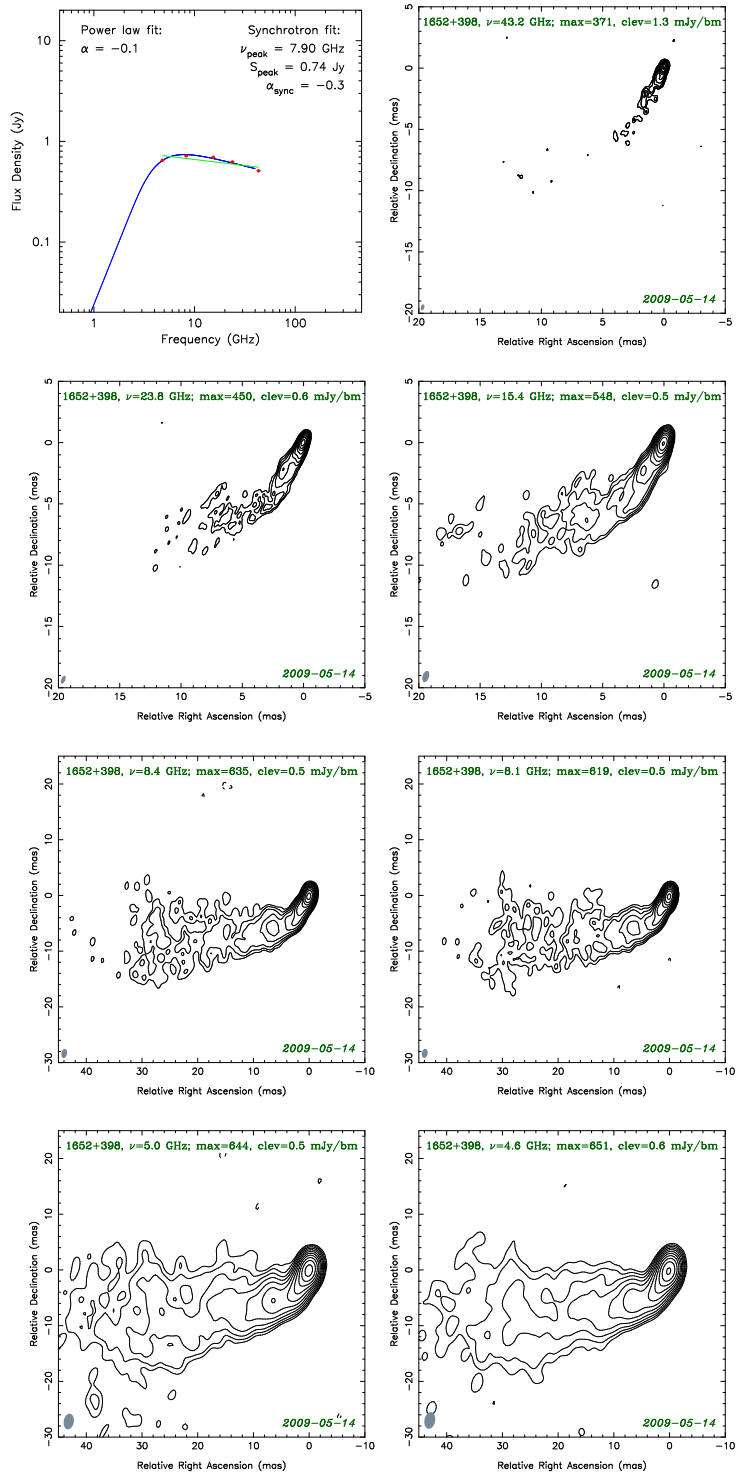


Figure 4.1 continued...

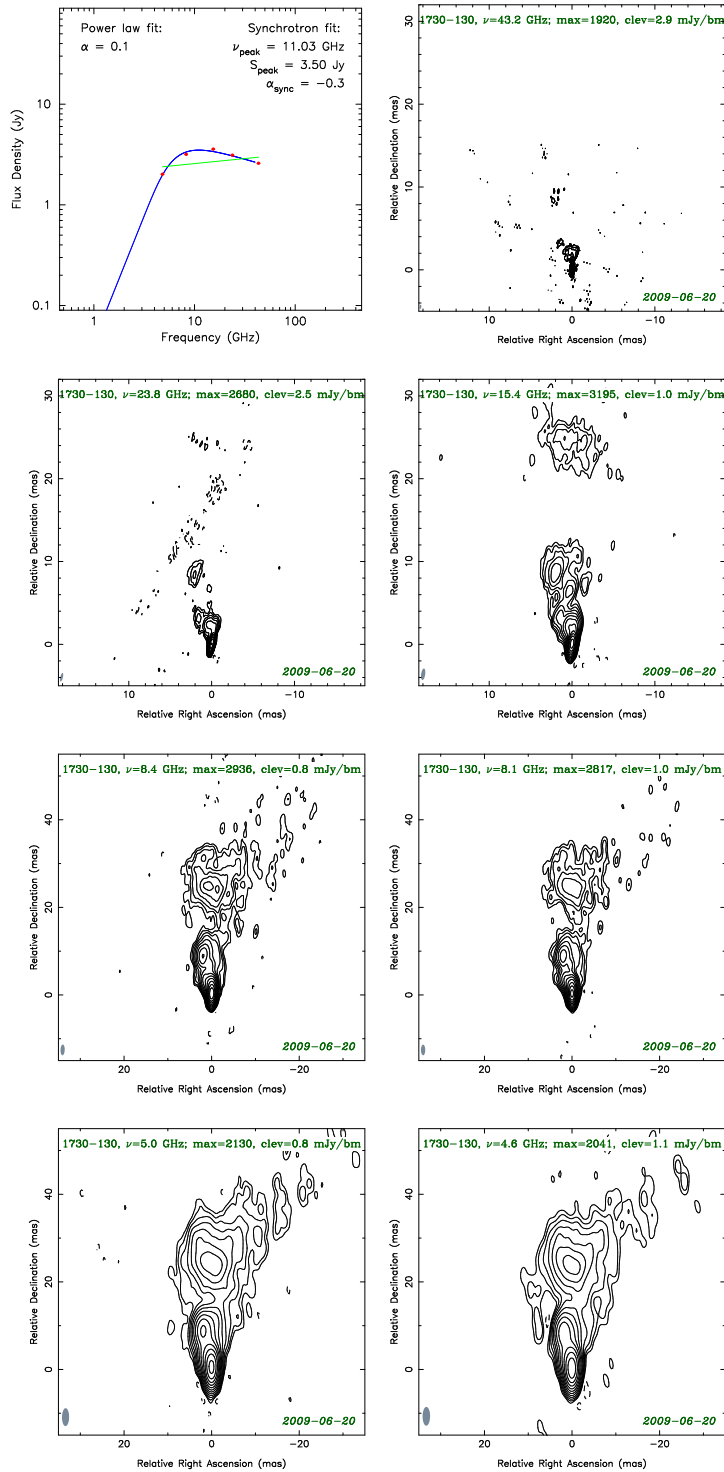


Figure 4.1 continued...

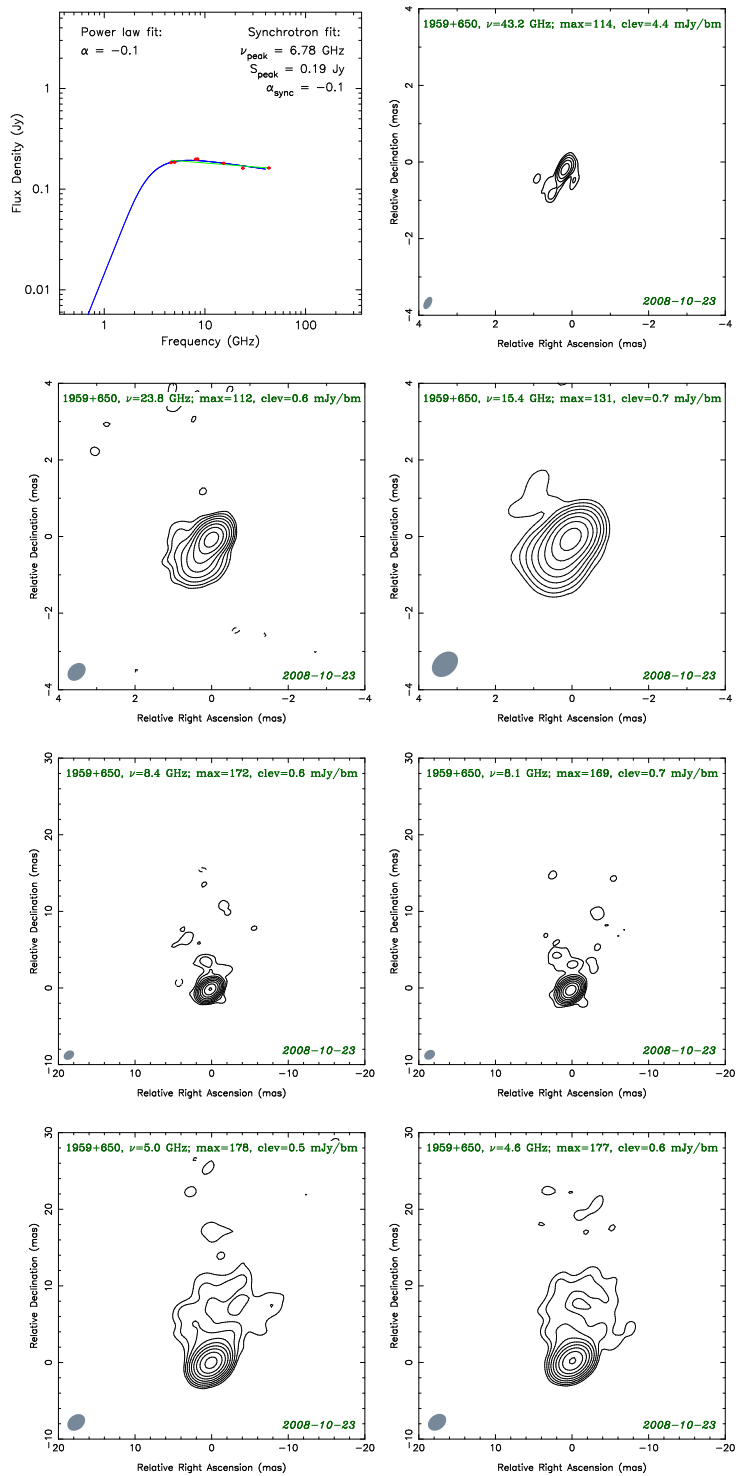


Figure 4.1 continued...

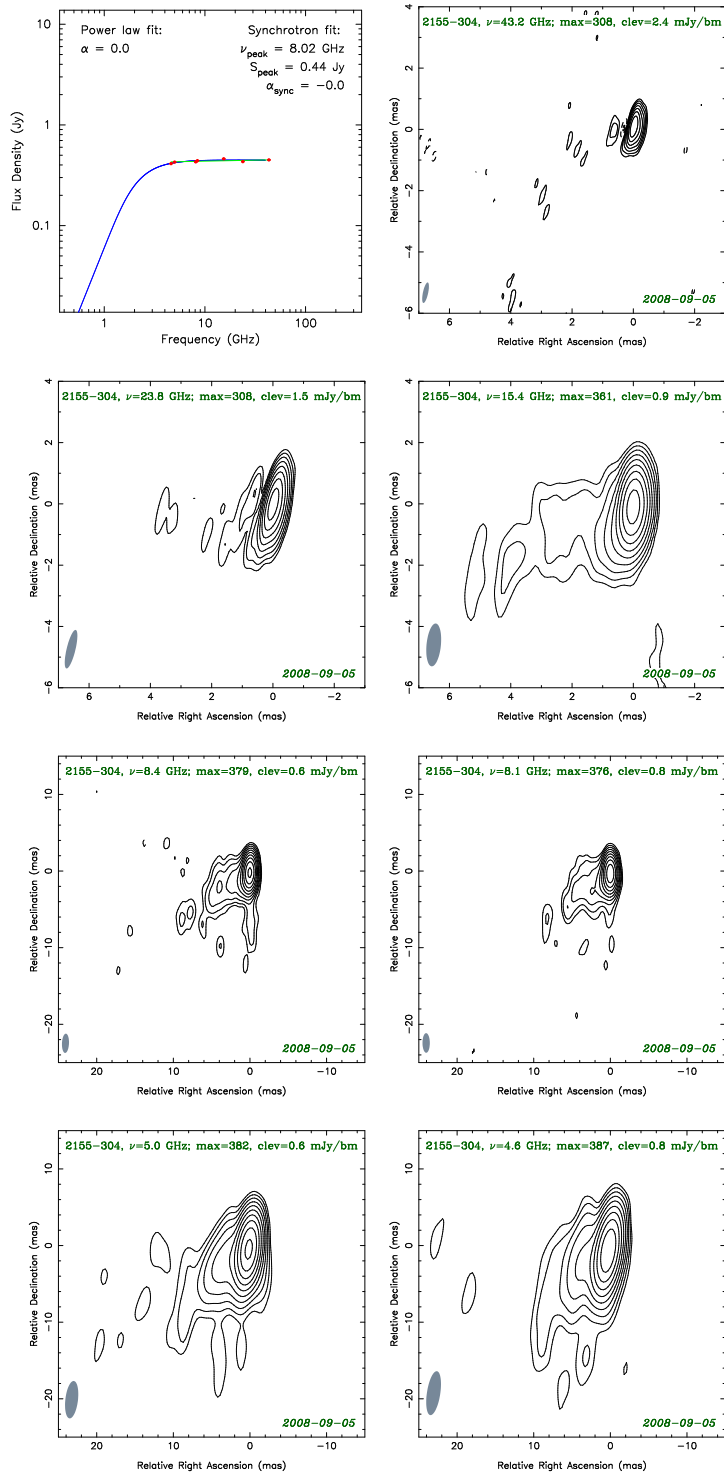


Figure 4.1 continued...

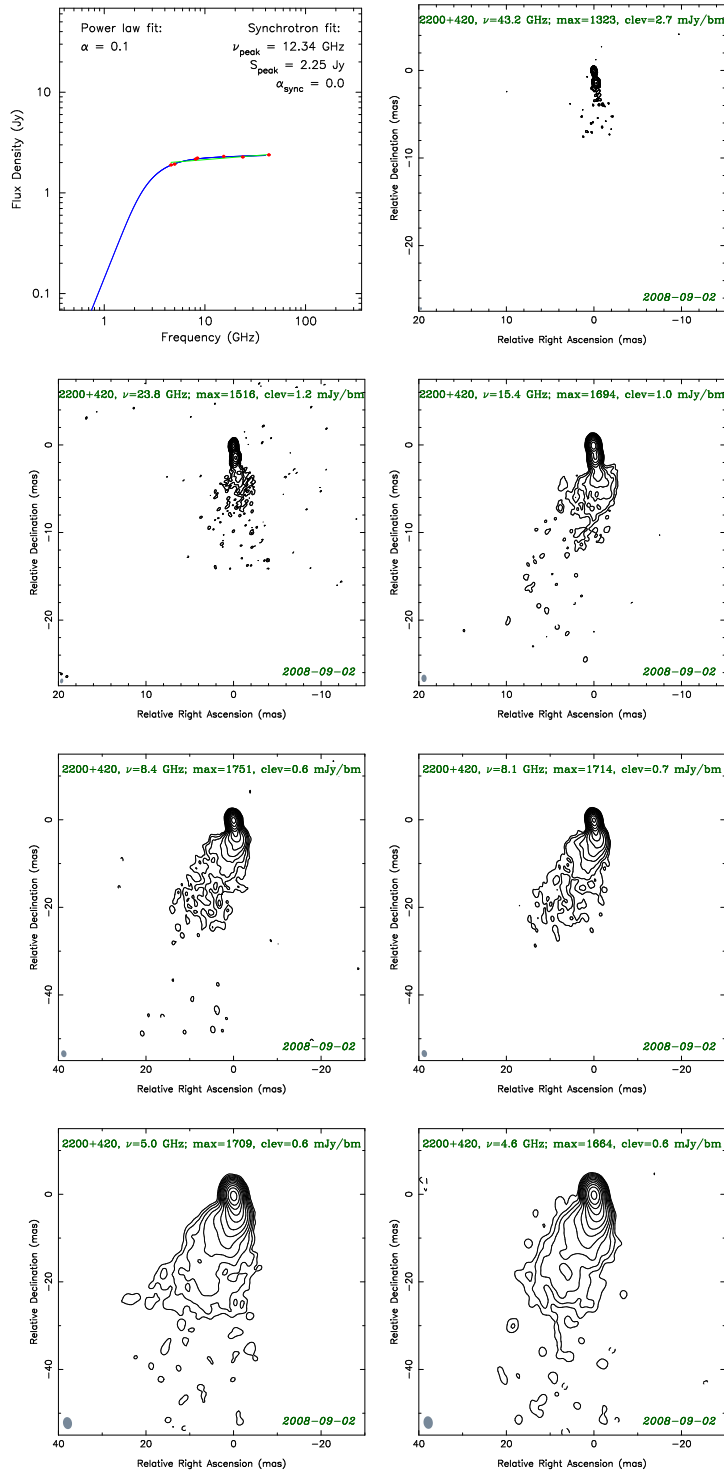


Figure 4.1 continued...

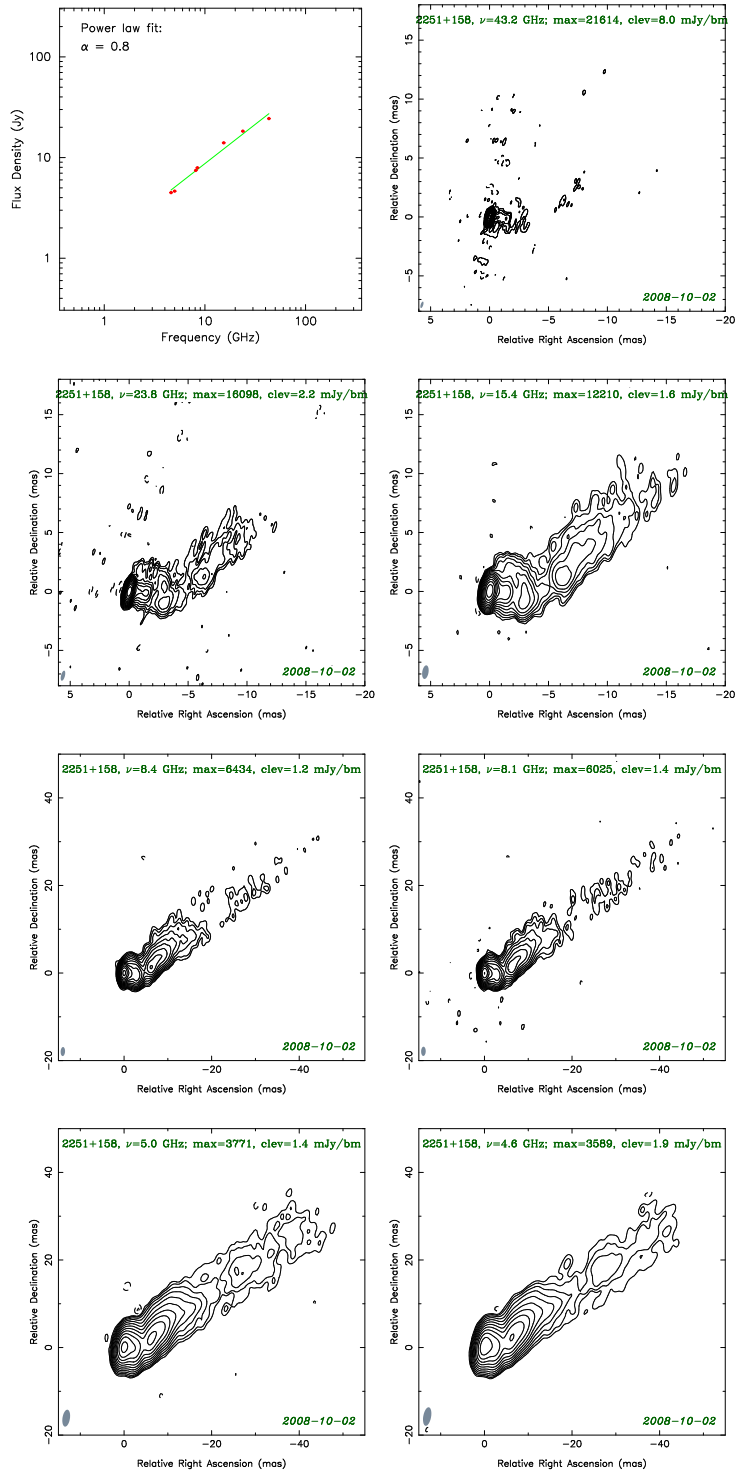


Figure 4.1 continued...

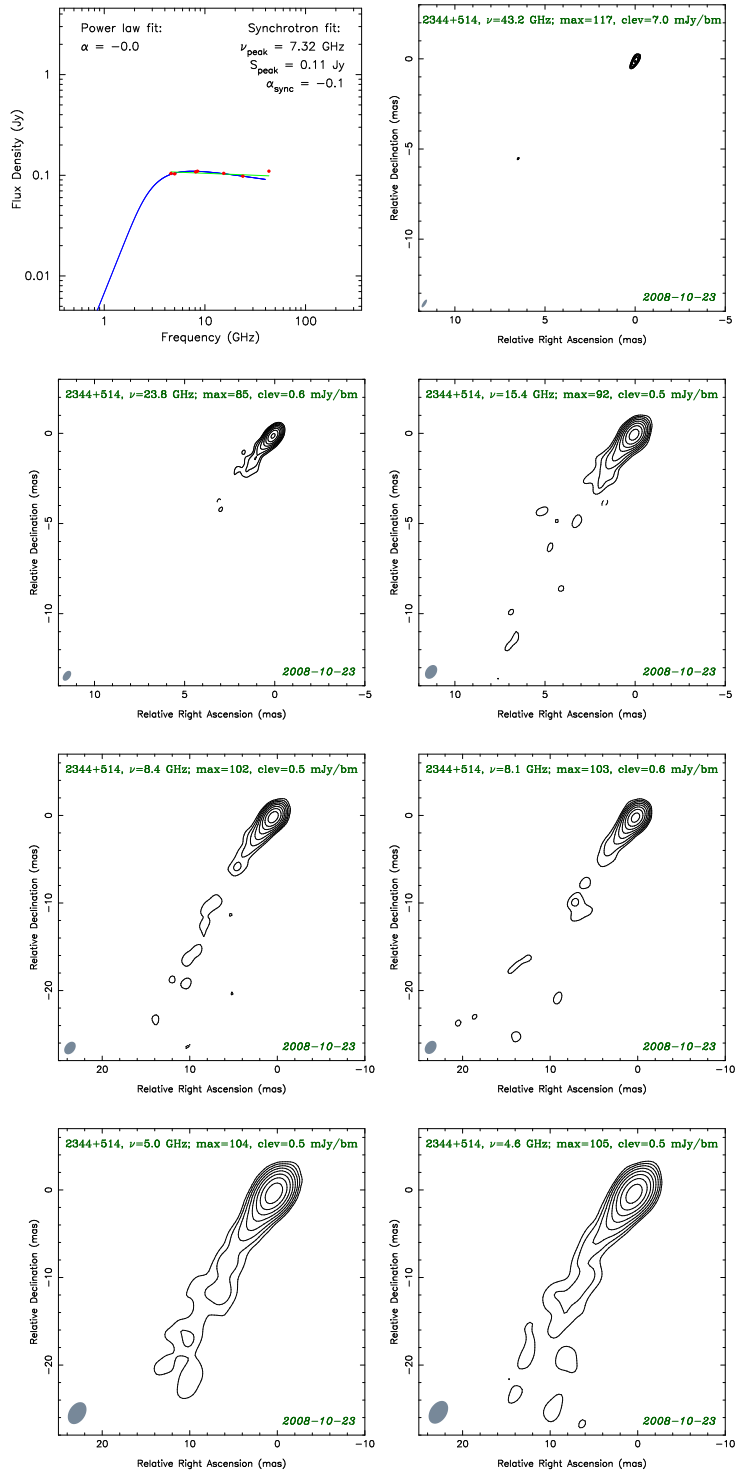


Figure 4.1 continued...

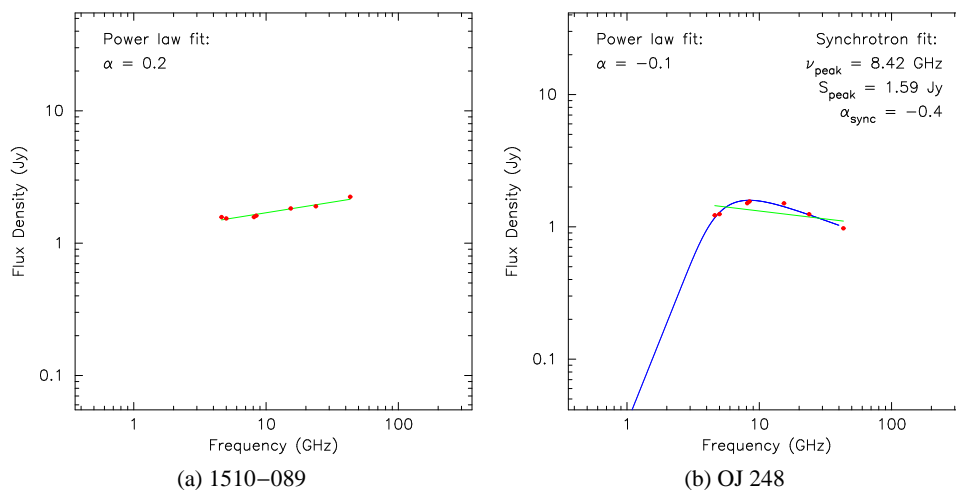


Figure 2.4: VLBA spectra of core regions of 1510–089 (a) and OJ 248 (b). The former spectrum is flat while the latter one shows a prominent synchrotron self-absorption peak. The green line is a power law fit. The blue curve is a homogeneous synchrotron source model.

We fit a homogeneous synchrotron source model (Pacholczyk 1970; Section 1.3.1) to the observed spectra in order to obtain the magnetic field strength and particle energy distribution. The “slab” shape of the source is assumed for simplicity and in the absence of better constraints on the actual source geometry. In particular, we see no reason to prefer a spherical model over the slab-shaped one.

The results of the spectral modeling are presented in Table 2.4. For 15 sources, the model provides an adequate fit to the observed spectra while five sources exhibit flat or inverted spectra that cannot be described by the homogeneous synchrotron model.

Table 2.4 also presents estimates of the core size obtained at the highest observing frequency (43.2 GHz). In order to measure the core size, the structure of each source was modeled in the visibility plane with a number of circular Gaussian components using *Difmap*. The size estimate given in Table 2.4 is the FWHM^2 of the Gaussian component which modeled the core. For all sources, except 2155–304 and 2344+514, it was possible to partially resolve the core and obtain an estimate of its size. For 2155–304 and 2344+514 only an upper limit on the 43.2 GHz core size could be placed. To distinguish between resolved and unresolved features we have used the criterium proposed by Kovalev et al. (2005); Lobanov (2005):

$$\psi > \text{BEAM} \sqrt{\frac{4 \ln 2}{\pi} \ln \frac{\text{SNR}}{\text{SNR} - 1}}$$

where BEAM accounts for a FWHM beam size, SNR is the ratio of the component peak intensity to the residual RMS on the map after subtracting the source model (this criterium is also used in Section 5.2). Typical uncertainty of the measured component size is $\sim 20\%$ according to the formulas by Lee et al. (2008). Additionally, the size estimates are model-dependent and may differ from the listed values significantly if a circular Gaussian shape is not a good approximation of the real shape of the core region.

²Full Width at Half Maximum

Table 2.4: Comparison of the emission region parameters estimated from the VLBA data and SED modeling

Multi-frequency VLBA results (this work)							Published SED model parameters			
Name	Alias	$R_{43 \text{ GHz}}$ [10^{15} cm]	$P_{\text{VLBA}}^{\text{a,b}}$	$B_{\text{VLBA}}^{\text{b}}$ [G]	$D_{\text{var}}^{\text{c}}$	D_{SED}	R_{SED} [10^{15} cm]	$p_{\text{SED}}^{\text{a}}$	B_{SED} [G]	Ref.
0235+164		1050	0.8	≤ 11	24.0					
0528+134		1564	1.4	≤ 1.2	31.2					
0716+714		293	$\alpha = 0.4^{\text{d}}$		10.9	14	40	2.0	1	(1)
0827+243	OJ 248	4882	1.6	≤ 23	13.1					
0851+202	OJ 287	719	$\alpha = 0.7^{\text{d}}$		17.0					
1101+384	Mrk 421	108	1.2	$\leq 10^{\text{c}}$...	20	3	2.6	0.48	(2)
1219+285	W Comae	468	0.8	≤ 118	1.2	20	3	2.55	0.35	(3)
1226+023	3C 273	850	2.0	≤ 0.2	17.0	9	20	2	12	(4)
1253-055	3C 279	1168	1.4	≤ 14	24.0	21.5	25	2.0	1.8	(5)
1406-076		1642	1.2	$\leq 24^{\text{c}}$...					
1510-089		864	$\alpha = 0.2^{\text{d}}$		16.7	37	18	1.9	0.09	(6)
1622-297		1341	$\alpha = 0.2^{\text{d}}$							
1633+383	4C 38.41	1291	1.0	≤ 1.8	21.5					
1652+398	Mrk 501	279	1.6	≤ 67	...	20	1.03	2	0.3	(7)
1730-130	NRAO 530	3692	1.6	≤ 20	10.7					
1959+650		270	1.4	≤ 300	...	18	7.3	2	0.25	(8)
2155-304		< 356	1.0	≤ 745	...	32	150	1.3	0.018	(9)
2200+420	BL Lacertae	494	1.0	≤ 3	7.3					
2251+158	3C 454.3	1497	$\alpha = 0.8^{\text{d}}$		33.2	26	15	1.1	5.4	(10)
2344+514		< 87	1.2	$\leq 57^{\text{c}}$...					

^a p is the power law index in the electron energy distribution $N(E) = N_0 E^{-p}$. For the optically thin part of the synchrotron spectrum $p = 1 - 2\alpha$ where α is defined as $F_\nu \sim \nu^\alpha$. ^b The estimates correspond to the parsec-scale radio core. ^c The value is in the observer's frame. ^d The homogeneous synchrotron source model is not applicable for such spectrum. ^e The variability Doppler factor from Hovatta et al. (2009) used to transform the observed magnetic field strength into the source frame. ^f The same Doppler factor as in the corresponding SED model was adopted.

References: 1: Chen et al. (2008); 2: Acciari et al. (2009c); 3: Acciari et al. (2009b); 4: Pacciani et al. (2009); 5: Giuliani et al. (2009); 6: Sokolovsky et al. (2010a); 7: Anderhub et al. (2009); 8: Tagliaferri et al. (2008); 9: Aharonian et al. (2009); 10: Bonnoli et al. (2010).

2.2.4 Discussion

Model reliability

The physical parameters presented in Table 2.4 correspond to typical values for emitting electrons inside a large area of a few milliarcseconds in size. In all cases, only an upper limit on the magnetic field strength could be placed, because regions where the spectral turnover is detected remain unresolved at the lowest observing frequency (4.6 GHz). The results are consistent with estimates obtained by a method based on model-fitting bright VLBI components with Gaussian components (Sokolovsky et al. 2010a). The model-fitting based method is described in detail in Savolainen et al. (2008) where it was applied to 3C 273 and the average magnetic field strength $B_\perp \sim 10^{-2}$ G was obtained for the 8 GHz core region which is comparable in size to the region probed in our research. This value is in a good agreement with our upper limit at $B_\perp \leq 0.14$ G given in Table 2.4.

Electron energy spectrum

The spectra above the synchrotron turnover are nearly flat or slightly inverted in core regions of all sources investigated in this work. This may result from blending of a few

emitting regions with different peak frequencies (an example of such blending may be found in the core region of BL Lacertae, see the top right panel in Fig. 3 in Sokolovsky et al. 2010b, see also Savolainen et al. (2008) for 3C 273).

Along the similar lines goes the other possible explanation of the observed flatness of the radio spectra above the turnover frequency. It is possible that the slab geometry is inappropriate to describe the parsec-scale core region. There are strong indication that a more accurate model of the core region is a continuous Blandford-Königl type jet with smooth gradients of physical properties along it (Blandford & Königl 1979; Chapter 4). In this model, the observed spectral index does not reflect the underlying particle energy distribution directly (due to changing opacity along the jet) but relates to it through other model parameters which cannot be easily constrained from observations. If this is the case, the derived magnetic field strength corresponds to the region where the smooth Blandford-Königl jet ends due to some kind of disruption.

Alternatively, a nearly flat spectrum may imply a hard energy spectrum of the emitting electrons (as may be the case for the component B1 in the jet of BL Lacertae whose spectrum is presented in the lower right panel of Fig. 3 in Sokolovsky et al. 2010b). The hard electron spectrum is difficult to explain by the conventional first-order Fermi acceleration mechanism. However, the hard spectrum can be produced by the second-order Fermi mechanism (“stochastic acceleration”; Virtanen & Vainio 2005).

We have placed upper limits of $B_{\perp} \leq 10^{-1}-10^2$ G (source frame) on the magnetic field strength in 15 out of 20 *Fermi* blazars (Table 2.4). Spectra of five blazars could not be described by the simple homogeneous synchrotron source model, and no constraints on the magnetic field and particle energy spectrum could be obtained for these sources. Hard spectra ($-0.5 \leq \alpha \leq +0.1$, $F_{\nu} \sim \nu^{\alpha}$) observed in the blazar cores above the synchrotron peak may either indicate a hard energy spectrum of the relativistic electron population in the jet or result from significant inhomogeneity (of the magnetic field and plasma parameters or just optical depth) across the emitting region.

Since γ -ray emission in blazars is suggested to originate from regions spatially close to the VLBI core (Kovalev et al. 2009), the estimates of the size, magnetic field strength and electron energy distribution presented in Table 2.4 could be used to constrain broad-band Spectral Energy Distribution (SED) models (see Chapter 3). Simultaneously with the VLBA observations described here, *Swift* X-ray/ultraviolet/optical target of opportunity observations were performed. When combined with the *Fermi* γ -ray data this will provide a unique data set for the SED modeling.

2.3 Magnetic field in the parsec-scale core regions of high core shift radio sources

The spectral analysis technique proposed in Section 2.1 has also been applied to another multi-frequency VLBA dataset: simultaneous nine frequency (1.4–15.4 GHz) observations of “high core shift” sources. These sources have been selected as showing prominent frequency-dependent shift in the observed position of the core, and the observations were originally obtained to investigate this effect. A detailed discussion of the observing program and its results is presented in Chapter 4.

Results of the spectral analysis are presented in Table 2.5. The spectral turnover has been detected in the core regions of 12 out of 20 observed sources. In all observed sources, the spectral turnover was not detected reliably in jet features downstream of the core within the investigated frequency range. However in a few cases like 1458+718

Table 2.5: Estimated physical parameters of parsec-scale cores of the “high core shift sample” sources

Name	Alias	$R_{15\text{ GHz}}$ [10^{15} cm]	p	B [G]
0148+274		< 1557	1.0	≤ 3.0
0342+147		3562	1.1	≤ 130
0425+048	OF 42	1413	...	no peak
0507+179		2346	1.3	≤ 85
0610+260	3C 154	2271	...	no peak
0839+187		< 6365	2.2	≤ 5.8
0952+179		< 1079	1.3	≤ 68
1004+141		3602	1.0	≤ 25
1011+250		4517	1.6	≤ 43
1049+215		2604	...	no peak
1219+285	W Comae	778	...	no peak
1406-076		3795	...	no peak
1458+718	3C 309.1	3282	1.4	≤ 1.3
1642+690		1973	1.5	≤ 16
1655+077		1444	1.2	≤ 22
1803+784		2287	1.2	≤ 4.0
1830+285		1352	...	no peak
1845+797	3C 390.3	360	...	no peak
2201+315		665	...	no peak
2320+506		3300	1.3	≤ 0.10

Column designation: Col. 1 – IAU source name (B1950), Col. 2 – commonly used source name, Col. 3 – core size measured at 15.4 GHz, Col. 4 – p is the power law index in the electron energy distribution $N(E) = N_0 E^{-p}$. For the optically thin part of the synchrotron spectrum $p = 1 - 2\alpha$ where α is defined as $F_\nu \sim \nu^\alpha$. Col. 5 – upper limit on the magnetic field strength (observer’s frame).

the presence of the spectral turnover close to the lowest observing frequency (1.4 GHz) might be suspected in the brightest jet features.

The upper limits on the core magnetic field strength values in Table 2.5 are given in the observers frame because, for most of the sources, no reliable estimations of the Doppler factor are available in the literature. The Doppler factor value together with redshift of the source are needed to compute the magnetic field strength in the source reference frame (Section 1.3.2). Also, for the majority of the sources no report of dedicated SED modeling could be found in the literature.

Table 2.5 also presents estimates of the core size obtained at the highest observing frequency (15.4 GHz). The size estimation technique was the same as described in Section 2.2.3. Cores of only three (0148+274, 0839+187, 0952+179) out of 20 observed sources have remained unresolved at 15.4 GHz according to the criterium of Kovalev et al. (2005); Lobanov (2005). As expected, the core sizes measured at 15.4 GHz (Table 2.5) are typically larger than those measured at 43.2 GHz (Table 2.4).

Two sources, W Comae and 1406-076 have been observed both as part of the “high core shift” sample (1.4–15.4 GHz observations) and “bright γ -ray blazars” sample (observed in 4.6–43.2 GHz range). In both cases the spectral turnover could not be detected in the first experiment, but was successfully measured in the second. The spectral turnover in W Comae was found at frequency $\nu_{\text{peak}} \simeq 21$ GHz, while in 1406-076 it is around $\nu_{\text{peak}} \simeq 14$ GHz. In both cases the estimated source size at 15.4 GHz is larger than at 43.2 GHz which is expected due to opacity effects.

2.4 Chapter summary

In this chapter we propose a novel technique of spatially resolved spectrum reconstruction from simultaneous multi-frequency VLBI observations. The technique has been applied to 38 sources observed with the VLBA in the course of two programs: “high core shift” sample (nine frequencies in 1.4–15.4 GHz range) and “bright γ -ray blazars” sample (seven frequencies in 4.6–43.2 GHz range). The spectral turnover attributed to synchrotron self absorption has been detected in parsec-scale core regions of 27 sources which allowed to constrain the magnetic field strength and particle energy spectrum in these regions. We have placed upper limits of $B_{\perp} \leq 10^{-1}$ – 10^2 G (source frame) on the magnetic field strength in these sources (Table 2.4 and 2.5). Hard spectra ($-0.5 \leq \alpha \leq +0.1$, $F_{\nu} \sim \nu^{\alpha}$) observed in the blazar cores above the synchrotron peak may either indicate a hard energy spectrum of the relativistic electron population in the jet or result from significant inhomogeneity (of the magnetic field and plasma parameters or just optical depth) across the emitting region. Spectra of 11 blazars could not be described by the simple homogeneous synchrotron source model, and no constraints on the magnetic field and particle energy spectrum could be obtained for these objects.

Estimations (or in five cases – upper limits) of the core size has been obtained for the observed sources. These results provide constraints on blazar emission models.

Since γ -ray emission in blazars is suggested to originate from regions spatially close to the VLBI core (Kovalev et al. 2009), the estimates of the size, magnetic field strength and electron energy distribution presented in Table 2.4 could be used to constrain broad-band Spectral Energy Distribution (SED) models (see Chapter 3). Simultaneously with the VLBA observations described here, *Swift* X-ray/ultraviolet/optical target of opportunity observations were performed. When combined with the *Fermi* γ -ray data this will provide a unique data set for the SED modeling. We also plan to apply the Gaussian component-based method (Savolainen et al. 2008) to extract spectral information from the data described in this chapter in order to take advantage of the method’s superior angular resolution. It would be important to extend the comparison of CLEAN component-based and Gaussian component-based methods presented in Sokolovsky et al. (2010b) to all the observed sources.

Chapter 3

Individual blazars across the electromagnetic spectrum

Blazars are the class of AGN which show signs of extreme relativistic beaming. This class includes BL Lacertae-type objects and Flat Spectrum Radio Quasars (FSRQ). Blazars are characterized by intense non-thermal radiation across all the electromagnetic spectrum from radio to γ -rays.

Fermi Gamma-ray Space Telescope (FGST) is the new orbital observatory which is watching the γ -ray sky since June 2008. The main instrument of *Fermi* is the Large Area Telescope (LAT), a pair conversion telescope designed to cover the energy band from 20 MeV to greater than 300 GeV. The *Fermi*/LAT is providing a unique combination of high-sensitivity in this still poorly explored energy range and a wide field of view of about 60° . The *Fermi* is operated in the all-sky survey mode for most of the time which makes it an ideal hunter for flaring blazars which dominate extragalactic γ -ray sky.

While with its unprecedented sensitivity and broad energy coverage the *Fermi*/LAT has practically opened a new window in the world of γ -ray variability and spectral behavior of blazars it was well realized even before the launch of *Fermi* that in order to take full advantage of these new data, the γ -ray observations need to be supported by simultaneous observations in other bands. This multiwavelength approach to blazar studies appears to be our best hope to understand mechanisms and locations where blazar γ -ray radiation is generated and to understand the blazar phenomenon as a whole.

Coordinated observations across the entire electromagnetic spectrum from radio to GeV and sometimes (see Section 3.4) TeV energies together with the subsequent data analysis and theoretical interpretation of the results is an extraordinary effort requiring a team work of many, sometimes hundreds of people. In the following sections a special effort will be made to highlight the author's contribution to each observing campaign while, whenever possible, a reader will be directed to the corresponding publications for the full description and interpretation of the campaign results.

In this chapter we present results of multi-frequency VLBA observations of five blazars (3C 454.3, BL Lacertae, PKS 1510–089, Mrk 421, Mrk 501) and discuss them in the context of their broad-band emission across the electromagnetic spectrum. The results of this work are presented in Abdo et al. (2010a,b,c,d); Sokolovsky et al. (2010a); Vercellone et al. (2010).

3.1 VLBI radio behavior of 3C 454.3 during its 2008 activity period

The Flat Spectrum Radio Quasar 3C 454.3 (FSRQ, $z = 0.859$ Jackson & Browne 1991) was seen by *Fermi* as the brightest γ -ray source in the extragalactic sky right after its launch. The source has shown a remarkably bright γ -ray flare in August–September 2008 (e.g. Vercellone et al. (2010)) which was surpassed only by its own following flares in December 2009, April and November 2010 when it reached the flux ($E > 100$ MeV) of $56 \pm 4 \times 10^{-6}$ ph cm $^{-2}$ s $^{-1}$, representing the highest daily flux of any blazar ever recorded in high-energy gamma-rays (ATel¹ #3041, #3041, #3049, Ackermann et al. 2010; Pacciani et al. 2010). During this time 3C 454.3 was brighter than Vela pulsar – the brightest Galactic MeV γ -ray source. Naturally, all these flares were closely followed by many ground- and space-based observatories across the electromagnetic spectrum.

The results described in this section were partly reported by Vercellone et al. (2010) in the framework of the 2007–2008 *AGILE* observing campaign on 3C 454.3. The results are expected to be covered in greater detail in the paper on the 2008 activity of 3C 454.3 which is currently being prepared within the *Fermi*/LAT collaboration.

The 2008 flare of 3C 454.3 became the first opportunity to study in detail the relation between γ -ray activity of a blazar and changes in its parsec-scale morphology traced by high-frequency VLBI observations. This was made possible thanks to the 43 GHz VLBA monitoring program of bright blazars performed by the Boston University group Jorstad et al. (2010) and four epochs of 4.6–43 GHz VLBA observations performed within our program.

We have observed 3C 454.3 with the Very Long Baseline Array (VLBA) simultaneously at seven frequencies (4.6, 5.0, 8.1, 8.4, 15.4, 23.8 and 43.2 GHz) in the framework of our survey of parsec-scale radio spectra of twenty gamma-ray bright blazars (Sokolovsky et al. 2010a,b; Section 2.2). The source was observed at four epochs during the decline phase of its gamma-ray activity: on September 02, 05, October 02 and 23, 2008. On October 02 a “deep” observation was conducted with 16 on-source scans (each 4 - 7 minutes long depending on frequency) spread over 9 hours. This resulted in high-quality images with the dynamic range up to 1:8000 (at 15.4 GHz). At the three remaining epochs 3C 454.3 was observed as a calibrator for other sources in the survey with only 2 scans on it separated by about 3 hours. However, due to the high radio brightness of the source parsec-scale emission, even such short observations are sufficient to reconstruct images with dynamic range up to 1:3000 (15.4 GHz).

The data reduction was conducted in the standard manner using the *AIPS* package (Greisen 1990). A special procedure was developed and utilized to improve amplitude calibration of the correlated flux density resulting in $\sim 5\%$ calibration accuracy at 4.6–15.4 GHz range and $\sim 10\%$ accuracy at 23.8 and 43.2 GHz. The *Difmap* software (Shepherd et al. 1994) was used for imaging and modeling of the *uv*-data. The brightness distribution of the source has been modeled with a number of circular Gaussian components which were visually cross-identified across epochs and frequencies. The uncertainties of the model component parameters were estimated following Lee et al. (2008).

Figures 3.1 and 3.2 show total intensity VLBA images of 3C 454.3 at the highest (43.2 GHz) and lowest (4.6 GHz) frequency of our observations. The spectral index map of the source covering the intermediate frequencies of our observation (8.1–

¹The Astronomer’s Telegram: <http://astronomerstelegam.org/>

15.4 GHz) is presented on Fig. 3.3. While at 4.6 GHz the source shows a bright extended jet, at 43.2 GHz the source structure is dominated by the bright compact core and may be represented reasonably well by only three Gaussian components (Fig. 3.1, Table 3.1). It is evident from Fig. 3.1 that changes in the parsec-scale structure of the source during its 2008 activity period are confined to the core region.

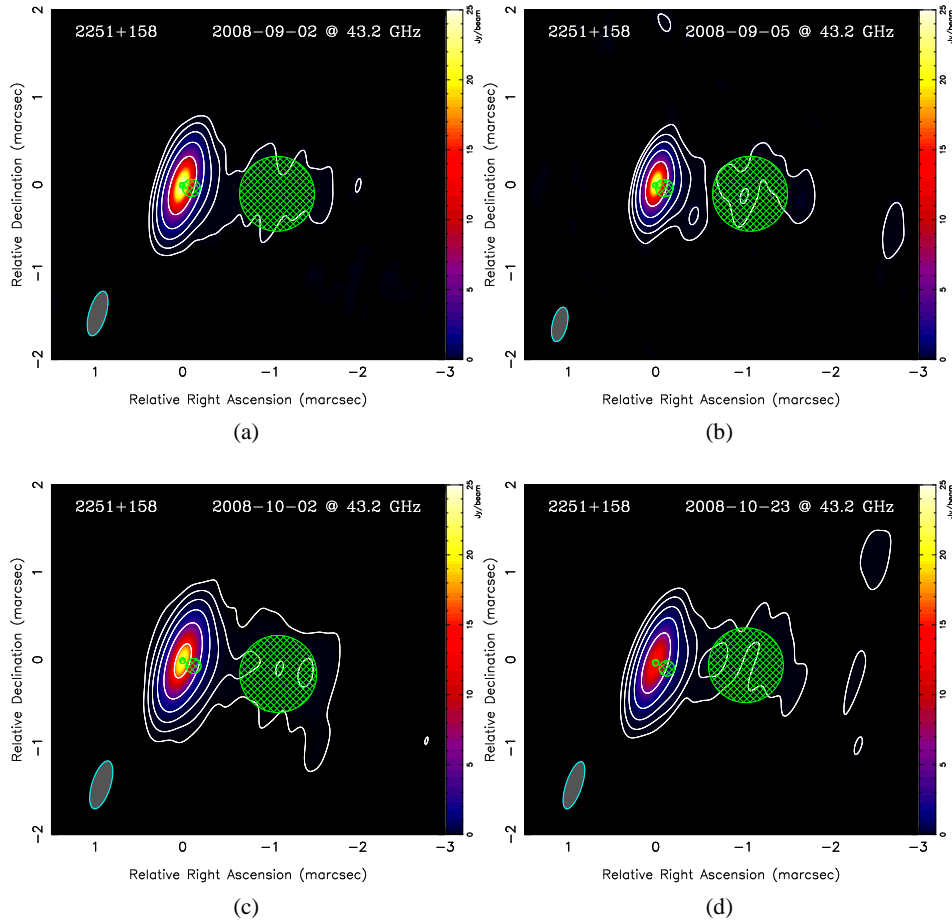


Figure 3.1: Total intensity VLBA images of 3C 454.3 at 43.2 GHz at four epochs covered by our multifrequency observations. Image details: 3.1a – peak 24.6 Jy/beam, first contour 0.030 Jy/beam; 3.1b – peak 23.4 Jy/beam, first contour 0.030 Jy/beam; 3.1c – peak 21.7 Jy/beam, first contour 0.015 Jy/beam; 3.1d – peak 15.6 Jy/beam, first contour 0.020 Jy/beam. Contours are a factor of 4 apart in all cases. The beam is plotted in the lower left corner of each image. Green circles represent Gaussian components used to model the 43.2 GHz brightness distribution of the source.

Table 3.1: Parameters of the core and jet components of 3C 454.3 at 43.2 GHz

Component	R (mas)	PA ^o	FWHM (mas)	Flux (Jy)	SNR	T_b
2008-09-02 = JD 2454711.8						
C00	0.000 ± 0.000	0.0 ± 0.0	0.060 ± 0.009	24.676 ± 0.918	1397.9	6.6 × 10 ⁺¹¹
C01	0.111 ± 0.019	-106.5 ± 9.9	0.200 ± 0.038	2.427 ± 0.297	102.5	5.8 × 10 ⁺⁰⁹
C02	1.089 ± 0.254	-95.1 ± 13.1	0.857 ± 0.507	0.562 ± 0.314	4.1	7.3 × 10 ⁺⁰⁷
2008-09-05 = JD 2454714.8						
C00	0.000 ± 0.000	0.0 ± 0.0	0.068 ± 0.013	24.536 ± 1.601	442.0	5.1 × 10 ⁺¹¹
C01	0.115 ± 0.036	-103.7 ± 17.6	0.218 ± 0.071	2.082 ± 0.508	23.6	4.2 × 10 ⁺⁰⁹
C02	0.967 ± 0.555	-94.7 ± 29.9	0.850 ± 1.110	0.714 ± 0.895	1.2	9.4 × 10 ⁺⁰⁷
2008-10-02 = JD 2454741.7						
C00	0.000 ± 0.000	0.0 ± 0.0	0.063 ± 0.011	21.909 ± 0.916	1109.9	5.2 × 10 ⁺¹¹
C01	0.140 ± 0.021	-115.7 ± 8.7	0.171 ± 0.042	2.082 ± 0.287	87.7	6.8 × 10 ⁺⁰⁹
C02	1.104 ± 0.290	-97.9 ± 14.7	0.881 ± 0.580	0.489 ± 0.302	3.4	6 × 10 ⁺⁰⁷
2008-10-23 = JD 2454762.7						
C00	0.000 ± 0.000	0.0 ± 0.0	0.071 ± 0.013	16.165 ± 0.874	653.4	3 × 10 ⁺¹¹
C01	0.145 ± 0.023	-116.8 ± 9.2	0.176 ± 0.045	2.060 ± 0.319	67.2	6.4 × 10 ⁺⁰⁹
C02	1.033 ± 0.332	-91.6 ± 17.8	0.856 ± 0.663	0.502 ± 0.367	2.6	6.6 × 10 ⁺⁰⁷

Column designation: Col. 1 – component name, Col. 2 – distance from the core in milliarcseconds, Col. 3 – Position Angle (PA) measured North through East in degrees, Col. 4 – FWHM size of the component in milliarcseconds, Col. 5 – component flux in Jansky. Col. 6 – Signal-to-Noise (SNR) ratio of the component, Col. 7 – T_b is the brightness temperature in K.

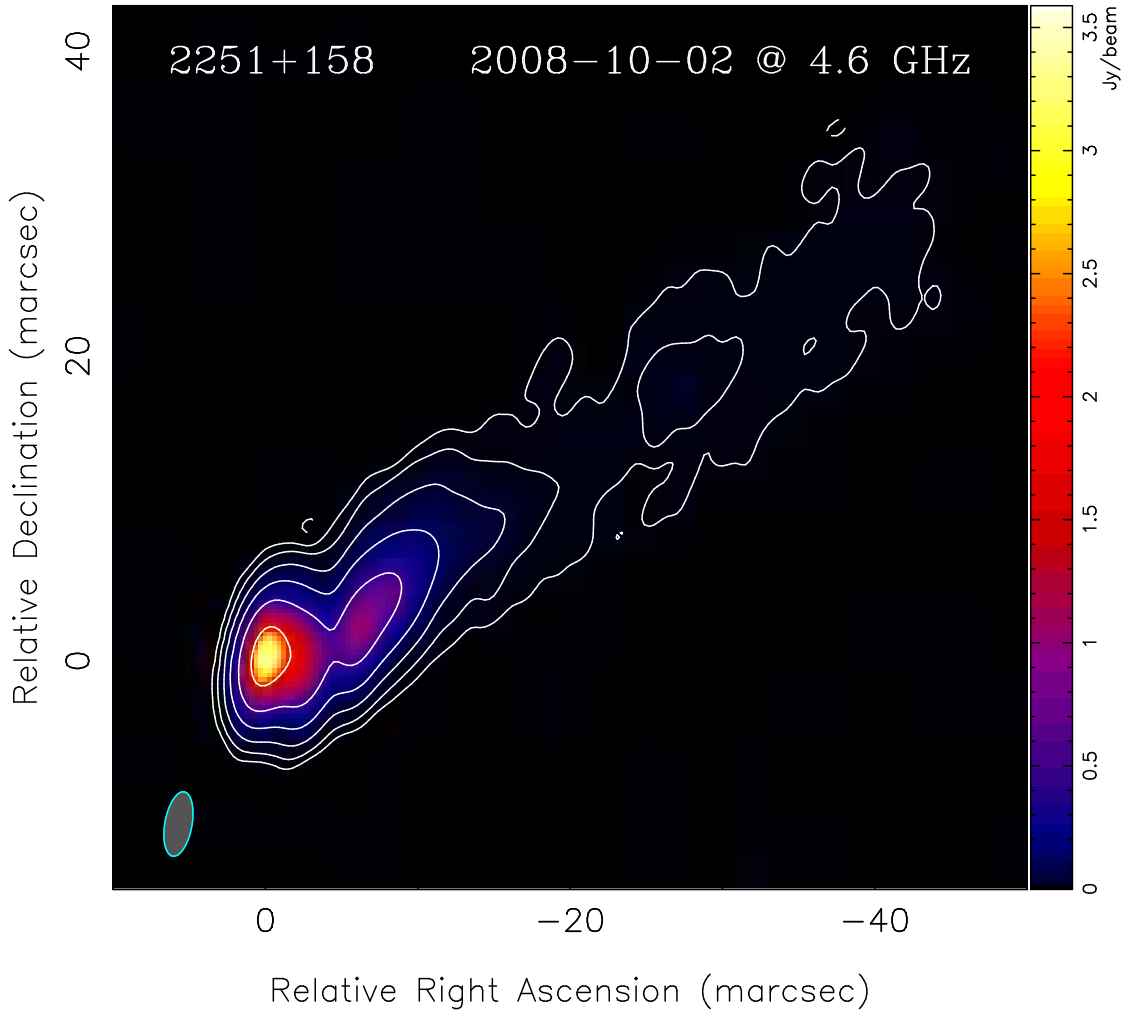


Figure 3.2: Total intensity VLBA image at 4.6 GHz. The first contour is 0.002 Jy/beam, factor = 4. The beam is shown in the lower left corner of the image.

In order to trace changes in the core region of 3C 454.3 during its period of γ -ray activity we have combined our four epochs of 43.2 GHz observations with the data of the Boston University group (Jorstad et al. 2010). The calibrated uv -data were downloaded from the group’s web page² and modeled in *Difmap* in the same way as data from our own VLBA experiments presented in Table 3.1. In the following, the core will be referred to as “C00”, the first jet component about 0.15 mas from the core as “C01” and the weak and extended component 1 mas from the core is marked “C02”.

Fig. 3.4 presents the lightcurve of the 43 GHz core (“C00”) and the first jet component “C01”. It is evident that while the core shows huge flux density changes, the flux of “C01” remains roughly constant. The peak of the core flux was observed on September 10, 2008, the same day as one of the secondary peaks of the γ -ray lightcurve³.

Fig. 3.6 shows the separation of the component “C01” from the core (“C00”) as a function of time. The linear fit to the data indicate the component speed of 0.130 ± 0.017 mas/year = 6.1 ± 0.8 c and the epoch of zero separation between C00

²<http://www.bu.edu/blazars/VLBAproject.html>

³See the *Fermi*/LAT public lightcurve at http://fermi.gsfc.nasa.gov/ssc/data/access/lat/msl_lc/

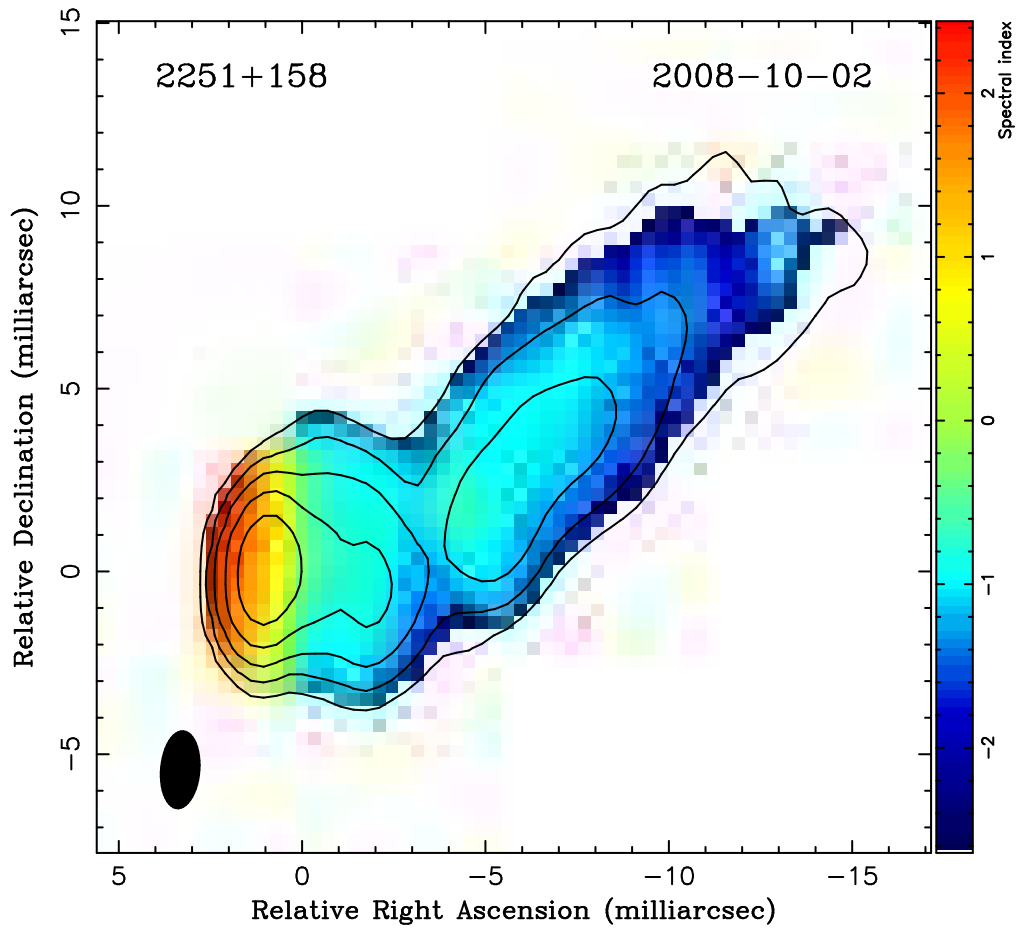


Figure 3.3: Spectral index map constructed by fitting a power law to observations at three frequencies: 8.1, 8.4 and 15.4 GHz. Contours represent total intensity at 8.4 GHz. Contour map peak = 6.442 Jy/beam, first contour 0.1% of the peak. Beam FWHM = 2.12×1.05 mas at PA = $-4^{\circ}.64$.

and C01 $\text{JD}2454370 \pm 46^{\text{d}}$ (September 26, 2007). Fig. 3.5 shows the size evolution of the component and the core. The component C01 is steadily increasing its size as it moves away from the core while the core size shows no major changes. It is interesting to note that C01 appears to be moving along a curved trajectory (Fig. 3.7).

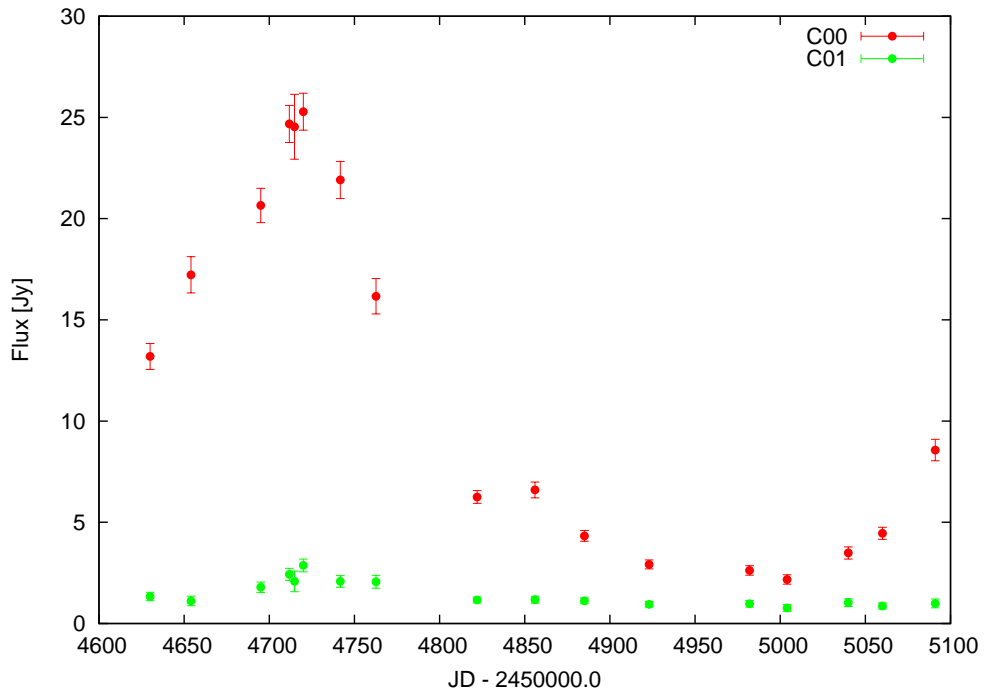


Figure 3.4: Lightcurve of the 43 GHz core of 3C 454.3 (marked “C00”) and the first jet component “C01” about 0.15 mas away from the core.

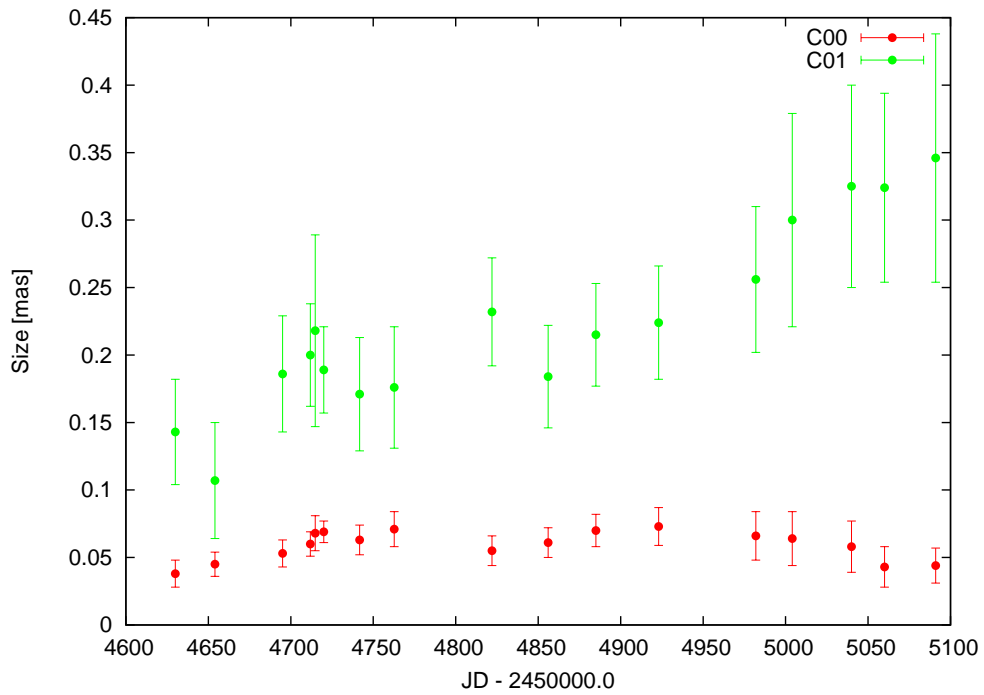


Figure 3.5: Size of the first jet component (C01) and the core (C00) as a function of time.

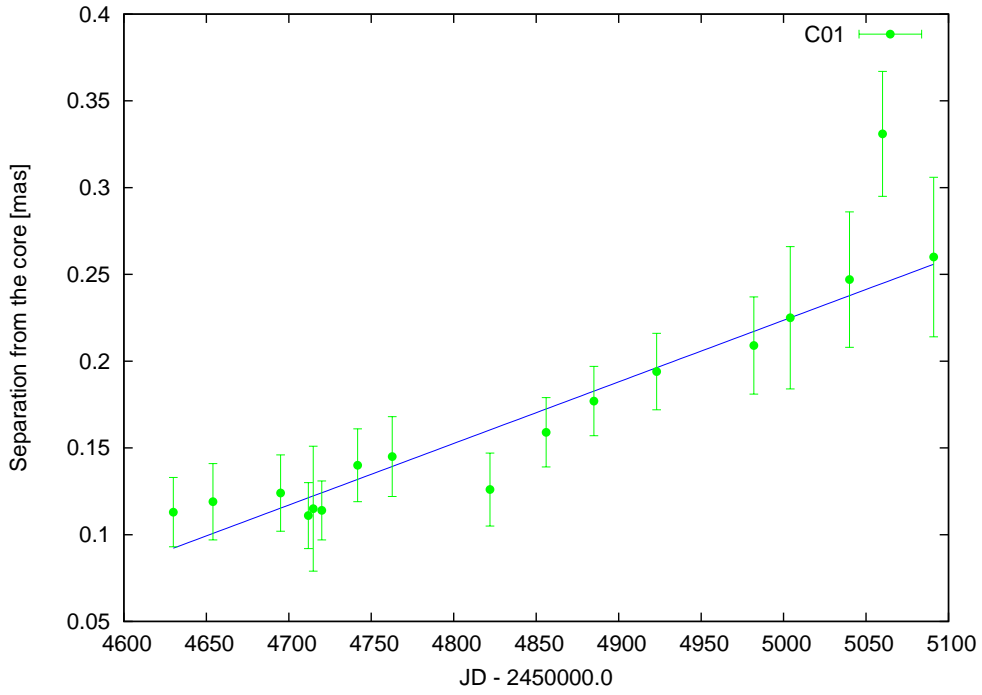


Figure 3.6: Separation of the component “C01” from the core (“C00”) of 3C 454.3 as a function of time. The blue line represents the least square fit to the data.

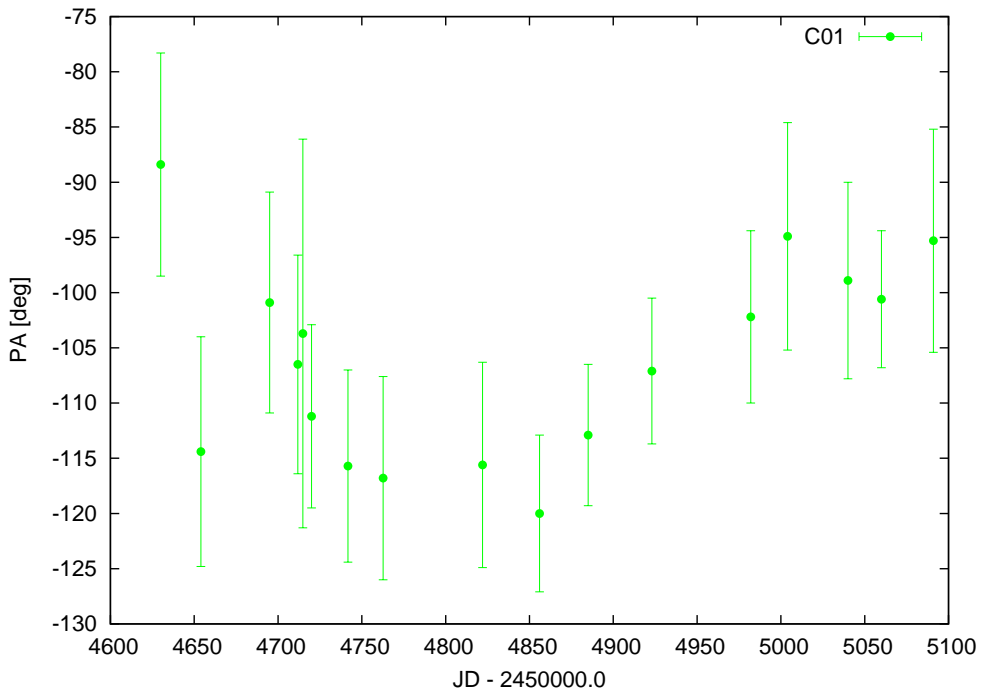


Figure 3.7: Position Angle (PA) of the component C01 with respect to the core.

Overall, the analysis of the 43 GHz data indicates that the parsec-scale core of 3C 454.3 may be directly related to its γ -ray activity (as indicated by the observed coincidence of the lightcurve peaks of the core and the γ -ray source). At the same time, the first jet component located just 0.10–0.15 mas from the core shows only gradual changes of its properties (size, flux, trajectory) which doesn't seem to be related with the γ -ray activity of the object. The estimated ejection epoch of the component predates the 2008 γ -ray flare considered here. This allows us to conclude that the observed jet component C01 is not related to the flare. The flare has occurred in the much smaller spatial region comparable or less than the 43 GHz core size (~ 0.06 mas = 0.46 pc).

Finally, on Fig. 3.8 we present the radio spectrum of the core obtained in the course of our four-epoch multifrequency observations. The spectrum is highly inverted indicating synchrotron self-absorbed region, however, the spectral index does not reach the value of $\alpha = 2.5$ expected for an optically-thick homogeneous synchrotron source indicating that the core is either inhomogeneous or is blended with one or more components which still can not be resolved.

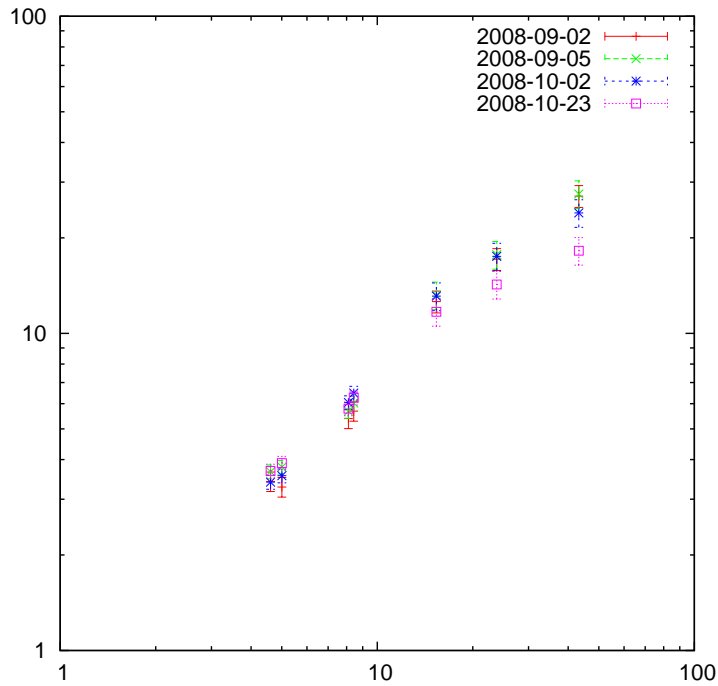


Figure 3.8: Core spectrum of 3C 454.3.

Table 3.2: VLBA flux measurements of 3C 454.3

Band	Frequency (GHz)	Total Flux (Jy)	Core Flux (Jy)
2008-09-02 = JD 2454711.8			
<i>C</i>	4.6085	9.369	3.412
<i>C</i>	5.0035	9.596	3.278
<i>X</i>	8.1085	10.222	5.390
<i>X</i>	8.4295	10.825	5.686
<i>K_u</i>	15.3655	15.110	12.595
<i>K</i>	23.8045	19.255	17.141

<i>Q</i>	43.2175	27.652	27.103
2008-09-05 = JD 2454714.8			
<i>C</i>	4.6085	9.615	3.662
<i>C</i>	5.0035	9.580	3.786
<i>X</i>	8.1085	10.432	5.686
<i>X</i>	8.4295	10.886	6.031
<i>K_u</i>	15.3655	15.772	13.195
<i>K</i>	23.8045	19.652	17.710
<i>Q</i>	43.2175	27.602	27.510
2008-10-02 = JD 2454741.7			
<i>C</i>	4.6085	9.628	3.395
<i>C</i>	5.0035	9.673	3.557
<i>X</i>	8.1085	10.835	6.049
<i>X</i>	8.4295	11.301	6.485
<i>K_u</i>	15.3655	15.889	13.105
<i>K</i>	23.8045	19.429	17.491
<i>Q</i>	43.2175	24.741	23.992
2008-10-23 = JD 2454762.7			
<i>C</i>	4.6085	9.663	3.683
<i>C</i>	5.0035	9.674	3.901
<i>X</i>	8.1085	10.794	5.787
<i>X</i>	8.4295	11.153	6.262
<i>K_u</i>	15.3655	14.227	11.697
<i>K</i>	23.8045	16.024	14.259
<i>Q</i>	43.2175	18.596	18.225

3.2 Multifrequency VLBA view of BL Lacertae during the *Fermi* campaign

This section describes the results of multifrequency VLBA observations of BL Lacertae which were contributed to the *Fermi* multifrequency campaign. The paper with the detailed discussion of the campaign results has recently been submitted to ApJ (Abdo et al. 2010d).

3.2.1 General properties

BL Lacertae (BL Lac) is the prototype of the BL Lac type of active galactic nuclei (AGN). Together with Flat Spectrum Radio Quasars (FSRQ), BL Lac-type objects form the class of blazars, famous for their ability to radiate across the entire electromagnetic spectrum, from radio to TeV energies. BL Lacs are distinguished from FSRQs mainly on the basis of their optical spectrum which typically lacks strong emission lines. However, the prototype of the class – BL Lacertae itself has shown during several epochs broad H_α and H_β emission lines with luminosity ($\sim 10^{41}$ erg s $^{-1}$) comparable to those of type I Seyfert galaxies Corbett et al. (2000, 1996); Vermeulen et al. (1995). There is evidence for an increase by $\sim 50\%$ in ten years of the broad H_α line and an underluminous broad line region (BLR), compared to other AGN (Abdo et al. 2010d). The narrow lines and radio luminosities of BL Lac match those of low-excitation and miniature radio galaxies (Capetti et al. 2010). Long term radio-optical flux density

monitoring and several multiwavelength campaigns have been carried out on BL Lac providing very complete datasets, for example Bloom et al. (1997); Böttcher et al. (2003); Madejski et al. (1999); Marscher et al. (2008); Raiteri et al. (2009); Ravasio et al. (2003); Sambruna et al. (1999); Villata et al. (2004, 2002). Following results of past multifrequency campaigns, possible different VLBI jet structures are assumed to contribute, sometimes with delays, to the radio flux density light curves, and sometimes are suggested to be responsible for optical to TeV γ -ray flares (Bach et al. 2006; Marscher et al. 2008).

3.2.2 Results of 5–43 GHz VLBA observations

BL Lac was observed with the Very Long Baseline Array (VLBA) at seven frequencies (4.6, 5.0, 8.1, 8.4, 15.4, 23.8 and 43.2 GHz) in the framework of a survey of parsec-scale radio spectra of twenty γ -ray bright blazars (Sokolovsky et al. 2010a,b). The multifrequency VLBA observation was carried out on 2008 September 2. The data reduction was conducted in the standard manner using the *AIPS* package (Greisen 1990), see Section 2.2 for the full description of the observing program and calibration procedures. The final amplitude calibration accuracy is estimated to be $\sim 5\%$ at 4.6–15.4 GHz range and $\sim 10\%$ at 23.8 and 43.2 GHz. The *Difmap* software (Shepherd 1997) was used for imaging and modeling of the visibility data.

The VLBA images (Fig. 3.9 and 3.10) reveal a wide, rather smooth, curved jet extending ~ 50 mas (at 5 GHz) south-east from the bright compact core. A few distinct, bright emission features aligned along the south–south-west direction can be seen in the inner jet at higher frequencies. We have modeled the observed brightness distribution with a small number of model components having two-dimensional Gaussian profiles. The core region (i.e., the bright feature at the north end of the jet) is elongated in the 43 GHz image and can be modeled by two Gaussian components separated by 0.25 mas (0.32 pc projected distance). At a distances of 1.5 mas and 3.4 mas from the core, there are two other distinct emission features in the jet. A table listing the parameters of the jet features (“components”) can be found in Sokolovsky et al. (2010b).

The inner 0.25 mas part of the jet (i.e., the “core”) may contain two (or more) distinct emission features or it may be a continuous emission region. The angular resolution even at 43 GHz is not sufficient to distinguish between these possibilities. However, it is evident that the radio spectrum is changing along this region and it cannot be described by a single, uniform, self-absorbed, synchrotron emitting component. A turnover caused by the synchrotron self-absorption is detected in the averaged core spectrum at a frequency of ~ 12 GHz (an average over the whole area with the negative spectral index at Fig. 3.10). Due to the inhomogeneity, the innermost component at mm-wavelengths has most likely even higher turnover frequency, $\gtrsim 40$ GHz. Using the method described in Sokolovsky et al. (2010b), the magnetic field, B , of the core, in the frame of the relativistic jet, can be constrained, given the Doppler factor, $\mathcal{D} = (\Gamma[1 - \beta \cos \theta])^{-1}$, where $\Gamma = (1 - \beta^2)^{-1/2}$ and θ here are the bulk Lorentz factor and jet angle to the line of sight, respectively. Assuming a Doppler factor $\mathcal{D} = 7.3$ Hovatta et al. (2009), an upper limit can be placed on the magnetic field strength in the core: $B < 3$ G. We note that this upper limit corresponds to a typical value across an extended and inhomogeneous region contributing the bulk of the radio emission in 4.6–43 GHz range. The magnetic field strength can exceed the above limit locally or in a more compact regions hidden from sight in the observed frequency range by synchrotron opacity.

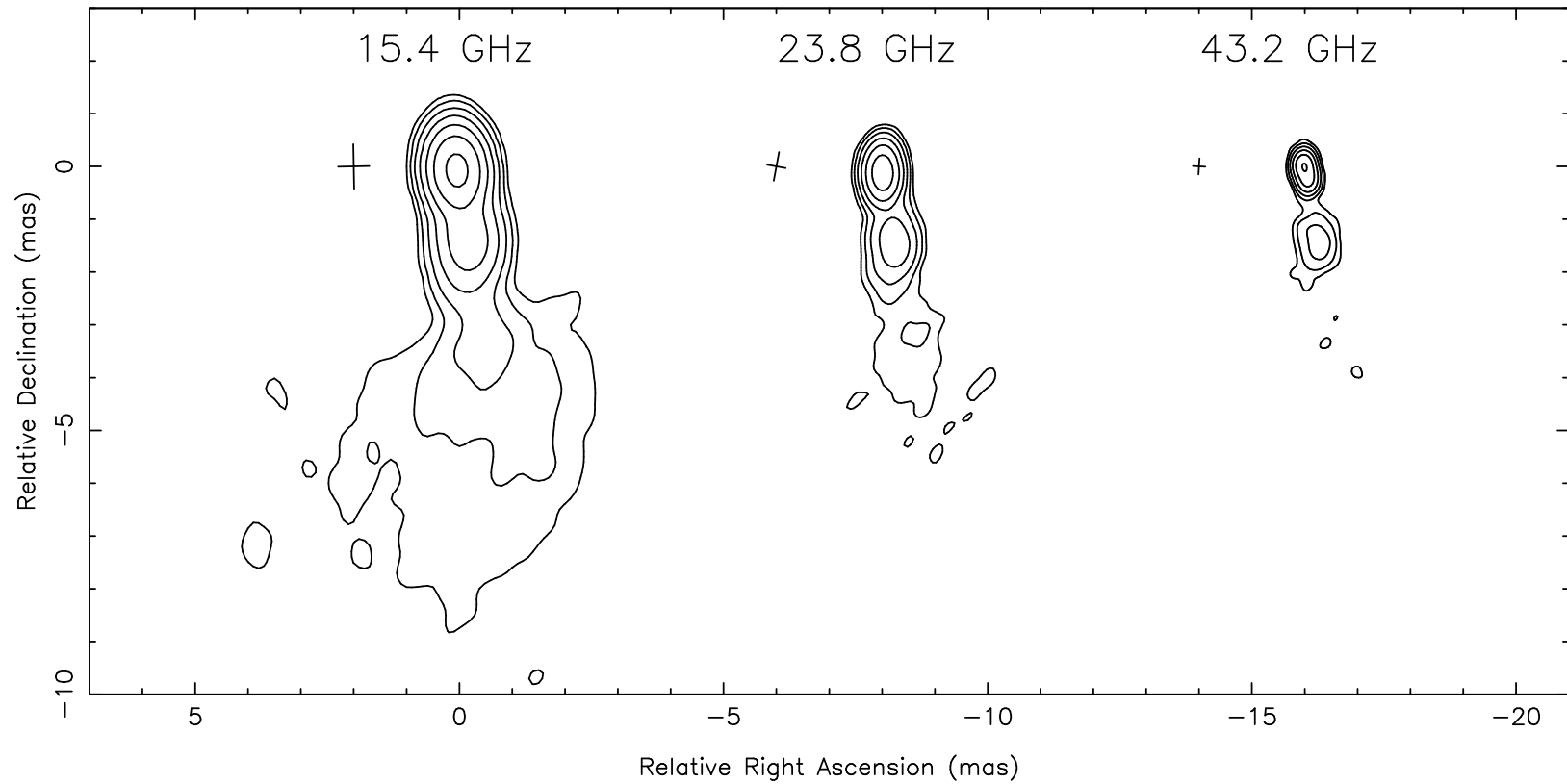


Figure 3.9: Inner jet of BL Lacertae as observed by the VLBA on September 02, 2008. Images at different frequencies are shifted by 8 mas in relative Right Ascension. For the 15.4, 23.8 and 43.2 GHz image map peaks are 1.69, 1.52, 1.32 Jy/beam, first contours are 1.70, 3.00, 5.00 mJy/beam respectively. The contour levels are increased by a factor of 3. Beam size (natural weighting) for each frequency is indicated by the cross to the left of the corresponding image.

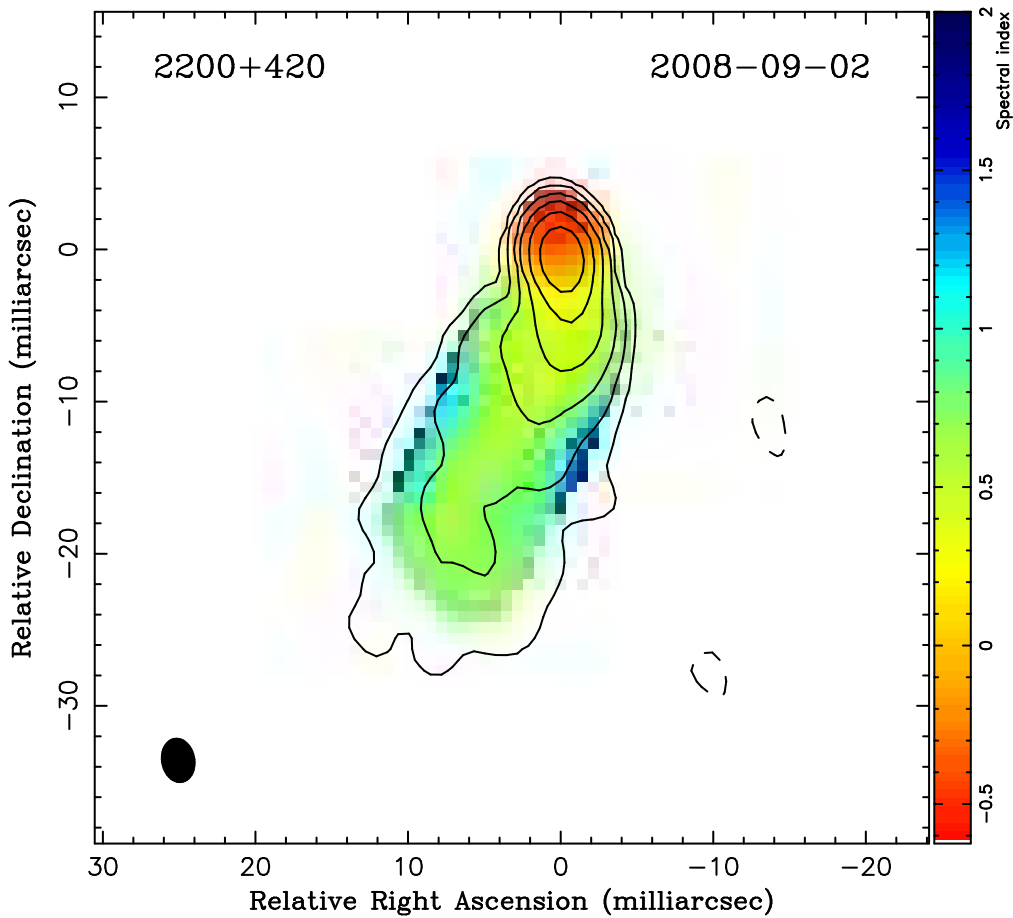


Figure 3.10: Spectral index map ($F_\nu \sim \nu^{-\alpha}$, α is shown in color) of BL Lacertae constructed using VLBA observations at 4.6, 5.0, 8.1 and 8.4 GHz. The overlaid contours represent total intensity at 8.4 GHz (the peak intensity is 1.75 Jy/beam, the first contour is 0.70 mJy/beam, the beam size is 1.57×1.22 mas at PA = $10^\circ.4$). The spectral index map was smoothed by a median filter with radius equal to the indicated beam size. The map shows an optically thin jet with $\alpha \sim 0.7$ and the self-absorbed core region ($\alpha < 0.0$). A 2D cross-correlation technique using the optically thin part of the jet was employed to align images at different frequencies allowing reliable extraction of the spectral information. The spectral steepening towards the jet edges visible on the spectral index map occurs on the angular scale comparable to the beam size and is likely an effect of the uneven uv -coverage at different frequencies.

3.3 Multiwavelength observations of PKS 1510–089

The results reported in this section were published in (i) Abdo et al. (2010a) which describes the *Fermi* multiwavelength campaign and (ii) Sokolovsky et al. (2010a) which presents a single-epoch quasi-simultaneous SED of the source obtained by us outside the *Fermi* campaign framework. While the SEDs reported in the above papers are averaged on different timescales (~ 1 month and ~ 1 week respectively) they look quite similar. It is interesting to compare the models used to describe SED of PKS 1510–089 in Abdo et al. (2010a) and Sokolovsky et al. (2010a). While both models provide a reasonably good fit to the NIR– γ -ray section of the SED, the source of the external

photons for the External inverse-Compton (EC) process and hence the location of the “blazar emission zone” with respect to the central engine envisioned in the models are substantially different. Clearly, more simultaneous multiwavelength observations, especially those including emission line monitoring, are needed to obtain an accurate understanding of the emission processes in this source.

3.3.1 General properties

Among blazars, Flat Spectrum Radio Quasars (FSRQ) are those objects characterized by prominent emission lines in the optical spectra. The typical spectral energy distribution (SED) of a blazar has a two bump shape (Abdo et al. 2010a). According to current models, the low energy bump is interpreted as synchrotron emission from highly relativistic electrons in the blazar jet, and the high energy bump is interpreted as inverse Compton (IC) emission. In FSRQs the IC bump can dominate over the synchrotron one by more than an order of magnitude. It is widely believed that in these sources the IC component is dominated by the scattering of soft photons produced externally to the jet (Dermer & Schlickeiser 2002; Sikora et al. 1994), rather than by the synchrotron self Compton emission (SSC, Ghisellini & Maraschi 1989; Jones et al. 1974). In the external radiation Compton scenario (EC), the seed photons for the IC process are typically UV photons generated by the accretion disk surrounding the black hole, and reflected toward the jet by the broad line region (BLR) within a typical distance from the disk in the sub-parsec scale. If the emission occurs at larger distances, the external radiation is likely to be provided by a dusty torus (DT; Sikora et al. 2002). In this case the radiation is typically peaked at IR frequencies.

PKS 1510–089 is one of the most active γ -ray blazars observed since the launch of *Fermi* Gamma-ray Space Telescope (Abdo et al. 2010a; D’Ammando et al. 2010). This object has an optical spectrum characterized by prominent emission lines overlying a blue continuum (Tadhunter et al. 1993) at a redshift $z = 0.361$ (Thompson et al. 1990). Radio images (Marscher et al. 2010b) show a bright core with a jet which has a large misalignment between the arcsecond and milliarcsecond scales. Superluminal velocities up to $\approx 20 c$ are observed (Homan et al. 2002; Lister et al. 2009) in the parsec-scale jet of PKS 1510–089.

3.3.2 VLBA observations of PKS 1510–089

Simultaneous multi-frequency 5–43 GHz VLBA measurements were done on 2009 April 09, in support of the first year *Fermi* observations (Sokolovsky et al. 2010a,b). Accuracy of flux density measurements is dominated by calibration uncertainties: about or less than 5% at 5, 8, and 15 GHz, about or less than 10% at 24 and 43 GHz. The full description of the observing program and analysis technique may be found in Section 2.2.

In Fig. 3.11 we present the three highest frequencies Stokes I parsec-scale images, from the 5-43 GHz VLBA measurements performed on 2009 April 9. The size of the bright parsec-scale core at 24 and 43 GHz is estimated to be about 60-70 μas or 0.3-0.4 pc. The core shows a flat radio spectrum (see Fig. 3.12) indicative of an inhomogeneous synchrotron self-absorbed region, while the first well resolved jet feature is already optically thin with the radio spectral index $\alpha = -0.9$ ($F(\nu) \propto \nu^\alpha$).

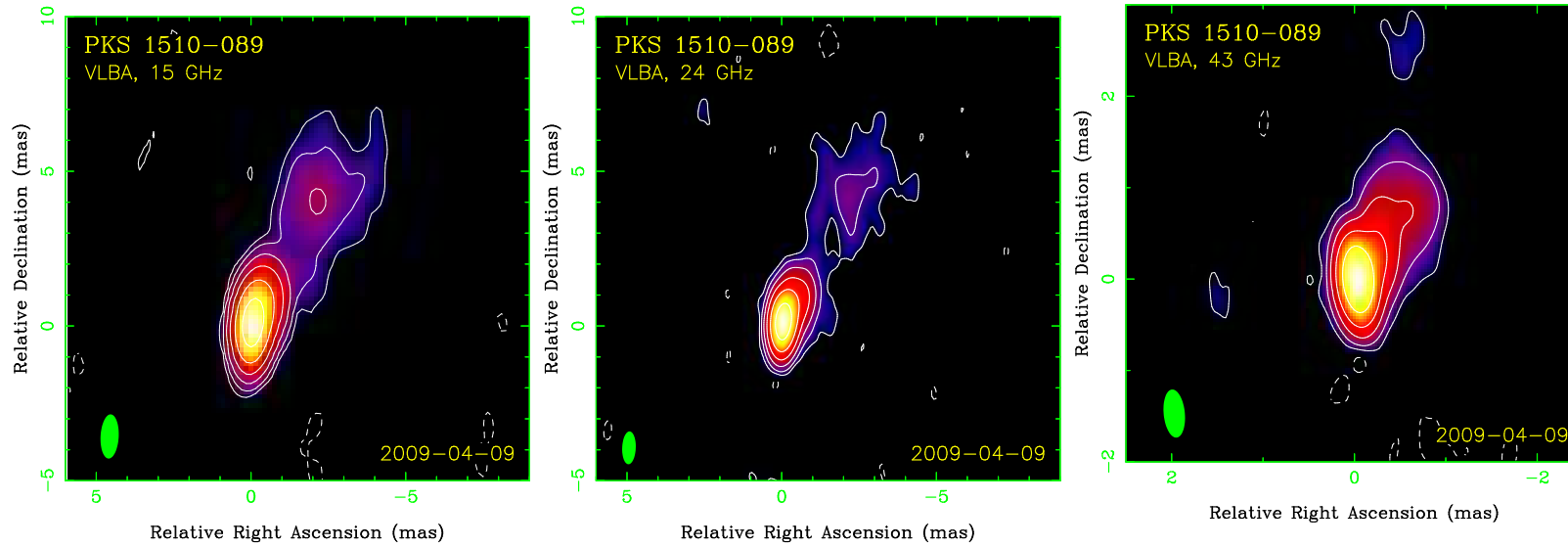


Figure 3.11: Stokes I CLEAN images of PKS 1510-089 observed by VLBA on 2009 April 9, at 15, 24, and 43 GHz. The lowest contour and peak intensity are 0.7 mJy/beam and 1.47 Jy/beam (15 GHz), 0.7 mJy/beam and 1.56 Jy/beam (24 GHz), 2 mJy/beam and 1.85 Jy/beam (43 GHz). Contours are plotted with a step $\times 4$. Natural weighting of visibility data is used, HPBW beam size is shown in the lower left corner. Angular size of 1 mas corresponds to 5 pc.

3.3.3 Quasi-simultaneous SED of PKS 1510–089

To obtain the quasi-simultaneous SED of PKS 1510–089 (Fig. 3.13) the VLBA, *Swift* and *Fermi*/LAT data collected during two days 2009 April 09 – 10 were complemented by *UBVR_ci* photometry obtained on April 12 with the 2.56 m Nordic Optical Telescope (NOT) and infrared *JHK_s* photometry obtained on April 07 and 17 with the 2.1 m telescope of Guillermo Haro Observatory in Cananea, México. The Submillimeter Array (SMA) provided flux density measurements at 1 mm from 2009 April 05 and 14. These observations resulted in the most well-sampled quasi-simultaneous SED (containing multi-frequency VLBI data) for that source.

UBV magnitudes of PKS 1510–089 observed by the *Swift*/UVOT are systematically (0^m5-0^m3) brighter than those observed by the NOT two days later. Since both observations were calibrated against the same set of comparison stars from González-Pérez et al. (2001), the difference can be interpreted as a clear sign of optical inter-day variability.

Parsec-scale radio emission of PKS 1510–089 is dominated by a bright unresolved core (the apparent origin of the jet, see a discussion by Marscher 2008) which exhibits high-amplitude flux density variability (Marscher et al. 2010a). The parsec-scale core is a natural candidate to be directly related to the bright variable emission at γ -rays (Kovalev et al. 2009; Marscher et al. 2010b, see also Section 3.1) and other bands.

To test the possible relation between the radio core and the emitting blob implied by single-zone SED models, we have constructed the quasi-simultaneous SED of PKS 1510–089 presented in Fig. 3.13. The use of the VLBI core flux density (instead of the total flux density obtained by single-dish radio observations) allows us to exclude the emission coming from the parsec-scale jet and larger scales. Our ambition was to check how this will affect the SED modeling.

Table 3.3: PKS 1510–089 SED model parameters from Sokolovsky et al. (2010a)

Minimum e^- Lorentz factor	$\gamma_{\min} = 30$
Brake Lorentz factor	$\gamma_{\text{brk}} = 1.9 \times 10^3$
Maximum e^- Lorentz factor	$\gamma_{\max} = 1.0 \times 10^5$
e^- energy slope below γ_{brk}	$p_1 = 1.9$
e^- energy slope above γ_{brk}	$p_2 = 3.9$
Doppler factor	$D = 37$
Bulk Lorentz factor	$\Gamma = 37$
Magnetic field strength	$B = 0.09 \text{ G}$
Variability time	$t_{\text{var}} = 2.16 \times 10^4 \text{ sec}$
Blob radius	$R = 1.8 \times 10^{16} \text{ cm}$
Jet power (magnetic field)	$P_{\text{jet, B}} = 2.8 \times 10^{43} \text{ erg/s}$
Jet power (electrons)	$P_{\text{jet } e^-} = 7.5 \times 10^{45} \text{ erg/s}$
Black hole mass	$M_{\text{BH}} = 1 \times 10^9 M_{\odot}$
Accretion efficiency	$\eta = 1/12$
Eddington ratio	$L_{\text{disk}}/L_{\text{Edd}} = 0.06$
Blob distance from disk	$r = 5.1 \times 10^{17} \text{ cm}$

The quasi-simultaneous SED of PKS 1510–089 (Fig. 3.13) has been modeled by Sokolovsky et al. (2010a). Contribution from a hot thermal component, probably the accretion disk, is evident in the optical and UV bands. The SED in the IR to γ -ray range can be explained by the single zone EC model with the Compton scattered accretion

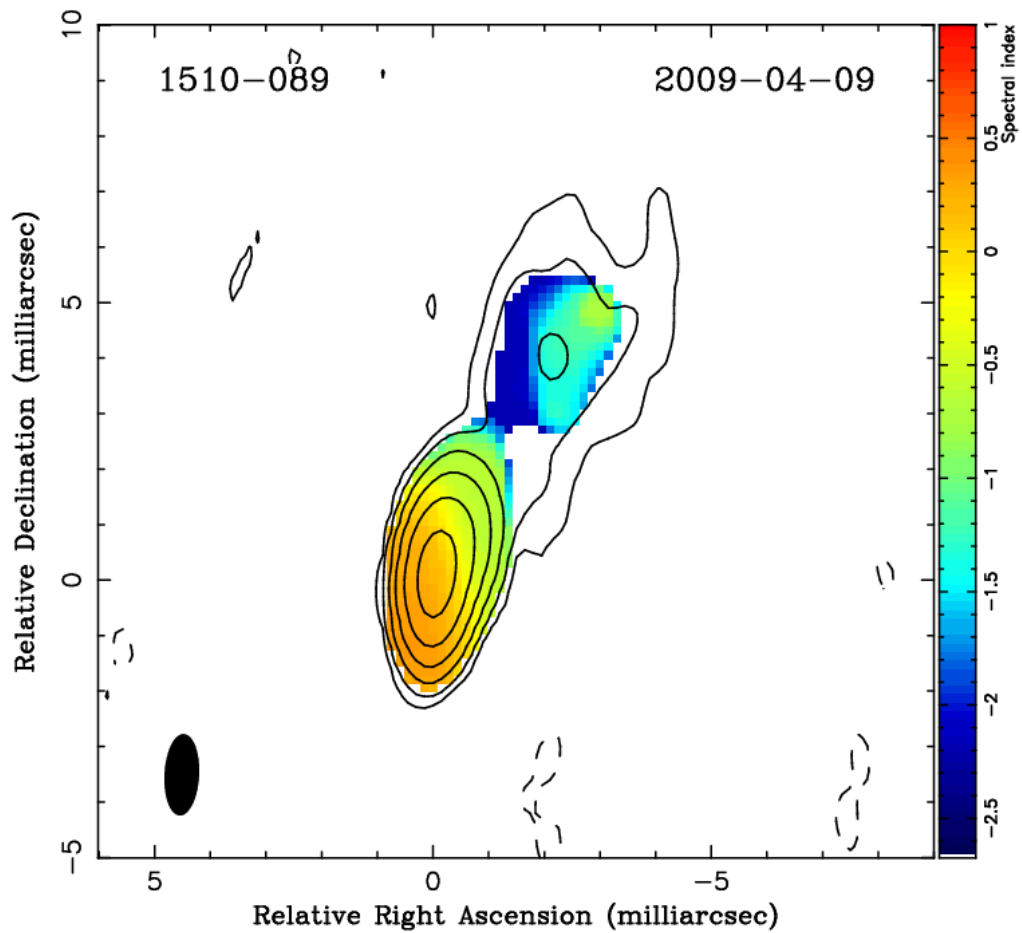


Figure 3.12: Spectral index α ($F(\nu) \propto \nu^\alpha$) map between 15.4 and 23.8 GHz (shown in color) of PKS 1510–089 as observed by the VLBA on 2009 April 9. The overlaid contours represent total intensity at 15.4 GHz (see Figure 3.11 for details). The spectral index map was smoothed by a median filter with a 0.6 mas radius.

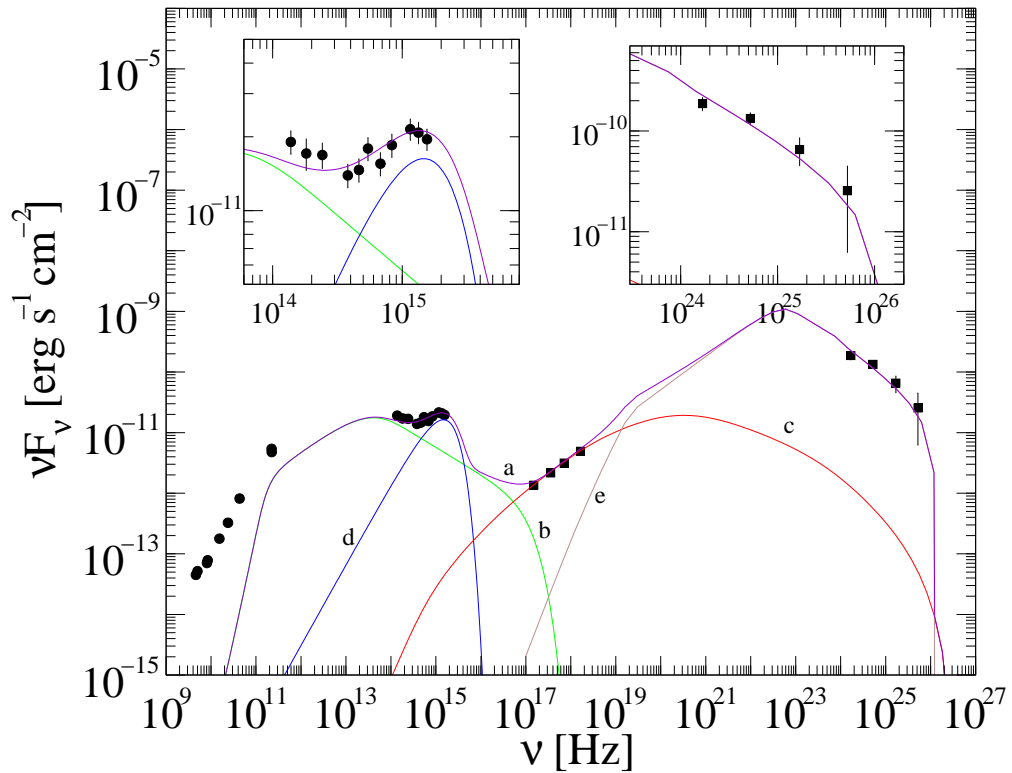


Figure 3.13: Quasi-simultaneous SED of PKS 1510–089 from Sokolovsky et al. (2010a) constructed using observations with the VLBA, *Swift*, *Fermi*/LAT, NOT, SMA and the 2.1 m telescope Guillermo Haro. The violet curve (a) represents the combined SED model: green curve (b) is the synchrotron component, red (c) is the SSC component, blue (d) is the accretion disk and brown (e) represents EC scattering of the disk radiation (see also Table 3.3).

disk photons being responsible for the bulk of the observed γ -ray emission. In this model, the blob is close enough to the accretion disk so the accretion disk photons can reach the blob directly, with no need to be scattered back from BLR clouds or dust. Note, that due to relativistic aberration some of the disk photons will be coming to the blob (nearly) head-on. The photons will primarily come from a radius of the disk of $\sqrt{3}r$ where r is the blob's distance from the black hole (Dermer & Schlickeiser 2002). The blob size was constrained by the observed γ -ray variability time scale of the order of a few hours (Abdo et al. 2010a). Parameters of the model are summarized in Table 3.3. We note that the model fit presented by Sokolovsky et al. (2010a) is not unique, single-zone models with a different source of seed photons could probably also produce an acceptable fit (cf. Abdo et al. 2010a).

The model constructed by Sokolovsky et al. (2010a) and reproduced here on Fig. 3.13 represents well the IR to γ -ray data, however it dramatically underpredicts the radio emission because of the synchrotron self-absorption occurring in the small blob at a high frequency. A significantly larger blob size would be inconsistent with the observed variability timescale. Even if the variability timescale argument were dismissed, a single-zone SED model with a larger blob would have difficulties in explaining the observed hard radio spectrum which is inconsistent with the softer X-ray spectrum or optically thick synchrotron radiation from a uniform source. One way to overcome this difficulty would be to introduce a second brake in the electron energy spectrum.

Alternatively, one could abandon the attempt to explain the whole SED of PKS 1510–089 with a single-zone model and assume that even the radio emission observed from the cm-mm band core is coming from a larger ($R_{\text{SED}} < R < R_{43 \text{ GHz}}$) structure downstream of the blob responsible for the IR-to- γ -ray emission. This structure (which cannot be observed separately from the blob due to limited resolution of the available VLBI data) could be a smooth jet (Blandford & Konigl 1979) or a number of distinct jet components (Marscher 1980) – perhaps the blobs which contributed to high-energy emission earlier... One could argue that currently this extended region does not contribute significantly to the optical and γ -ray emission on the basis of the observed short timescale variability in these bands. A more detailed SED modeling is needed to test this scenario. Especially, the relation between activity in the parsec-scale radio core observed in many sources (Section 3.1; Jorstad et al. 2010, 2001; Kovalev et al. 2009; Pushkarev et al. 2010) including PKS 1510–089 (Marscher et al. 2010b) would require an explanation in such models. This is currently one of the central problems with blazar studies across the electromagnetic spectrum. This situation of SED model not being able to reproduce the observed radio emission is, of course, not confined to PKS 1510–089, but is actually quite common (Bianchin et al. 2009; Boettcher 2010; Collmar et al. 2010 are just a few examples).

3.4 VLBA view of TeV blazars Mrk 421 and Mrk 501

This section summarizes the results of 5–43 GHz VLBA observations in the context of *Fermi* multiwavelength campaigns on two nearby BL Lac type objects: Mrk 421 ($z = 0.031$ Gorham et al. 2000) and Mrk 501 ($z = 0.033$ Stickel et al. 1993). Since these two objects are so close to us, the flux measurements by VLBA, especially the ones corresponding to the core, provide us with the radio flux density from a region that is presumably not much larger than the blazar emission region (Abdo et al. 2010c). They are expected to be close upper limits to the radio continuum of the blazar emission component.

Imaging Atmospheric Cherenkov Telescope (IACT) arrays MAGIC⁴ and VERITAS⁵ have participated in these two *Fermi* campaigns. Quasi-simultaneous SEDs of unprecedented quality covering radio to TeV energies have been obtained for these sources. The results will be discussed in detail in two papers recently submitted to ApJ Abdo et al. (2010b,c).

The VLBA data reduction was conducted in the similar fashion as described in the previous sections. The only difference is that for the data used in these campaigns *C* and *X*-band data were not split into two sub-bands, instead, all four IFs were combined to get a single image for each band. Integrated over parsec-scales flux values were obtained by summing all components of the CLEAN model. The flux errors are dominated by the uncertainties in the VLBA amplitude calibration and are $\sim 5\%$ for *C*, *X* and *K_u* bands, $\sim 10\%$ for *K* and *Q* bands.

Core flux was obtained by modeling the core region at each frequency with a circular Gaussian component. Flux corresponding to the extended jet of Mrk 501 was CLEANed because it could not be adequately fitted with multiple of Gaussian components. The jet of Mrk 421 on the other hand was successfully modeled with a series of circular Gaussian components. Uncertainties in modeling may introduce additional error in the core flux measurements compared to uncertainties in the total flux. The results of total parsec-scale and core flux density measurements for the two sources are presented in Table 3.4. The radio spectrum of Mrk 501 is presented on Fig. 3.14.

Table 3.4: VLBA flux measurements of Mrk 421 and Mrk 501

Band	Frequency (GHz)	Total Flux (Jy)	Core Flux (Jy)
Mrk 421			
2009-04-22 = JD 2454943.6			
<i>C</i>	4.8060	0.369	0.251
<i>X</i>	8.2690	0.343	0.247
<i>K_u</i>	15.3655	0.324	0.247
<i>K</i>	23.8045	0.299	0.233
<i>Q</i>	43.2175	0.267	0.223
Mrk 501			
2009-05-15 = JD 2454966.8			
<i>C</i>	4.8060	1.131	0.674
<i>X</i>	8.2690	1.118	0.664
<i>K_u</i>	15.3655	0.938	0.629
<i>K</i>	23.8045	0.789	0.548
<i>Q</i>	43.2175	0.615	0.427

The core of Mrk 421 is partially-resolved by our observations according to the resolution criterium proposed by Kovalev et al. (2005) and Lobanov (2005) (see Section 2.2). The VLBA core size was determined with two-dimensional Gaussian fits to the measured visibilities. The FWHM size of the core was estimated to be in the range 0.06–0.12 mas at the highest observing frequencies: 15, 24 and 43 GHz. Both the total and the core radio flux densities from the VLBA data are shown in Table 3.4.

The size of the VLBA core in the 2009 data from Mrk 421 at 15 GHz and 43 GHz is $1\text{--}2 \times 10^{17}$ cm (using the conversion scale 0.61 pc/mas). The VLBA size estima-

⁴<http://wwwmagic.mppmu.mpg.de/>

⁵<http://veritas.sao.arizona.edu/>

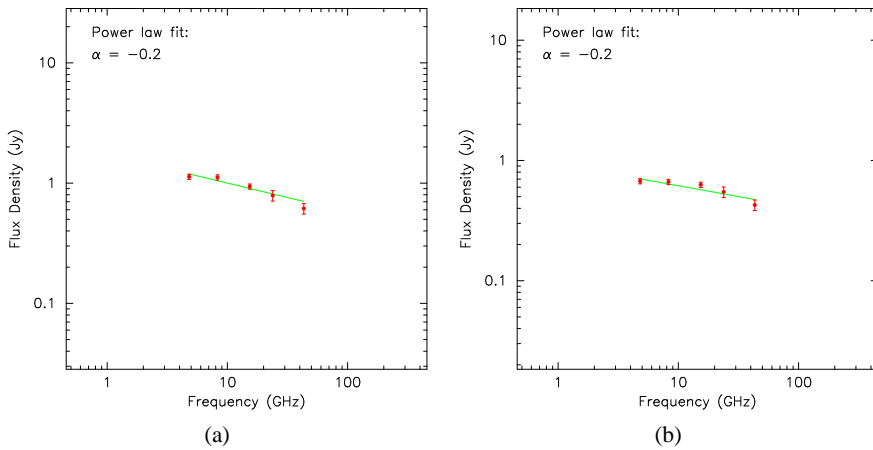


Figure 3.14: The VLBA spectrum of Mrk 501: 3.14a — integrated parsec-scale spectrum, 3.14b — core spectrum.

tion is the FWHM of a Gaussian representing the brightness distribution of the blob, which could be approximated as 0.9 times the radius of a corresponding spherical blob (Marscher 1983). That implies that the size of the VLBA core is comparable (factor 2–4 larger) to that of the blob derived from the SED model Abdo et al. (2010c). Therefore, it is reasonable to consider that the radio flux density from the VLBA core of Mrk 421 is indeed dominated by the radio flux density of the blazar emission. Forthcoming multi-band correlation studies (in particular VLBA and SMA radio with the γ -rays from *Fermi*/LAT) will shed light on this particular subject (Abdo et al. 2010c).

The estimated size of the partially-resolved VLBA core of Mrk 501 at 15 GHz and 43 GHz is 0.14–0.18 mas $\simeq 2.9$ – 3.7×10^{17} cm (with the appropriate conversion scale 0.67 pc/mas). The VLBA size estimation again is the FWHM of a Gaussian representing the brightness distribution of the blob, which could be approximated as 0.9 times the radius of a corresponding spherical blob (Marscher 1983). That implies that the size of the VLBA core is only a factor 2–3 larger than the emission region in the SSC model fit by Abdo et al. (2010b) ($R = 1.3 \times 10^{17}$ cm).

3.5 Chapter summary

In this chapter we have presented results of multi-frequency VLBA observations of 3C 454.3, BL Lacertae, PKS 1510–089, Mrk 421, and Mrk 501 in the context of their broad-band emission across the electromagnetic spectrum. VLBI data provide important constraints on the size, radio spectrum, magnetic field strength and particle energy distribution of the blazar emission zone. The obtained constraints were either directly used in the SED modeling (3C 454.3, BL Lacertae, PKS 1510–089) or found consistent with the modeling results (Mrk 421, and Mrk 501). Despite the initial success, clearly, more work needs to be done to fully incorporated VLBI results into existing blazar emission models.

Chapter 4

A VLBA survey of the core shift effect in AGN jets

The effect of a frequency dependent shift of the VLBI core position (known as the “core shift”) has been predicted more than three decades ago and has since been observed in a few sources, but often within a narrow frequency range. This effect has important astrophysical and astrometric applications. In order to achieve a broader understanding of the core shift effect and the physics behind it we have conducted a dedicated survey with NRAO’s Very Long Baseline Array (VLBA). We have used the VLBA to image 20 pre-selected sources simultaneously at nine frequencies in the 1.4–15.4 GHz range. The core position at each frequency was measured by referencing it to a bright, optically thin feature in the jet. A significant core shift has been successfully measured in each of the twenty sources observed. The core position, r_c , as a function of frequency, ν , is found to be consistent with a $r_c \propto \nu^{-1}$ law. Such behavior is predicted by the Blandford & Königl model of a purely synchrotron self-absorbed conical jet in equipartition. No systematic deviation from the power law index in the $r_c(\nu)$ relation has been convincingly detected. We conclude that neither free-free absorption nor gradients in pressure and/or density in the jet itself and in the ambient medium surrounding the jet play a significant role in the sources observed within the 1.4–15.4 GHz frequency range. These results support the interpretation of the parsec-scale core as a continuous Blandford-Königl type jet with smooth gradients of physical properties along it.

The results described in this chapter are described in the paper submitted to A&A(Sokolovsky et al. 2010d).

4.1 Introduction

In VLBI images of relativistic AGN jets the “core” is the most compact feature near the apparent base of the jet. It is identified with the surface at which the optical depth $\tau_\nu \approx 1$ (photosphere) in a continuous jet flow with gradually changing physical properties (Blandford & Königl 1979). The position of this surface is a function of the observation frequency, ν , and the exact form of this function depends on the absorption mechanism. The above interpretation of the core is supported by the observation of the “core shift” effect (e.g., Kovalev et al. 2008b; Lobanov 1998b; Marcaide et al. 1985; O’Sullivan &

Gabuzda 2009; Zensus et al. 1995) and the related increase of the apparent core size towards lower frequencies (Unwin et al. 1994; Yang et al. 2008).

An alternative interpretation of the VLBI core as a standing shock in the jet was discussed by Marscher (2006a, 2008). This interpretation may be relevant for high-frequency observations of some sources. The standing shock model does not predict a shift of the apparent core position with frequency unless one resorts to an assumption that there is a series of multiple standing shocks and different shocks are observed as the core at different frequencies. In some objects the core could be a region where the jet bends such that it is more aligned with the line of sight leading to an increased Doppler beaming factor relative to jet regions further upstream (Marscher 2006a). It has even been discussed sometimes, that the radio core may not be part of the jet at all (e.g. Bell & Comeau 2010; Falcke et al. 2001).

The most likely absorption mechanism acting in the compact jet is synchrotron self-absorption (Konigl 1981). If the jet is freely expanding and there is an equipartition between the particle and magnetic field energy densities, the position $r_c(\nu)$ of the $\tau_\nu = 1$ surface will be $r_c(\nu) \propto \nu^{-1/k}$, where the coefficient $k = 1$. If the above assumptions do not hold (e.g., synchrotron self-absorption is not the dominating absorption mechanism) we can expect a different dependency of $r_c(\nu)$.

Investigation of the core shift effect is important to gain deeper understanding of the structure and physical conditions in ultracompact AGN jets. It may also provide information about the pressure and density gradients in ambient medium surrounding VLBI-scale jets – the broad-line region (BLR) and the inner part of the narrow-line region (NLR) (e.g., Lobanov 2007). The impact of the effect on the interpretation of current and future radio Very Long Baseline Interferometry (VLBI) astrometric measurements has been discussed by Porcas (2009); Rioja et al. (2005). The core shift is expected to introduce a systematic offsets of approximately 0.1 mas between the optical (6000 Å) and radio (8 GHz) positions of reference extragalactic sources (Kovalev et al. 2008b), which needs to be taken into account for accurate radio–optical reference frame alignment in the era of modern space-based astrometric missions (Lindgren 2007) such as GAIA (Perryman et al. 2001) and for accurate spacecraft navigation with VLBI (e.g., Hildebrand et al. 1994; Pogrebenko et al. 2009; Sekido et al. 2004).

In this Chapter, we present observational results from a dedicated nine frequency (1.4–15.4 GHz) VLBA survey of the core shift effect in 20 compact extragalactic radio sources. The selection of targets, the VLBA observation setup, our data reduction strategy and the core shift measurement technique are described in Section 4.2. In Section 4.3, we discuss the results and their implication for the dominating absorption mechanism in the core region. Section 4.4 presents a brief summary of this work.

4.2 VLBA observations

4.2.1 Sample selection

A blind survey for sources with measurable core shifts would be an extraordinarily time consuming project because it requires performing simultaneous multi-frequency high resolution, high dynamic range VLBI observations. Therefore, we turned to an existing large-scale geodetic VLBI database in order to find promising candidates for the survey. Kovalev et al. (2008b) have imaged and analyzed 277 sources from the Research and Development VLBA program (RDV, see Fey & Charlot 1997 and Petrov et al. 2009) observations made in 2002–2003. RDV experiments involve simultaneous

Table 4.1: The high core shift source sample observed with the VLBA

Name	Alias	R.A. (J2000)	Dec. (J2000)	z	Optical class	VLBA epoch
0148+274		01:51:27.146174	+27:44:41.79363	1.26	QSO	2007-03-01
0342+147		03:45:06.416545	+14:53:49.55818	1.556	QSO	2007-06-01
0425+048	OF 42	04:27:47.570531	+04:57:08.32555	0.517 ^a	AGN	2007-04-30
0507+179		05:10:02.369133	+18:00:41.58160	0.416	AGN	2007-05-03
0610+260	3C 154	06:13:50.139161	+26:04:36.71971	0.580	QSO	2007-03-01
0839+187		08:42:05.094175	+18:35:40.99050	1.272	QSO	2007-06-01
0952+179		09:54:56.823616	+17:43:31.22204	1.478	QSO	2007-04-30
1004+141		10:07:41.498089	+13:56:29.60070	2.707	QSO	2007-05-03
1011+250		10:13:53.428771	+24:49:16.44062	1.636	QSO	2007-03-01
1049+215		10:51:48.789077	+21:19:52.31374	1.300	QSO	2007-06-01
1219+285	W Comae	12:21:31.690524	+28:13:58.50011	0.161 ^b	BL Lac	2007-04-30
1406-076		14:08:56.481198	-07:52:26.66661	1.493	QSO	2007-05-03
1458+718	3C 309.1	14:59:07.583927	+71:40:19.86646	0.904	QSO	2007-03-01
1642+690		16:42:07.848505	+68:56:39.75639	0.751	QSO	2007-04-30
1655+077		16:58:09.011464	+07:41:27.54034	0.621	QSO	2007-06-01
1803+784		18:00:45.683905	+78:28:04.01839	0.680	QSO	2007-05-03
1830+285		18:32:50.185622	+28:33:35.95514	0.594	QSO	2007-03-01
1845+797	3C 390.3	18:42:08.989895	+79:46:17.12825	0.056	AGN	2007-06-01
2201+315		22:03:14.975788	+31:45:38.26990	0.298	QSO	2007-04-30
2320+506		23:22:25.982173	+50:57:51.96364	1.279	QSO	2007-05-03

Column designation: Col. 1 – IAU source name (B1950), Col. 2 – commonly used source name, Col. 3 and 4 – VLBI position, for details see http://astrogeo.org/vlbi/solutions/rfc_2010c/ and Beasley et al. (2002); Fomalont et al. (2003); Kovalev et al. (2007); Petrov et al. (2009, 2005, 2006, 2008), Col. 5 and 6 – redshift and optical class from Véron-Cetty & Véron (2010), Col. 7 – epoch of multi-frequency VLBA observations reported in this work.

^a Spectroscopic redshift obtained by Afanas'ev et al. (2003).

^b Photometric redshift, see Finke et al. (2008).

dual frequency 2.3/8.6 GHz (*S/X* band) observations with the VLBA and up to ten other globally distributed antennas. The data processing technique and imaging results are described by Pushkarev & Kovalev (2010). The core shift was measured by Kovalev et al. (2008b) by referencing the core position to optically thin jet features, the positions of which are not expected to change with frequency.

We have selected 18 sources with large core shifts between 2.3 and 8.6 GHz from the list of Kovalev et al. (2008b). These sources were selected in such a way that they not only show large core shifts in this frequency range, but are also particularly suitable for measuring it by referencing the core position to bright jet features – the technique used in this Chapter. This procedure is needed because the absolute position information is lost during the phase self-calibration process necessary for VLBI imaging; therefore it is not known a priori how images at different frequencies should be aligned. Two more sources, 2201+315 and 3C 309.1 (1458+718), were added to the list in order to continue our previous core shift studies (Homan & Kovalev 2010; Lobanov 1998b; Ros & Lobanov 2002).

4.2.2 VLBA observation setup

Twenty sources selected as promising candidates for a detailed core shift investigation were observed with the VLBA (Napier 1994) during four 24 h sessions in March – June 2007. The list of the observed sources is presented in Table 4.1. Each source was observed simultaneously using *L*, *S*, *C*, *X*, and *K_u* band receivers (according to the Institute of Electrical and Electronics Engineers or IEEE nomenclature, see Table 4.2) in the 1.4–15.4 GHz range. At each band four 8 MHz-wide frequency channels (IFs, Table 4.2) were recorded in both right and left circular polarizations with 2-bit sampling and a total aggregate bit rate of 256 Mbits/sec. The correlation of the data was performed at the VLBA Array Operation Center in Socorro, NM, USA, with an averaging

Table 4.2: IF central frequencies

IEEE Band	IF	Frequency (MHz)
<i>L</i>	1	1404.49
<i>L</i>	2	1412.49
<i>L</i>	3	1658.49
<i>L</i>	4	1666.49
<i>S</i>	1	2275.49
<i>S</i>	2	2283.49
<i>S</i>	3	2383.49
<i>S</i>	4	2391.49
<i>C</i>	1	4604.49
<i>C</i>	2	4612.49
<i>C</i>	3	4999.49
<i>C</i>	4	5007.49
<i>X</i>	1	8104.49
<i>X</i>	2	8112.49
<i>X</i>	3	8425.49
<i>X</i>	4	8433.49
<i>K_u</i>	1	15353.49
<i>K_u</i>	2	15361.49
<i>K_u</i>	3	15369.49
<i>K_u</i>	4	15377.49

Column designation: Col. 1 – Radio band name according to the IEEE radar band nomenclature, Col. 2 – number of the frequency channel (IF), Col. 3 – central frequency of the frequency channel (IF).

time of 2 seconds. Data in *L*, *S*, *C*, and *X* bands were divided in two sub-bands (two IFs in each sub-band) centered at 1.4, 1.7, 2.3, 2.4, 4.6, 5.0, 8.1, and 8.4 GHz respectively. *K_u* band was not divided into sub-bands in order to achieve image sensitivity similar to other frequencies in a comparable integration time; all four IFs were stacked together around 15.4 GHz. The central frequencies of the sub-bands were chosen in such a way that at least one sub-band in each band is centered at a frequency for which antenna gain curve measurements are available. A special procedure was applied to ensure accurate amplitude calibration of all sub-bands (Section 4.2.3).

4.2.3 Data calibration and imaging

The initial calibration was conducted in *AIPS* (Greisen 2003) following the standard VLBA calibration procedure involving a priori amplitude calibration with measured antenna gain curves and system temperatures, phase calibration using the phase-cal signal injected during observations and fringe fitting. The fringe fitting was performed by the task *FRING*. A separate solution for the group delay and phase rate was made for each frequency channel (IF). As the final step of calibration, bandpass corrections were applied utilizing the task *BPASS*.

The sources were imaged independently in each band, using the CLEAN algorithm ((Högbom 1974); Section 2.1.1) implemented in the *Difmap* software (Shepherd 1997). Global amplitude corrections for left and right circular polarization for each IF at each antenna were determined by comparing the total intensity CLEAN model obtained with the initially calibrated data (again using *Difmap*). The amplitude corrections obtained were averaged over all the sources observed in the experiment with the exception of 0610+260 and 1830+285. The latter two sources have steep radio spectra (Kovalev et al. 2002, 1999b) and were not used for the amplitude corrections

computation in order to avoid introducing systematic errors in the corrections. The significant amplitude correction factors which were found are listed in Table 4.3. These amplitude corrections were introduced into the dataset using the *AIPS* task *CLCOR*. After that *L*, *S*, *C* and *X* band data were split into two sub-bands as described above and final total intensity imaging for each sub-band was conducted independently using *Difmap*. The resulting accuracy of the amplitude calibration is expected to be $\sim 5\%$. Naturally weighted CLEAN images of the observed sources between 1.4 and 15.4 GHz are presented in Fig. 4.1.

The structure of each source at each frequency has been modeled by Sokolovsky et al. (2010d) in the visibility (*uv*) plane with a number of circular Gaussian components using the *Difmap* software (Shepherd 1997). The components were visually cross-identified between frequencies. One suitable bright optically-thin jet component was chosen and its distance from the VLBI core (the optically-thick feature at the apparent base of the jet) was measured at each frequency. Model component positions and sizes for the core as well as the jet feature used for this analysis are indicated in Fig. 4.1. In some rare cases we were unable to construct a consistent model to allow for accurate and robust component cross-identification with other frequencies. In these cases no model components are shown in Fig. 4.1 and no data are used in the analysis.

The technique of using an optically thin jet component as a reference point for the core position measurement has previously been successfully tested on *S/X* band RDV data by Kovalev et al. (2008b) in several ways: (i) similar core shift values were obtained referencing to different jet features of the same source; (ii) the core shift for the quasar 1655+077 agreed within the errors with previous phase-referenced measurements by Homan & Kovalev (2010); (iii) two RDV epochs of the quasar 1642+690 resulted in values being in good agreement. Kovalev et al. (2008b) have also investigated the effect of the different *uv*-coverage resulting in a different resolution (and amount of blending between the core and nearby jet regions) at *S* and *X* band on core shift measurements. The effect was found to be small compared to the core position shift between these bands (see Fig. 5 in Kovalev et al. 2008b).

In addition to that, we have performed the following test to look for indications of blending in our 1.4–15.4 GHz results. If significant blending is present, we should measure systematically larger core shifts for sources with jet directions aligned with the P.A. of the elongated VLBA beam. However, no such dependence is found in the data.

An alternative approach to multi-frequency VLBI image alignment based on two-dimensional cross-correlation has been proposed by Walker et al. (2000). It has been successfully applied for core shift measurements by O’Sullivan & Gabuzda (2009) in sources with smooth jets where referencing to a distinct bright jet component was not possible. A potential disadvantage of this method is that, in principle, it may introduce artificial offsets between frequencies in the presence of spectral gradients along the jet. A similar problem may affect the model component-based method used here, if there is a large spectral gradient across a resolved reference component. However, the spectral index gradient is smaller for an individual component than for a large section of parsec-scale jet used in cross-correlation analysis. Early observations of the frequency dependent difference in distance between the core and jet components were actually interpreted by Biretta et al. (1986) as a sign of spectral gradients across the components. This interpretation is disfavored by the detection of core position shift with frequency in phase-referenced experiments (Homan & Kovalev 2010; Marcaide et al. 1985; Rioja et al. 1997) and the fact that strong spectral gradients across individual jet components are not routinely observed.

A significant core shift has been detected in each of the twenty sources observed within our VLBA program. The effect is especially pronounced at frequencies below 5 GHz. The results are discussed in detail in Section 4.3 and presented visually in Fig. 4.2.

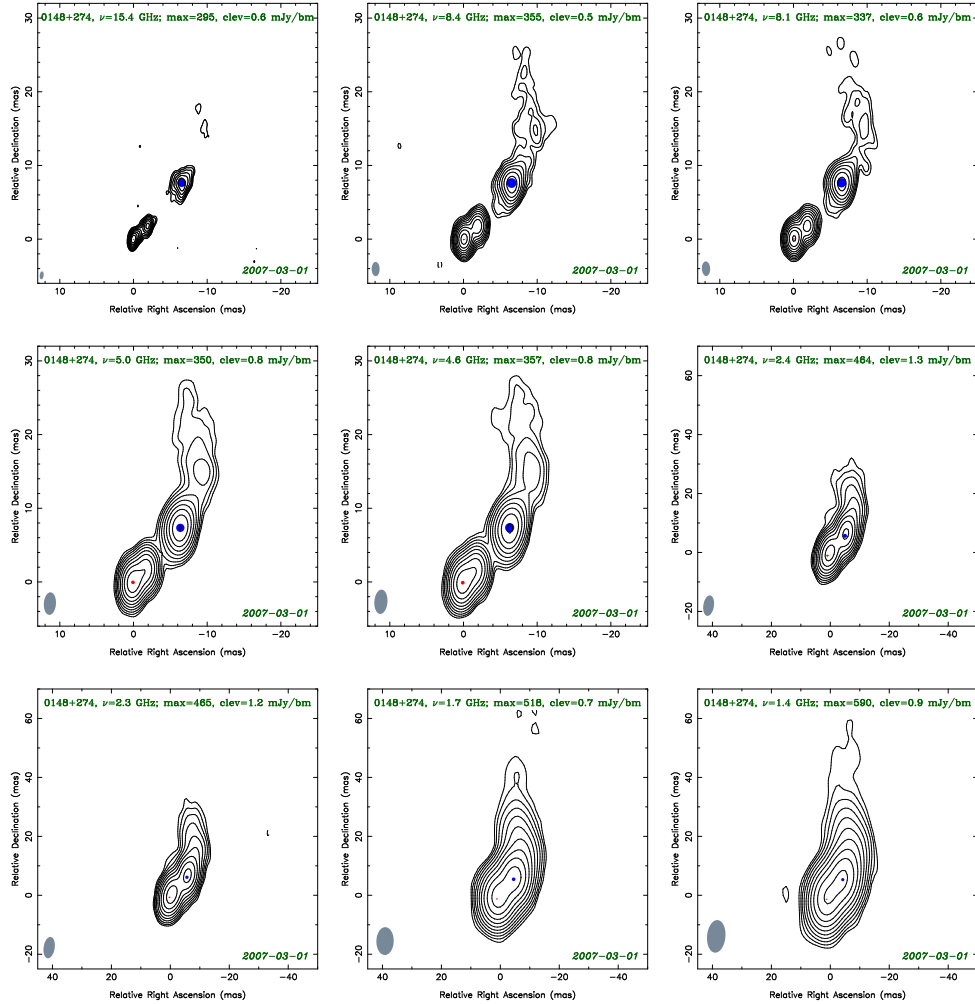


Figure 4.1: Naturally weighted CLEAN images of the observed sources between 1.4 and 15 GHz. The lowest contour value ‘clev’ is chosen at four times the rms noise, the peak brightness is given by ‘max’. The contour levels increase by factors of two. The dashed contours indicate negative brightness. The beam’s full width at half maximum (FWHM) is shown in the bottom left corner of the images in grey. An epoch of observation is shown in the bottom right corner. Red and blue spots indicate the positions and sizes (FWHM) of Gaussian model components for the core and the jet features respectively.

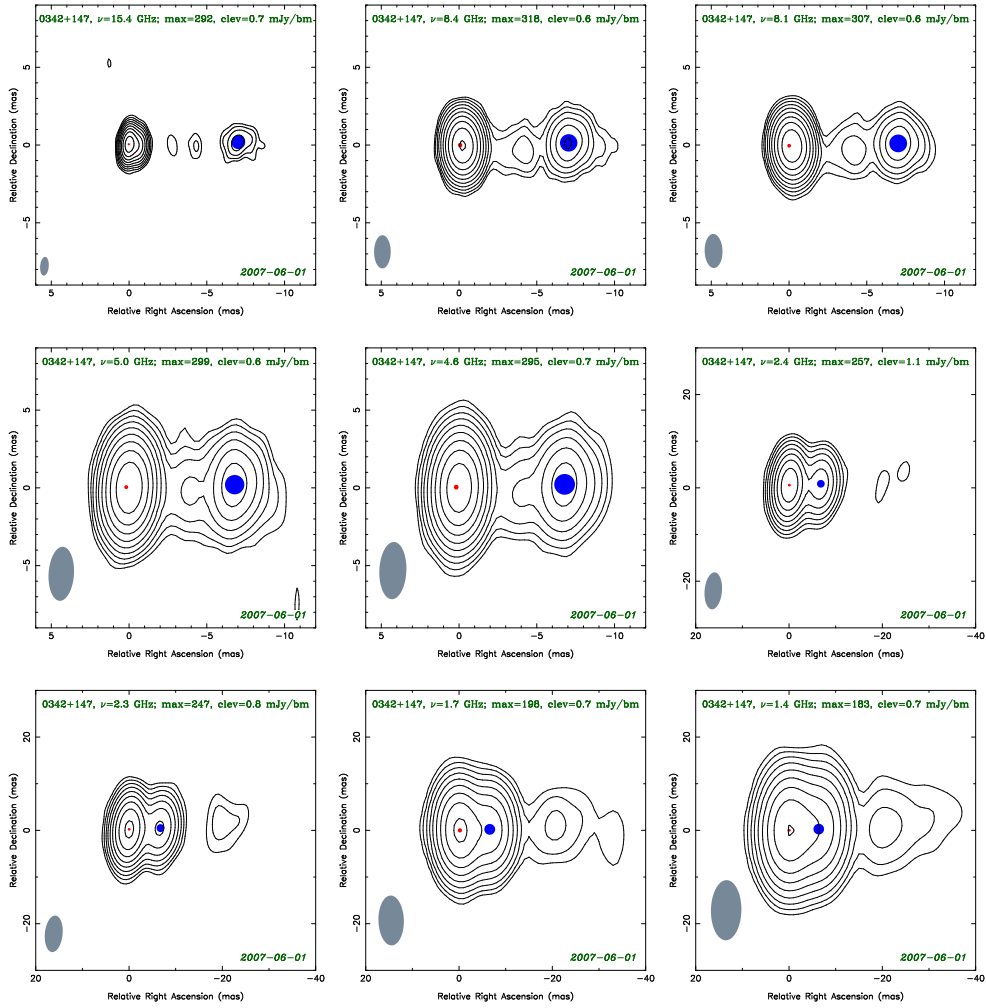


Figure 4.1 continued...

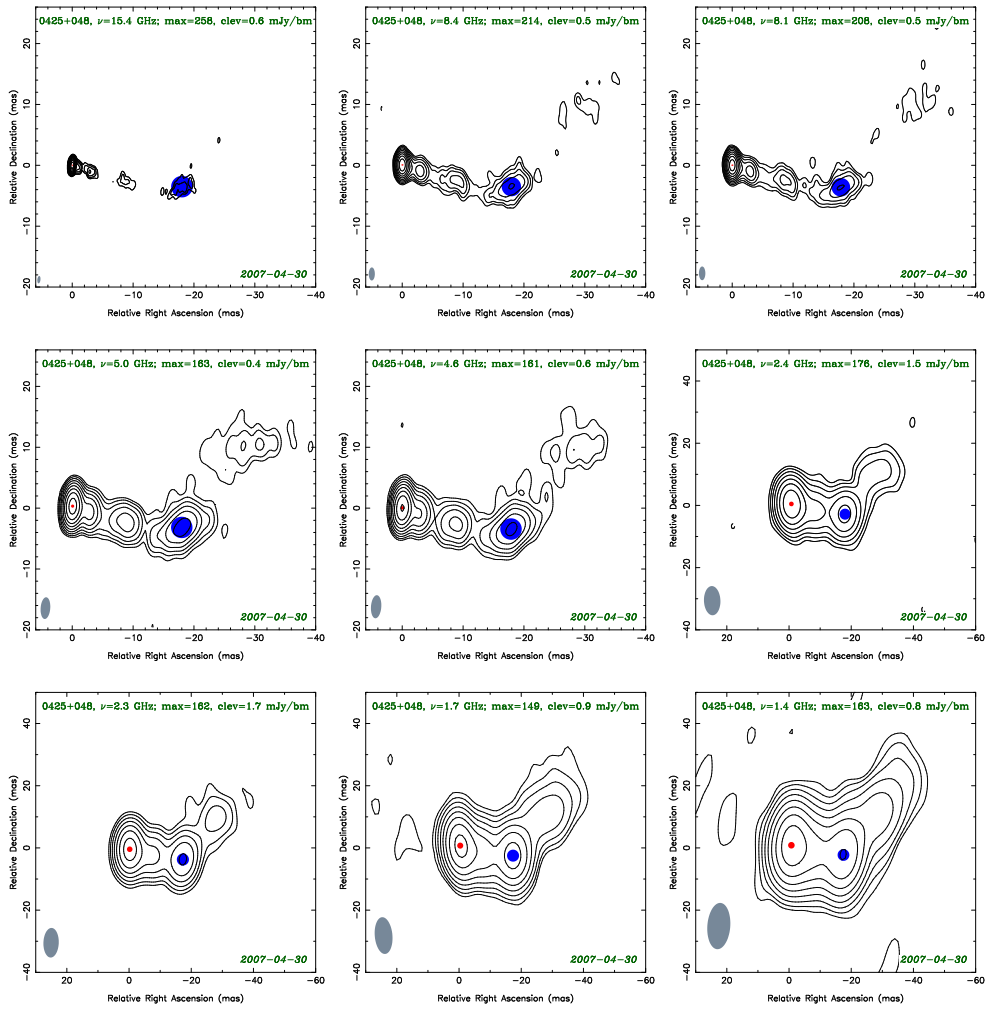


Figure 4.1 continued...

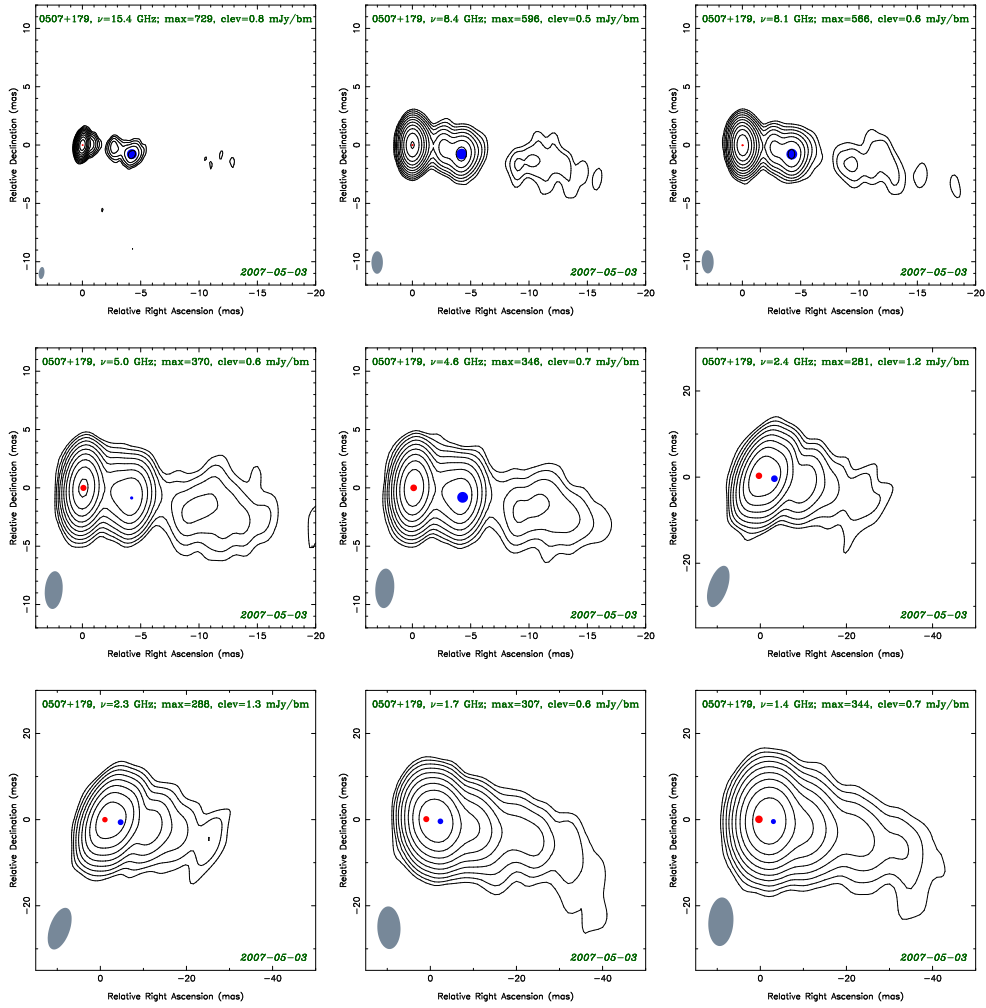


Figure 4.1 continued...

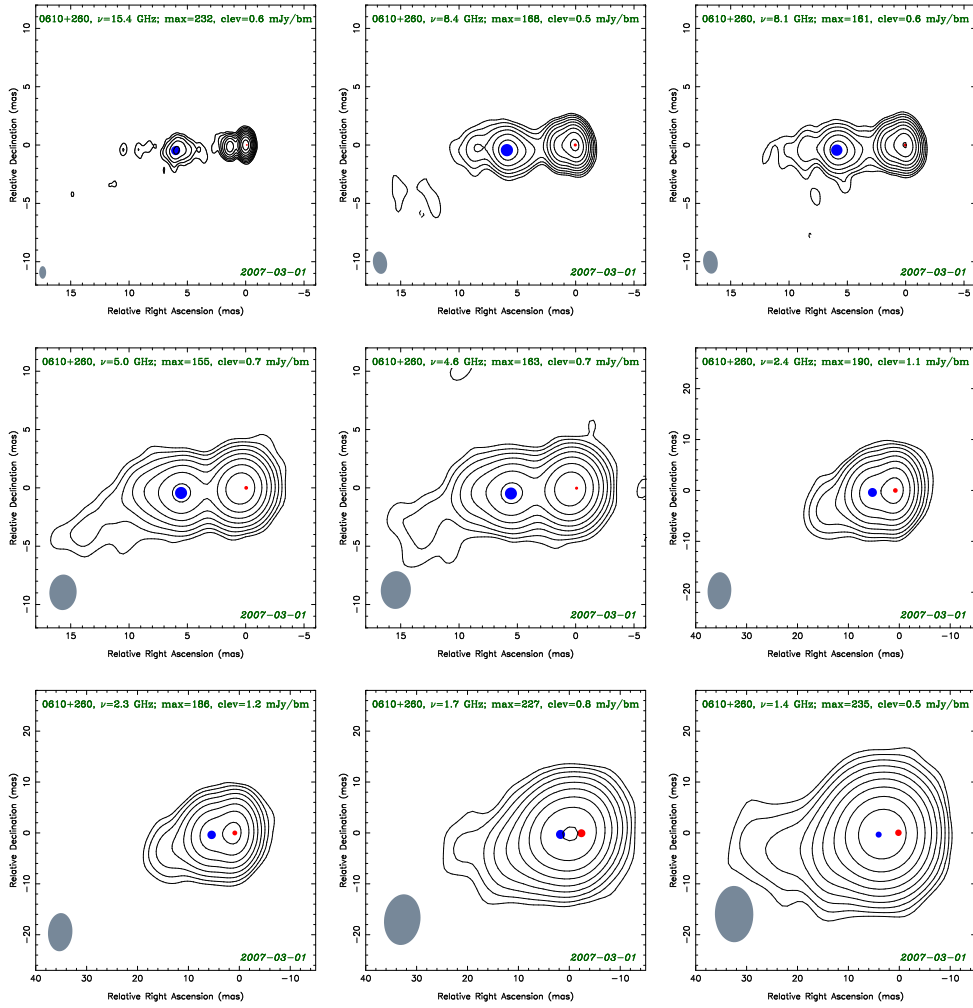


Figure 4.1 continued...

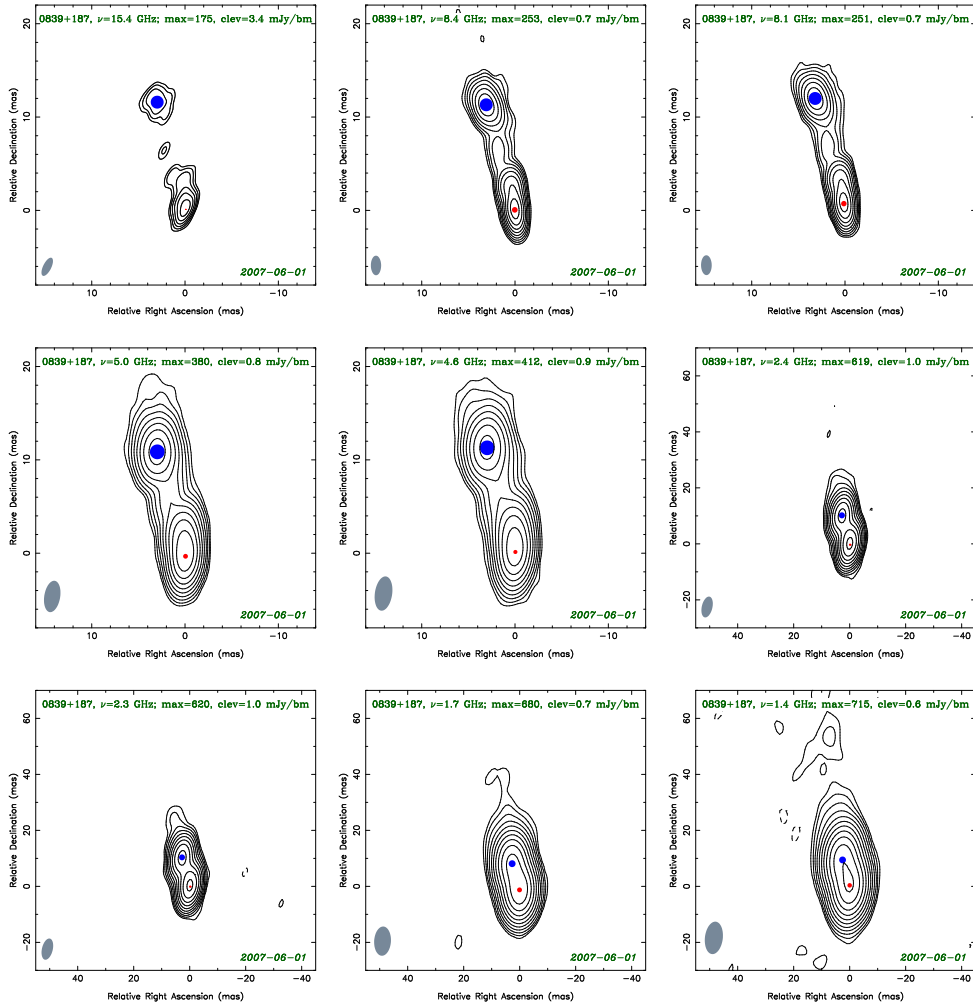


Figure 4.1 continued...

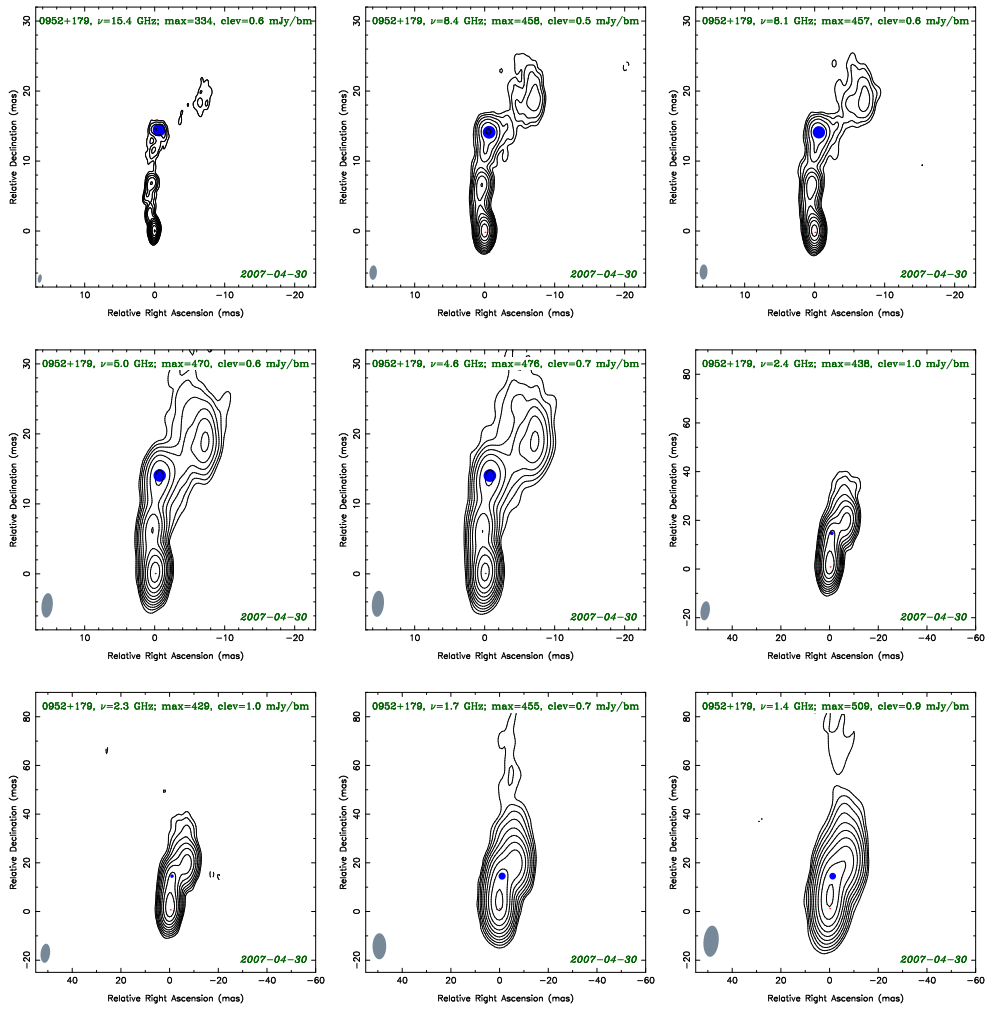


Figure 4.1 continued...

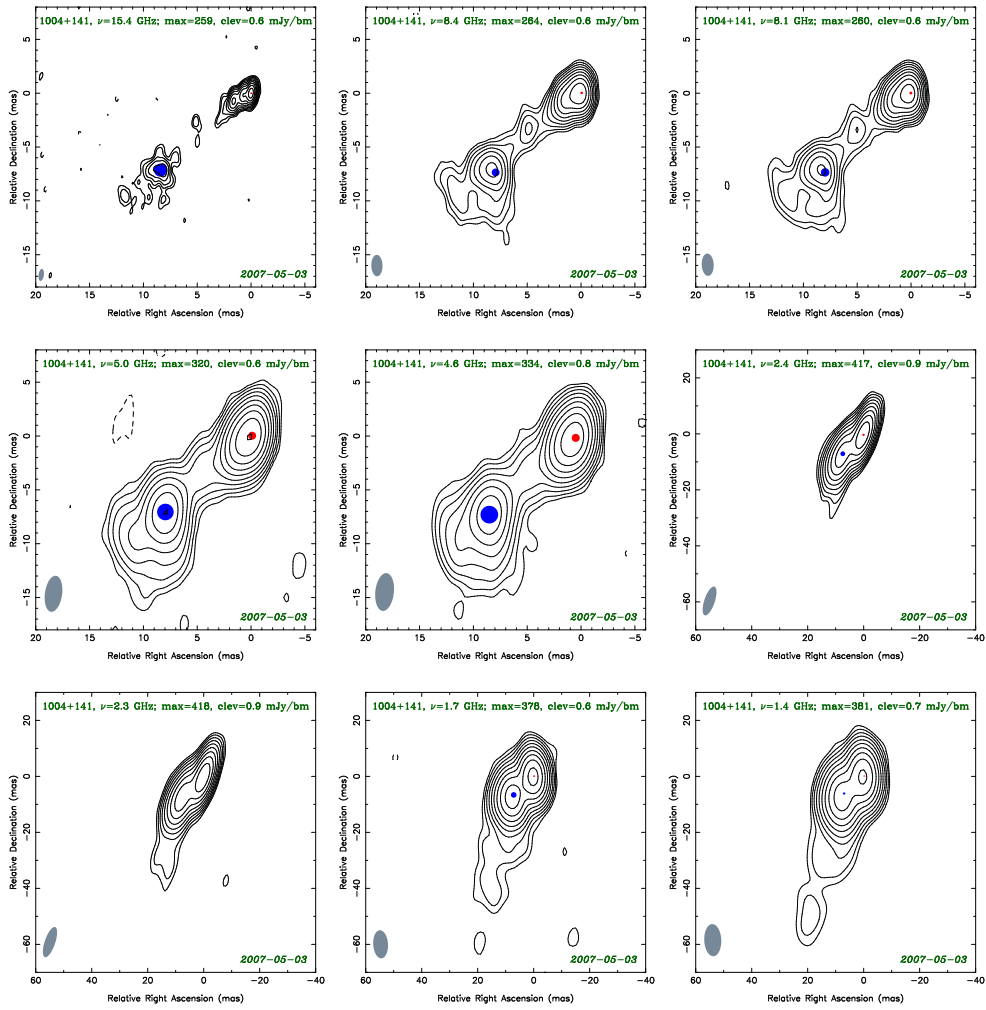


Figure 4.1 continued...

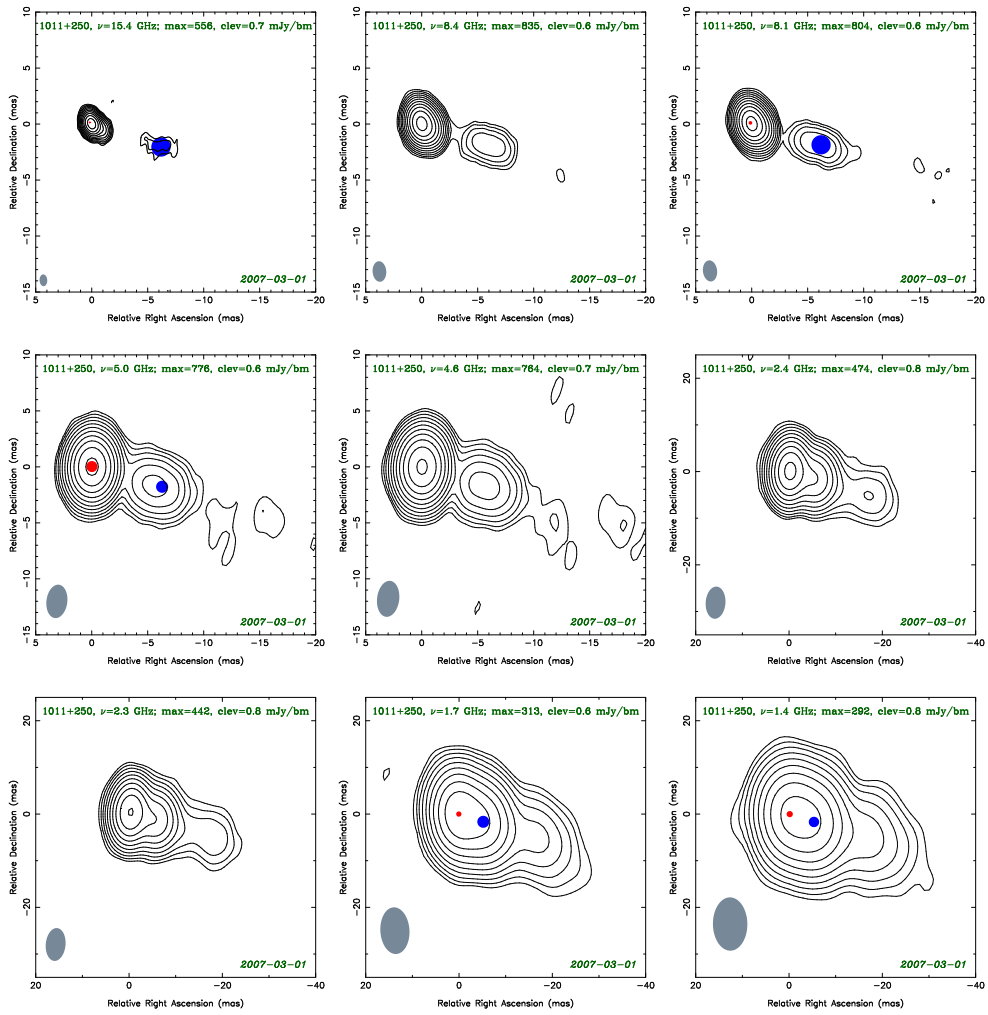


Figure 4.1 continued...

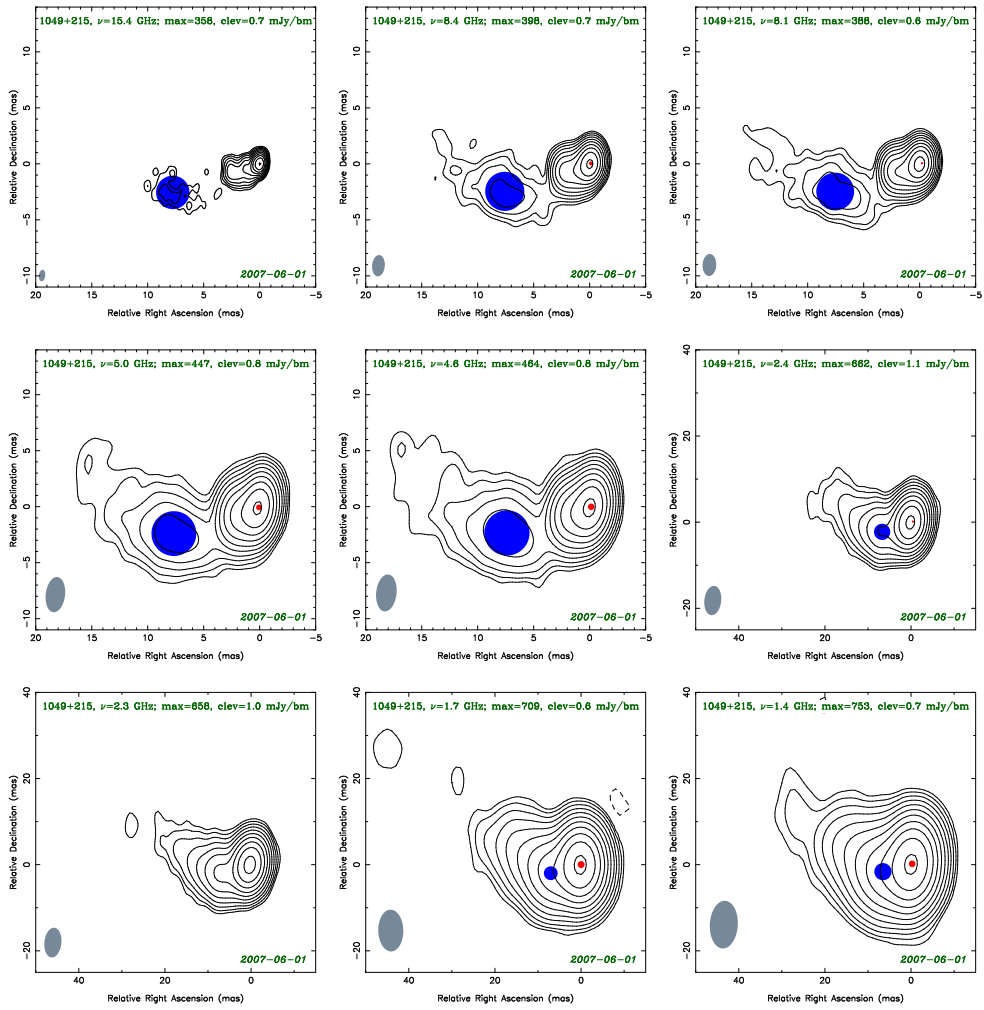


Figure 4.1 continued...

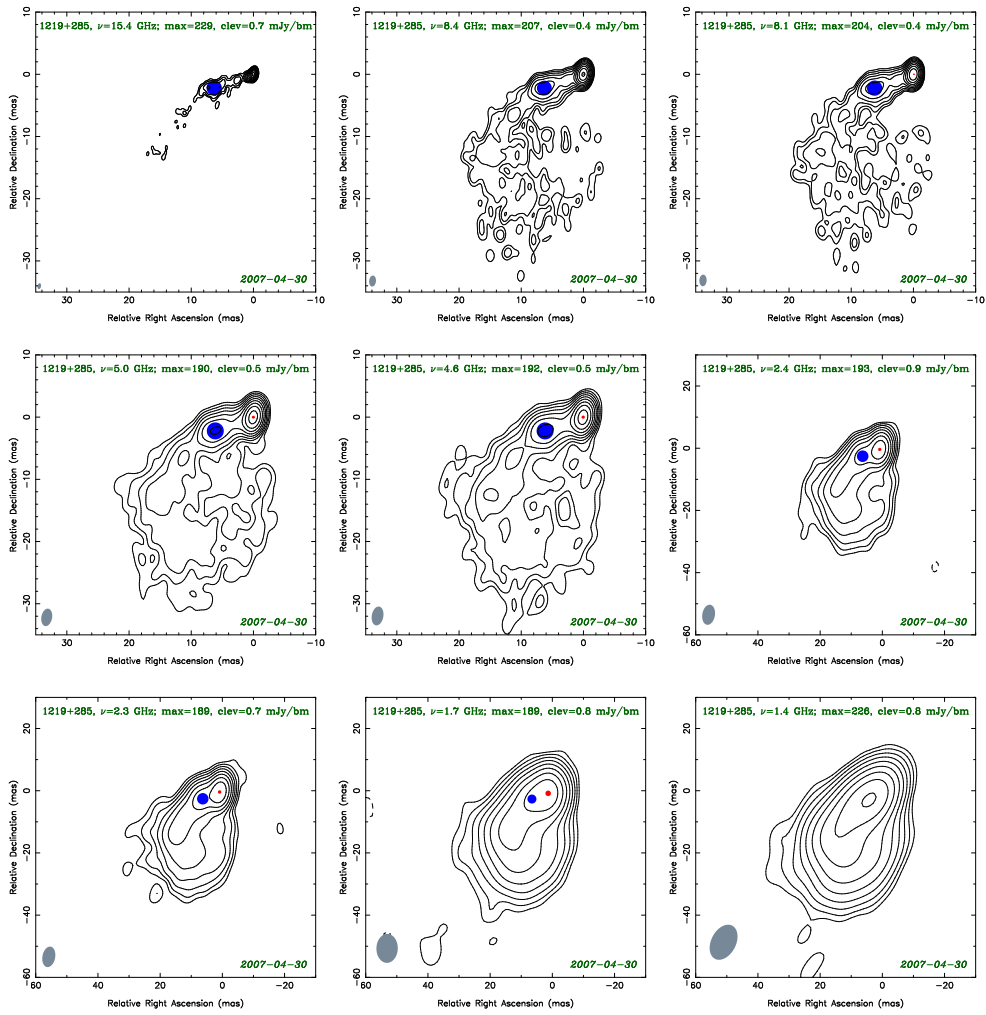


Figure 4.1 continued...

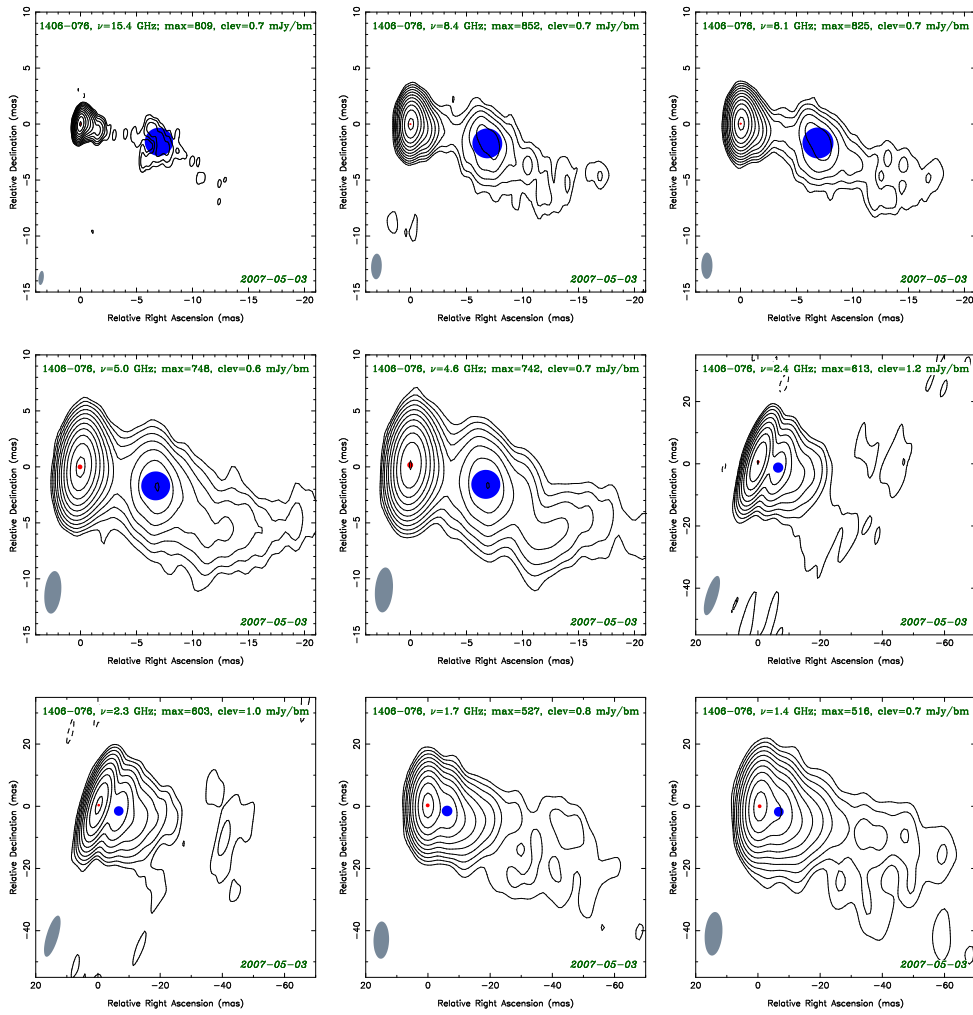


Figure 4.1 continued...

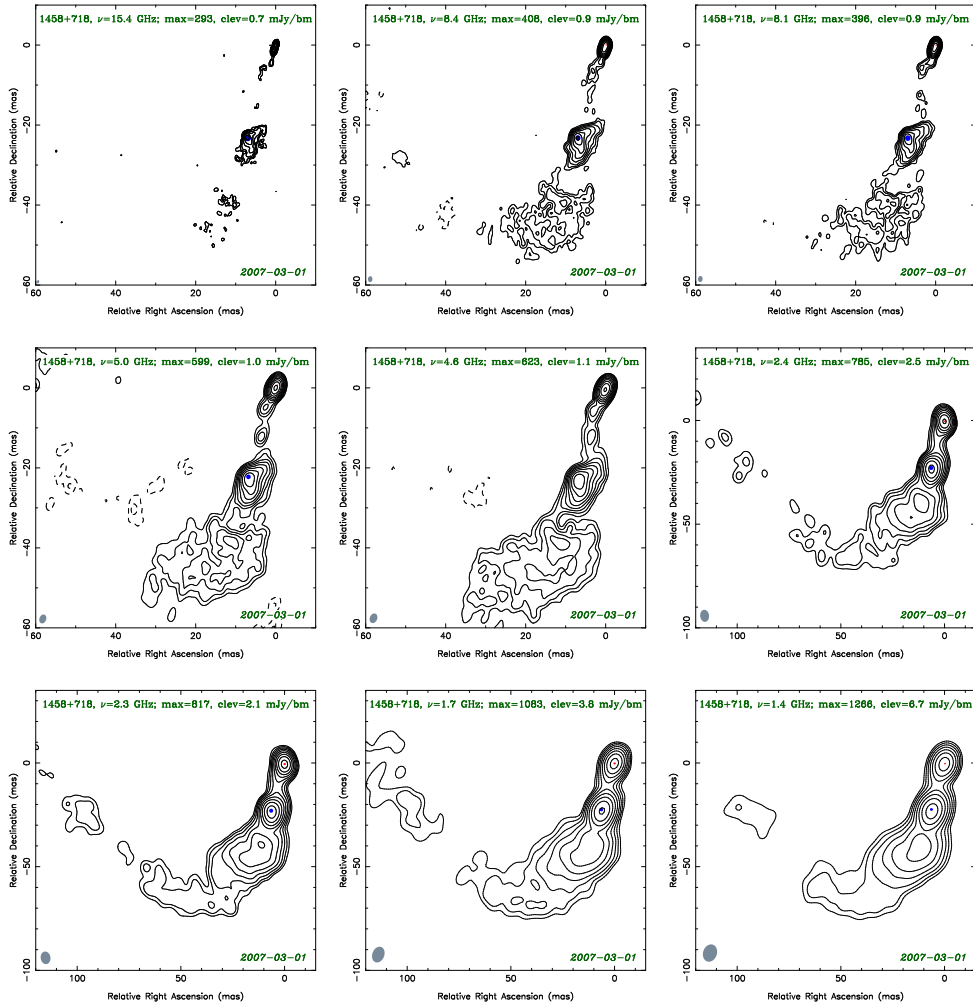


Figure 4.1 continued...

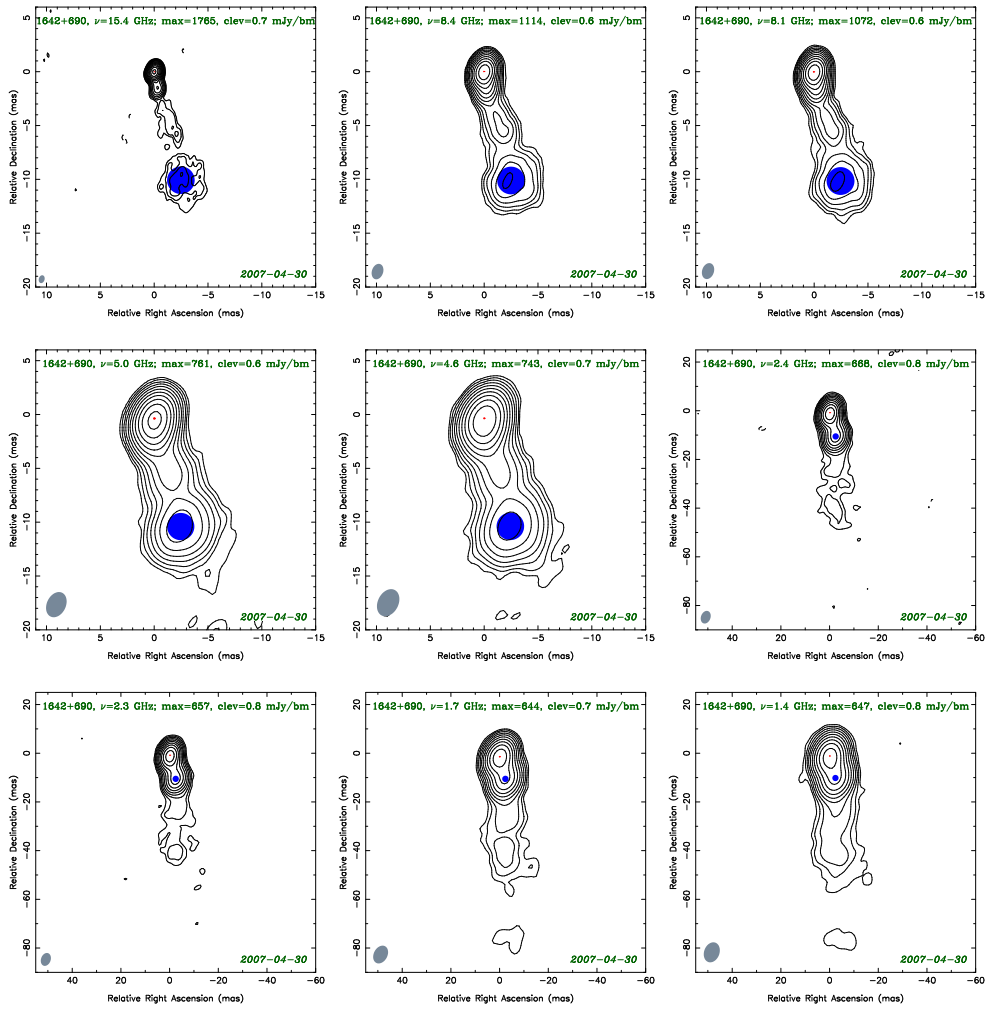


Figure 4.1 continued...

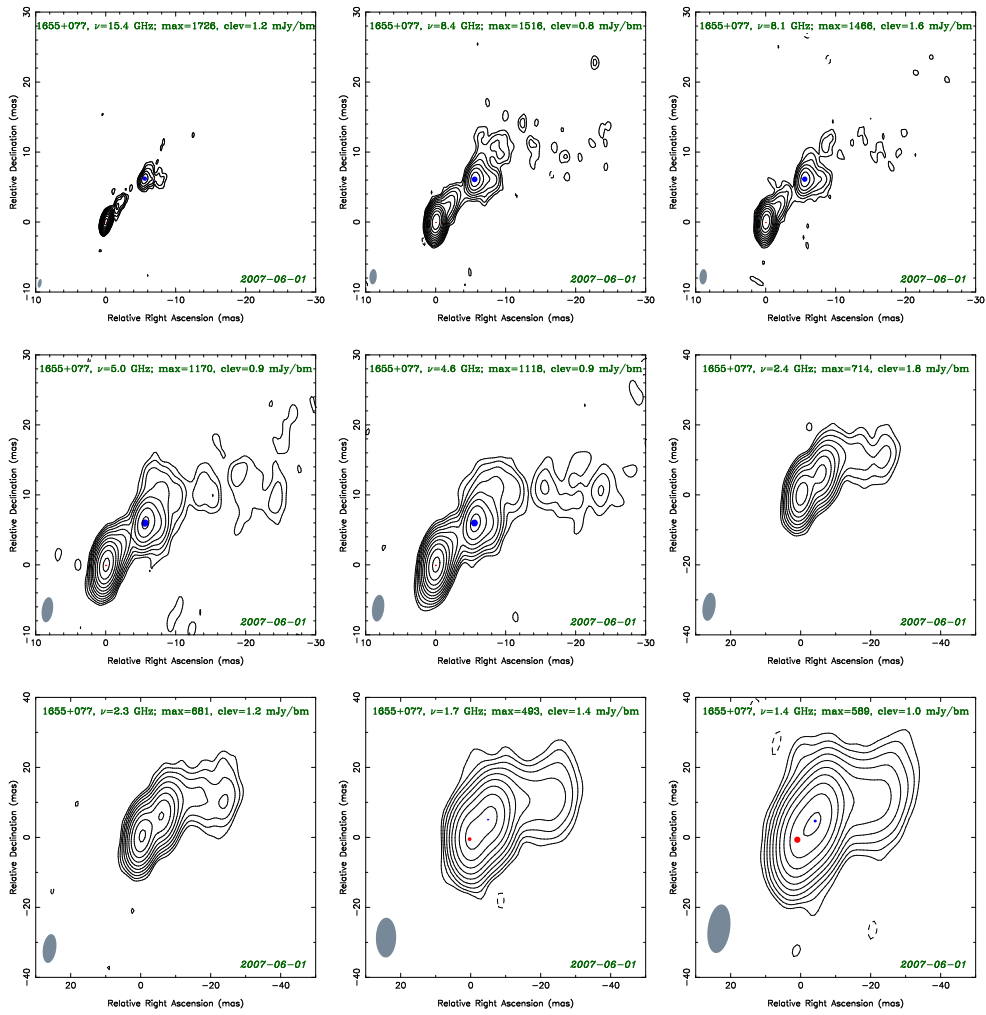


Figure 4.1 continued...

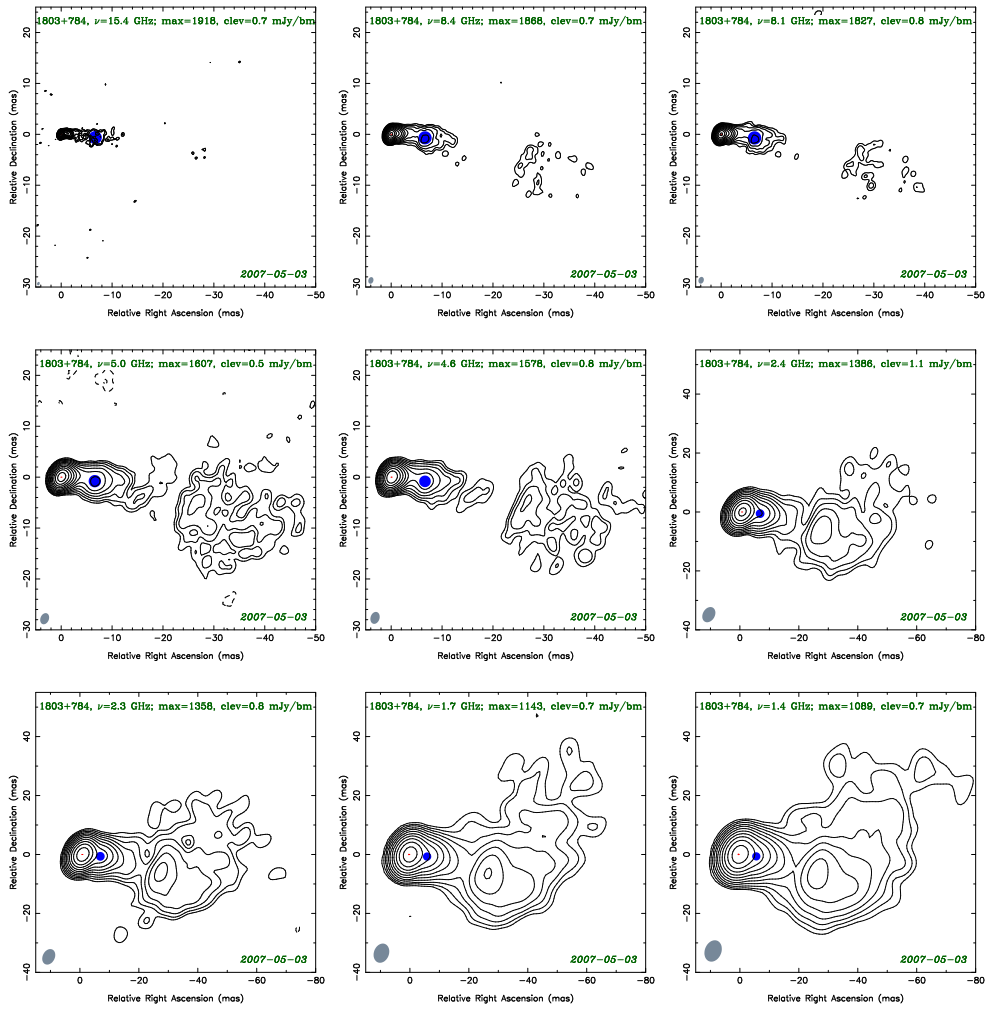


Figure 4.1 continued...

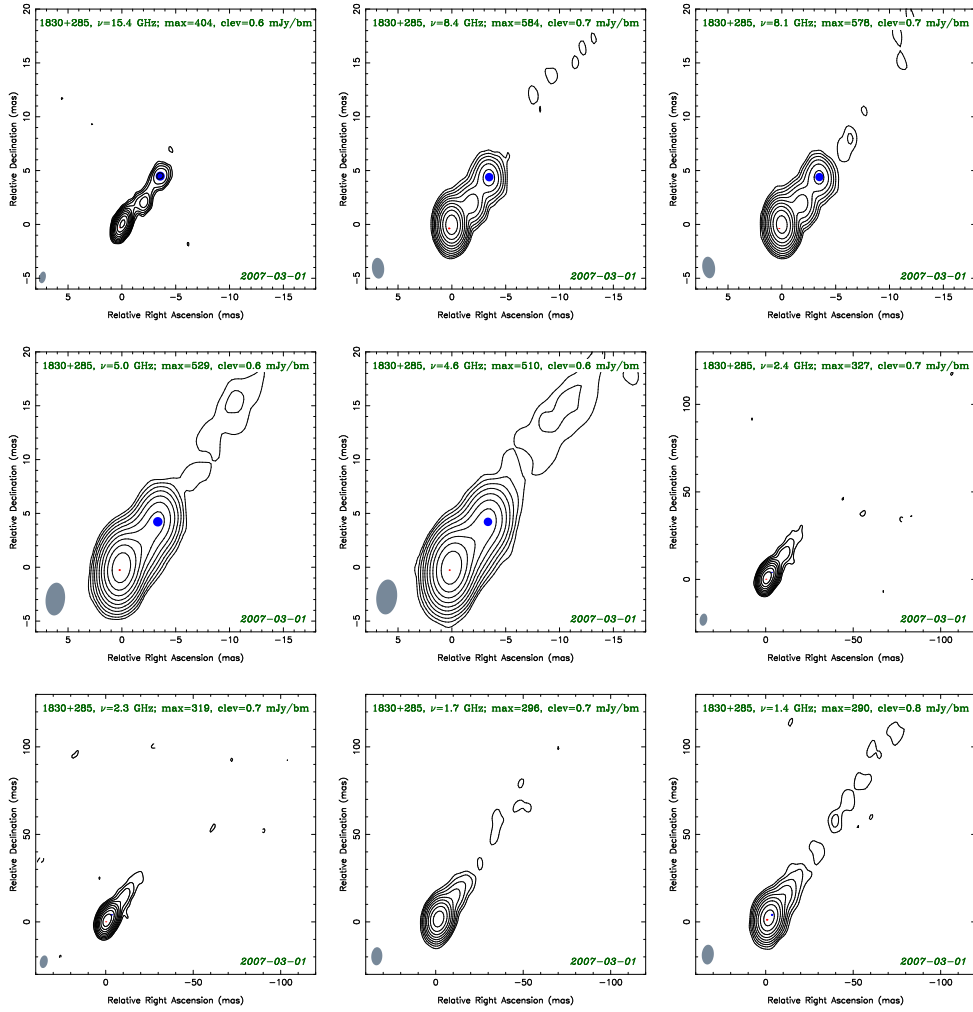


Figure 4.1 continued...

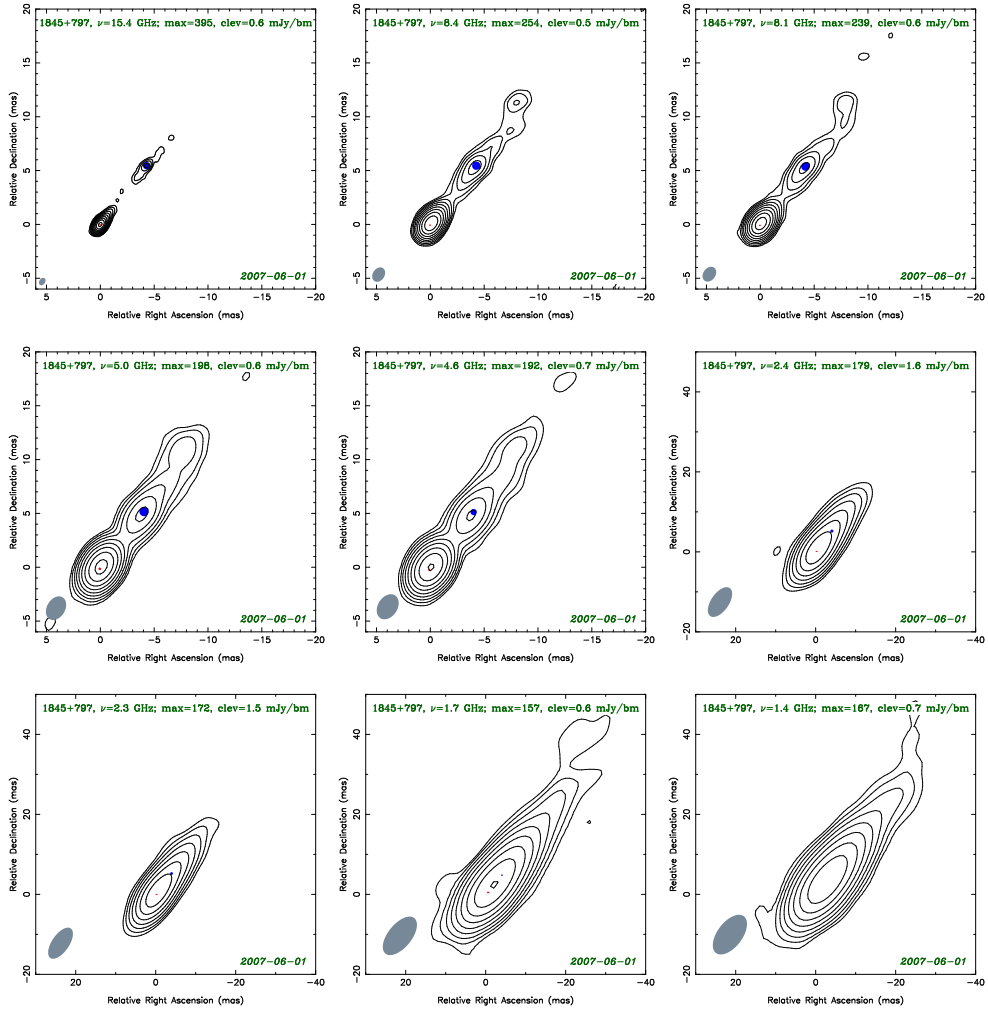


Figure 4.1 continued...

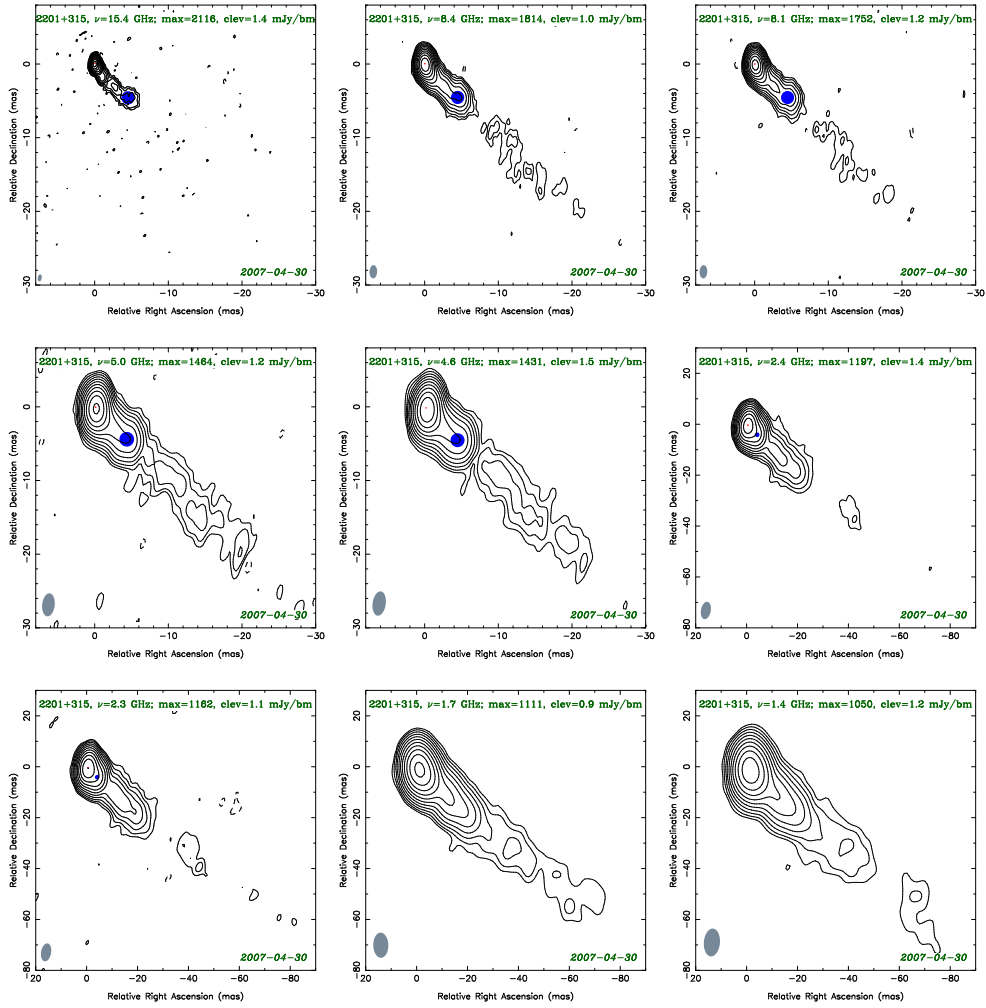


Figure 4.1 continued...

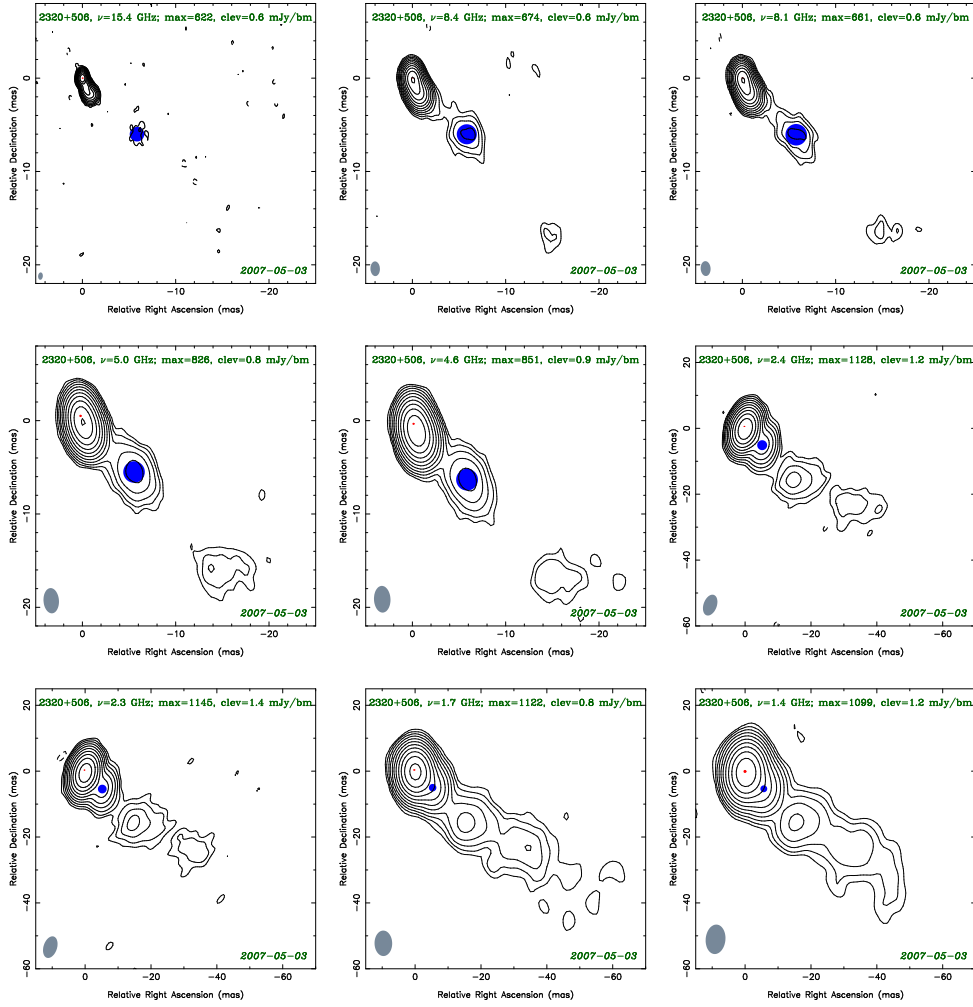


Figure 4.1 continued...

In order to estimate the uncertainties of the measured distance between the core and reference component, we have used pairs of sub-bands of X , C , S , and L bands, assuming that the source structure at these closely-separated frequencies is essentially the same and the difference in the model fit parameters thus determined purely by errors (Fig. 4.3). This assumption turns out to be correct for X , C , and S bands, while at L band the core shift between the sub-bands becomes evident. We note that this approach is possible since data processing of these sub-bands was done completely independently. We have also tried to estimate uncertainties using formulas (3) and (4) from Lee et al. (2008) which are modified versions of the formulas introduced by Fomalont (1999). We found that for all sources in X , C , and S bands the theoretically estimated error is 3 – 40 times larger than the standard deviation, σ , of the measured distance difference between sub-bands of the corresponding band computed using all sources.

In the following, for X , C , and S bands we adopt a single typical uncertainty of the distance between the core and reference component, which is the standard deviation of the distance difference measurements made in the two sub-bands of each band, computed using all the sources in our experiment (Fig. 4.3). For X band the

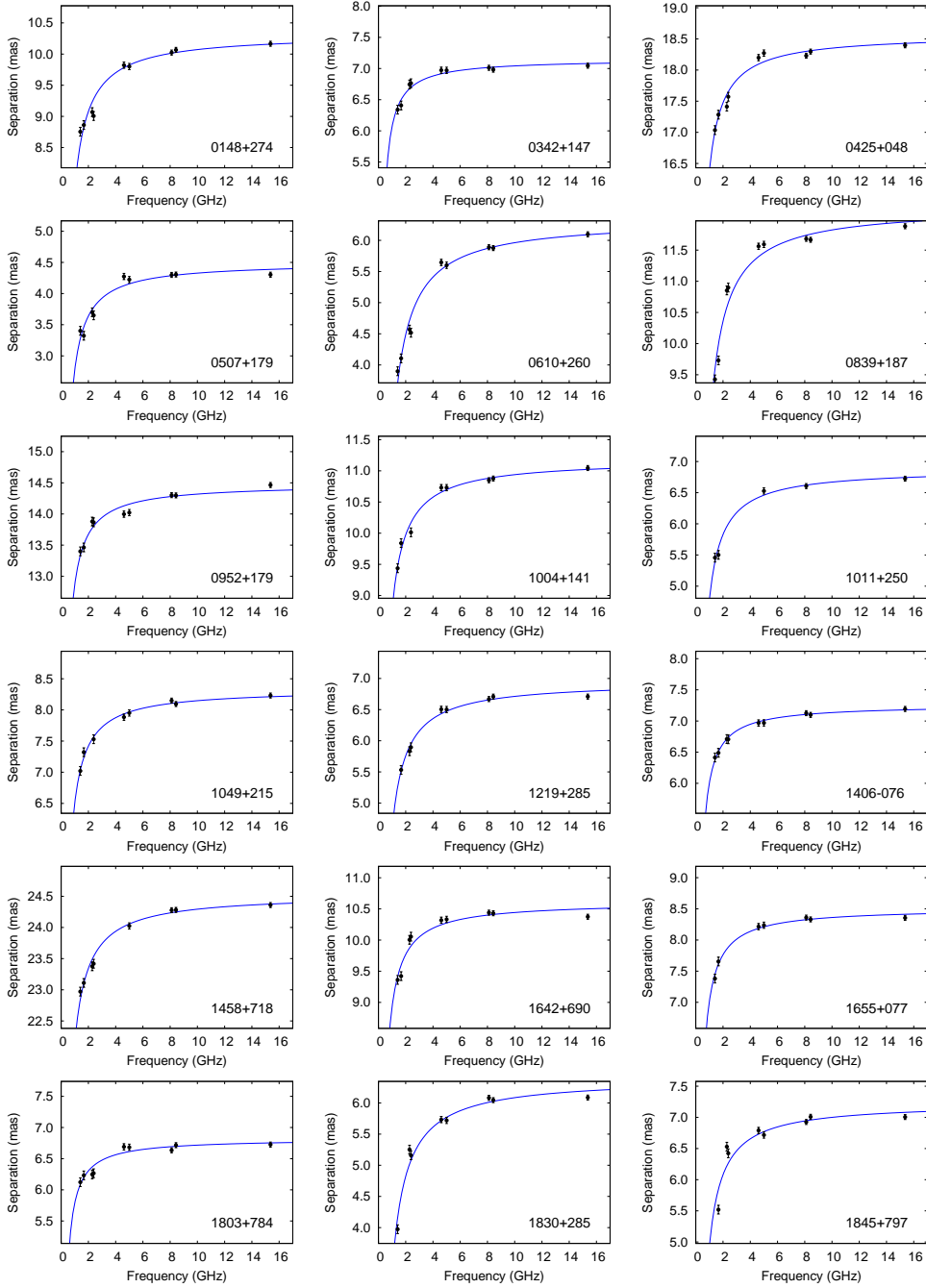


Figure 4.2: Separation of the core from a reference optically-thin jet component as a function of frequency. The curve represents the best-fit function $r_c(\nu) = a + b\nu^{-1/k}$, the coefficient $k = 1$ was fixed during the fitting. The best-fit parameters are presented in Table 4.4.

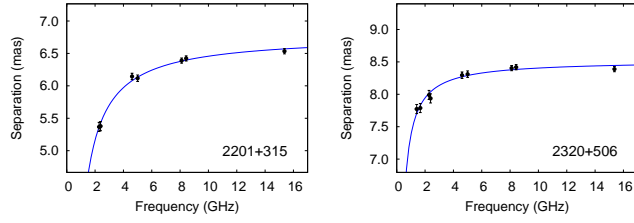


Figure 4.2: continued...

Table 4.3: Amplitude corrections for the BK134 VLBA experiment

Ant.	Band	IF	Epoch	Polarization	Corr.
BR	<i>L</i>	1	All	L	1.17
BR	<i>L</i>	2	All	L	1.13
LA	<i>L</i>	1	All	L	0.89
LA	<i>L</i>	2	All	L	0.90
HN	<i>L</i>	1-4	2007-06-01	L,R	0.75
OV	<i>L</i>	1	All	R	1.17
OV	<i>L</i>	2	All	R	1.15
BR	<i>S</i>	3	All	L	1.13
LA	<i>S</i>	1	All	L	1.12
LA	<i>S</i>	2	All	L	1.09
LA	<i>S</i>	3	All	L	1.19
LA	<i>S</i>	4	All	L	1.23
HN	<i>S</i>	3	All	L	0.90
HN	<i>S</i>	4	All	L	0.89
KP	<i>S</i>	1	All	L	1.09
KP	<i>S</i>	2	All	L	1.13
NL	<i>S</i>	3	All	L	1.09
MK	<i>S</i>	3	All	L	1.13
MK	<i>S</i>	4	All	L	1.14
LA	<i>S</i>	1	All	R	0.85
LA	<i>S</i>	2	All	R	0.85
LA	<i>S</i>	3	All	R	0.76
LA	<i>S</i>	4	All	R	0.79
OV	<i>S</i>	3	All	R	0.86
OV	<i>S</i>	4	All	R	0.89
KP	<i>C</i>	1	All	L	1.10
KP	<i>C</i>	2	All	L	1.11
BR	<i>C</i>	1	All	L	0.91
KP	<i>C</i>	1	All	R	1.11
KP	<i>C</i>	2	All	R	1.09
MK	<i>C</i>	1	All	R	1.24
MK	<i>C</i>	2	All	R	1.17
OV	<i>X</i>	1	All	L	1.21
OV	<i>X</i>	2	All	L	1.20
KP	<i>X</i>	1	All	R	0.91
KP	<i>X</i>	2	All	R	0.93
BR	K_H	1	All	L	0.94
BR	K_H	4	All	L	0.95
SC	K_H	1	All	L	1.05
KP	K_H	2	All	R	1.42

Column designation: Col. 1 – Antenna name, Col. 2 – radio band name, Col. 3 – number of the frequency channel (IF), Col. 4 – epoch to which the amplitude correction was applied, Col. 5 – polarization (right or left circular), Col. 6 – amplitude correction coefficient.

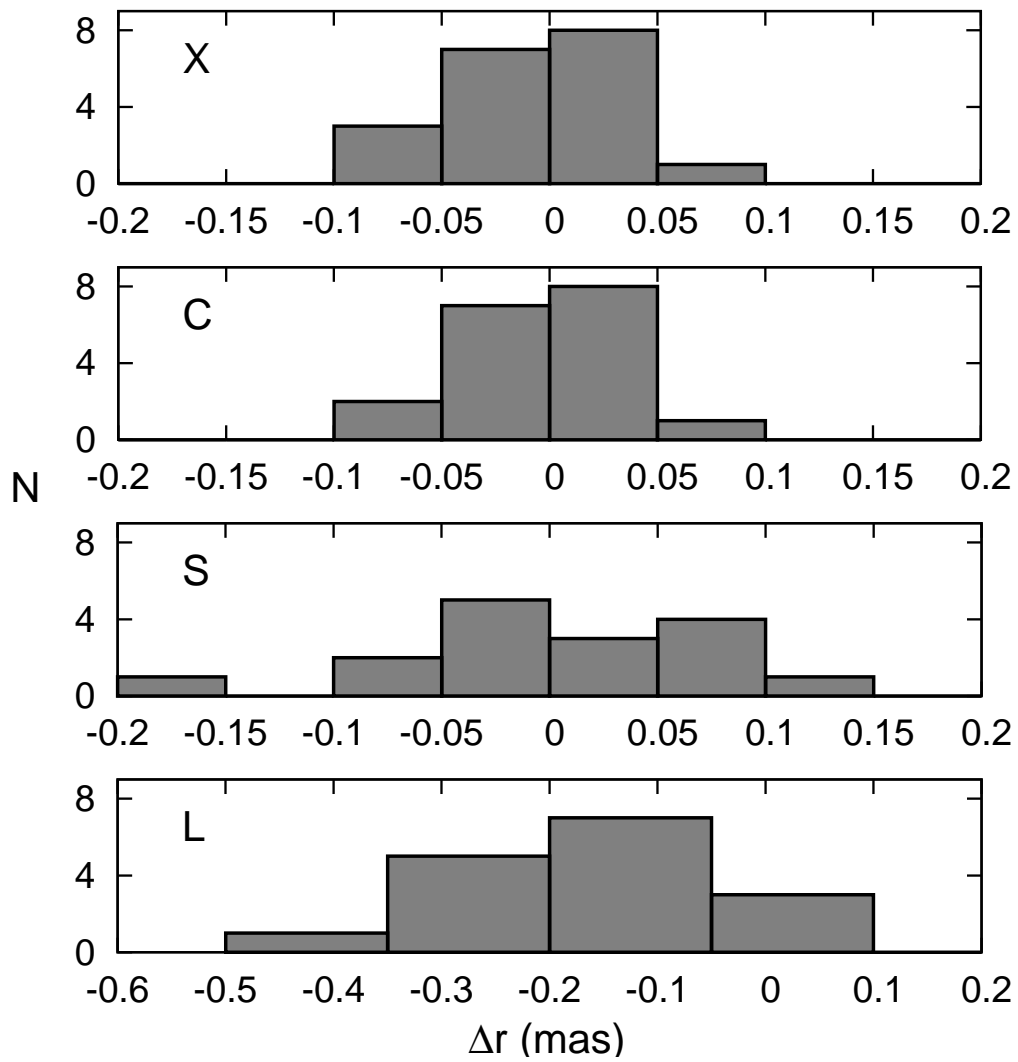


Figure 4.3: Distribution of the observed difference in distance between the core and reference component measured at two sub-bands of X , C , S and L band.

adopted distance error is $\sigma_X = 0.04$ mas, for C band $\sigma_C = 0.05$ mas, and for S band $\sigma_S = 0.07$ mas. The K_u band has not been divided in two independent sub-bands and for that band we adopt the same position uncertainty as for X band: $\sigma_{K_u} = \sigma_X = 0.04$ mas. In the L band the mean difference between the distance measured at the lower sub-band (1.4 GHz) and the higher sub-band (1.7 GHz) is -0.15 ± 0.03 which is significantly different from zero. We interpret this as a sign of the core shift effect (which should be more pronounced at lower frequencies) and use the uncertainty derived from the scatter of S band measurements as an estimate of the L band error instead: $\sigma_L = \sigma_S = 0.07$ mas. We note that σ_L may be underestimated.

4.3 Discussion

4.3.1 Core position as a function of frequency

According to Lobanov (1998b) the position of the core $r_c(\nu) \propto \nu^{-1/k}$ where the coefficient $k = 1$ if (i) the dominating absorption mechanism is synchrotron self-absorption, (ii) the jet has a conical shape and (iii) is in equipartition. These assumptions must hold for the ultracompact jet region which we observe as the VLBI core and do not need to be correct all the way along the extended parsec-scale jet.

In order to test the above assumptions, we fitted the observed distances between the reference jet component and the core in each source with the function $r_c(\nu) = a + b\nu^{-1/k}$ leaving the coefficients a , b and k as free parameters. The Levenberg–Marquardt algorithm (e.g., Press et al. 2002) was used to perform the nonlinear least-squares fit. Fig. 4.4 shows the distribution of the estimated k values. The mean value of the distribution is $k = 0.98 \pm 0.11$. This suggests that for a typical source in the sample in the frequency range of our observations the above assumptions about the structure of the inner jet (which we observe as the VLBI core) are generally correct. Specifically, we conclude that our observations are consistent with synchrotron self-absorption being the dominating opacity mechanism acting in parsec-scale core regions in the GHz frequency range.

It should be noted that, since the core shift effect is most pronounced at lower frequencies, the best-fit values of k obtained are heavily dependent on the L -band measurements. At the same time, L -band data are also more likely to be affected by blending, an effect which could interfere with the core shift measurements (Kovalev et al. 2008b). In order to test how sensitive our conclusions are to the L -band results, we have repeated the above fitting procedure excluding all L -band data. The resulting values of k are on average 30 % smaller compared to those obtained with L -band data included. Naturally, a larger uncertainty is associated with the values of k obtained without L -band data. The mean values of the two distributions of best-fit k values are consistent at the 2σ level.

The values of k presented in Fig. 4.4 are similar to those obtained for 1038+528 A by Marcaide & Shapiro (1984); Marcaide et al. (1985), 3C 345 by Lobanov (1998b), 3C 309.1 by Ros & Lobanov (2002), 0850+581 by Kovalev et al. (2008a), 1418+546, 2007+777, and BL Lac by O’Sullivan & Gabuzda (2009) and Mrk 501 by Croke et al. (2010). The values obtained also agree with the results of Yang et al. (2008); they have estimated k from a statistical analysis of parsec-scale core sizes of ~ 3000 sources. The core size is expected to be directly related to the observed position of the core along the conical jet (Unwin et al. 1994). The value of $k < 1$ was obtained from analysis of the core size in 3C 345 measured between 5 and 22 GHz by Unwin et al. (1994). Values of

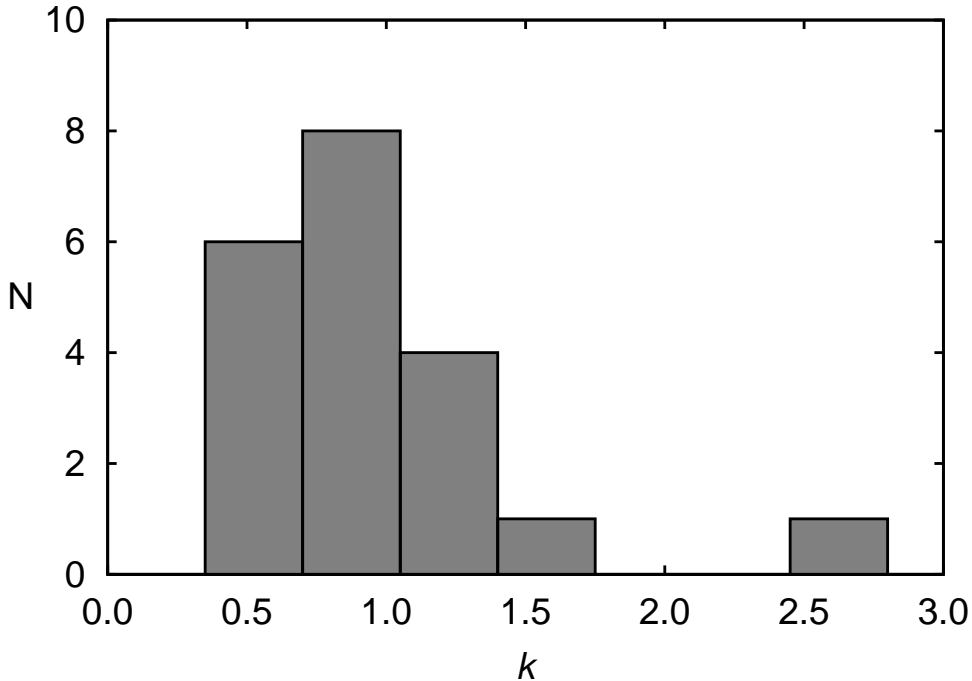


Figure 4.4: Distribution of the k parameter in the core position as a function of frequency fit: $r_c(\nu) \propto \nu^{-1/k}$. The mean value is $k = 0.98 \pm 0.11$ while the median is 0.89. One discrepant measurement on the histogram corresponds to the source 0952+179 where the value of k is not well constrained: $k = 2.7 \pm 1.7$.

k slightly larger than unity were estimated for BL Lac by analyzing time lags between radio lightcurves obtained at different frequencies (Bach et al. 2006). We also note that Lobanov (1998b) has found an indication for k to change with frequency up to values greater than 1 for the quasar 3C 309.1. Kadler et al. (2004) found much larger values of k indicating free-free absorption in the radio galaxy NGC 1052. The key difference between NGC 1052 and the sources observed in our sample is that this radio galaxy shows a two-sided parsec-scale jet. The inner part of the receding jet of NGC 1052 is likely to be obscured by a circumnuclear torus (Kadler et al. 2004).

The applicability of the $r_c \propto \nu^{-1/k}$ relation to many extragalactic sources has important consequences for the radio–optical reference frame alignment. In the particular case of $k = 1$, if the radio structure is strongly core-dominated, the source position measured using the group delay technique at any frequency (such as those currently used to define the the International Celestial Reference Frame, ICRF; Fey et al. 2004; Ma et al. 1998) corresponds to the jet base, not the radio core position at a given frequency (Porcas 2009). This is due to the additional time delay introduced by the core shift across the observing band (Porcas 2009). The optical emission of an AGN jet is expected to originate much closer to the jet base than the radio core position. Therefore, if the source radio emission is dominated by the core, there is no need to introduce core shift corrections to the radio source positions determined from group delays before matching them with optical positions. This is not true however for radio source positions determined from phase referencing (Porcas 2009). Also, if the source has bright distinct components in the jet (which is indeed the case for the sources presented in

Table 4.4: Core distance from the reference jet component as a function of frequency: fit results ($r = a + b/\nu$)

Source	a (mas)	b (mas · GHz)	a (pc)	b (pc · GHz)	PA°
0148+274	10.32 ± 0.06	-2.48 ± 0.19	86.75 ± 0.50	-47.11 ± 3.61	-40.9
0342+147	7.15 ± 0.03	-1.08 ± 0.09	61.14 ± 0.26	-23.61 ± 1.97	-88.5
0425+048	18.57 ± 0.05	-2.19 ± 0.17	114.99 ± 0.31	-20.57 ± 1.60	-100.7
0507+179	4.50 ± 0.05	-1.72 ± 0.17	24.63 ± 0.27	-13.33 ± 1.32	-100.3
0610+260	6.33 ± 0.06	-3.68 ± 0.19	41.56 ± 0.39	-38.17 ± 1.97	-94.5
0839+187	12.19 ± 0.09	-3.66 ± 0.29	102.60 ± 0.76	-69.99 ± 5.55	15.2
0952+179	14.48 ± 0.05	-1.61 ± 0.17	123.56 ± 0.43	-34.04 ± 3.59	-3.5
1004+141	11.18 ± 0.04	-2.41 ± 0.13	89.97 ± 0.32	-71.89 ± 3.88	132.2
1011+250	6.88 ± 0.04	-2.10 ± 0.14	58.88 ± 0.34	-47.37 ± 3.16	-107.3
1049+215	8.33 ± 0.02	-1.82 ± 0.08	70.30 ± 0.17	-35.33 ± 1.55	108.0
1219+285	6.95 ± 0.04	-2.38 ± 0.15	19.06 ± 0.11	-7.58 ± 0.48	109.8
1406-076	7.26 ± 0.01	-1.25 ± 0.05	61.98 ± 0.09	-26.61 ± 1.06	-103.5
1458+718	24.53 ± 0.04	-2.37 ± 0.12	191.90 ± 0.31	-35.30 ± 1.79	163.7
1642+690	10.61 ± 0.05	-1.68 ± 0.18	77.94 ± 0.37	-21.61 ± 2.32	-167.0
1655+077	8.51 ± 0.03	-1.49 ± 0.10	57.71 ± 0.20	-16.38 ± 1.10	-42.9
1803+784	6.82 ± 0.04	-1.03 ± 0.13	48.14 ± 0.28	-12.21 ± 1.54	-96.0
1830+285	6.40 ± 0.06	-3.15 ± 0.24	42.50 ± 0.40	-33.34 ± 2.54	-38.5
1845+797	7.23 ± 0.09	-2.30 ± 0.35	7.76 ± 0.10	-2.61 ± 0.40	-38.0
2201+315	6.78 ± 0.03	-3.23 ± 0.14	29.83 ± 0.13	-18.45 ± 0.80	-135.3
2320+506	8.52 ± 0.03	-1.15 ± 0.09	71.76 ± 0.25	-22.07 ± 1.73	-135.8

Column designation: Col. 1 – IAU source name (B1950), Col. 2 and 3 – coefficients of the best-fit curve $r = a + b/\nu$ with their uncertainties. Col. 3 and 4 – same coefficients converted to the projected linear scale. Col. 5 – median (across all frequencies) position angle of the reference jet component; it marks the direction along which the core shift was measured.

Fig. 4.1), the group delay will not be a good position estimator for the comparison with the optical position since estimated position will not be the position of the jet base. The source structure needs to be modeled to determine the correct position corresponding to the jet base for comparison with optical astrometry.

4.3.2 Fitting results assuming synchrotron self-absorption opacity

As discussed above, our observations are consistent with the assumption of synchrotron self-absorption dominated opacity across the frequency range of this VLBI experiment. We repeated the fit of the function $r_c(\nu) = a + b\nu^{-1/k}$ to the observational data, fixing the value of $k = 1$, which is our best estimate. The results are presented in Table 4.4 and Fig. 4.2. The values of a and b are given in Table 4.4. The projected core distance in parsecs is

$$r_c(\nu) [\text{pc}] = \frac{D_A}{N_{\text{rad}}} \left(a [\text{mas}] + b [\text{mas} \cdot \text{GHz}] \cdot \frac{1+z}{\nu_{\text{em}} [\text{GHz}]} \right),$$

where a [mas] and b [mas · GHz] are the coefficients obtained from observations, D_A is the angular size distance to the source in parsecs, $N_{\text{rad}} \simeq 206264800$ is the number of milliarcseconds in one radian, z is the source redshift and ν_{em} [GHz] is the emission frequency in the source frame.

We have investigated deviations of the measured distances from the best-fit curve presented in Fig. 4.2 for each frequency. In all cases the mean difference between the measurement and the model curve is consistent with zero, and its standard deviation is consistent within a factor of two with the adopted typical measurement uncertainties.

It can be seen from Fig. 4.2 that, while the $r_c(\nu) \propto \nu^{-1}$ law generally provides a good fit to the data over the whole observed frequency range with no systematic deviations, there are indications of possible local deviations. This may be due to local deviations from equipartition or conical shape of the jet. Another possibility is that the scatter in

distance measurements at two sub-bands used for error estimation does not reflect the total measurement uncertainty. This may happen if there is a systematic factor which influences distance measurements at both sub-bands in a similar way. However, after a careful review of our analysis procedures we could not identify any such factor.

4.3.3 Comparison with previous 2.3/8.6 GHz measurements

The new measurements of core shifts between 2.3 and 8.4 GHz may be compared to the previous measurements at similar frequencies obtained using the RDV data by Kovalev et al. (2008b). As expected for a big enough sample of variable sources, the mean difference between the measurements obtained at two epochs (2002 for RDV global VLBI data and 2007 for this VLBA dataset) is consistent with zero: (0.01 ± 0.08) mas. The mean absolute value of this difference is (0.22 ± 0.05) mas which is a measure of a typical long-term core-shift variability in the studied sample within the accuracy of our measurements.

According to formula (1) in Kovalev et al. (2008b), if jet orientation and velocity remain unchanged, an increasing value of core shift (due to an increase in particle density and/or jet magnetic field strength) should be associated with increase in the flux density of the core. Fig. 4.5 shows the core shift ratio versus X band core flux density ratio at two epochs (2002 and 2007). No significant correlation is found between the core shift and flux ratios at different epochs. This may reflect the fact that there is no single dominant physical reason for core flares and subsequent core shift variations,

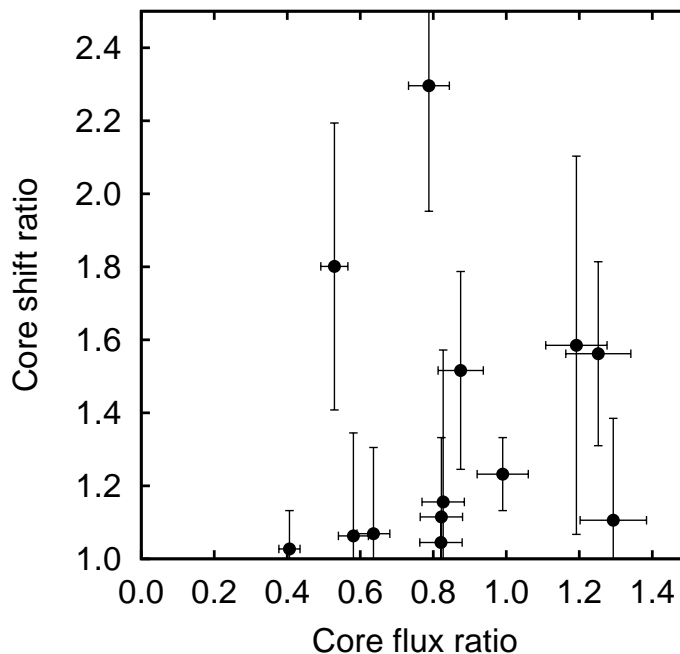


Figure 4.5: Core shift ratio versus X band core flux density ratio. The core shift ratio is defined to be greater than unity, i.e., for each pair of measurements, the larger value of the shift is in the numerator of the ratio. The one source (not shown in this plot) which exhibited a large core shift change without a major change in flux density is W Com (1219+285); it has a core shift ratio of 3.67 ± 0.36 and core flux ratio of 1.19 ± 0.08 .

despite the suggestion by Kovalev et al. (2008b). A higher accuracy of core-shift ratio measurements is required to probe this in details.

4.4 Chapter summary

Dedicated VLBA observations of twenty AGN jets showing large frequency dependent core shifts were conducted at nine frequencies in the 1.4–15.4 GHz range. Analysis of these data has resulted in 180 high dynamic range (up to 13000 for 1803+784 in C band; typical value ~ 2300) images of the sources. The obtained images are ready for a spatially resolved spectral analysis and investigation of the core position displacement with frequency (“core shift”). The latter effect is especially interesting since it provides a probe of physical conditions in the inner jet – the likely site of the observed high-energy emission of blazars.

Significant core shifts have been detected and confirmed in all observed sources. The effect is more pronounced at lower frequencies. The core position, r_c , shift as a function of frequency, ν , is consistent with the $r_c(\nu) \propto \nu^{-1}$ pattern expected for a purely synchrotron self-absorbed conical jet in equipartition (Blandford & Königl 1979; Lobanov 1998b). These results support the interpretation of the parsec-scale core as a continuous Blandford-Königl type jet with smooth gradients of physical properties (including opacity) along it. No systematic change with frequency of the power law index in the $r_c(\nu)$ relation has been convincingly detected. However, some local changes might be present in a few sources, especially at higher frequencies.

The general applicability of the $r_c(\nu) \propto \nu^{-1}$ relation to all the observed sources is a promising indication that radio source positions obtained using group delays (such as those currently used to define the ICRF) may be compared to optical counterpart positions directly, with no need to apply a correction for the source core shift (Porcas 2009). This may be important in the era of the future space-based optical astrometry missions aiming for μas -level accuracy. A correction for the core shift in the reference source(s) is still required if a high-precision absolute position of a celestial radio source (or tracked spacecraft) is to be determined through a phase referencing VLBI experiment. Also if the radio source is not strongly core dominated, its structure needs to be taken into account for accurate determination of jet base position which should be compared to the optical position.

While in the work described in this Chapter we have tried to concentrate on the observational results, independent of specific assumptions about jet geometry and Lorentz factor, in future work based the dataset presented here we plan to estimate geometry, magnetic field strength and total (kinetic plus magnetic field) power of the flows and relate the observed shifts to the properties of the central black hole and broad-line region in its vicinity. Polarization information will be used to constrain the physical interpretation of core shift measurements and to investigate the effect of the core shift on Faraday rotation measurements.

It would be important to confirm, and investigate possible changes of, the coefficient k in the $r_c(\nu) \propto \nu^{-1/k}$ relation with frequency, which may be hinted at in our observations. In order to achieve greater accuracy in measuring k one would need to obtain more independent core position measurements across the whole frequency range accessible to VLBI. The use of phase-referenced observations may also be helpful to minimize ambiguities inevitably associated with the model fitting procedure and quantify position measurement errors more accurately.

Chapter 5

The quest for young radio sources seen edge-on

How would a young radio galaxy look like? One possibility is that it would be simply a scaled-down version of a large galaxy. Such object may have all (or some of) the usual elements of radio morphology like two-sided jets, hot-spots, lobes and a bright compact core, but be much smaller. As a consequence of the smaller angular size, the object may also have a spectrum which is noticeably different from the one of its larger cousins: the spectral peak caused by synchrotron self-absorption will be shifted to higher frequency in a smaller source.

These basic ideas determine two main strategies of young radio source identification. The “spectral” approach suggests to search for compact (on arcsecond-scale) radio sources which show the self-absorption peak at high frequencies (at cm-band). The “imaging” approach implies direct imaging of radio sources with the Very Long Baseline Interferometry (VLBI) technique in search of parsec-scale morphological features resembling those of Megaparsec-scale radio galaxies. A combination of the two techniques is also possible.

In this work we try both approaches to the young radio source identification. First we use data from the 1–22 GHz spectral survey conducted with the RATAN-600 radio telescope to construct the largest homogeneously selected sample of radio sources with synchrotron peak in the GHz-range (Section 5.1). The parsec-scale properties of the sources from this spectrally selected sample are characterized using the publicly-available VLBI data (Section 5.2). Second, we use the archival VLBI data to identify the promising young radio source candidates based on their parsec-scale morphology and later characterize their spectral properties using data from the RATAN-600 spectral survey (Section 5.3). Finally, in Section 5.4 we discuss cross-identification of the selected candidates with γ -ray sources from the first-year *Fermi*/LAT catalog and discuss the implications for identification of the of the blazar γ -ray emission site.

Main results of this work were presented in Sokolovsky & Kovalev (2008); Sokolovsky et al. (2009, 2010c).

5.1 A sample of GHz-peaked spectrum sources selected with RATAN-600: spectral and variability properties

Gigahertz Peaked Spectrum (GPS) sources are compact extragalactic radio sources characterized by a turnover in their spectra at frequency of about a few GHz. Class of GPS sources is a mixture of AGN with different physical characteristics. It is widely accepted that progenitors of large scale FR I/FR II radio galaxies can be found among them. The construction of a complete flux density limited sample is essential to understand the nature of GPS sources. In this section we describe a new sample of 226 GPS candidates selected using simultaneous 1–22 GHz multi-frequency multi-epoch observations with the RATAN-600 radio telescope. Sixty objects in our sample are identified as GPS source candidates for the first time. The candidates were selected on the basis of their broad-band radio spectra only. We discuss the spectral and variability properties of selected objects of different optical classes.

5.1.1 General remarks

Gigahertz Peaked Spectrum (GPS) sources are among the brightest radio sources in the sky at centimeter-band. They are compact extragalactic objects characterized by a turnover in their radio spectra at frequency of about a few gigahertz. The low frequency decline in their spectra is probably due to synchrotron self-absorption, but free-free absorption in an inhomogeneous screen may also play a role in some objects. These explanations correspond to the two main models of GPS sources: 1) they are young and evolving objects that will become large-scale radio sources, or 2) they are frustrated by interaction with surrounding dense interstellar medium. It is possible that both mechanisms act simultaneously.

A general review of GPS source properties was presented by O’Dea (1998).

VLBI observations reveal a variety of pc-scale structures in GPS sources. Sources associated with quasars often have “core – jet” or “naked core” morphology (e.g., Stanghellini et al. 1997b). The effect of Doppler boosting should be significant for these objects. Many GPS galaxies have double or triple radio structure (mini-lobes or hot spots on both sides of a core). This structures were called Compact Symmetric Objects (CSO) by Readhead et al. (1996a). Doppler boosting is minimal in CSO. Measured proper motion of CSO components (projected separation velocities $\sim 0.2c$ ¹) suggest dynamical ages $\sim 10^3$ years which supports the youth model for (at least this subclass of) GPS sources (Polatidis & Conway 2003).

Optical counterparts of GPS sources are a mixture of radio galaxies and quasars, with quasars tend to be found at high ($z > 1$) redshift. Hosts of GPS galaxies are giant ellipticals, similar to hosts of large-scale FRI/FR II radio sources Labiano et al. (2007); Snellen et al. (1999).

Many authors argue, that GPS galaxies and GPS quasars are two different populations of radio sources which show the same shape of radio spectra accidently. But, probably, it would be more correct to distinguish between two populations of GPS sources not on the basis of the (variable) contribution of AGN to their optical light (galaxies vs quasars), but on the basis of pc-scale radio morphology (CSO vs. “core

¹ c is the speed of light in vacuum

– jet”) which indicates the value of Doppler boosting for the brightest radio source components.

The first samples of GHz-Peaked Spectrum sources (e.g., Gopal-Krishna et al. 1983) were selected solely on the basis of the radio spectrum properties. Later samples, like the one presented by Snellen et al. (2002) were considering other factors such as optical counterpart type during the selection process. The very meaning of the word “GPS source” has shifted from the description of spectral shape to something close to “probable young radio source” which are believed to be found among sources with convex spectra.

Nearly 500 GPS source candidates were reported in the literature to date. Just about a half of them are true GPS sources. The others are highly variable sources which do not show peaked spectral shape all the time. The construction of complete flux density limited sample is essential to understand the nature of GPS sources. It is important to maximize the number of sources in the sample to eliminate the influence of small number of objects to the statistics, therefore, the limiting flux density of the complete sample should be as low as possible.

In this work we use the “old fashioned” spectral-only approach to select one of the largest samples of peaked spectrum sources to date. Special care is taken to keep the sample as free as possible from sources which change their overall spectral shape due to variability. We have searched for GPS source candidates the dataset from multi-frequency AGN monitoring campaign which is conducted at RATAN–600 radio telescope by Kovalev et al. (2002, 1999b). The main motivation of this work was to find missing bright GPS sources and to confirm the GPS classification for candidates previously reported in the literature. We investigate the observed properties of sources from the sample to test the idea that sources with peaked spectra are a mixture of intrinsically different types of AGN (e.g., Stanghellini 2003).

5.1.2 Observational data and sample selection

To select GPS source candidates we use 1–22 GHz multi-frequency data from the RATAN–600 telescope of the Special Astrophysical Observatory, Russian Academy of Sciences. It is a 576 m diameter ring radio telescope situated at stanitsa Zelenchuk-skaya, Karachay-Cherkessia, Russia. The telescope is mostly operated in transit mode. Emission from a radio source is measured as it crosses the feed beams of the broadband receivers operating at 1, 2.3, 3.9 (or 4.8), 7.7, 11 and 22 GHz. This allows us to obtain the source spectra over a few minutes only. The exact time it takes the source to cross all beams (and hence the integration time) is a function of the source declination. Details of the method used for observations and data processing can be found in Kovalev et al. (2002, 1999b).

We use spectra of 4047 sources observed with RATAN from 1997 to 2006 during multifrequency monitoring and survey campaigns conducted by Kovalev et al. (2000, 2002, 1999b). The observed source list includes a complete sample of sources with $\delta > -30^\circ$ and a total VLBI flux density at 8 GHz greater than 200 mJy (Kovalev et al. 2007). The observing program consists of two parts: a list of 550 monitoring sources which are observed during every observation set (2–4 times a year) and a list of survey sources which are inserted in the observation schedule in gaps between monitoring sources. For most of the survey sources, we have only 1–5 observations. To improve the frequency coverage, we combine our RATAN–600 data with previously published

non-simultaneous measurements collected by the CATS database² (Verkhodanov et al. 2005).

We inspected all of the collected broad-band spectra to select sources which show a prominent spectral peak at all epochs for which we have RATAN data (supplemented by the CATS data). To derive the peak flux density (S_{ν_0}) and peak frequency (ν_0), we followed Edwards & Tingay (2004); O’Dea et al. (1990); Snellen et al. (2002) and fitted each source spectrum in the log-log scale with a parabola $\log_{10} S_{\nu} = a(\log_{10} \nu)^2 + b \log_{10} \nu + c$, where S_{ν} is the flux density at frequency ν , a , b , and c are coefficients determined using a least square regression method. Despite having no physical meaning, this simple fit can represent observations reasonably well. The spectral indexes³ were determined by fitting the high- and low-frequency regions of the spectra with a linear function in the log-log scale. We have used similar criteria to those suggested by de Vries et al. (1997) to select the final list of GPS candidates: (i) source spectra show a defined peak at a frequency above 500 MHz, (ii) the difference between the high- and low-frequency spectral indexes is greater than 0.6. We use the traditional 500 MHz boundary between GPS and Compact Steep Spectrum (CSS) sources, despite there is no clear physical boundary between them, because we do not have our own observations at frequencies below 1 GHz. Also, we do not distinguish between GPS sources and High Frequency Peakers (HFP) which have peaks at frequencies above 5 GHz and, as in the case of CSS sources, they are not separated from GPS sources by any gap in their properties. Twenty three sources from our GPS list are present in the HFP sample by Dallacasa et al. (2000).

We have also tried to fit the source spectra with the function $S_{\nu} = \frac{S_0}{1-e^{-1}} \left(\frac{\nu}{\nu_0}\right)^{\alpha_2} \left(1 - e^{-\left(\frac{\nu}{\nu_0}\right)^{\alpha_1 - \alpha_2}}\right)$ following Vollmer et al. (2008a). Such fit gives consistent peak frequency and flux compared to the parabolic fit, but spectral indexes obtained using this function are systematically steeper than those obtained from linear fits. Since manual linear fit visually better represents observational data, we use spectral indexes derived that way for the further analysis.

The sample of 226 GPS has been selected, 60 objects from the sample have never been reported before as GPS source candidates (see examples in Fig. 5.1). Optical identifications and redshift information were extracted from the Véron-Cetty & Véron (2006) catalog and the NASA/IPAC Extragalactic Database (NED⁴). Published spectroscopic redshifts were found for 128 sources, 39 sources are identified with galaxies, 98 are identified with quasars, three sources (PKS 0637–337, PKS 1300–105, and PKS 1519–273) are BL Lacertae objects. For 86 sources no optical identification was found (“empty fields”).

5.1.3 Spectral properties

An “average” GPS spectrum in our sample is characterized by the peak frequency $\nu_0 = 2.4$ GHz and the flux density $S_{\nu_0} = 0.8$ Jy. The spectral indexes above and below the turnover frequency are $\alpha_1 = -0.77$ and $\alpha_2 = 0.66$.

To provide an impression of the spectra selected, we present Fig. 5.2. An average spectrum of a GPS source was constructed by combining the individual source spectra normalized by their peak frequency and flux density. This combined spectrum is com-

²Astrophysical CATalogs support System: <http://www.sao.ru/cats/>

³We use the following spectral index α definition: $S_{\nu} \propto \nu^{\alpha}$. α_1 is a spectral index above the peak frequency ν_0 , α_2 – below the peak.

⁴<http://nedwww.ipac.caltech.edu/>

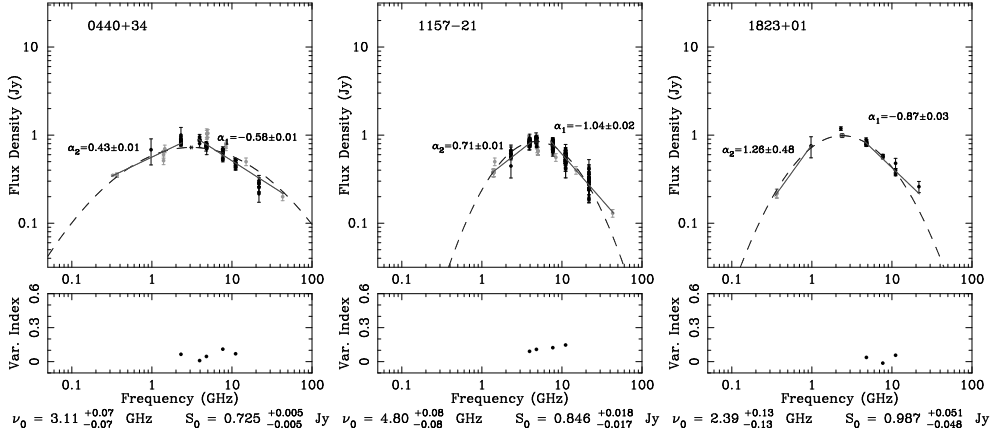


Figure 5.1: Radio spectra of 3 out of 60 newly identified GPS source candidates. Variability index as a function of frequency is presented in the panels under the spectra plots. Black points correspond to RATAN-600 data, grey points represent data collected from the literature.

pared to a theoretical spectrum of a homogeneous synchrotron emitting cloud with a spectral index above the peak equal to the median value for our sample.

As can be seen from Fig. 5.2, the observed spectra of GPS sources are wider and do not reach $\alpha_2 = 5/2$ which is predicted by synchrotron self-absorption. In fact, no single source in our sample approaches this value. The most inverted $\alpha_2 = 1.76 \pm 0.03$ is found in the known GPS quasar 0457+024. Among the 10 sources with the most inverted spectra there are five quasars, one radio galaxy and four empty fields. The absence of observed $\alpha_2 \sim 5/2$ means that the radiation of GPS sources can not be described assuming one homogeneous synchrotron self-absorbed cloud. There should be a significant non-homogeneity in the properties across the volume of the radio-emitting region.

The broad-band radio spectra of GPS galaxies and quasars look very much alike. We found no significant differences in the low-frequency spectral index distribution between subgroups of our sample: galaxies, quasars and unidentified radio sources. This may be an indication of a common mechanism responsible for the absorption at low frequencies, such as the synchrotron self-absorption. The median value of high-frequency spectral index is $\alpha_1^{\text{gal}} = -0.80$ for galaxies and $\alpha_1^{\text{qso}} = -0.71$ for quasars. The Kolmogorov-Smirnov (KS) test has also confirmed that the distribution for galaxies and quasars do not differ significantly.

No difference was found in the observed peak flux density between galaxies and quasars. However, when it comes to the peak frequency distribution (Fig. 5.3), the KS test shows that there is only a 10% chance that the observed peak frequency distributions of galaxies and quasars are drawn from the same parent distribution. If we consider the peak frequency in the source frame, this probability drops to 0.01%. Galaxies in our sample are characterized by a lower intrinsic peak frequency (median value 3 GHz) than quasars (8.8 GHz). This is expected since quasars are found, in general, at higher redshifts than galaxies, but their radio spectra are studied in the same limited frequency range. It would be interesting to have data in, say, an order of magnitude wider frequency range than we have now for a large number of sources. This would allow one to effectively select sources based on their intrinsic peak frequency and not

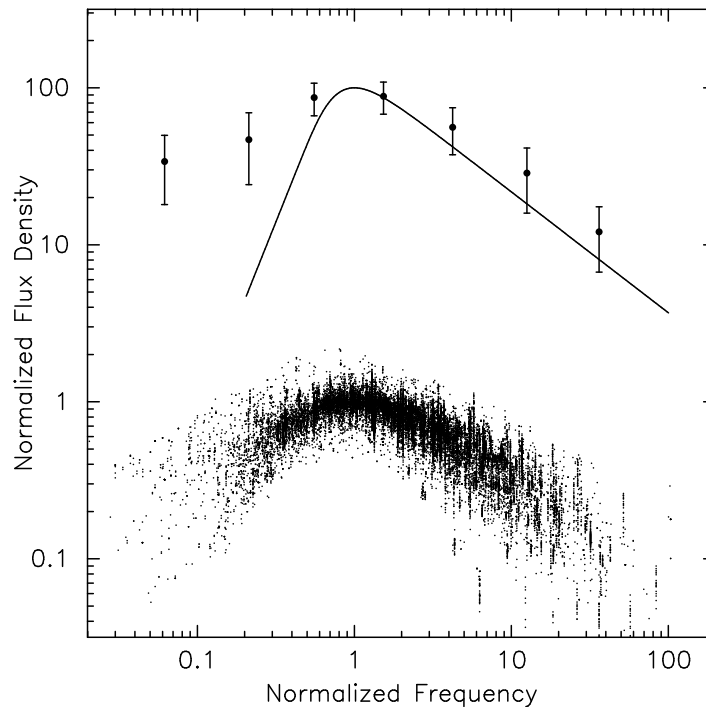


Figure 5.2: Combined spectra of all selected 226 GPS candidates normalized by peak flux density and peak frequency values. Filled circles represent the observed spectra binned and shifted along the vertical axis. The solid line is a normalized and shifted theoretical spectrum of a homogeneous synchrotron emitting cloud with self-absorption and power index $\gamma = 2.54$ of the electron energy distribution.

on the basis of our current observing capabilities. There is one more interesting thing to note. We convert the observed peak frequency to the source reference frame using the redshift measured for its host galaxy. But, the radio source component which is responsible for observed spectral shape may actually move *toward us* with a large γ -factor, typical for quasars. If this effect really plays a role, the simple correction for the host galaxy redshift is unapplicable to the radio spectrum, and the additional correction for the relativistic bulk motion of the radio emitting component is required.

Following Tinti et al. (2005) we have searched for decrease of the peak frequency with time. After selecting subsample of 17 sources for which peak frequency can be reliably determined on the basis of RATAN-600 observations solely (without addition of literature data from CATS) and for which we have observations both in 1997 and in 2006 (maximum time difference between observations) we compared their peak frequencies at this two epochs. Despite both mean and median peak frequency at the first epoch ($\nu_0 \text{ mean } 1997 = 5.42 \text{ GHz}$, $\nu_0 \text{ median } 1997 = 5.07 \text{ GHz}$) are higher than in the second epoch ($\nu_0 \text{ mean } 2006 = 4.56 \text{ GHz}$, $\nu_0 \text{ median } 2006 = 4.35 \text{ GHz}$) KS test tells, that the difference between the distributions of ν_0 at two epochs is not statistically significant. Just the same result was obtained by Tinti et al. (2005) for the HFP sample.

5.1.4 Variability

For the 108 sources which have observations with RATAN-600 at three or more epochs, a variability study was carried out. We concentrate on the variability properties at

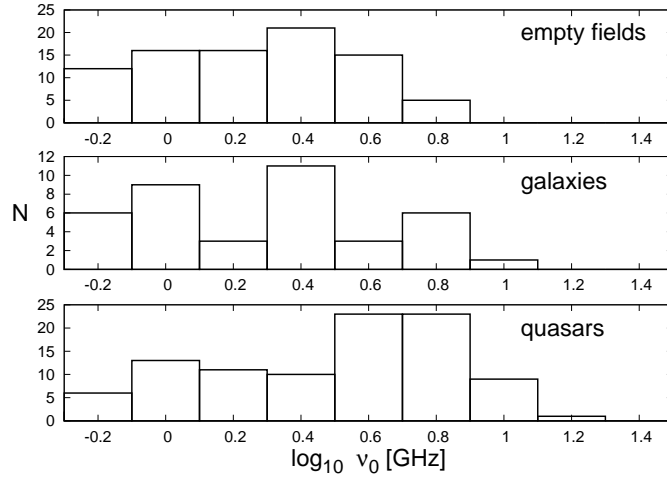


Figure 5.3: Peak frequency distribution for GPS quasars, galaxies and unidentified radio sources (empty fields).

11 GHz which corresponds to the optically thin part of the synchrotron spectrum for the majority of the sources. In addition, this band is almost RFI free, has high sensitivity and is not affected significantly by weather. Sources with a peak frequency around or above 11 GHz are excluded from the analysis in order to probe variability at a frequency with no self-absorption.

To characterize the variability amplitude of sources we use the variability index (e.g., used by Aller et al. 1992) applying the modified robust form (Hovatta et al. 2008):

$$v = \frac{(S_i - \sigma_i)_{\max} - (S_i + \sigma_i)_{\min}}{(S_i - \sigma_i)_{\max} + (S_i + \sigma_i)_{\min}}$$

S_i and σ_i are the source flux density and RMS error measured at i 'th epoch, max/min indexes correspond to the maximum/minimum value among all epochs. Note, that v can be negative if the estimated error σ is greater than the observed scatter of the data. The relative accuracy of flux density measurements as well as the number of observations influence the value of v . Let us consider the imaginary sample of 108 non-variable sources with *the same distribution of number of observations* as real sources observed by us. Flux of every imaginary source is measured with the given uncertainty σ . The distribution of variability indexes for this model sources is presented on the Fig. 5.4. The model helps to interpret the variability index distribution of real sources. For the number of observations used in our analysis, sources with $v > 0.15$ can be considered as strongly variable.

The distribution of v_{11} is found to be different for galaxies and quasars (Fig. 5.5). There are many variable sources among quasars. The statistics for galaxies is suffering from the small number of objects, but it can be clearly divided into two groups: the main distribution which is consistent with non-variable or weakly variable sources, with variations under 9–10%. The second group consist of three strongly variable galaxies: PKS 0500+019, note that this object is listed as a quasar by Becker et al. (1991); TXS 1404+286 (OQ 208, Mkn 668), its variability at a frequency above the peak was first reported by Stanghellini et al. (1997a); and B2 1600+33.

A KS test gives a 63% probability that galaxies (with the exception of three clearly variable cases) and “empty fields” are drawn from the same distribution of variability

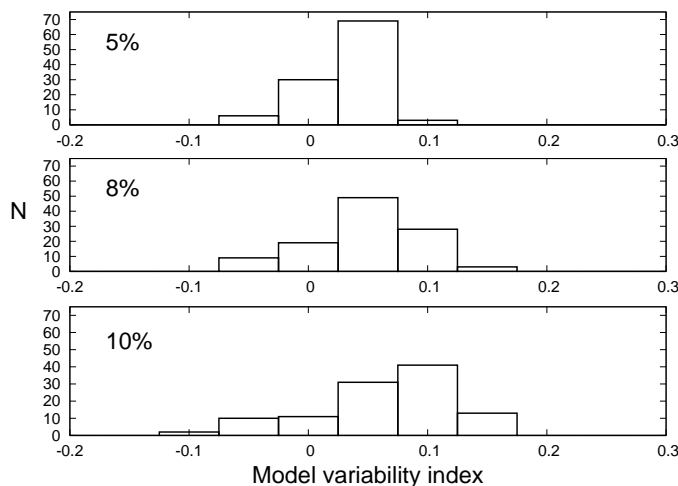


Figure 5.4: Distribution of variability index ν for the model non-variable sources measured with the relative accuracy of 5, 8 and 10% respectively.

index at 11 GHz. The same probability for galaxies and quasars is neglectable ($< 0.01\%$). This implies that most of the optically unidentified GPS sources might be faint distant galaxies and not quasars. The similarity of the observed peak frequency distribution for galaxies and “empty fields” (Fig. 5.3) supports this conclusion. This may suggest, that the observed difference in redshift distributions of GPS quasars and galaxies (Fig. 5.6) can not be used as an argument in support of the idea that these two types of GPS sources are intrinsically different. If there is a large number of distant GPS galaxies which lack an optical identification because they are far away and therefore optically faint, then the difference in the redshift distribution may be attributed to the selection effect.

A correlation between the variability index at 11 GHz ν_{11} and the high-frequency spectral index α_1 can be seen from our data. The value of correlation coefficient $r = 0.32$ correspond to 99.8% probability that correlation is real for that number of points. Exclusion of a few extreme points do not significantly influence this value. The flatter spectral index correspond, on average, to larger variability, despite the large scatter of individual points (Fig. 5.7).

5.1.5 Summary of the sample properties

We have selected a sample of 226 GPS source candidates from multi-frequency multi-epoch observations conducted at the RATAN-600 radio telescope, supplemented by the literature; 60 objects from the sample are reported as GPS candidates for the first time. We have searched the literature for information about optical counterparts of the selected sources and found them for 140 sources (62% of sources). The fraction of galaxies (39 objects, 28% of identified sources) and quasars (98 objects, 70%) in our sample is close to that in samples of HFP Dallacasa et al. (2002) and GPS sources (with relatively faint limiting flux) (eg. Snellen et al. (1998a)). 3 sources are identified with BL Lacertae type objects. 86 sources from the sample still lack optical identification.

The observed spectrum of an “average” GPS source from our sample is characterized by the peak frequency $\nu_0 = 2.4$ GHz and flux density $S_{\nu_0} = 0.8$ Jy, high-frequency spectral index $\alpha_1 = -0.77$ and low-frequency index $\alpha_2 = 0.66$. The shape of the radio

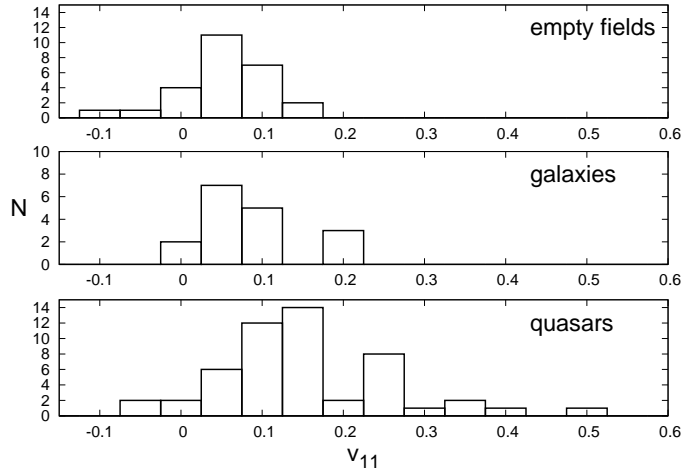


Figure 5.5: Distribution of the observed variability index v_{11} at 11 GHz for GPS quasars, galaxies and unidentified radio sources (empty fields) in our sample.

spectrum do not allow one to distinguish between GPS galaxies and quasars.

GPS quasars tend to show significantly stronger variability than GPS galaxies, which is in agreement with previously published results for both GPS (e.g., O’Dea 1998) and high frequency peaked Tinti et al. 2005 sources. Most GPS galaxies and “empty fields” show no significant variability with three noticeable exceptions: PKS 0500+019, TXS 1404+28, and B2 1600+33. The low variability of GPS sources with no optical identification suggests that a significant fraction of them might be optically faint and, possibly, distant GPS galaxies. GPS galaxies and GPS quasars have significantly different variability properties and intrinsic peak frequencies. However, no clear boundary can be drawn between them on the basis of single-dish radio observations because GPS galaxies and GPS quasars strongly overlap in their observed properties.

With 99.8% probability there is a correlation between the variability index at 11 GHz v_{11} and the high-frequency spectral index α_1 . The flatter spectral index correspond to higher variability.

In Section 5.2 we extend our study of the selected GPS sample to parsec scales by analyzing simultaneous 2 and 8 GHz VLBA observations from the VLBA Calibrator survey Beasley et al. (2002); Fomalont et al. (2003); Kovalev et al. (2007); Petrov et al. (2005, 2006, 2008).

Table 5.1: RATAN–600 sample of GPS sources

IAU name	v_0	S_0	α_1	α_2	Type	z	GPS References
0000+21	$5.66^{+2.01}_{-1.49}$	$0.265^{+0.165}_{-0.102}$	-0.82 ± 0.07	0.86 ± 0.07	G	0.450	1,26,35g,36,L
0001–12	$6.23^{+0.39}_{-0.52}$	$0.830^{+0.051}_{-0.048}$	-0.72 ± 0.11	0.54 ± 0.02	R		9
0002+05	$4.96^{+0.45}_{-0.41}$	$0.267^{+0.027}_{-0.024}$	-0.75 ± 0.03	0.61 ± 0.01	Q	1.900	1,26,L
0015+52	$7.74^{+2.41}_{-2.26}$	$0.653^{+0.089}_{-0.078}$	-0.39 ± 0.16	0.59 ± 0.41	Q	2.574	4,36
0018+72	$0.92^{+0.02}_{-0.02}$	$0.719^{+0.012}_{-0.012}$	-0.91 ± 0.01		G	0.821	L,8,15,18,21,22,35
0026+34	$1.41^{+0.07}_{-0.01}$	$1.898^{+0.011}_{-0.001}$	-0.52 ± 0.01	1.58 ± 0.38	G	0.517	3,18,23,30,35g,L
0057+67	$0.81^{+0.01}_{-0.01}$	$1.943^{+0.003}_{-0.003}$	-0.61 ± 0.04	0.83 ± 0.27	R		NEW
0102+51	$1.43^{+0.02}_{-0.02}$	$0.564^{+0.003}_{-0.004}$	-1.00 ± 0.05	0.87 ± 0.01	R		4
0102+48	$4.14^{+0.33}_{-0.30}$	$1.103^{+0.057}_{-0.054}$	-0.64 ± 0.05	0.49 ± 0.05	R		4
0108+38	$4.64^{+0.03}_{-0.03}$	$1.279^{+0.013}_{-0.013}$	-1.20 ± 0.01	1.32 ± 0.02	G	0.668	1,2,3,8,15,18,21,22,26,35c,36,L
0111+21	$1.13^{+0.04}_{-0.04}$	$0.483^{+0.014}_{-0.013}$	-1.36 ± 0.04		R		NEW
0129+56	$3.01^{+0.15}_{-0.12}$	$0.495^{+0.012}_{-0.012}$	-1.35 ± 0.10	0.88 ± 0.01	G	0.450	4
0132–09	$2.07^{+0.12}_{-0.11}$	$0.977^{+0.029}_{-0.028}$	-1.03 ± 0.11	0.75 ± 0.04	G	2.216	NEW
0134+31	$2.86^{+0.65}_{-0.53}$	$0.478^{+0.048}_{-0.044}$	-1.20 ± 0.05	0.11 ± 0.12	R		NEW

IAU name	v_0	S_0	α_1	α_2	Type	z	GPS References
0144+20	$1.00^{+0.01}_{-0.01}$	$1.211^{+0.003}_{-0.003}$	-1.01 ± 0.01	0.82 ± 0.05	R		L,8,16,18
0146+05	$4.82^{+0.14}_{-0.14}$	$1.305^{+0.013}_{-0.013}$	-0.53 ± 0.03	0.54 ± 0.01	Q	2.345	NEW
0153+74	$2.03^{+0.02}_{-0.02}$	$1.917^{+0.012}_{-0.012}$	-1.28 ± 0.01	0.15 ± 0.18	Q	2.341	10,18,31c
0201+11	$3.26^{+0.08}_{-0.08}$	$0.866^{+0.006}_{-0.006}$	-0.33 ± 0.01	0.58 ± 0.01	Q	3.61	L,3,8,18,21,22,36
0201+08	$1.09^{+0.01}_{-0.01}$	$1.866^{+0.006}_{-0.006}$	-1.02 ± 0.03		R		23,L
0201+43	$0.76^{+0.02}_{-0.02}$	$0.558^{+0.002}_{-0.002}$	-0.59 ± 0.06	0.48 ± 0.09	R		29
0203+62	$2.50^{+0.03}_{-0.03}$	$1.897^{+0.016}_{-0.016}$	-1.14 ± 0.04	1.52 ± 0.23	R		NEW
0237-23	$0.57^{+0.01}_{-0.01}$	$7.217^{+0.009}_{-0.009}$	-0.95 ± 0.01	0.95 ± 0.12	Q	2.225	3,7,8,11,18,19,21,22,34,L
0316+16	$0.60^{+0.01}_{-0.01}$	$9.709^{+0.008}_{-0.008}$	-1.17 ± 0.01	0.08 ± 0.21	R		2,3,8,18,35fs,L
0317+18	$3.99^{+0.05}_{-0.05}$	$0.766^{+0.013}_{-0.013}$	-1.14 ± 0.02	0.94 ± 0.02	G	0.300	9
0320+01	$2.98^{+0.30}_{-0.28}$	$0.479^{+0.024}_{-0.024}$	-0.55 ± 0.06	0.90 ± 0.13	R		NEW
0326+27	$1.22^{+0.02}_{-0.02}$	$1.275^{+0.002}_{-0.002}$	-0.62 ± 0.01	0.49 ± 0.05	Q	1.533	NEW
0344+19	$1.12^{+0.03}_{-0.03}$	$0.520^{+0.002}_{-0.002}$	-0.70 ± 0.01	0.14 ± 0.08	R		NEW
0411+05	$0.26^{+0.01}_{-0.01}$	$2.970^{+0.019}_{-0.019}$	-0.92 ± 0.01	1.22 ± 0.56	Q	2.639	NEW
0411+34	$1.27^{+0.01}_{-0.01}$	$1.918^{+0.002}_{-0.002}$	-0.74 ± 0.07	0.27 ± 0.11	R		NEW
0420+07	$0.87^{+0.05}_{-0.05}$	$0.365^{+0.004}_{-0.004}$	-0.74 ± 0.04		R		NEW
0424+32	$7.36^{+0.38}_{-0.38}$	$0.520^{+0.034}_{-0.034}$	-0.66 ± 0.06	1.04 ± 0.01	R		1,26,35g,36
0424+41	$4.03^{+0.26}_{-0.19}$	$0.815^{+0.018}_{-0.017}$	-0.66 ± 0.04	0.82 ± 0.01	R		23,L
0428+20	$1.08^{+0.01}_{-0.01}$	$3.809^{+0.003}_{-0.003}$	-0.84 ± 0.01	0.61 ± 0.14	G	0.219	2,3,8,14,18,35g,L
0434-18	$4.01^{+0.07}_{-0.06}$	$1.075^{+0.014}_{-0.014}$	-0.82 ± 0.01	1.01 ± 0.02	Q	2.702	11,36,L
0439-33	$2.21^{+0.05}_{-0.05}$	$1.230^{+0.012}_{-0.012}$	-0.89 ± 0.04	0.63 ± 0.02	R		5,33,35g,L
0440-00	$3.30^{+0.03}_{-0.03}$	$2.030^{+0.017}_{-0.017}$	-0.46 ± 0.01	0.28 ± 0.02	Q	0.844	3,6,30
0440+34	$3.11^{+0.07}_{-0.07}$	$0.725^{+0.005}_{-0.005}$	-0.58 ± 0.01	0.43 ± 0.01	R		NEW
0442+38	$5.20^{+1.08}_{-0.89}$	$0.477^{+0.011}_{-0.094}$	-0.64 ± 0.02	1.08 ± 0.04	Q	0.413	36
0448-39	$5.14^{+0.70}_{-0.62}$	$1.053^{+0.164}_{-0.142}$	-0.99 ± 0.04	0.81 ± 0.14	Q	1.288	NEW
0448-18	$2.87^{+0.21}_{-0.20}$	$0.513^{+0.026}_{-0.019}$	-0.91 ± 0.05	0.10 ± 0.06	Q	2.05	NEW
0457+02	$1.73^{+0.02}_{-0.02}$	$1.847^{+0.009}_{-0.009}$	-0.77 ± 0.01	1.76 ± 0.03	Q	2.384	2,3,11,18
0500+01	$2.16^{+0.02}_{-0.02}$	$2.362^{+0.007}_{-0.007}$	-0.76 ± 0.01	1.19 ± 0.03	G	0.584	2,3,5,7,8,11,13,15,18,21,22,35g,L
0512-20	$7.53^{+4.74}_{-2.91}$	$0.640^{+0.994}_{-0.389}$	-0.54 ± 0.26	0.77 ± 0.19	R		NEW
0514+47	$2.17^{+0.05}_{-0.05}$	$0.866^{+0.013}_{-0.013}$	-0.67 ± 0.22	1.18 ± 0.01	R		4
0513+71	$1.53^{+0.06}_{-0.06}$	$0.244^{+0.003}_{-0.003}$	-0.86 ± 0.04	0.48 ± 0.01	R		27,28
0528-25	$2.34^{+0.04}_{-0.04}$	$1.250^{+0.008}_{-0.008}$	-0.62 ± 0.01	0.22 ± 0.13	Q	2.788	6,8,18,24,L
0552+39	$6.42^{+0.04}_{-0.04}$	$5.579^{+0.008}_{-0.109}$	-0.57 ± 0.04	1.69 ± 0.06	Q	2.363	3,8,9,12,18,21,22,31c,36
0554-02	$1.23^{+0.03}_{-0.03}$	$0.724^{+0.006}_{-0.006}$	-1.22 ± 0.06		Q	0.235	12,16,18,35n,L
0554+24	$3.04^{+0.12}_{-0.11}$	$0.966^{+0.017}_{-0.017}$	-0.92 ± 0.03	0.41 ± 0.03	R		NEW
0617+21	$1.51^{+0.05}_{-0.04}$	$0.900^{+0.011}_{-0.011}$	-0.99 ± 0.04	0.66 ± 0.03	R		NEW
0627+53	$0.95^{+0.01}_{-0.01}$	$0.783^{+0.002}_{-0.002}$	-0.92 ± 0.04	0.31 ± 0.09	Q	2.204	4
0629+32	$8.60^{+9.85}_{-4.59}$	$0.185^{+0.715}_{-0.147}$		1.07 ± 0.04	Q	1.831	36
0632+19	$1.28^{+0.33}_{-0.26}$	$0.514^{+0.027}_{-0.026}$	-1.13 ± 0.04		R		NEW
0637-33	$5.61^{+0.24}_{-0.23}$	$0.863^{+0.071}_{-0.066}$	-1.02 ± 0.02	1.05 ± 0.02	B		NEW
0636+68	$5.03^{+0.28}_{-0.25}$	$0.419^{+0.026}_{-0.025}$	-0.53 ± 0.02	0.70 ± 0.02	Q	3.177	1,8,18,26,36,L
0642-34	$3.51^{+0.19}_{-0.14}$	$0.987^{+0.030}_{-0.029}$	-0.94 ± 0.02	0.42 ± 0.08	Q	2.165	11,L
0643+30	$0.72^{+0.01}_{-0.01}$	$0.919^{+0.002}_{-0.002}$	-0.56 ± 0.03		R		NEW
0642+44	$11.65^{+0.09}_{-0.09}$	$3.784^{+0.091}_{-0.050}$	-0.46 ± 0.05	1.51 ± 0.02	Q	3.408	1,14,L
0645+20	$2.47^{+0.47}_{-0.49}$	$0.379^{+0.051}_{-0.043}$	-0.72 ± 0.05		R		NEW
0646+60	$6.14^{+0.21}_{-0.21}$	$1.038^{+0.025}_{-0.033}$	-0.82 ± 0.05	1.24 ± 0.06	Q	0.455	1,8,15,18,21,22,26,L
0653+32	$4.25^{+0.32}_{-0.46}$	$0.226^{+0.026}_{-0.023}$	-0.89 ± 0.05	0.52 ± 0.01	R		NEW
0700+47	$0.71^{+0.01}_{-0.01}$	$0.884^{+0.002}_{-0.002}$	-0.65 ± 0.02		R		14,35f
0710+43	$2.22^{+0.01}_{-0.01}$	$2.163^{+0.006}_{-0.006}$	-0.61 ± 0.01	0.84 ± 0.01	G	0.518	2,3,8,18,35g,36,L
0711+35	$1.48^{+0.01}_{-0.01}$	$1.513^{+0.002}_{-0.002}$	-0.71 ± 0.01	0.67 ± 0.02	Q	1.620	3,8,18,23,30,L
0718+37	$4.23^{+0.40}_{-0.36}$	$0.209^{+0.012}_{-0.011}$	-0.32 ± 0.01	0.95 ± 0.10	Q	1.629	1,4,36
0729-22	$1.89^{+0.06}_{-0.06}$	$1.861^{+0.021}_{-0.021}$	-1.01 ± 0.02	0.66 ± 0.65	R		NEW
0733-17	$1.13^{+0.01}_{-0.01}$	$2.934^{+0.010}_{-0.010}$	-0.75 ± 0.01		R		34
0736-33	$2.94^{+0.15}_{-0.15}$	$1.036^{+0.070}_{-0.070}$	-1.29 ± 0.05	0.66 ± 0.20	R		NEW
0738+31	$3.87^{+0.04}_{-0.04}$	$2.910^{+0.018}_{-0.017}$	-0.51 ± 0.02	0.65 ± 0.03	Q	0.630	2,3,13,18,30
0741-06	$0.38^{+0.01}_{-0.01}$	$11.456^{+0.043}_{-0.043}$	-1.16 ± 0.01	0.80 ± 0.48	R		31g,34
0742+10	$2.63^{+0.01}_{-0.01}$	$4.027^{+0.013}_{-0.008}$	-0.76 ± 0.01	0.69 ± 0.04	G		L,3,8,9,13,16,17,18,31g
0743-00	$7.06^{+0.14}_{-0.14}$	$2.027^{+0.035}_{-0.035}$	-0.61 ± 0.02	0.95 ± 0.02	Q	0.994	2,3,6,7,8,11,13,18,31g,36,L
0748+04	$1.87^{+0.60}_{-0.46}$	$0.241^{+0.022}_{-0.022}$	-0.71 ± 0.03		R		NEW
0749+42	$1.01^{+0.01}_{-0.01}$	$0.714^{+0.001}_{-0.001}$	-0.86 ± 0.03		Q	3.59	NEW
0750+53	$1.49^{+0.03}_{-0.03}$	$0.678^{+0.006}_{-0.006}$	-1.20 ± 0.09	0.95 ± 0.01	R		4,23,L
0752+63	$5.01^{+0.21}_{-0.20}$	$0.434^{+0.018}_{-0.018}$	-0.67 ± 0.01		R		27,28
0753+37	$2.81^{+0.32}_{-0.29}$	$0.309^{+0.029}_{-0.027}$	-0.79 ± 0.02		Q	2.514	4
0802+21	$0.78^{+0.02}_{-0.02}$	$0.915^{+0.003}_{-0.003}$	-0.64 ± 0.01		G		L,8,15,18,21,22
0819-03	$1.46^{+0.08}_{-0.07}$	$0.565^{+0.007}_{-0.007}$	-0.73 ± 0.05	0.46 ± 0.02	Q	2.352	NEW
0830+16	$2.72^{+0.31}_{-0.63}$	$0.367^{+0.089}_{-0.071}$	-0.59 ± 0.07	0.98 ± 0.23	R		NEW
0839+18	$1.17^{+0.02}_{-0.02}$	$1.287^{+0.002}_{-0.002}$	-0.57 ± 0.01		Q	1.272	NEW
0858-27	$5.72^{+0.05}_{-0.05}$	$3.264^{+0.028}_{-0.027}$	-0.82 ± 0.03	0.75 ± 0.01	Q	2.152	8,11,16,18,19,25,L
0903+68	$3.33^{+0.35}_{-0.32}$	$0.319^{+0.037}_{-0.033}$	-0.78 ± 0.04	0.66 ± 0.04	R		17

IAU name	v_0	S_0	α_1	α_2	Type	z	GPS References
0904+03	$0.58^{+0.01}_{-0.01}$	$1.030^{+0.005}_{-0.005}$	-1.25 ± 0.01		G		3,8,18,23,35n,L
0906-04	$1.35^{+0.08}_{-0.08}$	$0.473^{+0.010}_{-0.009}$	-0.56 ± 0.03		R		NEW
0919-26	$6.80^{+0.09}_{-0.09}$	$2.630^{+0.028}_{-0.027}$	-0.90 ± 0.04	0.51 ± 0.01	Q	2.300	NEW
0920+57	$0.57^{+0.02}_{-0.02}$	$0.282^{+0.002}_{-0.002}$	-0.62 ± 0.01	0.43 ± 0.02	R		29
1019+30	$1.49^{+0.01}_{-0.01}$	$0.920^{+0.002}_{-0.002}$	-0.74 ± 0.01	1.06 ± 0.03	Q	1.319	30
1031+56	$1.08^{+0.01}_{-0.01}$	$1.902^{+0.001}_{-0.001}$	-1.01 ± 0.01	0.29 ± 0.06	G	0.460	2,3,8,18,35g,L
1100+22	$2.77^{+0.04}_{-0.04}$	$0.639^{+0.008}_{-0.008}$	-0.87 ± 0.01	0.62 ± 0.04	R		8,15,18,21,22,23,L
1100+79	$1.19^{+0.05}_{-0.05}$	$0.517^{+0.004}_{-0.004}$	-0.62 ± 0.02		R		NEW
1107+48	$0.55^{+0.05}_{-0.05}$	$0.647^{+0.004}_{-0.003}$	-0.89 ± 0.03	0.37 ± 0.04	Q	0.74	4
1108+20	$1.17^{+0.02}_{-0.02}$	$1.235^{+0.005}_{-0.005}$	-0.91 ± 0.03		G	0.299	23,29,L
1120-27	$2.03^{+0.04}_{-0.04}$	$0.748^{+0.010}_{-0.010}$	-1.12 ± 0.01		R		L,5,33,35
1133-03	$7.62^{+0.94}_{-0.84}$	$0.524^{+0.065}_{-0.058}$	-0.63 ± 0.10	0.87 ± 0.04	Q	1.648	36
1136-15	$7.87^{+0.27}_{-0.26}$	$1.027^{+0.044}_{-0.043}$	-0.60 ± 0.06	0.99 ± 0.01	Q	2.625	9
1141+01	$2.65^{+0.33}_{-0.44}$	$0.350^{+0.052}_{-0.045}$	-0.85 ± 0.05		R		NEW
1143-24	$3.26^{+0.03}_{-0.03}$	$1.888^{+0.014}_{-0.014}$	-0.92 ± 0.01	1.31 ± 0.01	Q	1.940	2,3,7,8,11,13,18,36,L
1152+46	$0.66^{+0.02}_{-0.02}$	$0.682^{+0.003}_{-0.003}$	-0.66 ± 0.07		R		NEW
1157-21	$4.80^{+0.08}_{-0.15}$	$0.832^{+0.017}_{-0.017}$	-0.98 ± 0.02	0.70 ± 0.01	Q	0.927	NEW
1209-19	$1.59^{+0.15}_{-0.13}$	$0.488^{+0.015}_{-0.014}$	-0.68 ± 0.02	0.36 ± 0.05	R		NEW
1205+01	$3.08^{+0.84}_{-0.84}$	$0.247^{+0.055}_{-0.055}$	-0.83 ± 0.07	0.25 ± 0.04	G		36
1225+36	$1.18^{+0.01}_{-0.01}$	$2.115^{+0.001}_{-0.001}$	-1.27 ± 0.01	1.58 ± 0.02	Q	1.975	2,8,14,15,18,21,22,30,L
1226+63	$1.84^{+0.05}_{-0.05}$	$0.419^{+0.005}_{-0.005}$	-1.01 ± 0.06	0.80 ± 0.01	R		4
1239+55	$1.53^{+0.05}_{-0.05}$	$0.285^{+0.002}_{-0.002}$	-1.14 ± 0.16	0.47 ± 0.01	R		29
1239+60	$1.97^{+0.37}_{-0.31}$	$0.462^{+0.061}_{-0.054}$	-1.13 ± 0.06		Q	2.069	4
1255-31	$5.65^{+0.13}_{-0.13}$	$2.844^{+0.074}_{-0.072}$	-0.55 ± 0.16	0.88 ± 0.03	Q	1.924	NEW
1300-10	$3.79^{+0.99}_{-0.78}$	$0.362^{+0.067}_{-0.057}$	-0.83 ± 0.08	0.34 ± 0.11	B		36
1308+14	$1.17^{+0.03}_{-0.03}$	$0.766^{+0.003}_{-0.003}$	-0.89 ± 0.01	0.75 ± 0.05	Q	1.952	30
1311+55	$0.56^{+0.01}_{-0.01}$	$1.572^{+0.003}_{-0.003}$	-0.80 ± 0.01		Q	0.613	4
1312+53	$3.79^{+0.61}_{-0.53}$	$0.417^{+0.061}_{-0.053}$	-0.57 ± 0.07	0.62 ± 0.04	R		NEW
1320+39	$6.08^{+1.40}_{-1.14}$	$0.220^{+0.043}_{-0.037}$	-0.41 ± 0.06	0.68 ± 0.01	Q	2.985	36
1321+41	$2.79^{+0.44}_{-0.38}$	$0.455^{+0.052}_{-0.047}$	-0.78 ± 0.05	0.35 ± 0.17	Q	0.495	4
1333+45	$4.74^{+0.14}_{-0.13}$	$0.709^{+0.031}_{-0.030}$	-0.92 ± 0.02	0.99 ± 0.02	Q	2.450	1,8,15,18,21,22,26,L
1333+58	$6.45^{+0.35}_{-0.35}$	$0.687^{+0.034}_{-0.030}$	-0.72 ± 0.04	0.71 ± 0.01	R		1,26,L
1338+38	$2.78^{+0.20}_{-0.19}$	$0.375^{+0.030}_{-0.028}$	-1.19 ± 0.03	0.45 ± 0.04	Q	3.103	4
1347-21	$0.65^{+0.01}_{-0.01}$	$1.229^{+0.004}_{-0.004}$	-0.84 ± 0.01		R		5,35n,L
1347+09	$3.08^{+0.91}_{-0.26}$	$0.400^{+0.030}_{-0.028}$	-0.74 ± 0.02	0.61 ± 0.23	G	0.132	NEW
1351-01	$3.99^{+0.12}_{-0.12}$	$0.902^{+0.012}_{-0.011}$	-0.36 ± 0.02	0.49 ± 0.02	Q	3.707	8,16,18
1352+75	$12.52^{+3.68}_{-2.84}$	$0.371^{+0.248}_{-0.149}$		1.07 ± 0.04	Q		36
1354-17	$0.42^{+0.02}_{-0.02}$	$2.062^{+0.020}_{-0.020}$	-0.74 ± 0.02		Q	3.147	8,11,18,25,34,35f,L
1355+44	$1.75^{+0.01}_{-0.01}$	$0.694^{+0.001}_{-0.001}$	-0.80 ± 0.01	0.45 ± 0.01	G	0.646	8,14,17,35g
1356+47	$2.41^{+0.05}_{-0.05}$	$0.719^{+0.010}_{-0.010}$	-0.50 ± 0.02	1.19 ± 0.01	G	0.230	NEW
1404+28	$5.05^{+0.02}_{-0.02}$	$2.384^{+0.015}_{-0.015}$	-1.08 ± 0.01	1.11 ± 0.01	G	0.077	1,2,3,8,13,18,26,30,35g,36,L
1406-26	$8.19^{+0.12}_{-0.12}$	$1.314^{+0.029}_{-0.028}$	-0.45 ± 0.04	1.22 ± 0.01	Q	2.43	NEW
1413+37	$2.27^{+0.09}_{-0.09}$	$0.428^{+0.004}_{-0.004}$	-0.52 ± 0.08	0.51 ± 0.01	Q	2.370	NEW
1413+34	$0.82^{+0.01}_{-0.01}$	$1.941^{+0.001}_{-0.001}$	-0.71 ± 0.01	0.52 ± 0.03	R		2,8,15,18,21,22,30
1422+23	$4.06^{+0.02}_{-0.02}$	$0.673^{+0.006}_{-0.006}$	-0.82 ± 0.01	1.29 ± 0.01	Q	3.62	1,26,L
1424+11	$1.65^{+0.07}_{-0.63}$	$0.248^{+0.009}_{-0.053}$	-1.09 ± 0.07		R		NEW
1427+10	$5.74^{+0.06}_{-0.95}$	$0.858^{+0.010}_{-0.010}$	-0.44 ± 0.01	1.00 ± 0.01	Q	1.71	1,26,36,L
1430-15	$5.38^{+0.24}_{-0.23}$	$0.911^{+0.028}_{-0.027}$	-0.72 ± 0.03	0.50 ± 0.01	G	1.573	NEW
1436+44	$3.35^{+0.67}_{-0.56}$	$0.310^{+0.055}_{-0.047}$	-1.34 ± 0.05	0.29 ± 0.04	Q	2.10	4
1437+62	$0.54^{+0.01}_{-0.01}$	$3.023^{+0.004}_{-0.004}$	-1.00 ± 0.02		Q	1.090	NEW
1440+30	$0.69^{+0.01}_{-0.01}$	$0.617^{+0.001}_{-0.001}$	-0.98 ± 0.02	1.35 ± 0.02	R		NEW
1442+63	$1.53^{+0.02}_{-0.02}$	$0.688^{+0.003}_{-0.003}$	-0.73 ± 0.04	0.42 ± 0.01	Q	1.380	NEW
1442+00	$2.02^{+0.77}_{-0.56}$	$0.202^{+0.040}_{-0.033}$	-0.69 ± 0.03		Q		NEW
1442+10	$0.74^{+0.01}_{-0.01}$	$2.688^{+0.004}_{-0.004}$	-0.97 ± 0.01	0.51 ± 0.33	Q	3.535	2,3,5,8,11,18,L
1448-23	$1.71^{+0.07}_{-0.07}$	$0.444^{+0.005}_{-0.005}$	-0.55 ± 0.04	0.45 ± 0.01	Q	2.220	NEW
1455+09	$3.16^{+0.56}_{-0.48}$	$0.264^{+0.058}_{-0.047}$	-1.01 ± 0.05		R		NEW
1503-09	$0.68^{+0.01}_{-0.01}$	$1.536^{+0.008}_{-0.008}$	-1.06 ± 0.10		G		L,5,33,35
1509+05	$11.38^{+2.71}_{-2.19}$	$0.731^{+0.265}_{-0.193}$	-0.33 ± 0.15	1.22 ± 0.06	G	0.084	1,12,26,35g,L
1518+04	$1.77^{+0.01}_{-0.01}$	$4.151^{+0.004}_{-0.004}$	-1.68 ± 0.01	1.15 ± 0.32	G	1.294	L,3,5,7,8,12,18,33
1519-27	$8.85^{+0.19}_{-0.19}$	$2.004^{+0.022}_{-0.022}$	-0.47 ± 0.03	0.36 ± 0.01	B	1.297	6,8,11,15,18,L
1526+67	$5.52^{+0.53}_{-0.49}$	$0.410^{+0.087}_{-0.072}$	-1.07 ± 0.03	1.03 ± 0.02	Q	3.02	1,26,L
1528+38	$3.77^{+0.98}_{-0.78}$	$0.145^{+0.024}_{-0.021}$	-0.31 ± 0.02		G	0.152	29
1532+68	$1.24^{+0.02}_{-0.02}$	$0.554^{+0.002}_{-0.002}$	-0.78 ± 0.01	1.23 ± 0.16	R		4,29
1535+00	$1.13^{+0.03}_{-0.03}$	$0.760^{+0.002}_{-0.002}$	-0.61 ± 0.01	0.60 ± 0.03	Q	3.497	NEW
1540-07	$0.72^{+0.02}_{-0.02}$	$1.893^{+0.012}_{-0.012}$	-0.68 ± 0.01		G	0.172	5,11,35n,L
1555-14	$2.39^{+0.07}_{-0.07}$	$0.698^{+0.014}_{-0.014}$	-0.76 ± 0.01	0.82 ± 0.03	G	0.097	NEW
1600+33	$0.87^{+0.01}_{-0.01}$	$3.084^{+0.001}_{-0.001}$	-0.50 ± 0.01	0.15 ± 0.08	G	1.100	2,3,8,18,35g,L
1601-22	$0.95^{+0.02}_{-0.02}$	$0.934^{+0.003}_{-0.003}$	-0.80 ± 0.03		G	0.141	8,15,18,35n
1602+19	$2.74^{+0.70}_{-0.56}$	$0.277^{+0.064}_{-0.052}$	-1.00 ± 0.05		R		NEW

IAU name	v_0	S_0	α_1	α_2	Type	z	GPS References
1604+31	2.87 ^{+0.07} _{-0.07}	0.774 ^{+0.008} _{-0.008}	-0.74 ± 0.01	0.33 ± 0.03	R		8,16,18,23,35f,L
1607+26	0.83 ^{+0.01} _{-0.01}	5.339 ^{+0.006} _{-0.006}	-1.19 ± 0.01	1.03 ± 0.18	G	0.473	2,3,7,8,15,18,30,32,35c,L
1614+05	5.02 ^{+0.06} _{-0.06}	0.843 ^{+0.013} _{-0.012}	-0.54 ± 0.02	1.13 ± 0.02	Q	3.217	1,18,26,L
1615+02	4.05 ^{+0.10} _{-0.10}	0.758 ^{+0.009} _{-0.009}	-0.31 ± 0.01	0.51 ± 0.03	Q	1.341	NEW
1622+66	5.26 ^{+0.59} _{-0.53}	0.348 ^{+0.044} _{-0.039}	-0.40 ± 0.04	0.56 ± 0.02	Q	0.203	1,26,27,28,35n,L
1627+47	1.18 ^{+0.03} _{-0.03}	0.283 ^{+0.002} _{-0.002}	-0.76 ± 0.03		G	1.629	4,29
1630+35	1.10 ^{+0.01} _{-0.01}	0.565 ^{+0.002} _{-0.002}	-0.67 ± 0.01		R		4,29
1656-07	3.65 ^{+0.26} _{-0.24}	1.207 ^{+0.024} _{-0.023}	-1.18 ± 0.08	0.21 ± 0.03	R		11,L
1658+03	4.54 ^{+0.80} _{-0.68}	0.246 ^{+0.053} _{-0.044}	-0.77 ± 0.11	0.72 ± 0.02	R		NEW
1717+08	5.76 ^{+0.29} _{-0.27}	0.614 ^{+0.026} _{-0.025}	-0.61 ± 0.03	0.60 ± 0.01	Q	1.185	36
1720+25	1.07 ^{+0.05} _{-0.05}	0.590 ^{+0.004} _{-0.004}	-0.93 ± 0.04		Q	2.25	NEW
1732+09	2.18 ^{+0.02} _{-0.02}	1.191 ^{+0.008} _{-0.008}	-1.01 ± 0.01	1.03 ± 0.12	R		3,5,8,16,18,35n,L
1734+50	6.82 ^{+0.44} _{-0.42}	0.873 ^{+0.033} _{-0.032}	-0.51 ± 0.05	0.44 ± 0.02	G		L,1,26,35
1745+67	0.98 ^{+0.02} _{-0.02}	0.659 ^{+0.018} _{-0.017}	-0.79 ± 0.03	1.39 ± 0.90	R		4,29
1748-25	0.60 ^{+0.07} _{-0.05}	1.427 ^{+0.036} _{-0.035}	-0.72 ± 0.01		R		NEW
1755+57	1.79 ^{+0.02} _{-0.02}	0.761 ^{+0.004} _{-0.004}	-1.22 ± 0.04	0.83 ± 0.01	Q	2.110	4
1758+38	15.15 ^{+0.77} _{-0.77}	1.264 ^{+0.096} _{-0.096}	-0.41 ± 0.11	0.81 ± 0.01	Q	2.092	1,26
1800+17	1.25 ^{+0.07} _{-0.07}	0.474 ^{+0.005} _{-0.005}	-0.69 ± 0.03		R		NEW
1815+61	0.85 ^{+0.01} _{-0.01}	0.884 ^{+0.001} _{-0.001}	-0.71 ± 0.02	1.36 ± 0.08	Q	0.601	4,29
1816-02	1.51 ^{+0.01} _{-0.03}	1.739 ^{+0.001} _{-0.013}	-0.97 ± 0.03	0.42 ± 0.06	R		NEW
1820+39	0.93 ^{+0.34} _{-0.25}	0.624 ^{+0.059} _{-0.054}	-0.77 ± 0.03		R		4
1826+79	5.11 ^{+0.72} _{-0.63}	0.535 ^{+0.046} _{-0.042}	-0.51 ± 0.03	0.63 ± 0.02	Q	0.224	36
1821+10	1.53 ^{+0.04} _{-0.04}	0.970 ^{+0.004} _{-0.004}	-0.55 ± 0.02	0.39 ± 0.03	Q	1.364	NEW
1822+03	0.88 ^{+0.04} _{-0.04}	0.589 ^{+0.006} _{-0.006}	-0.77 ± 0.01		R		NEW
1823+01	2.39 ^{+0.13} _{-0.13}	0.987 ^{+0.051} _{-0.048}	-0.87 ± 0.03	1.26 ± 0.48	Q	1.771	NEW
1843+35	2.50 ^{+0.05} _{-0.05}	0.971 ^{+0.012} _{-0.012}	-1.20 ± 0.04	0.23 ± 0.05	G	0.764	8,16,18,35c,L
1848+28	10.21 ^{+0.10} _{-0.10}	1.434 ^{+0.021} _{-0.021}	-0.66 ± 0.02	1.26 ± 0.01	Q	2.56	1,7,8,18,26,36,L
1908+23	0.63 ^{+0.02} _{-0.02}	1.302 ^{+0.007} _{-0.007}	-0.89 ± 0.03		R		NEW
1909+26	1.92 ^{+0.05} _{-0.05}	0.756 ^{+0.006} _{-0.006}	-0.63 ± 0.01	0.45 ± 0.04	R		NEW
1926+23	4.32 ^{+0.38} _{-0.38}	0.348 ^{+0.039} _{-0.037}	-0.67 ± 0.03	0.75 ± 0.06	R		36
1939+81	3.41 ^{+0.48} _{-0.42}	0.373 ^{+0.037} _{-0.034}	-0.53 ± 0.04	0.43 ± 0.04	R		NEW
1943+54	1.06 ^{+0.01} _{-0.01}	1.787 ^{+0.001} _{-0.001}	-0.73 ± 0.01	0.35 ± 0.05	G	0.263	NEW
1946+70	2.04 ^{+0.03} _{-0.03}	1.002 ^{+0.001} _{-0.001}	-0.50 ± 0.02	0.96 ± 0.01	G	0.101	4,20,27,28
1947+07	2.43 ^{+0.03} _{-0.03}	1.222 ^{+0.007} _{-0.007}	-0.79 ± 0.01	0.33 ± 0.03	R		30
2000+47	4.44 ^{+0.34} _{-0.32}	0.733 ^{+0.032} _{-0.031}	-0.27 ± 0.12	1.00 ± 0.01	R		4,36
2000-33	4.93 ^{+0.26} _{-0.24}	1.089 ^{+0.083} _{-0.077}	-0.79 ± 0.06	0.96 ± 0.04	Q	3.783	8,11,18,25,L
2003+66	0.52 ^{+0.01} _{-0.01}	1.224 ^{+0.004} _{-0.004}	-0.72 ± 0.01		Q	0.456	29
2005+40	4.06 ^{+0.03} _{-0.03}	2.957 ^{+0.008} _{-0.008}	-0.38 ± 0.01	0.27 ± 0.01	Q	1.736	36
2008-06	1.22 ^{+0.01} _{-0.01}	2.615 ^{+0.005} _{-0.005}	-0.97 ± 0.01	0.70 ± 0.08	G	0.547	2,3,5,8,16,18,35g,L
2015-11	4.72 ^{+0.63} _{-0.56}	0.373 ^{+0.083} _{-0.068}	-0.77 ± 0.04	1.30 ± 0.08	R		36
2019+05	4.04 ^{+0.18} _{-0.17}	0.525 ^{+0.020} _{-0.019}	-0.85 ± 0.04	0.84 ± 0.05	R		1,26,35g,L
2021+61	5.91 ^{+0.08} _{-0.07}	2.875 ^{+0.015} _{-0.015}	-0.50 ± 0.02	0.61 ± 0.01	G	0.227	3,18,31g,35c,36
2022+17	7.02 ^{+0.39} _{-0.37}	0.586 ^{+0.025} _{-0.024}	-0.43 ± 0.04	0.56 ± 0.01	Q	1.05	1,26,31c,L
2039+03	2.82 ^{+0.72} _{-0.59}	0.246 ^{+0.090} _{-0.066}	-1.21 ± 0.05	0.50 ± 0.28	R		NEW
2050+36	1.40 ^{+0.01} _{-0.01}	5.145 ^{+0.001} _{-0.001}	-1.13 ± 0.01	0.47 ± 0.04	R		3,8,18,23,35g,L
2107-10	2.20 ^{+0.05} _{-0.05}	1.257 ^{+0.001} _{-0.010}	-0.58 ± 0.01	1.40 ± 0.03	R		NEW
2112-14	7.27 ^{+7.89} _{-3.78}	0.507 ^{+0.750} _{-0.303}	-0.54 ± 0.16	0.16 ± 0.28	Q	1.70	NEW
2114+02	3.30 ^{+0.52} _{-0.45}	0.282 ^{+0.083} _{-0.066}	-1.34 ± 0.06	0.58 ± 0.07	Q		NEW
2124+64	0.72 ^{+0.01} _{-0.01}	2.316 ^{+0.005} _{-0.005}	-0.90 ± 0.10	0.47 ± 0.12	R		NEW
2126-15	7.12 ^{+0.10} _{-0.10}	1.388 ^{+0.017} _{-0.017}	-0.61 ± 0.02	0.73 ± 0.01	Q	3.28	2,3,6,7,8,11,13,18,34,36,L
2126-18	1.04 ^{+0.02} _{-0.02}	1.432 ^{+0.003} _{-0.003}	-0.90 ± 0.02	0.33 ± 0.06	Q	0.680	19
2128+04	0.59 ^{+0.01} _{-0.01}	4.694 ^{+0.007} _{-0.007}	-0.85 ± 0.01	1.07 ± 0.53	G	0.990	2,3,8,13,15,18,35g,L
2128-12	10.90 ^{+0.33} _{-0.23}	3.700 ^{+0.040} _{-0.039}	-0.59 ± 0.05	0.35 ± 0.01	Q	0.501	6
2134+00	6.19 ^{+0.01} _{-0.01}	9.913 ^{+0.024} _{-0.024}	-0.59 ± 0.02	1.29 ± 0.01	Q	1.932	1,2,3,6,9,11,13,30,31g,32,36
2136+14	8.13 ^{+0.10} _{-0.10}	2.155 ^{+0.016} _{-0.016}	-0.52 ± 0.02	0.42 ± 0.01	Q	2.427	30,31f
2145+08	1.18 ^{+0.09} _{-0.09}	0.517 ^{+0.006} _{-0.006}	-0.88 ± 0.05		Q	2.61	NEW
2145+07	0.72 ^{+0.02} _{-0.02}	0.469 ^{+0.005} _{-0.005}	-0.60 ± 0.01		R		NEW
2149+06	3.61 ^{+0.08} _{-0.08}	1.089 ^{+0.011} _{-0.011}	-0.49 ± 0.02	0.53 ± 0.02	Q	1.364	NEW
2149+05	3.45 ^{+0.05} _{-0.05}	0.886 ^{+0.008} _{-0.008}	-0.60 ± 0.01	0.56 ± 0.02	Q	0.740	3,5,8,15,18,25,35g,36,L
2201+09	4.58 ^{+0.24} _{-0.23}	0.311 ^{+0.026} _{-0.024}	-1.00 ± 0.05	0.95 ± 0.01	R		1,26,35g
2207+08	3.42 ^{+0.36} _{-0.48}	0.240 ^{+0.051} _{-0.042}	-0.89 ± 0.04	1.44 ± 0.36	R		NEW
2304-23	5.22 ^{+0.31} _{-0.29}	0.709 ^{+0.037} _{-0.035}	-0.73 ± 0.10	0.66 ± 0.01	R		36
2310+38	1.92 ^{+0.03} _{-0.03}	0.668 ^{+0.003} _{-0.003}	-0.62 ± 0.02	0.53 ± 0.01	Q	2.181	4
2314-34	3.91 ^{+0.26} _{-0.24}	0.723 ^{+0.053} _{-0.051}	-1.28 ± 0.05	1.06 ± 0.03	Q	3.100	NEW
2325-15	10.66 ^{+2.28} _{-1.88}	0.825 ^{+0.015} _{-0.015}	-0.58 ± 0.04	0.22 ± 0.01	Q	2.465	NEW
2328+31	1.12 ^{+0.01} _{-0.01}	1.179 ^{+0.001} _{-0.001}	-0.81 ± 0.01	0.66 ± 0.02	R		NEW
2337+26	2.58 ^{+0.03} _{-0.03}	1.140 ^{+0.006} _{-0.006}	-0.86 ± 0.01	0.61 ± 0.06	Q		L,3,8,15,18,35
2344-19	2.07 ^{+0.05} _{-0.05}	0.684 ^{+0.012} _{-0.012}	-0.63 ± 0.02	0.44 ± 0.03	R		NEW
2347+07	1.66 ^{+0.29} _{-0.25}	0.385 ^{+0.020} _{-0.019}	-0.72 ± 0.03		Q	1.70	NEW

IAU name	v_0	S_0	α_1	α_2	Type	z	GPS References
2351+55	$4.42^{+1.83}_{-1.29}$	$0.332^{+0.090}_{-0.071}$	-0.48 ± 0.06	0.44 ± 0.09	Q	1.927	4
2351-00	$3.18^{+0.11}_{-0.10}$	$0.435^{+0.009}_{-0.009}$	-0.51 ± 0.01	0.56 ± 0.02	Q	0.462	7
2352+49	$0.71^{+0.01}_{-0.01}$	$2.463^{+0.001}_{-0.001}$	-0.61 ± 0.01	0.43 ± 0.09	G	0.238	2,3,8,35g
2356+38	$6.03^{+3.65}_{-2.27}$	$0.668^{+1.162}_{-0.424}$	-0.64 ± 0.12	1.27 ± 0.22	Q	2.704	29
2357-31	$7.99^{+0.69}_{-0.64}$	$1.164^{+0.113}_{-0.103}$	-0.66 ± 0.19	0.84 ± 0.03	Q	0.991	NEW

GPS References:

1 Dallacasa et al. (2000), **2** O’Dea (1998), **3** Stanghellini et al. (1998), **4** Marecki et al. (1999), **5** Snellen et al. (2002), **6** Tornikoski et al. (2001), **7** Dallacasa et al. (1998), **8** de Vries et al. (1997), **9** Kovalev (2005), **10** Rossetti et al. (2003), **11** Edwards & Tingay (2004), **12** Xiang et al. (2006), **13** Stanghellini et al. (2001), **14** Snellen et al. (1995), **15** Gopal-Krishna et al. (1983), **16** Spoelstra et al. (1985), **17** Gopal-Krishna & Spoelstra (1993), **18** O’Dea et al. (1991), **19** Cersosimo et al. (1994), **20** Snellen et al. (1999), **21** O’Dea et al. (1990), **22** Stanghellini et al. (1990), **23** Becker et al. (1991), **24** Kuehr et al. (1981), **25** Wright & Otrupcek (1990), **26** Tinti et al. (2005), **27** Snellen et al. (1998b), **28** Snellen et al. (1998a), **29** Panajian (1998), **30** Kraus et al. (1968) **31** Tornainen et al. (2005) (31f - flat, 31g - genuine GPS source, 31c - convex spectra), **32** Lister et al. (2002), **33** de Vries et al. (2007), **34** Jauncey et al. (2003), **35** Tornainen et al. (2007) (35g - genuine GPS source, 35c - convex spectra, variable, 35f - flat, 35fs - flat at lower and steep at higher frequencies, 35n - possible GPS source but not enough data), **36** Vollmer et al. (2008a), **37** Bai & Lee (2005), **L** Labiano et al. (2007).

5.2 Parsec-scale properties of the RATAN-600 GPS sources derived from 2.3 and 8.6 GHz VLBI surveys

5.2.1 Morphological classification

We use publicly available⁵ 2.3 and 8.6 GHz VLBI data from the VLBA Calibrator Survey (VCS; Beasley et al. 2002; Fomalont et al. 2003; Kovalev et al. 2007; Petrov et al. 2005, 2006, 2008) and the Research and Development – VLBA (RDV; Petrov et al. (2009); Pushkarev & Kovalev (2008)) project to characterize pc-scale properties of 226 GPS sources from the RATAN–600 sample (Sokolovsky et al. 2009; Section 5.1). After a visual inspection of the naturally weighted CLEAN VLBI images at both frequencies we have divided the sources into three groups: 1) “core-jet/naked core” sources, 2) possible Compact Symmetric Objects (CSO) and 3) sources with complex pc-scale morphology.

Just 18 objects from our sample were classified as “complex”. There is an equal number of such complex parsec-scale structures among galaxies, quasars and “empty fields” - 6 in each of these classes. We found no information in the literature about VLBI observations of 13 objects from our sample.

There is no significant difference in the spectral index distributions (both, above and below the peak) between GPS sources with different morphological type. The distributions of the observed peak frequency of objects with “core-jet/naked core” and CSO-type morphology are significantly different (Fig. 5.10). KS-test gives probability $\sim 2 \times 10^{-5}$ that this two samples are drawn from the same parent distribution. Sources with the “core-jet/naked core” type morphology are characterized by, on average, higher peak frequency (median value = 3.5 GHz), then CSO type sources (median value = 1.9 GHz). This is expected since “core-jet” type sources should be more compact than CSO.

There is no statistically significant difference between the observed flux density of sources with different morphology. This does not support the conclusion by Xiang et al. (2005) that CSO objects are more frequently found among the bright sources than

⁵Compilation of publicly available VLBI data at <http://astrogeo.org/images/>

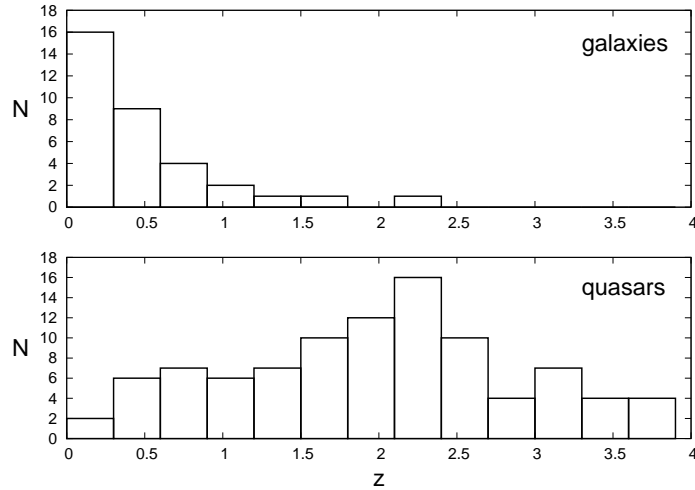


Figure 5.6: Redshift distribution of GPS galaxies and GPS quasars from the sample.

among the faint ones. This is, probably, a result of the selection method, by which CSO objects are found. In general, the strategy of search for CSO among GPS sources looks promising.

Contrary to expectation, 5 out of 32 CSO candidates, for which we have information about flux density variability at 11 GHz from RATAN–600 monitoring, were found significantly variable. They are B0711+35, B0738+31, B0839+18, B1404+28 and B2351–00. For three of them (B0711+35, B0738+31 and B2351–00) classification as CSO candidate is based only on X band images since at S band this sources are not resolved. It is likely that these three objects are not CSO, but “core–jet” sources with a single bright jet component. This can be confirmed by future VLBI observations which could construct the spectra of individual components, or detect a superluminal motion (which is not expected in a true CSO).

To further distinguish between true CSO and core-jet sources with two dominating components (a core and a jet feature), we have modeled the visibility data for all CSO candidates using *Difmap* package (Shepherd 1997) with two circular Gaussian components. We have selected sources which have two components detected at both 2.3 and 8.6 GHz images and constructed the spectral indices (between 2.3 and 8.6 GHz) for each component (Fig. 5.8a). The distribution of the difference between the spectral indices of two components of these sources is presented on Fig. 5.8b. Since two bright components of a CSO are expected to have close spectral indices⁶, we selected 24 sources with spectral index difference between two pc-scale components less than 0.5 as “highly probable CSO candidates”. Example of a newly identified GPS galaxy associated with a CSO is presented on Fig. 5.9.

Information about the optical identification for the sources was taken from Véron-Cetty & Véron (2006) and from the NASA/IPAC Extragalactic Database. We found, with a few exceptions, that CSOs are associated with GPS galaxies and core-jet sources are associated with GPS quasars. This is in good agreement with previous results (e.g., Stanghellini et al. 2001). The distributions of the observed peak frequency for GPS sources with different optical counterparts and with different pc-scale morphology are presented on Fig. 5.10.

⁶ $F_\nu \propto \nu^\alpha$

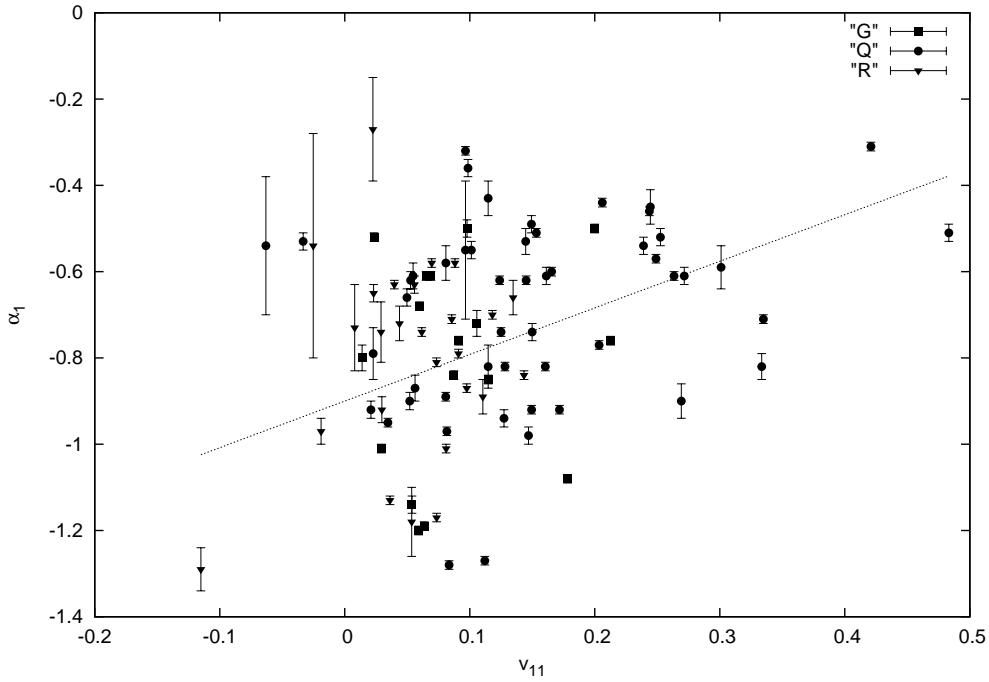
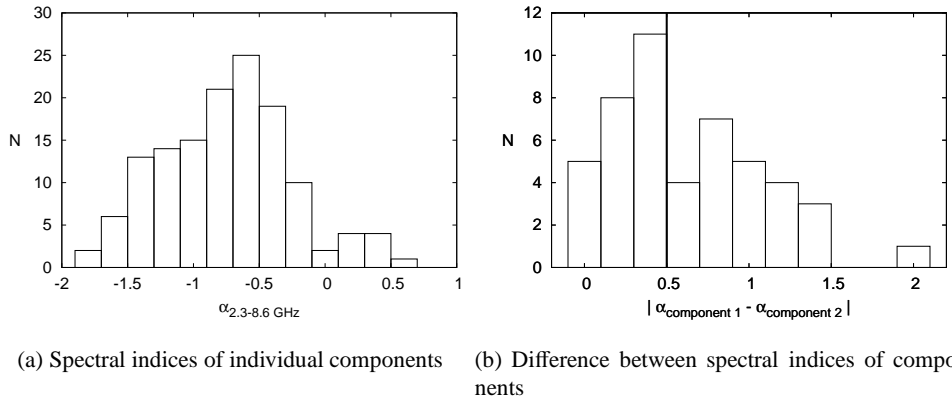


Figure 5.7: Relation between the variability index at 11 GHz v_{11} and the high-frequency spectral index α_1 for galaxies (G), quasars (Q) and unidentified radio sources (R). The line is a least square fit to the data: $\alpha_1 \approx 1.08(\pm 0.02) v_{11} - 0.90(\pm 0.002)$.



(a) Spectral indices of individual components (b) Difference between spectral indices of components

Figure 5.8: Distributions of 2.3–8.6 GHz spectral indices of VLBI components of CSO candidates.

5.2.2 VLBI-scale compactness

The degree, to which the radio source was resolved in a given VLBI experiment can be quantitatively characterized by the “compactness index” which is the ratio of correlated flux density at longest baselines to the total correlated flux density Kovalev et al. (2005). Compactness of an unresolved source equals to unity. If the source has no unresolved details, “compactness index” will be equal to zero.

Figure 5.11 shows the distributions of the “compactness index” for the RATAN–

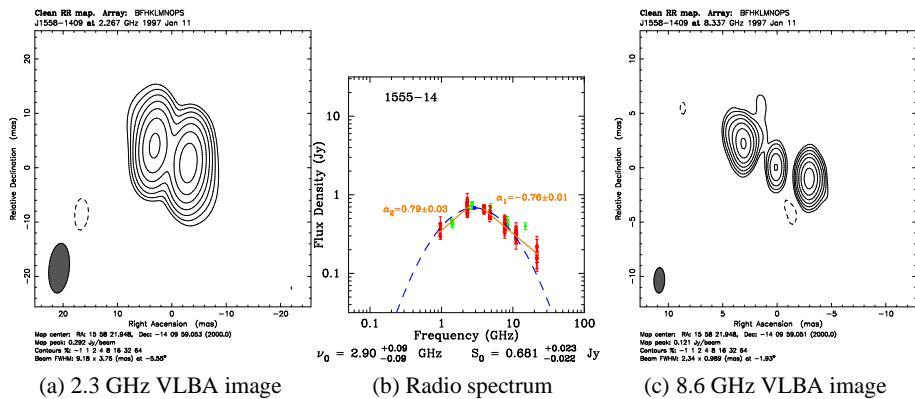


Figure 5.9: PKS 1555–140 – new GPS galaxy with CSO morphology at $z = 0.097$. Red points on the panel (b) denote RATAN–600 observations, green points represent literature data.

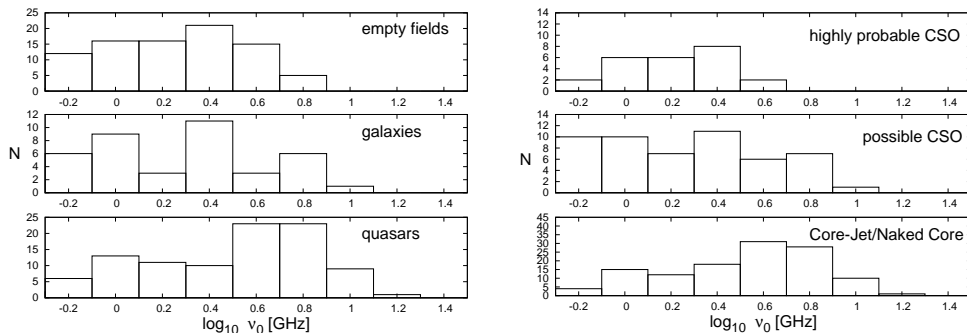


Figure 5.10: Observed peak frequency distribution for GPS sources with different optical identification and parsec-scale radio structure.

600 GPS sample (Fig. 5.11a) and for the complete sample of flat spectrum sources ($\alpha > -0.5$, Fig. 5.11b) based on VCS data. These distributions are significantly different. The GPS sources are, on average, more extended on mas-scale than most compact extragalactic radio sources. This also implies, that GPS sources (both, galaxies and quasars) form a distinct class of extragalactic radio sources, which really differs in its physical properties (the liner size) from other compact radio sources.

5.2.3 Magnetic field in the dominating source components

By combining the single-dish spectrum with VLBI angular size measurements we can estimate the magnetic field in pc-scale components of a radio source using simple synchrotron model (e.g., Marscher 1983; Slish 1963, see Section 1.3 for the detailed discussion). The VLBA calibrator survey data are available for 190 sources from the RATAN–600 GPS sample. In order to measure the angular size of dominating components in these sources, we have modeled the VCS visibility data at X band with one or two circular Gaussian components using the *Difmap* software (Shepherd et al. 1994). Circular Gaussian models were preferred to the elliptical ones in order to minimize the number of free parameters of the model. However, we have conducted the same mod-

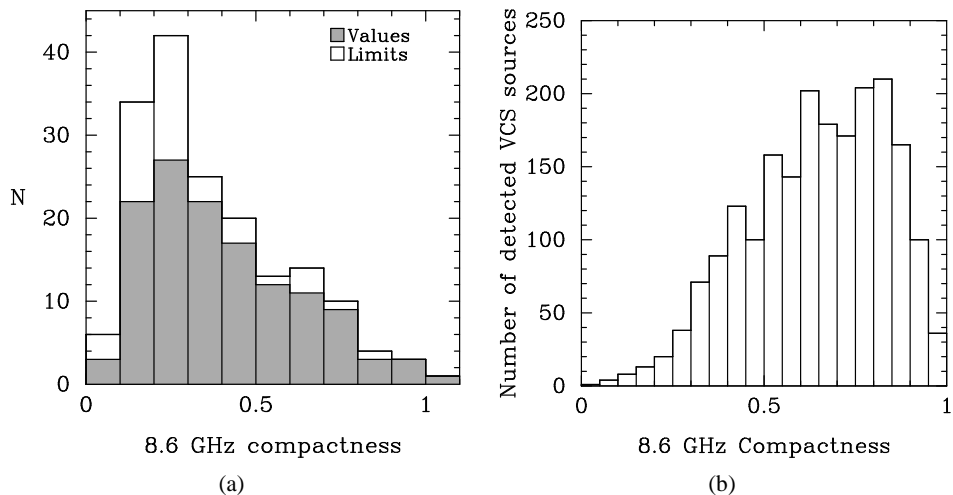


Figure 5.11: “Compactness index” for sources from the RATAN–600 GPS sample (a) and from the complete sample of flat spectrum sources (b).

eling with one or two elliptical Gaussian components an fond no systematic difference in the results. Derived FWHM size of each component was multiplied by 1.8 following Marscher (1983) to account for difference between the FWHM of a Gaussian fit and the diameter of a spherical component with the same total flux.

In the analysis we have used only the brightest component (if the source was modeled with two components), which was considered as resolved according to the criterion proposed by Kovalev et al. (2005); Lobanov (2005). In the optically thick regime, the measured source size is a function of frequency. To ensure that we measure the source in the optically thin part part of the spectrum, we have analyzed only sources with peak frequency below 4 GHz. Since we have no information about the Doppler factor, it was chosen to be $\delta = 1$.

The distribution of magnetic field estimated in the framework of the above model is presented of Fig. 5.12. For sources with unknown redshift (plotted as empty bars) we choose $z = 1$. The distributions of estimated magnetic field are significantly different for “core-jet” sources and CSO, but that only reflects the difference in the observed peak frequency distribution between these two subsamples (compare Fig. 5.12 to Fig. 5.10). We estimate the characteristic magnetic field in the pc-scale components of GPS sources to be $B \sim 10$ mG.

5.2.4 Summary

We have investigated the sample of 226 GPS sources selected from simultaneous multi-frequency 1–22 GHz observations obtained with RATAN–600 radio telescope. We use publicly available data to characterize parsec-scale structure of the selected sources. Among them we found 121 core dominated sources, 76 Compact Symmetric Object (CSO) candidates (24 of them are highly probable), 16 sources have complex parsec-scale morphology. Most of GPS galaxies are characterized by CSO-type morphology and lower observed peak frequency (~ 1.8 GHz). Most of GPS quasars are characterized by “core-jet”-type morphology and higher observed peak frequency (~ 3.6 GHz). This is in a good agreement with previous results. However, we found a number of sources for which the general relation CSO – galaxy, core-jet – quasar does not hold.

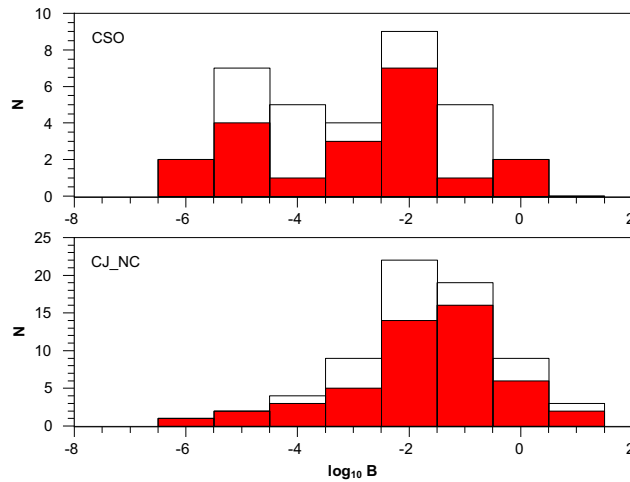


Figure 5.12: Distribution of estimated $\log_{10} B$ (G) for sources with different morphological types. Filled bars - sources with known redshift. Empty bars - sources with unknown redshift.

These sources deserve detailed investigation. Assuming simple synchrotron model of a homogeneous cloud we estimate characteristic magnetic field in parsec-scale components of GPS sources to be $B \sim 10$ mG.

5.3 A VLBI selected sample of Compact Symmetric Object candidates and frequency dependent position of hotspots

5.3.1 Introduction

The Compact Symmetric Objects (CSOs) are small (< 1 kiloparsec), powerful extragalactic radio sources which show emission on both sides of an active galactic nucleus (Readhead et al. 1996b; Wilkinson et al. 1994). In contrast to the majority of compact radio sources, relativistic beaming effects are believed to be small in CSOs due to their orientation close to the plane of the sky.⁷ The parsec-scale core which marks position of the central engine is often weak or not detected at all. Kinematic studies of CSOs reveal no superluminal motion and suggest source ages of the order of a few hundred to a few thousand years (Owsianik & Conway 1998; Polatidis 2009). CSOs may be progenitors of large-scale Fanaroff-Riley type II radio galaxies (Fanti et al. 1995; Perucho & Martí 2002; Readhead et al. 1996a). To draw solid conclusions about properties of CSOs as a class, it is important to construct a large representative sample of such objects.

An interesting side-effect of a large CSO candidate sample investigation is the possibility to find a supermassive binary black hole pair (Rodríguez et al. 2006; Tremblay et al. 2009) which can mimic a CSO. It has also been suggested that true CSOs are the likely hosts of supermassive black hole binaries (Willett et al. 2010).

⁷It is interesting to speculate how a CSO aligned with the line of sight would look like. The emission from such CSO would likely be dominated by the relativistically enhanced jet which would outshine hotspots and minilobes. Such object would probably be indistinguishable from an ordinary blazar.

Finally, CSOs may be useful as calibrators for continuum observations of other radio sources due to their stable flux density and low fractional polarization (Taylor & Peck 2003).

The largest homogeneously selected CSO sample to date is the COINS sample by Peck & Taylor (2000). An initial list of candidates for this sample was selected from Pearson & Readhead (1988) and Caltech–Jodrell Bank (Taylor et al. 1994) VLBI surveys and from the first VLBA Calibrator Survey Beasley et al. (2002). Dedicated multifrequency polarimetric VLBA observations of the candidates were performed to distinguish between true CSOs and contaminating core-jet type sources. The sample was further extended to the northern and southern extremities of the VLBA Calibrator Survey by Taylor & Peck (2003). Another CSO sample based on the VLBA Imaging and Polarization Survey is being constructed by Tremblay et al. (2009).

In this section we present a list of CSO candidates selected using publicly available⁸ 2 GHz (*S* band) and 8 GHz (*X* band) VLBI data collected in the course of the VLBA Calibrator Survey (VCS) 1 to 6 (Beasley et al. 2002; Fomalont et al. 2003; Kovalev et al. 2007; Petrov et al. 2005, 2006, 2008) and the Research and Development VLBA program (RDV; e.g., Fey & Charlot 1997; Fey et al. 1996; Petrov et al. 2009; Pushkarev & Kovalev 2008). We discuss basic properties of the compiled sample of candidates including an unexpected systematic difference in CSO component positions measured at the lower and higher frequencies and an attempt to reproduce this effect with detailed numerical modeling.

5.3.2 The VLBI-selected sample of CSO candidates and its basic characteristics

Among 4170 radio sources observed in the course of VCS and RDV VLBI experiments we have selected a list of 75 CSO candidates which meet the following criteria:

1. *S* and *X* band images show two dominating components of comparable brightness which are presumed to be hotspots on both sides of a two-sided jet.
2. Most of residual emission, if present, is located between the two brightest components — this emission may come from the core, mini-lobes or from the jet itself.

The second criterium is meant to distinguish CSO from sources with a bright core and one-sided jet showing a single jet component comparable in brightness to the core (see the images of 1458+718 in Fig. 4.1 for an example of such structure).

The list of selected sources is presented in Table 5.2. We have followed Fomalont (1999) to estimate errors of the model component parameters. The dual-frequency 2 and 8 GHz naturally weighted CLEAN images of the first three sources in the sample are shown in Fig. 5.13⁹. The lowest contour level is chosen at four times the image rms, plotted contour levels increase by a factors of two. The beam is shown in the bottom left corner of the images. Light blue and orange spots indicate Gaussian model components 1 and 2 from Table 5.2 respectively..

The information about broad-band radio spectra of the sources was obtained from the RATAN-600 multi-frequency 1–22 GHz survey (Kovalev et al. 2002, 1999a) and data from the literature collected by means of the CATS database (Verkhodanov et al.

⁸Find a compilation of publicly available VLBI data at <http://astrogeo.org/images/>

⁹The full version of Fig. 5.13 is available electronically at http://scan.sai.msu.ru/~kirx/data/images_of_cso_candidates_v01/

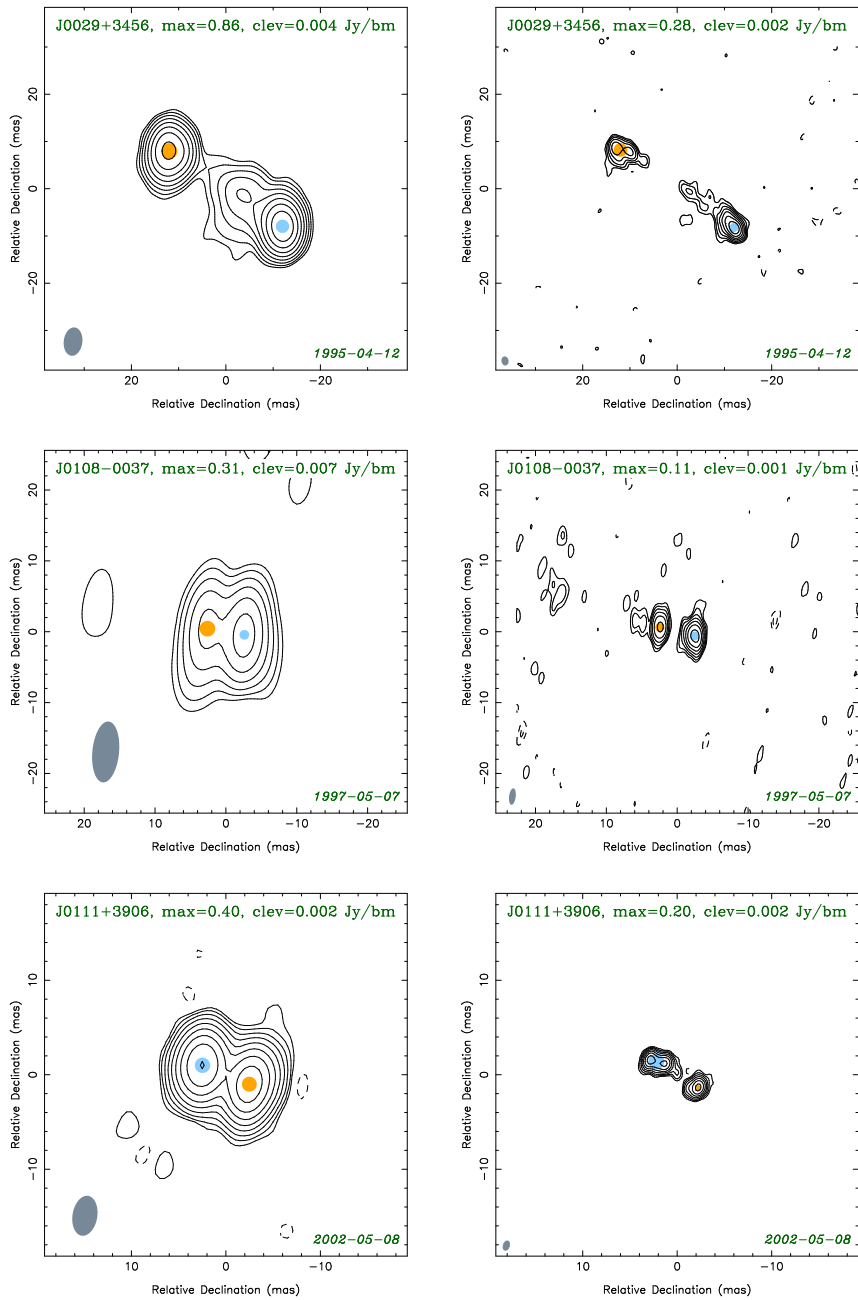


Figure 5.13: Dual-frequency simultaneous 2 and 8 GHz naturally weighted CLEAN images. The lowest contour value ‘clev’ is chosen at four times the rms level, the peak brightness is given by ‘max’ (Jy/beam). The contour levels increase by factors of two. The dashed contours indicate negative flux. The beam is shown in the bottom left corner of the images. An epoch of observation is shown in the bottom right corner. Light blue and orange spots indicate Gaussian model components 1 and 2 respectively.

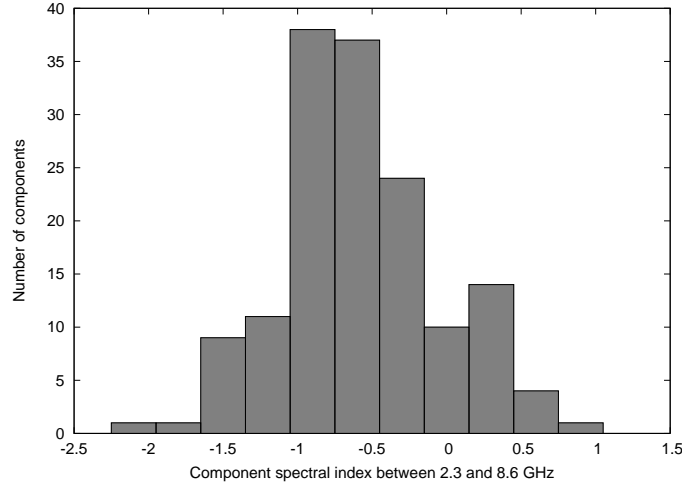


Figure 5.14: Spectral index, α , distribution (2 – 8 GHz) for bright CSO components ($F_\nu \propto \nu^\alpha$).

2005). Among the selected CSO candidates we identify 34 GHz–Peaked Spectrum (GPS) sources, 16 steep spectrum sources, 25 flat spectrum sources. For a discussion of GPS sources observed by RATAN-600 see Sokolovsky et al. (2009), and Sokolovsky & Kovalev (2008). We consider sources with peaked or steep spectra as the most promising CSO candidates.

Among 75 selected candidates, 13 are part of the COINS CSO sample (Peck & Taylor 2000) and three more sources are listed as rejected candidates for the COINS sample on the basis of their parsec-scale spectra and polarization properties. Two of them (0357+057, 1734+063) have flat single-dish spectra while the third source (0839+187) shows spectral peak at ~ 1.2 GHz. The latter source is an important example of a kind of GPS quasar with core-jet morphology which may contaminate CSO samples including the one presented in this paper.

Optical identifications and redshifts of 33 CSO candidates are available from the Véron-Cetty & Véron (2006) catalog: 24 of them are quasars, 7 are active galaxies and 2 are BL Lac type objects. Quasars are intrinsically brighter in optical band and therefore, they are more likely to be detected compared to radio galaxies (similar effect for GPS sources was reported by Sokolovsky et al. 2009). However, we expect that at least half of the CSO candidates presented in this paper are associated with quasars.

5.3.3 Properties of the dominating parsec-scale components

As described above, we have selected sources which show only two dominating components both at 2 and 8 GHz. We associate these components with hotspots at opposite ends of a two-sided jet. In order to quantify position, flux density and size of the hotspots, each source was modeled in the visibility plane by two circular Gaussian components using the *Difmap* software (Shepherd et al. 1994).

The distribution of the two-point simultaneous 2-8 GHz spectral index of the components is presented on Fig. 5.14. It shows values in the range from -2.0 to $+0.95$ with the median of -0.66 . It is evident that most of the observed components in the selected CSO candidates have spectral indexes not typical for flat-spectrum cores.

Similarity of broad-band spectra of parsec-scale features is expected to be one

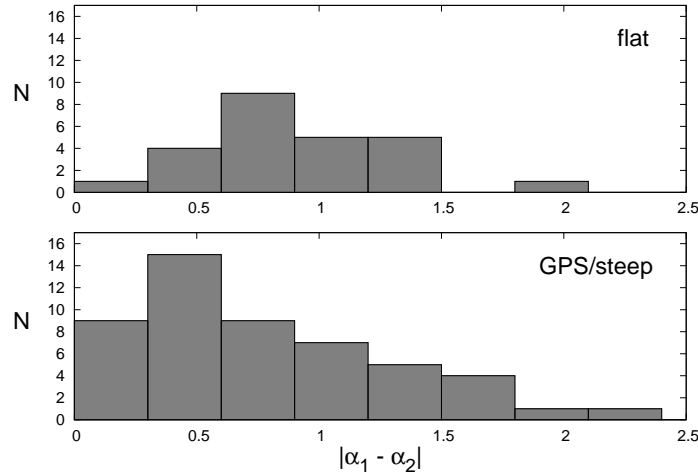


Figure 5.15: Absolute difference between 2-8 GHz spectral index of the components 1 and 2 for objects of different spectral type as presented in Table 5.2.

of the most important indications of a true CSO. To establish this similarity, multi-frequency VLBI follow-up observations of the selected sample of not-yet-confirmed CSO, similar to the study by Peck & Taylor (2000), are needed. Comparison of two-point simultaneous 2–8 GHz spectral indices available from our modeling is not sufficient. However, it may provide a hint on a probability for a source to be a true CSO, since majority of true CSO sources (e.g., from the COINS sample) are found to have similar 2–8 GHz spectral indices, α_1 and α_2 , for the two brightest parsec-scale components (Table 5.2). At the same time, a typical core-jet source is expected to show significantly different spectral indices (absolute difference about or greater than 0.7) due to the flat radio spectrum of the synchrotron self-absorbed core and steep-spectrum synchrotron radiation of optically thin jet features. Figure 5.15 presents a distribution of the absolute difference $|\alpha_1 - \alpha_2|$ of the indices for sources in our sample separated on the basis of their single-dish radio spectrum type — GPS/steep versus flat. Indeed, our assumption is confirmed. The median differences are 0.73 and 0.48 for the flat and GPS/steep sub-samples respectively. The Kolmogorov-Smirnov tests confirms that the distributions are different at the 96 % confidence level. Most of the core-jet sources — not true CSO — are expected to be found within the flat-spectrum sub-sample of the selected sample of CSO candidates.

We have also estimated the brightness temperature of the components at 8 GHz which is found to be typically $T_b \sim 10^9$ K in the observer’s frame (see Table 5.2 and Fig. 5.16) — systematically lower than the one measured in the parsec-scale cores of typical bright extragalactic Doppler-boosted core-jet sources (e.g., Kovalev et al. 2005; Pushkarev & Kovalev 2010).

5.3.4 Frequency dependent component position

Interestingly, we found that distances between the two dominating parsec-scale components are systematically larger when measured at 8 GHz than those measured at 2 GHz (see Fig. 5.17 for a distribution of these values). The mean difference is 0.44 ± 0.07 mas while the median value is 0.39 mas if all 75 CSO candidates are considered. We did not recalculate this value in the source frame since many sources in our sample have

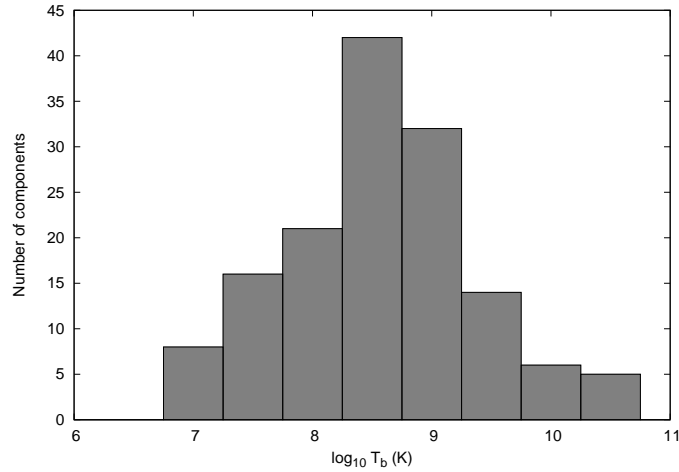


Figure 5.16: Brightness temperature distribution (measured at 8 GHz) for bright CSO components.

no redshift information available. The sign test (e.g., Mendenhall et al. 1989) confirms that the observed median difference is indeed greater than zero with a probability $> 99.99\%$. The sign test was chosen because it is a non-parametric test and makes very few assumptions about the nature of the distribution under investigation. Fig. 5.18 illustrates it as a function of component distance measured at 8 GHz for all CSO candidates, flat- and GPS/steep-spectrum candidates. The correlation analysis indicates a positive correlation between the 2/8 GHz distance difference and the distance measured at 8 GHz with the Pearson’s correlation coefficient $r = 0.33$ which corresponds to 99.57% probability of true correlation.

The observed frequency dependent difference in component positions could be trivially explained as the well known “core shift” effect (e.g., Kovalev et al. 2008b; Lobanov 1998b) if the presented sample of CSO candidates is heavily contaminated with core-jet type sources where one of the observed two bright components is actually a core instead of a hot spot. Spectral index of a component should be flat or inverted ($\alpha \geq 0$) if it is a core, so one may expect a positive correlation between α and the distance difference. However, no such correlation is observed. Also, no correlation was found between T_b and the observed distance difference. Moreover, most of the dominating parsec-scale features have steep spectral indices and relatively low brightness temperatures which is not typical for Doppler boosted opaque parsec-scale cores.

To further test the core shift possibility, we have divided the CSO candidates in two groups based on their single-dish radio spectra similar to the analysis presented in Fig. 5.15. The first group contained flat-spectrum sources which are more likely to be blazars with core-jet type morphology. The second group included sources with peaked and steep spectra which are more likely to be true CSO. For the flat-spectrum group the mean position difference was found to be 0.43 ± 0.08 , median value 0.33 with $> 99.99\%$ probability that the median value is greater than zero. For the GPS/steep spectrum group the mean difference is 0.44 ± 0.09 , the median value 0.39 with 99.8% probability of it being higher than zero. A Kolmogorov-Smirnov test cannot exclude the possibility that the frequency dependent position differences observed in flat-spectrum and GPS/steep-spectrum sources are drawn from the same parent distribution ($p = 65.2\%$). This implies that either most of the flat spectrum sources in the

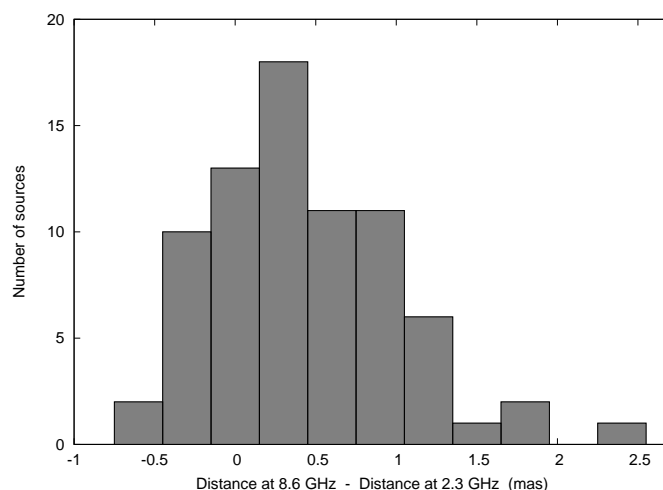


Figure 5.17: Difference in distances between two dominating source components measured at 2 and 8 GHz. The median value of the distribution is 0.39 which is significantly (99.9997 % probability according to the sign test) greater than zero.

presented sample are true CSOs, or most of the peaked/steep-spectrum ones are in fact core-jet sources (which seems unlikely), or this is an, e.g., observational effect which affects both CSO and core-jet sources in a similar way.

It is widely accepted (e.g., Ostorero et al. 2010; Stanghellini et al. 1997b) that CSOs are often found among GPS sources identified with galaxies (as opposed to blazars). In the presented sample of CSO candidates there are only five GPS sources associated with galaxies which is not enough for a statistical analysis. However, we note that among these five sources (which should be considered the best CSO candidates), four have a positive difference between component distances measured at 8 and 2 GHz.

Overall, it seems highly unlikely that the systematic difference in component positions at 2 and 8 GHz in the selected sources can be attributed to the core shift effect in core-jet type sources contaminating the CSO candidate sample. Intrigued by the observed effect, Sokolovsky et al. (2010c) have turned to detailed numerical modeling in search for an explanation.

5.3.5 Summary

We have selected a sample of 75 candidate compact symmetric objects using simultaneous 2 and 8 GHz VLBI data for 4170 extragalactic radio sources from VLBA Calibrator Survey and Research and Development VLBA projects. Among the candidates we have identified 34 GPS, 16 steep-spectrum, and 25 flat-spectrum radio sources. The median two-point 2-8 GHz spectral index for dominating parsec-scale components is found to be -0.66 while median brightness temperature is of an order of 10^9 K. A multi-frequency follow-up VLBI study of the whole selected sample is necessary to confirm true CSO cases.

A systematic difference in distance measured at 2 and 8 GHz between the outer CSO components (presumed to be associated with hotspots) was detected. The 8 GHz distance is found to be larger for most sources. Even if some CSO candidates are misclassified and have a core-jet parsec-scale morphology, our analysis rules out the apparent frequency dependent shift of the core position as the cause of the observed

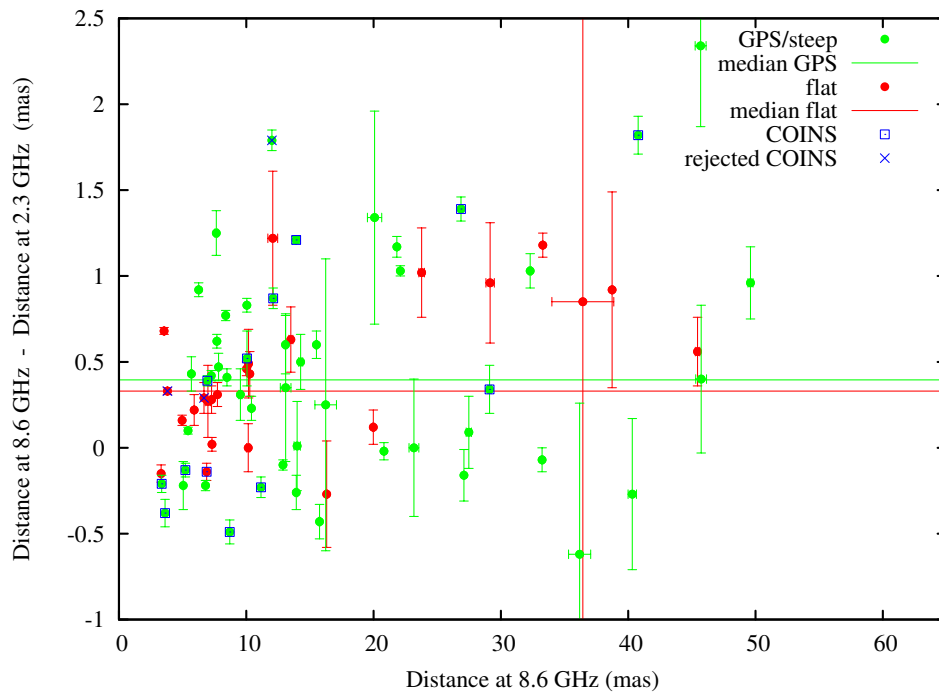


Figure 5.18: Difference in distances between two dominating source components measured at 2 and 8 GHz as a function of distance measured at 8 GHz. Green points represent GPS and steep spectrum sources, red points represent flat spectrum sources. Objects included in the COINS sample are marked with blue triangles, while objects rejected from the COINS sample as probable core-jet sources are marked with blue crosses. The green line marks the median distance difference for GPS/steep spectrum sources, the red line marks the same for flat spectrum sources.

effect. Two possible mechanisms responsible for the observed effect are suggested: the “physical” mechanism related to particle acceleration in a shock wave associated with the hotspot and the “observational” resulting from a different amount of blending between the compact hotspot and extended jet structures due to different angular resolution at different frequencies. A numerical modeling of a CSO hotspot was conducted by Sokolovsky et al. (2010c) but failed to reproduce the magnitude of the observed difference with the above scenarios. However, the model suggested the observational blending effect as the dominating mechanism responsible for the position difference. A more detailed modeling and dedicated simultaneous multifrequency VLBI observations are needed to determine exact origin of the hotspot position difference effect.

Table 5.2: List of CSO candidates selected from VCS and RDV surveys

Name ^I	Comp. ^{II}	F _S ^{III} (Jy)	F _X ^{III} (Jy)	α ^{IV}	R _X ^{V,XII} (mas)	T _{b,X} ^{VI,XII} (K)	D _X ^{VII} (mas)	D _X - D _S ^{VIII} (mas)	opt. ^{IX}	z ^X	Comments ^{XI}
J0029+3456	1	1.181 ± 0.129	0.595 ± 0.086	-0.52	1.88 ± 0.04	4.1 × 10 ⁸	29.11 ± 0.13	0.34 ± 0.14	a	0.517	COINS, GPS $v_m=1.41$
	2	0.846 ± 0.112	0.229 ± 0.068	-0.99	2.88 ± 0.26	6.7 × 10 ⁷					
J0108-0037	1	0.335 ± 0.064	0.222 ± 0.032	-0.31	1.26 ± 0.03	3.4 × 10 ⁸	5.05 ± 0.04	-0.22 ± 0.14	q	1.378	STEEP
	2	0.170 ± 0.046	0.096 ± 0.021	-0.44	1.27 ± 0.07	1.4 × 10 ⁸					
J0111+3906	1	0.496 ± 0.030	0.572 ± 0.112	+0.11	1.67 ± 0.07	5.0 × 10 ⁸	5.22 ± 0.04	-0.13 ± 0.04	COINS, GPS $v_m=4.64$
	2	0.400 ± 0.027	0.254 ± 0.052	-0.35	0.56 ± 0.03	1.9 × 10 ⁹					
J0127+7323	1	0.266 ± 0.030	0.096 ± 0.019	-0.78	1.51 ± 0.08	1.0 × 10 ⁸	14.00 ± 0.25	0.01 ± 0.26	GPS ^{XIII,XIV}
	2	0.110 ± 0.021	0.013 ± 0.008	-1.59	1.25 ± 0.49	> 2.1 × 10 ⁷					
J0132+5620	1	0.460 ± 0.045	0.290 ± 0.033	-0.35	0.51 ± 0.01	2.7 × 10 ⁹	12.11 ± 0.05	0.87 ± 0.06	COINS, GPS $v_m=3.01$
	2	0.381 ± 0.041	0.039 ± 0.013	-1.72	0.87 ± 0.10	1.2 × 10 ⁸					
J0207+6246	1	1.114 ± 0.099	0.645 ± 0.056	-0.41	0.73 ± 0.01	2.9 × 10 ⁹	21.83 ± 0.05	1.17 ± 0.06	GPS $v_m=2.50$
	2	0.328 ± 0.054	0.058 ± 0.017	-1.31	0.85 ± 0.09	1.9 × 10 ⁸					
J0209+2932	1	0.363 ± 0.040	0.115 ± 0.024	-0.87	1.44 ± 0.07	1.3 × 10 ⁸	7.82 ± 0.05	0.47 ± 0.08	q	2.195	STEEP
	2	0.101 ± 0.021	0.063 ± 0.016	-0.36	0.73 ± 0.06	2.8 × 10 ⁸					
J0304+7727	1	0.321 ± 0.034	0.123 ± 0.022	-0.73	0.79 ± 0.03	4.8 × 10 ⁸	10.41 ± 0.06	0.23 ± 0.07	GPS ^{XIII,XVI}
	2	0.489 ± 0.041	0.117 ± 0.027	-1.08	2.16 ± 0.12	6.1 × 10 ⁷					
J0400+0550	1	0.345 ± 0.046	0.361 ± 0.038	+0.03	0.38 ± 0.01	6.0 × 10 ⁹	6.68 ± 0.03	0.29 ± 0.09	q	0.761	COINS-REJ, FLAT
	2	0.112 ± 0.026	0.068 ± 0.017	-0.38	0.78 ± 0.06	2.7 × 10 ⁸					
J0424+0204	1	0.463 ± 0.073	0.494 ± 0.047	+0.05	0.34 ± 0.01	1.0 × 10 ¹⁰	15.51 ± 0.07	0.60 ± 0.08	q	2.056	STEEP
	2	0.510 ± 0.077	0.035 ± 0.013	-2.03	0.80 ± 0.13	1.3 × 10 ⁸					
J0429+3319	1	0.449 ± 0.030	0.271 ± 0.034	-0.38	0.70 ± 0.01	1.3 × 10 ⁹	7.25 ± 0.02	0.42 ± 0.03	STEEP
	2	0.150 ± 0.017	0.079 ± 0.018	-0.49	0.41 ± 0.04	1.1 × 10 ⁹					
J0440-4333	1	1.228 ± 0.189	1.809 ± 0.195	+0.29	0.33 ± 0.01	4.0 × 10 ¹⁰	36.44 ± 2.43	0.85 ± 2.43	q	2.852	FLAT
	2	1.065 ± 0.221	0.278 ± 0.326	-1.02	6.12 ± 4.85	1.8 × 10 ⁷					
J0511+0110	1	0.133 ± 0.028	0.168 ± 0.026	+0.17	0.64 ± 0.02	9.8 × 10 ⁸	23.77 ± 0.22	1.02 ± 0.26	FLAT
	2	0.098 ± 0.025	0.039 ± 0.018	-0.71	2.14 ± 0.45	2.0 × 10 ⁷					
J0518+4730	1	0.556 ± 0.042	0.156 ± 0.035	-0.96	1.22 ± 0.07	2.5 × 10 ⁸	3.36 ± 0.04	-0.21 ± 0.05	COINS, GPS $v_m=2.17$
	2	0.382 ± 0.034	0.134 ± 0.031	-0.79	0.82 ± 0.05	4.8 × 10 ⁸					

J0620+2102	1	0.433 ± 0.060	0.158 ± 0.027	-0.77	0.77 ± 0.03	6.5×10^8	26.87 ± 0.05	1.39 ± 0.07	COINS, GPS $v_m=1.51$
	2	0.375 ± 0.056	0.082 ± 0.021	-1.16	1.24 ± 0.09	1.3×10^8					
J0736+2604	1	0.107 ± 0.026	0.237 ± 0.025	+0.61	0.18 ± 0.01	1.8×10^{10}	5.91 ± 0.02	0.22 ± 0.09	FLAT
	2	0.188 ± 0.034	0.073 ± 0.014	-0.72	0.59 ± 0.03	5.1×10^8					
J0753+4231	1	0.235 ± 0.036	0.199 ± 0.022	-0.13	0.49 ± 0.01	2.0×10^9	8.70 ± 0.06	-0.49 ± 0.07	q	3.59	COINS, GPS $v_m=1.01$
	2	0.465 ± 0.051	0.072 ± 0.018	-1.42	1.85 ± 0.12	5.1×10^7					
J0814-1806	1	0.225 ± 0.028	0.110 ± 0.027	-0.54	1.73 ± 0.13	8.9×10^7	23.17 ± 0.39	-0.00 ± 0.40	STEEP
	2	0.105 ± 0.019	0.018 ± 0.012	-1.32	2.28 ± 0.77	$> 8.5 \times 10^6$					
J0821-0323	1	0.343 ± 0.048	0.118 ± 0.026	-0.81	0.95 ± 0.05	3.2×10^8	5.69 ± 0.05	0.43 ± 0.10	q	2.352	GPS $v_m=1.46$
	2	0.134 ± 0.030	0.058 ± 0.018	-0.63	0.69 ± 0.08	2.9×10^8					
J0842+1835	1	0.506 ± 0.063	0.371 ± 0.057	-0.24	0.46 ± 0.01	4.2×10^9	12.01 ± 0.05	1.79 ± 0.06	q	1.272	COINS-REJ, GPS $v_m=1.17$
	2	0.381 ± 0.055	0.093 ± 0.032	-1.07	0.84 ± 0.10	3.2×10^8					
J0932+6507	1	0.154 ± 0.038	0.124 ± 0.022	-0.16	0.50 ± 0.03	1.2×10^9	40.32 ± 0.33	-0.27 ± 0.44	STEEP
	2	0.178 ± 0.053	0.028 ± 0.016	-1.41	2.20 ± 0.66	1.4×10^7					
J0935+3633	1	0.092 ± 0.014	0.121 ± 0.015	+0.21	0.45 ± 0.01	1.4×10^9	4.96 ± 0.01	0.16 ± 0.03	q	2.835	FLAT
	2	0.212 ± 0.021	0.076 ± 0.012	-0.78	0.60 ± 0.02	5.1×10^8					
J1008-0933	1	0.507 ± 0.039	0.212 ± 0.025	-0.66	0.97 ± 0.02	5.5×10^8	7.73 ± 0.02	0.31 ± 0.07	FLAT
	2	0.061 ± 0.014	0.067 ± 0.014	+0.07	0.41 ± 0.03	9.6×10^8					
J1035+5040	1	0.234 ± 0.022	0.129 ± 0.018	-0.45	0.55 ± 0.02	1.0×10^9	10.15 ± 0.13	0.00 ± 0.14	FLAT, GPS-REJ
	2	0.099 ± 0.015	0.032 ± 0.012	-0.86	1.89 ± 0.27	2.1×10^7					
J1035+5628	1	0.913 ± 0.124	0.383 ± 0.065	-0.66	1.45 ± 0.05	4.4×10^8	32.30 ± 0.09	1.03 ± 0.10	a	0.460	GPS $v_m=1.08$
	2	0.846 ± 0.121	0.268 ± 0.071	-0.87	2.31 ± 0.16	1.2×10^8					
J1036-0605	1	0.146 ± 0.018	0.271 ± 0.028	+0.47	0.64 ± 0.01	1.6×10^9	8.38 ± 0.02	0.77 ± 0.03	GPS $v_m=4.50$
	2	0.305 ± 0.026	0.091 ± 0.017	-0.91	0.71 ± 0.03	4.4×10^8					
J1110-1858	1	0.719 ± 0.058	0.183 ± 0.029	-1.04	1.46 ± 0.04	2.1×10^8	15.75 ± 0.07	-0.43 ± 0.10	a	0.497	STEEP, GPS-REJ
	2	0.146 ± 0.026	0.057 ± 0.016	-0.71	1.41 ± 0.13	6.9×10^7					
J1143+1834	1	0.189 ± 0.024	0.101 ± 0.024	-0.48	0.44 ± 0.05	1.3×10^9	6.89 ± 0.04	-0.14 ± 0.05	COINS, FLAT
	2	0.166 ± 0.022	0.086 ± 0.022	-0.50	0.51 ± 0.06	7.9×10^8					
J1207+2754	1	0.504 ± 0.064	0.334 ± 0.031	-0.31	0.39 ± 0.01	5.3×10^9	10.18 ± 0.18	0.49 ± 0.20	q	2.177	FLAT
	2	0.202 ± 0.042	0.043 ± 0.017	-1.17	2.29 ± 0.35	2.0×10^7					
J1213-1003	1	0.120 ± 0.022	0.213 ± 0.019	+0.44	0.19 ± 0.01	1.4×10^{10}	7.27 ± 0.05	0.28 ± 0.08	b	FLAT

	2	0.182 ± 0.027	0.075 ± 0.015	-0.68	2.19 ± 0.10	3.8×10^7						
J1224+0330	1	0.262 ± 0.027	0.368 ± 0.035	+0.26	0.20 ± 0.01	2.3×10^{10}	3.54 ± 0.01	0.68 ± 0.02	q	0.960	FLAT	
	2	1.021 ± 0.053	0.284 ± 0.031	-0.97	0.87 ± 0.01	9.1×10^8						
J1247+6723	1	0.147 ± 0.016	0.091 ± 0.016	-0.36	0.85 ± 0.03	3.0×10^8	7.69 ± 0.03	0.62 ± 0.04	GPS	
	2	0.104 ± 0.014	0.047 ± 0.011	-0.60	0.68 ± 0.05	2.5×10^8						
J1248-1959	1	1.334 ± 0.274	0.488 ± 0.144	-0.76	2.80 ± 0.25	1.5×10^8	20.08 ± 0.56	1.34 ± 0.62	q	1.275	STEEP	
	2	0.789 ± 0.227	0.381 ± 0.202	-0.55	4.57 ± 1.09	4.4×10^7						
J1259+5140	1	0.113 ± 0.020	0.396 ± 0.027	+0.95	0.15 ± 0.00	4.3×10^{10}	19.98 ± 0.05	0.12 ± 0.10	FLAT	
	2	0.069 ± 0.016	0.019 ± 0.006	-0.96	0.85 ± 0.10	6.5×10^7						
J1302+6902	1	0.122 ± 0.032	0.151 ± 0.021	+0.16	0.42 ± 0.01	2.1×10^9	16.32 ± 0.07	-0.27 ± 0.31	a	0.57	FLAT	
	2	0.043 ± 0.019	0.021 ± 0.008	-0.55	0.84 ± 0.15	7.3×10^7						
J1311+1417	1	0.727 ± 0.079	0.139 ± 0.025	-1.25	1.06 ± 0.04	3.0×10^8	3.62 ± 0.03	-0.38 ± 0.08	q	1.952	COINS, GPS $v_m=1.17$	
	2	0.148 ± 0.035	0.101 ± 0.021	-0.29	0.79 ± 0.04	3.9×10^8						
J1319-0049	1	0.245 ± 0.039	0.208 ± 0.028	-0.13	0.57 ± 0.02	1.5×10^9	45.73 ± 0.42	0.40 ± 0.43	q	0.892	STEEP	
	2	0.156 ± 0.032	0.046 ± 0.025	-0.92	3.27 ± 0.83	1.1×10^7						
J1320+0140	1	0.258 ± 0.039	0.330 ± 0.037	+0.19	0.35 ± 0.01	6.4×10^9	29.16 ± 0.33	0.96 ± 0.35	q	1.232	FLAT	
	2	0.202 ± 0.038	0.098 ± 0.044	-0.55	3.71 ± 0.66	1.7×10^7						
J1324+4048	1	0.367 ± 0.029	0.126 ± 0.017	-0.81	0.62 ± 0.02	7.9×10^8	5.42 ± 0.01	0.10 ± 0.02	q	0.495	GPS $v_m=2.79$	
	2	0.282 ± 0.026	0.118 ± 0.016	-0.66	0.59 ± 0.02	8.2×10^8						
J1335+5844	1	0.199 ± 0.027	0.432 ± 0.040	+0.59	0.43 ± 0.01	5.5×10^9	12.88 ± 0.02	-0.10 ± 0.03	GPS $v_m=6.45$	
	2	0.493 ± 0.043	0.171 ± 0.027	-0.80	1.17 ± 0.03	3.0×10^8						
J1350-2204	1	0.527 ± 0.050	0.191 ± 0.026	-0.77	1.02 ± 0.02	4.4×10^8	27.48 ± 0.21	0.09 ± 0.21	GPS $v_m=0.65$	
	2	0.401 ± 0.045	0.056 ± 0.022	-1.50	2.66 ± 0.41	1.9×10^7						
J1357+4353	1	0.431 ± 0.043	0.227 ± 0.033	-0.49	1.94 ± 0.04	1.5×10^8	11.16 ± 0.04	-0.23 ± 0.06	COINS, GPS $v_m=1.75$	
	2	0.294 ± 0.037	0.105 ± 0.021	-0.78	1.73 ± 0.08	8.4×10^7						
J1358+4737	1	0.453 ± 0.029	0.166 ± 0.024	-0.76	1.02 ± 0.03	3.9×10^8	6.26 ± 0.03	0.92 ± 0.04	a	0.230	GPS $v_m=2.41$	
	2	0.156 ± 0.017	0.056 ± 0.014	-0.78	0.64 ± 0.05	3.3×10^8						
J1443+6332	1	0.192 ± 0.029	0.320 ± 0.028	+0.39	0.24 ± 0.01	1.3×10^{10}	8.48 ± 0.04	0.41 ± 0.05	q	1.380	GPS $v_m=1.53$	
	2	0.536 ± 0.048	0.068 ± 0.016	-1.57	1.49 ± 0.09	7.4×10^7						
J1451+1343	1	0.186 ± 0.048	0.077 ± 0.016	-0.66	0.47 ± 0.04	8.4×10^8	27.10 ± 0.03	-0.16 ± 0.15	STEEP	
	2	0.231 ± 0.055	0.073 ± 0.016	-0.87	0.93 ± 0.06	2.1×10^8						

J1503+0917	1	0.337 ± 0.035	0.185 ± 0.023	-0.45	0.89 ± 0.02	5.7×10^8	13.08 ± 0.10	0.60 ± 0.17	STEEP
	2	0.071 ± 0.017	0.009 ± 0.005	-1.56	0.77 ± 0.20	$> 3.7 \times 10^7$					
J1543-0757	1	1.080 ± 0.159	0.487 ± 0.138	-0.60	4.36 ± 0.34	6.2×10^7	45.69 ± 0.43	2.34 ± 0.47	GPS $v_m=0.72$
	2	0.439 ± 0.107	0.130 ± 0.064	-0.92	3.60 ± 0.78	2.4×10^7					
J1558-1409	1	0.309 ± 0.033	0.156 ± 0.021	-0.52	0.64 ± 0.02	9.4×10^8	6.80 ± 0.01	-0.22 ± 0.03	a	0.097	GPS $v_m=2.39$
	2	0.227 ± 0.028	0.136 ± 0.019	-0.39	0.80 ± 0.02	5.1×10^8					
J1602+2418	1	0.068 ± 0.010	0.093 ± 0.013	+0.24	0.55 ± 0.02	7.4×10^8	7.30 ± 0.02	0.02 ± 0.04	FLAT
	2	0.174 ± 0.016	0.068 ± 0.012	-0.72	0.94 ± 0.03	1.8×10^8					
J1609+2641	1	2.180 ± 0.305	0.406 ± 0.059	-1.27	1.18 ± 0.03	7.1×10^8	49.61 ± 0.20	0.96 ± 0.21	GPS $v_m=0.83$
	2	1.734 ± 0.284	0.284 ± 0.096	-1.37	3.58 ± 0.39	5.3×10^7					
J1656-0206	1	0.090 ± 0.025	0.190 ± 0.027	+0.56	0.36 ± 0.02	3.5×10^9	36.19 ± 0.87	-0.62 ± 0.88	q	2.00	STEEP
	2	0.365 ± 0.052	0.113 ± 0.069	-0.89	5.77 ± 1.73	8.2×10^6					
J1734+0926	1	0.902 ± 0.059	0.305 ± 0.040	-0.82	0.99 ± 0.02	7.4×10^8	13.92 ± 0.02	1.21 ± 0.02	COINS, GPS $v_m=2.18$
	2	0.637 ± 0.049	0.196 ± 0.032	-0.90	1.06 ± 0.03	4.2×10^8					
J1737+0621	1	0.819 ± 0.062	0.701 ± 0.051	-0.12	0.35 ± 0.00	1.4×10^{10}	3.81 ± 0.02	0.33 ± 0.02	q	1.207	COINS-REJ, FLAT
	2	0.524 ± 0.050	0.177 ± 0.029	-0.82	1.31 ± 0.04	2.5×10^8					
J1742-1517	1	0.064 ± 0.039	0.109 ± 0.015	+0.40	0.20 ± 0.01	$> 6.7 \times 10^9$	38.74 ± 0.06	0.92 ± 0.57	FLAT ^{XIII.XVI}
	2	0.143 ± 0.057	0.058 ± 0.014	-0.69	1.93 ± 0.12	3.7×10^7					
J1819-0258	1	0.885 ± 0.077	0.354 ± 0.071	-0.70	1.98 ± 0.09	2.2×10^8	16.24 ± 0.85	0.25 ± 0.85	GPS $v_m=1.51$
	2	0.833 ± 0.079	0.247 ± 0.148	-0.92	5.91 ± 1.70	1.7×10^7					
J1921+4333	1	0.110 ± 0.014	0.114 ± 0.019	+0.03	1.24 ± 0.04	1.8×10^8	3.31 ± 0.04	-0.15 ± 0.05	FLAT
	2	0.152 ± 0.017	0.084 ± 0.017	-0.45	1.39 ± 0.06	1.1×10^8					
J1929+0507	1	0.194 ± 0.036	0.107 ± 0.023	-0.45	0.42 ± 0.04	1.4×10^9	12.08 ± 0.38	1.22 ± 0.39	FLAT
	2	0.247 ± 0.039	0.062 ± 0.033	-1.05	3.10 ± 0.75	1.6×10^7					
J1933+1504	1	0.143 ± 0.024	0.095 ± 0.024	-0.32	0.46 ± 0.05	1.1×10^9	7.65 ± 0.11	1.25 ± 0.13	STEEP
	2	0.224 ± 0.030	0.031 ± 0.015	-1.50	0.82 ± 0.21	$> 1.1 \times 10^8$					
J1935-1602	1	0.202 ± 0.030	0.137 ± 0.021	-0.29	0.33 ± 0.02	3.0×10^9	10.28 ± 0.02	0.43 ± 0.13	q	1.460	FLAT
	2	0.069 ± 0.018	0.118 ± 0.020	+0.41	0.92 ± 0.03	3.3×10^8					
J1935+8130	1	0.355 ± 0.034	0.142 ± 0.025	-0.69	0.64 ± 0.03	8.3×10^8	10.05 ± 0.03	0.83 ± 0.04	GPS $v_m=3.41$
	2	0.181 ± 0.024	0.083 ± 0.019	-0.59	0.57 ± 0.04	6.2×10^8					
J1944+5448	1	1.019 ± 0.152	0.309 ± 0.051	-0.90	1.03 ± 0.03	7.1×10^8	40.78 ± 0.05	1.82 ± 0.11	COINS, GPS $v_m=1.06$

	2	0.448 ± 0.098	0.100 ± 0.029	-1.14	0.90 ± 0.09	3.0×10^8						
J1950+0807	1	0.904 ± 0.087	0.474 ± 0.045	-0.49	0.52 ± 0.01	4.2×10^9	22.10 ± 0.01	1.03 ± 0.03	GPS $v_m=2.43$	
	2	0.658 ± 0.074	0.215 ± 0.031	-0.85	0.71 ± 0.02	1.0×10^9						
J1951+5727	1	0.341 ± 0.043	0.176 ± 0.027	-0.50	1.01 ± 0.03	4.2×10^8	13.09 ± 0.42	0.35 ± 0.43	q	0.652	STEEP	
	2	0.117 ± 0.026	0.027 ± 0.017	-1.12	2.51 ± 0.84	1.0×10^7						
J2022+6136	1	1.244 ± 0.140	2.132 ± 0.129	+0.41	0.54 ± 0.00	1.8×10^{10}	6.94 ± 0.00	0.39 ± 0.03	a	0.227	COINS, GPS $v_m=5.91$	
	2	1.489 ± 0.152	0.852 ± 0.082	-0.42	0.62 ± 0.01	5.3×10^9						
J2120+6642	1	0.166 ± 0.019	0.094 ± 0.016	-0.43	0.58 ± 0.02	6.7×10^8	10.02 ± 0.02	0.46 ± 0.04	FLAT	
	2	0.119 ± 0.016	0.051 ± 0.012	-0.64	0.50 ± 0.04	4.9×10^8						
J2123+1007	1	0.446 ± 0.048	0.119 ± 0.033	-1.00	3.21 ± 0.24	2.8×10^7	9.54 ± 0.12	0.31 ± 0.15	q	0.932	STEEP	
	2	0.095 ± 0.022	0.117 ± 0.020	+0.16	0.41 ± 0.03	1.7×10^9						
J2131+8430	1	0.341 ± 0.036	0.131 ± 0.018	-0.72	0.71 ± 0.02	6.3×10^8	13.93 ± 0.09	-0.26 ± 0.10	STEEP ^{XIII,XVI}	
	2	0.222 ± 0.029	0.034 ± 0.011	-1.41	1.81 ± 0.18	2.5×10^7						
J2137+3455	1	0.211 ± 0.028	0.084 ± 0.019	-0.70	0.71 ± 0.06	4.0×10^8	6.99 ± 0.21	0.27 ± 0.21	FLAT	
	2	0.125 ± 0.022	0.031 ± 0.014	-1.06	2.11 ± 0.41	1.7×10^7						
J2203+1007	1	0.156 ± 0.032	0.146 ± 0.026	-0.05	0.99 ± 0.04	3.6×10^8	10.06 ± 0.07	0.52 ± 0.16	COINS, GPS $v_m=4.58$	
	2	0.115 ± 0.027	0.055 ± 0.017	-0.56	1.27 ± 0.13	8.2×10^7						
J2253+0236	1	0.196 ± 0.020	0.090 ± 0.017	-0.59	0.79 ± 0.04	3.5×10^8	33.29 ± 0.03	1.18 ± 0.07	FLAT	
	2	0.047 ± 0.010	0.061 ± 0.014	+0.19	0.50 ± 0.05	$> 5.9 \times 10^8$						
J2254+0054	1	0.214 ± 0.041	0.199 ± 0.026	-0.06	0.41 ± 0.01	2.8×10^9	13.50 ± 0.16	0.63 ± 0.19	b	FLAT	
	2	0.188 ± 0.039	0.087 ± 0.029	-0.59	2.80 ± 0.32	2.7×10^7						
J2333+3901	1	0.368 ± 0.060	0.178 ± 0.030	-0.55	0.85 ± 0.03	5.9×10^8	45.45 ± 0.18	0.56 ± 0.20	q	0.319	FLAT	
	2	0.325 ± 0.059	0.085 ± 0.032	-1.02	2.68 ± 0.37	2.9×10^7						
J2347-1856	1	0.493 ± 0.054	0.167 ± 0.040	-0.82	1.02 ± 0.07	3.8×10^8	33.24 ± 0.06	-0.07 ± 0.07	GPS ^{XVII} $v_m=2.07$	
	2	0.333 ± 0.045	0.127 ± 0.035	-0.73	1.05 ± 0.09	2.8×10^8						
J2355-2125	1	0.305 ± 0.030	0.226 ± 0.025	-0.23	0.73 ± 0.01	1.0×10^9	20.82 ± 0.04	-0.02 ± 0.05	GPS ^{XIII,XV}	
	2	0.219 ± 0.025	0.071 ± 0.014	-0.86	1.57 ± 0.08	6.9×10^7						
J2358+1955	1	0.581 ± 0.048	0.341 ± 0.036	-0.40	0.59 ± 0.01	2.4×10^9	14.27 ± 0.16	0.50 ± 0.16	q	1.066	STEEP	
	2	0.262 ± 0.033	0.081 ± 0.028	-0.89	2.74 ± 0.32	2.6×10^7						

^ISource J2000 epoch name. Precise VLBI positions of these sources may be obtained from <http://astrogeo.org/rfc/>

^{II}Component number. Each source was modeled with two circular Gaussian components. The first component is the one which is brighter at 8 GHz.

^{III} F_X (F_S) is the component flux in Jansky measured at 8 GHz (2 GHz).

^{IV} α is the component spectral index between 2 and 8 GHz.

^V R_X is the component size (FWHM of the Gaussian model) in milliarcseconds measured at 8 GHz.

^{VI} T_{bX} is the component brightness temperature in Kelvin measured at 8 GHz.

^{VII} D_X is the distance in milliarcseconds between CSO components measured at 8 GHz.

^{VIII} $D_X - D_S$ is the distance difference (milliarcseconds) between CSO components measured at 8 and 2 GHz.

^{IX}opt. — optical classification according to Véron-Cetty & Véron (2006): 'q' stands for quasar, 'a' is an active galaxy, 'b' is a BL Lacertae type object.

^X z — redshift from Véron-Cetty & Véron (2006).

^{XI}Comments: COINS — the source is part of the COINS sample (Peck & Taylor 2000); COINS-REJ — the source was considered as a candidate for the COINS sample but was rejected (Peck & Taylor 2000); GPS — GPS source, part of the RATAN-600 GPS sample Sokolovsky et al. (2009) (unless stated otherwise), for these sources approximate spectral peak frequency (in GHz) is indicated; GPS-REJ the source was reported in the literature as a GPS candidate but was not confirmed by RATAN-600 observations; STEEP — steep spectrum source, FLAT — flat spectrum source.

^{XII}To distinguish between resolved and unresolved components we use the criterium proposed by Kovalev, Kellermann, Lister, Homan, Vermeulen, Cohen, Ros, Kadler, Lobanov, Zensus, Kardashev, Gurvits, Aller, & Aller 2005): $\psi > \text{HPBW} \sqrt{\frac{4 \ln 2}{\pi} \ln \frac{\text{SNR}}{\text{SNR}-1}}$ where ψ is the component best-fit angular size, HPBW is the Half Power Beam Width, SNR is the signal to noise ratio of the component.

^{XIII}No RATAN-600 observations available for this source.

^{XIV}Reported as GPS by Marecki et al. (1999).

^{XV}Reported as GPS by Vollmer et al. (2008b).

^{XVI}Spectral classification based on non-simultaneous literature data collected by the CATS database (Verkhodanov et al. 2005).

^{XVII}Listed as the confirmed CSO by Taylor & Peck (2003).

5.4 γ -ray counterparts of candidate young radio sources seen edge-on

As discussed in Chapter 1, γ -ray radiation from extragalactic sources is usually associated with relativistic jets aligned with the line of sight. Short-timescale variability observed in many γ -ray-bright AGN also suggest that the radiation is relativistically beamed: the time dilation effect allows to reconcile the expected size of structures responsible for AGN emission with the observed variability timescale.

There are a few exceptions: 11 non-blazar AGNs were recently detected by *Fermi*/LAT, including 7 FRI and 4 FR II radio galaxies (Fermi-LAT Collaboration 2010). γ -ray radiation not associated with AGN activity was recently detected from the two starburst galaxies M82 and NGC 253 (Abdo et al. 2010g). However, these objects still form a very small fraction of extragalactic γ -ray sources known to date.

We have attempted a search for γ -ray counterparts of candidate young radio sources described in Sections 5.1 and 5.3 in the Fermi Large Area Telescope First Source Catalog (1FGL; Abdo et al. 2010e). The results are not unexpected. None of the candidate CSOs selected on the basis of parsec-scale morphology (Section 5.3) is found within the 95% confidence localization region of an 1FGL source. Among the GPS candidates selected on the basis of their convex single-dish spectrum (Section 5.1) three objects were identified with γ -ray sources: quasars PKS 0440–00, PKS 1157–215 and the BL Lac-type object PKS 1519–273 (Abdo et al. 2010e). It is likely that these three sources are in fact relativistically-beamed blazar-type AGN which show GPS-type radio spectrum only temporary.

The non-detection of the selected candidate sources in γ -rays confirms that the criteria used to select candidates are reliable and allow us to identify members of a population distinguished from the majority of compact extragalactic sources with comparable levels of radio flux. The reality of the distinction is also supported by two facts. First, radio sources selected on the basis of their convex spectrum are less compact (Section 5.2) than typical extragalactic sources which are detected in γ -rays (Kovalev 2009; Kovalev et al. 2009). Second, brightness temperatures of the dominating radio components of CSO objects (Section 5.3) are systematically lower than those associated with radio cores of *Fermi*/LAT-detected blazars (Kovalev 2009; Kovalev et al. 2009; Linford et al. 2010). The non-detection of the selected candidate young radio sources which are expected to be not aligned with the line of sight is consistent with the idea that γ -ray emission of blazars is associated with a relativistically-beamed jet aligned with the line of sight. We observe this section of the jet as the compact core which is weak or absent in CSO sources but is the dominating parsec-scale feature of γ -ray-detected blazars.

5.5 Chapter summary

In this chapter we have presented two samples of candidate young radio sources aligned at large angles to the line of sight. The larger sample described in Section 5.1 was selected on the basis of single-dish radio spectra. Despite the use of multi-epoch observations to select the candidates, the resulting sample may still be significantly contaminated with relativistically beamed blazars showing peaked radio spectrum during a flare. The second sample presented in Section 5.3 was selected on the basis of parsec-scale morphology using the large archive of geodetical VLBI data. However, some contamination with relativistically beamed sources is also possible in this sample. An

interesting effect of the frequency-dependent difference in position of hotspots associated with young radio sources is identified. The effect deserves detailed investigation with dedicated multifrequency VLBI observations. The sample selected on the basis of their parsec-scale morphology is expected to be a “cleaner” list of candidate young radio sources compared to the radio spectrum-selected sample which is confirmed by the non-detection of γ -ray emission from the selected candidates.

Chapter 6

Conclusions

We analyzed simultaneous multi-frequency VLBA observations of 38 extragalactic radio sources (blazars) observed in the course of two programs: “high core shift” sample (nine frequencies in 1.4–15.4 GHz range) and “bright γ -ray blazars” sample (seven frequencies in 4.6–43.2 GHz range). A novel technique is developed applied to extract spatially resolved spectra from VLBI data (Chapter 2). The spectral turnover attributed to synchrotron self absorption has been detected in parsec-scale core regions of 27 sources which allowed to constrain the magnetic field strength and particle energy spectrum in these regions. We have placed upper limits of $B_{\perp} \leq 10^{-1}–10^2$ G (source frame) on the magnetic field strength in these sources (Table 2.4 and 2.5). Hard spectra ($-0.5 \leq \alpha \leq +0.1$, $F_{\nu} \sim \nu^{\alpha}$) observed in the blazar cores above the synchrotron peak may either indicate a hard energy spectrum of the relativistic electron population in the jet or result from significant inhomogeneity (of the magnetic field and plasma parameters or just optical depth) across the emitting region. Estimations (or in five cases – upper limits) of the core size have been obtained for the observed sources. Since γ -ray emission in blazars is suggested to originate from regions spatially close to the VLBI core, the estimates of the size, magnetic field strength and electron energy distribution presented in Table 2.4 are useful to constrain broad-band Spectral Energy Distribution (SED) models (see Chapter 3).

Significant shift of the observed radio core position with frequency has been detected and studied in 20 sources (Chapter 4). This effect is especially interesting since it provides a probe of physical conditions in the inner jet – the likely site of the observed high-energy emission of blazars. The effect has also important astrometric implications. The core position, r_c , shift as a function of frequency, ν , is consistent with the $r_c(\nu) \propto \nu^{-1}$ pattern expected for a purely synchrotron self-absorbed conical jet in equipartition. These results support the interpretation of the parsec-scale core as a continuous Blandford-Königl type jet with smooth gradients of physical properties (including opacity) along it. No systematic change with frequency of the power law index in the $r_c(\nu)$ relation has been convincingly detected. However, some local changes might be present in a few sources, especially at higher frequencies.

Two samples of candidate young radio sources seen edge-on are presented in Chapter 5. The larger sample described in Section 5.1 was selected on the basis of single-dish radio spectra. Despite the use of multi-epoch observations to select the candidates, the resulting sample may still be significantly contaminated with relativistically beamed blazars showing peaked radio spectrum during a flare. The second sample presented in Section 5.3 was selected on the basis of parsec-scale morphology using the

large archive of geodetical VLBI data. This sample is expected to be a “cleaner” list of candidate young radio sources compared to the radio spectrum-selected sample which is confirmed by the non-detection of γ -ray emission from the selected candidates. An interesting effect of the frequency-dependent difference in position of hotspots associated with young radio sources is identified. The effect deserves detailed investigation with dedicated multifrequency VLBI observations. A comparison between blazars possessing jets aligned closely to the line of sight with radio sources aligned at large angles to it supports the idea that the bright extragalactic γ -ray sources are associated with jets affected by relativistic beaming.

Bibliography

- Abdo, A. A., Ackermann, M., Agudo, I., et al. 2010a, *ApJ*, 721, 1425
- Abdo, A. A., Ackermann, M., Agudo, I., et al. 2010b, accepted to *ApJ*
- Abdo, A. A., Ackermann, M., Agudo, I., et al. 2010c, submitted to *ApJ*
- Abdo, A. A., Ackermann, M., Agudo, I., et al. 2010d, submitted to *ApJ*
- Abdo, A. A., Ackermann, M., Ajello, M., et al. 2010e, *ApJS*, 188, 405
- Abdo, A. A., Ackermann, M., Ajello, M., et al. 2009, *ApJ*, 700, 597
- Abdo, A. A., Ackermann, M., Ajello, M., et al. 2010f, *ApJ*, 710, 810
- Abdo, A. A., Ackermann, M., Ajello, M., et al. 2010g, *ApJ*, 709, L152
- Acciari, V. A., Aliu, E., Arlen, T., et al. 2009a, *Science*, 325, 444
- Acciari, V. A., Aliu, E., Aune, T., et al. 2009b, *ApJ*, 707, 612
- Acciari, V. A., Aliu, E., Aune, T., et al. 2009c, *ApJ*, 703, 169
- Ackermann, M., Ajello, M., Baldini, L., et al. 2010, *ApJ*, 721, 1383
- Afanas'ev, V. L., Dodonov, S. N., Moiseev, A. V., et al. 2003, *Astronomy Reports*, 47, 458
- Aharonian, F., Akhperjanian, A. G., Anton, G., et al. 2009, *ApJ*, 696, L150
- Aller, M. F., Aller, H. D., & Hughes, P. A. 1992, *ApJ*, 399, 16
- Aller, M. F., Hughes, P. A., & Aller, H. D. 2010, arXiv:1007.0258
- Anderhub, H., Antonelli, L. A., Antoranz, P., et al. 2009, *ApJ*, 705, 1624
- Angelakis, E., Fuhrmann, L., Nestoras, I., et al. 2010, arXiv:1006.5610
- Angelakis, E., Fuhrmann, L., Zensus, J. A., et al. 2009, arXiv:0910.0643
- Antonucci, R. 1993, *ARA&A*, 31, 473
- Arshakian, T. G., León-Tavares, J., Lobanov, A. P., et al. 2010, *MNRAS*, 401, 1231
- Atwood, W. B., Abdo, A. A., Ackermann, M., et al. 2009, *ApJ*, 697, 1071

- Bach, U., Kadler, M., Krichbaum, T. P., et al. 2005, in *Astronomical Society of the Pacific Conference Series*, Vol. 340, *Future Directions in High Resolution Astronomy*, ed. J. Romney & M. Reid, 30
- Bach, U., Krichbaum, T. P., Middelberg, E., Alef, W., & Zensus, A. J. 2008, in *The role of VLBI in the Golden Age for Radio Astronomy*
- Bach, U., Villata, M., Raiteri, C. M., et al. 2006, *A&A*, 456, 105
- Bai, J. M. & Lee, M. G. 2005, *Journal of Korean Astronomical Society*, 38, 125
- Beasley, A. J., Gordon, D., Peck, A. B., et al. 2002, *ApJS*, 141, 13
- Becker, R. H., White, R. L., & Edwards, A. L. 1991, *ApJS*, 75, 1
- Begelman, M. C., Blandford, R. D., & Rees, M. J. 1980, *Nature*, 287, 307
- Bell, M. B. & Comeau, S. P. 2010, *Ap&SS*, 325, 31
- Bianchin, V., Foschini, L., Ghisellini, G., et al. 2009, *A&A*, 496, 423
- Biretta, J. A., Moore, R. L., & Cohen, M. H. 1986, *ApJ*, 308, 93
- Blandford, R. D. & Konigl, A. 1979, *ApJ*, 232, 34
- Blandford, R. D. & Payne, D. G. 1982, *MNRAS*, 199, 883
- Blandford, R. D. & Znajek, R. L. 1977, *MNRAS*, 179, 433
- Bloom, S. D. 2008, *AJ*, 136, 1533
- Bloom, S. D., Bertsch, D. L., Hartman, R. C., et al. 1997, *ApJ*, 490, L145+
- Boettcher, M. 2010, arXiv:1006.5048
- Bonnoli, G., Ghisellini, G., Foschini, L., Tavecchio, F., & Ghirlanda, G. 2010, *MNRAS*, 1476
- Böttcher, M. 2002, *Bulletin of the Astronomical Society of India*, 30, 115
- Böttcher, M., Marscher, A. P., Rivasio, M., et al. 2003, *ApJ*, 596, 847
- Briggs, D. S., Schwab, F. R., & Sramek, R. A. 1999, in *Astronomical Society of the Pacific Conference Series*, Vol. 180, *Synthesis Imaging in Radio Astronomy II*, ed. G. B. Taylor, C. L. Carilli, & R. A. Perley, 127
- Camenzind, M. & Krockenberger, M. 1992, *A&A*, 255, 59
- Capetti, A., Raiteri, C. M., & Buttiglione, S. 2010, *A&A*, 516, A59+
- Carvalho, J. C. 1994, *A&A*, 292, 392
- Carvalho, J. C. 1998, *A&A*, 329, 845
- Celotti, A. & Ghisellini, G. 2008, *MNRAS*, 385, 283
- Cersosimo, J. C., Santos, M. L., Cintron, S. I., & Quiniento, Z. M. 1994, *ApJS*, 95, 157
- Charlot, P., Gabuzda, D. C., Sol, H., Degrange, B., & Piron, F. 2006, *A&A*, 457, 455

- Chatterjee, R., Marscher, A. P., Jorstad, S. G., et al. 2009, *ApJ*, 704, 1689
- Chen, A. W., D'Ammando, F., Villata, M., et al. 2008, *A&A*, 489, L37
- Collmar, W., Böttcher, M., Krichbaum, T. P., et al. 2010, *A&A*, 522, A66+
- Corbett, E. A., Robinson, A., Axon, D. J., & Hough, J. H. 2000, *MNRAS*, 311, 485
- Corbett, E. A., Robinson, A., Axon, D. J., et al. 1996, *MNRAS*, 281, 737
- Cornwell, T., Braun, R., & Briggs, D. S. 1999, in *Astronomical Society of the Pacific Conference Series*, Vol. 180, *Synthesis Imaging in Radio Astronomy II*, ed. G. B. Taylor, C. L. Carilli, & R. A. Perley, 151
- Croke, S. M., O'Sullivan, S. P., & Gabuzda, D. C. 2010, *MNRAS*, 402, 259
- Dallacasa, D., Bondi, M., Alef, W., & Mantovani, F. 1998, *A&AS*, 129, 219
- Dallacasa, D., Falomo, R., & Stanghellini, C. 2002, *A&A*, 382, 53
- Dallacasa, D., Stanghellini, C., Centonza, M., & Fanti, R. 2000, *A&A*, 363, 887
- D'Ammando, F., Vercellone, S., Donnarumma, I., et al. 2010, in *American Institute of Physics Conference Series*, Vol. 1248, *American Institute of Physics Conference Series*, ed. A. Comastri, L. Angelini, & M. Cappi, 415–416
- D'Arcangelo, F. D., Marscher, A. P., Jorstad, S. G., et al. 2007, *ApJ*, 659, L107
- de Vries, N., Snellen, I. A. G., Schilizzi, R. T., Lehnert, M. D., & Bremer, M. N. 2007, *A&A*, 464, 879
- de Vries, W. H., Barthel, P. D., & O'Dea, C. P. 1997, *A&A*, 321, 105
- Dermer, C. D. & Schlickeiser, R. 2002, *ApJ*, 575, 667
- Edwards, P. G. & Tingay, S. J. 2004, *A&A*, 424, 91
- Falcke, H. 2001, in *Reviews in Modern Astronomy*, Vol. 14, *Reviews in Modern Astronomy*, ed. R. E. Schielicke, 15
- Falcke, H., Nagar, N. M., Wilson, A. S., Ho, L. C., & Ulvestad, J. S. 2001, in *Black Holes in Binaries and Galactic Nuclei*, ed. L. Kaper, E. P. J. van den Heuvel, & P. A. Woudt, 218
- Fanti, C., Fanti, R., Dallacasa, D., et al. 1995, *A&A*, 302, 317
- Fermi-LAT Collaboration. 2010, *ArXiv e-prints*
- Fey, A. L. & Charlot, P. 1997, *ApJS*, 111, 95
- Fey, A. L., Clegg, A. W., & Fomalont, E. B. 1996, *ApJS*, 105, 299
- Fey, A. L., Ma, C., Arias, E. F., et al. 2004, *AJ*, 127, 3587
- Finke, J. D. & Dermer, C. D. 2010, *ApJ*, 714, L303
- Finke, J. D., Shields, J. C., Böttcher, M., & Basu, S. 2008, *A&A*, 477, 513

- Fomalont, E. B. 1999, in *Astronomical Society of the Pacific Conference Series*, Vol. 180, *Synthesis Imaging in Radio Astronomy II*, ed. G. B. Taylor, C. L. Carilli, & R. A. Perley, 301
- Fomalont, E. B., Petrov, L., MacMillan, D. S., Gordon, D., & Ma, C. 2003, *AJ*, 126, 2562
- Ghisellini, G. & Maraschi, L. 1989, *ApJ*, 340, 181
- Ghisellini, G. & Tavecchio, F. 2009, *MNRAS*, 397, 985
- Ginzburg, V. L. & Syrovatskii, S. I. 1965, *ARA&A*, 3, 297
- Giroletti, M., Reimer, A., Fuhrmann, L., Pavlidou, V., & Richards, J. L. 2010, arXiv:1001.5123
- Giuliani, A., D'Ammando, F., Vercellone, S., et al. 2009, *A&A*, 494, 509
- González-Pérez, J. N., Kidger, M. R., & Martín-Luis, F. 2001, *AJ*, 122, 2055
- Gopal-Krishna, Patnaik, A. R., & Steppe, H. 1983, *A&A*, 123, 107
- Gopal-Krishna & Spoelstra, T. A. T. 1993, *A&A*, 271, 101
- Gorham, P. W., van Zee, L., Unwin, S. C., & Jacobs, C. 2000, *AJ*, 119, 1677
- Gould, R. J. 1979, *A&A*, 76, 306
- Greisen, E. W. 1990, in *Acquisition, Processing and Archiving of Astronomical Images*, ed. G. Longo & G. Sedmak, 125–142
- Greisen, E. W. 2003, *Information Handling in Astronomy - Historical Vistas*, 285, 109
- Guetta, D., Ghisellini, G., Lazzati, D., & Celotti, A. 2004, *A&A*, 421, 877
- Gugliucci, N. E., Taylor, G. B., Peck, A. B., & Giroletti, M. 2005, *ApJ*, 622, 136
- Gugliucci, N. E., Taylor, G. B., Peck, A. B., & Giroletti, M. 2007, *ApJ*, 661, 78
- Gupta, N., Salter, C. J., Saikia, D. J., Ghosh, T., & Jeyakumar, S. 2006, *MNRAS*, 373, 972
- Hartman, R. C., Bertsch, D. L., Bloom, S. D., et al. 1999, *ApJS*, 123, 79
- Hildebrand, C. E., Iijima, B. A., Kroger, P. M., Folkner, W. M., & Edwards, C. D. 1994, in *In its The Telecommunications and Data Acquisition Report*, ed. J. H. Yuen, 46–82
- Högbom, J. A. 1974, *A&AS*, 15, 417
- Homan, D. & Kovalev, Y. Y. 2010, in preparation
- Homan, D. C., Wardle, J. F. C., Cheung, C. C., Roberts, D. H., & Attridge, J. M. 2002, *ApJ*, 580, 742
- Hovatta, T., Nieppola, E., Tornikoski, M., et al. 2008, *A&A*, 485, 51
- Hovatta, T., Valtaoja, E., Tornikoski, M., & Lähteenmäki, A. 2009, *A&A*, 494, 527

- Hughes, P. A., Aller, H. D., & Aller, M. F. 1985, *ApJ*, 298, 301
- Hujeirat, A., Livio, M., Camenzind, M., & Burkert, A. 2003, *A&A*, 408, 415
- Ishibashi, W. & Courvoisier, T. 2010, arXiv:1010.5591
- Jackson, N. & Browne, I. W. A. 1991, *MNRAS*, 250, 414
- Jauncey, D. L., King, E. A., Bignall, H. E., et al. 2003, *Publications of the Astronomical Society of Australia*, 20, 151
- Jones, T. W., O'dell, S. L., & Stein, W. A. 1974, *ApJ*, 188, 353
- Jorstad, S. G., Marscher, A. P., Larionov, V. M., et al. 2010, *ApJ*, 715, 362
- Jorstad, S. G., Marscher, A. P., Mattox, J. R., et al. 2001, *ApJ*, 556, 738
- Kadler, M., Ros, E., Lobanov, A. P., Falcke, H., & Zensus, J. A. 2004, *A&A*, 426, 481
- Kardashev, N. S., Kuz'min, A. D., & Syrovatskii, S. I. 1962, *Soviet Ast.*, 6, 167
- Kellermann, K. I., Sramek, R. A., Schmidt, M., Green, R. F., & Shaffer, D. B. 1994, *AJ*, 108, 1163
- Komatsu, E., Dunkley, J., Nolta, M. R., et al. 2009, *ApJS*, 180, 330
- Konigl, A. 1981, *ApJ*, 243, 700
- Königl, A. 2007, in *Revista Mexicana de Astronomia y Astrofisica*, vol. 27, Vol. 27, *Revista Mexicana de Astronomia y Astrofisica*, vol. 27, 91–101
- Kovalev, Y. A. & Kovalev, Y. Y. 2006, in *Astronomical Society of the Pacific Conference Series*, Vol. 360, *Astronomical Society of the Pacific Conference Series*, ed. C. M. Gaskell, I. M. McHardy, B. M. Peterson, & S. G. Sergeev , 137
- Kovalev, Y. A., Kovalev, Y. Y., & Nizhelsky, N. A. 2000, *PASJ*, 52, 1027
- Kovalev, Y. Y. 2005, *Baltic Astronomy*, 14, 413
- Kovalev, Y. Y. 2009, *ApJ*, 707, L56
- Kovalev, Y. Y., Aller, H. D., Aller, M. F., et al. 2009, *ApJ*, 696, L17
- Kovalev, Y. Y., Kellermann, K. I., Lister, M. L., et al. 2005, *AJ*, 130, 2473
- Kovalev, Y. Y., Kovalev, Y. A., Nizhelsky, N. A., & Bogdantsov, A. B. 2002, *PASA*, 19, 83
- Kovalev, Y. Y., Lobanov, A. P., & Pushkarev, A. B. 2008a, *Mem. Soc. Astron. Italiana*, 79, 1153
- Kovalev, Y. Y., Lobanov, A. P., Pushkarev, A. B., & Zensus, J. A. 2008b, *A&A*, 483, 759
- Kovalev, Y. Y., Nizhelsky, N. A., Kovalev, Y. A., et al. 1999a, *A&AS*, 139, 545
- Kovalev, Y. Y., Nizhelsky, N. A., Kovalev, Y. A., et al. 1999b, in *IAU Symposium*, Vol. 194, *Activity in Galaxies and Related Phenomena*, ed. Y. Terzian, E. Khachikian, & D. Weedman, 177

- Kovalev, Y. Y., Petrov, L., Fomalont, E. B., & Gordon, D. 2007, *AJ*, 133, 1236
- Kraus, J. D., Scheer, D. J., Dixon, R. S., Fitch, L. T., & Andrew, B. H. 1968, *ApJ*, 152, L35+
- Krolik, J. H. 1999, *Active galactic nuclei : from the central black hole to the galactic environment*, ed. Krolik, J. H.
- Kuehr, H., Witzel, A., Pauliny-Toth, I. I. K., & Nauber, U. 1981, *A&AS*, 45, 367
- Labiano, A., Barthel, P. D., O’Dea, C. P., et al. 2007, *A&A*, 463, 97
- Lähteenmäki, A. & Valtaoja, E. 2003, *ApJ*, 590, 95
- Lee, S., Lobanov, A. P., Krichbaum, T. P., et al. 2008, *AJ*, 136, 159
- León-Tavares, J., Lobanov, A. P., Chavushyan, V. H., et al. 2010, *ApJ*, 715, 355
- Lindgren, L. 2007, *Highlights of Astronomy*, 14, 481
- Linford, J. D., Taylor, G. B., Romani, R., et al. 2010, *ArXiv e-prints*
- Lister, M. L., Cohen, M. H., Homan, D. C., et al. 2009, *AJ*, 138, 1874
- Lister, M. L., Kellermann, K. I., & Pauliny-Toth, I. I. K. 2002, in *Proceedings of the 6th EVN Symposium*, ed. E. Ros, R. W. Porcas, A. P. Lobanov, & J. A. Zensus, 135
- Lo, K. Y. 2005, *ARA&A*, 43, 625
- Lobanov, A. 2007, *Ap&SS*, 311, 263
- Lobanov, A. 2010a, *arXiv:1010.2856*
- Lobanov, A. P. 1998a, *A&AS*, 132, 261
- Lobanov, A. P. 1998b, *A&A*, 330, 79
- Lobanov, A. P. 2005, *arXiv:astro-ph/0503225*
- Lobanov, A. P. 2010b, *arXiv:1011.0572*
- Lobanov, A. P. & Zensus, J. A. 1998, in *Astronomical Society of the Pacific Conference Series*, Vol. 144, *IAU Colloq. 164: Radio Emission from Galactic and Extragalactic Compact Sources*, ed. J. A. Zensus, G. B. Taylor, & J. M. Wrobel, 53
- Lobanov, A. P. & Zensus, J. A. 2001, *Science*, 294, 128
- Ma, C., Arias, E. F., Eubanks, T. M., et al. 1998, *AJ*, 116, 516
- Madejski, G. M., Sikora, M., Jaffe, T., et al. 1999, *ApJ*, 521, 145
- Marcaide, J. M. & Shapiro, I. I. 1984, *ApJ*, 276, 56
- Marcaide, J. M., Shapiro, I. I., Corey, B. E., et al. 1985, *A&A*, 142, 71
- Marecki, A., Falcke, H., Niezgodna, J., Garrington, S. T., & Patnaik, A. R. 1999, *A&AS*, 135, 273
- Marscher, A. P. 1980, *Nature*, 288, 12

- Marscher, A. P. 1983, *ApJ*, 264, 296
- Marscher, A. P. 1996, in *Astronomical Society of the Pacific Conference Series*, Vol. 110, *Blazar Continuum Variability*, ed. H. R. Miller, J. R. Webb, & J. C. Noble, 248
- Marscher, A. P. 2006a, in *American Institute of Physics Conference Series*, Vol. 856, *Relativistic Jets: The Common Physics of AGN, Microquasars, and Gamma-Ray Bursts*, ed. P. A. Hughes & J. N. Bregman, 1–22
- Marscher, A. P. 2006b, *Chinese Journal of Astronomy and Astrophysics Supplement*, 6, 010000
- Marscher, A. P. 2008, in *Astronomical Society of the Pacific Conference Series*, Vol. 386, *Extragalactic Jets: Theory and Observation from Radio to Gamma Ray*, ed. T. A. Rector & D. S. De Young, 437
- Marscher, A. P. 2009, arXiv:0909.2576
- Marscher, A. P. & Gear, W. K. 1985, *ApJ*, 298, 114
- Marscher, A. P., Jorstad, S. G., D’Arcangelo, F. D., et al. 2010a, arXiv:1002.0806
- Marscher, A. P., Jorstad, S. G., D’Arcangelo, F. D., et al. 2008, *Nature*, 452, 966
- Marscher, A. P., Jorstad, S. G., Larionov, V. M., et al. 2010b, *ApJ*, 710, L126
- Marscher, A. P., Jorstad, S. G., Larionov, V. M., et al. 2009, in *Bulletin of the American Astronomical Society*, Vol. 41, *Bulletin of the American Astronomical Society*, 382
- Max-Moerbeck, W., for the Fermi-LAT Collaboration, & for the F-GAMMA collaboration. 2009, arXiv:0912.3817
- Mendenhall, W., Wackerly, D. D., & L., S. R. 1989, 15: *Nonparametric statistics*
- Mücke, A. & Protheroe, R. J. 2001, *Astroparticle Physics*, 15, 121
- Mücke, A., Protheroe, R. J., Engel, R., Rachen, J. P., & Stanev, T. 2003, *Astroparticle Physics*, 18, 593
- Muecke, A., Pohl, M., Reich, P., et al. 1997, *A&A*, 320, 33
- Napier, P. J. 1994, in *IAU Symposium*, Vol. 158, *Very High Angular Resolution Imaging*, ed. J. G. Robertson & W. J. Tango, 117
- Narayan, R. 2005, *New Journal of Physics*, 7, 199
- Nilsson, K., Pursimo, T., Sillanpää, A., Takalo, L. O., & Lindfors, E. 2008, *A&A*, 487, L29
- O’Dea, C. P. 1998, *PASP*, 110, 493
- O’Dea, C. P., Baum, S. A., & Stanghellini, C. 1991, *ApJ*, 380, 66
- O’Dea, C. P., Baum, S. A., Stanghellini, C., et al. 1990, *A&AS*, 84, 549
- Ojha, R., Kadler, M., Böck, M., et al. 2010, *A&A*, 519, A45+
- Ostorero, L., Moderski, R., Stawarz, Ł., et al. 2010, *ApJ*, 715, 1071

- O'Sullivan, S. P. & Gabuzda, D. C. 2009, MNRAS, 400, 26
- Otterbein, K., Krichbaum, T. P., Kraus, A., et al. 1998, A&A, 334, 489
- Owsianik, I. & Conway, J. E. 1998, A&A, 337, 69
- Pacciani, L., Donnarumma, I., Vittorini, V., et al. 2009, A&A, 494, 49
- Pacciani, L., Vittorini, V., Tavani, M., et al. 2010, ApJ, 716, L170
- Pacholczyk, A. G. 1970, Radio astrophysics. Nonthermal processes in galactic and extragalactic sources, ed. Pacholczyk, A. G.
- Panajian, V. G. 1998, Afz, 41, 246
- Pearson, T. J. & Readhead, A. C. S. 1988, ApJ, 328, 114
- Peck, A. B. & Taylor, G. B. 2000, ApJ, 534, 90
- Peck, A. B., Taylor, G. B., & Conway, J. E. 1999, ApJ, 521, 103
- Peck, A. B., Taylor, G. B., Fassnacht, C. D., Readhead, A. C. S., & Vermeulen, R. C. 2000, ApJ, 534, 104
- Perryman, M. A. C., de Boer, K. S., Gilmore, G., et al. 2001, A&A, 369, 339
- Perucho, M. & Martí, J. M. 2002, ApJ, 568, 639
- Petrov, L., Gordon, D., Gipson, J., et al. 2009, Journal of Geodesy, 83, 859
- Petrov, L., Kovalev, Y. Y., Fomalont, E. B., & Gordon, D. 2005, AJ, 129, 1163
- Petrov, L., Kovalev, Y. Y., Fomalont, E. B., & Gordon, D. 2006, AJ, 131, 1872
- Petrov, L., Kovalev, Y. Y., Fomalont, E. B., & Gordon, D. 2008, AJ, 136, 580
- Phillips, R. B. & Mutel, R. L. 1982, A&A, 106, 21
- Pihlström, Y. M., Conway, J. E., & Vermeulen, R. C. 2003, A&A, 404, 871
- Piner, B. G. & Edwards, P. G. 2004, ApJ, 600, 115
- Pogrebenko, S. V., Gurvits, L. I., Avruch, I. M., & Cimo, G. 2009, in European Planetary Science Congress 2009, 199
- Polatidis, A. G. 2009, Astronomische Nachrichten, 330, 149
- Polatidis, A. G. & Conway, J. E. 2003, PASA, 20, 69
- Porcas, R. 2008, in 2nd MCCT-SKADS Training School. Radio Astronomy: Fundamentals and the New Instruments
- Porcas, R. W. 2009, A&A, 505, L1
- Press, W. H., Teukolsky, S. A., Vetterling, W. T., & Flannery, B. P. 2002, Numerical Recipes in C, second edition, ed. Press, W. H. and Teukolsky, S. A. and Vetterling, W. T. and Flannery, B. P.

- Pushkarev, A. & Kovalev, Y. 2008, in *The role of VLBI in the Golden Age for Radio Astronomy*
- Pushkarev, A. B. & Kovalev, Y. Y. 2010, in preparation
- Pushkarev, A. B., Kovalev, Y. Y., & Lister, M. L. 2010, *ApJ*, 722, L7
- Raiteri, C. M., Villata, M., Capetti, A., et al. 2009, *A&A*, 507, 769
- Ravasio, M., Tagliaferri, G., Ghisellini, G., et al. 2003, *A&A*, 408, 479
- Readhead, A. C. S., Taylor, G. B., Pearson, T. J., & Wilkinson, P. N. 1996a, *ApJ*, 460, 634
- Readhead, A. C. S., Taylor, G. B., Xu, W., et al. 1996b, *ApJ*, 460, 612
- Richards, J. L., Max-Moerbeck, W., Pavlidou, V., et al. 2010, in *American Institute of Physics Conference Series*, Vol. 1248, *American Institute of Physics Conference Series*, ed. A. Comastri, L. Angelini, & M. Cappi, 503–504
- Rioja, M. J., Dodson, R., Porcas, R. W., Suda, H., & Colomer, F. 2005, arXiv:astro-ph/0505475
- Rioja, M. J., Marcaide, J. M., Elosegui, P., & Shapiro, I. I. 1997, *A&A*, 325, 383
- Rodriguez, C., Taylor, G. B., Zavala, R. T., et al. 2006, *ApJ*, 646, 49
- Ros, E. & Lobanov, A. P. 2002, arXiv:astro-ph/0211200
- Rossetti, A., Mantovani, F., Fanti, C., & Fanti, R. 2003, *PASA*, 20, 35
- Salamon, M. H. & Stecker, F. W. 1994, *ApJ*, 430, L21
- Sambruna, R. M., Ghisellini, G., Hooper, E., et al. 1999, *ApJ*, 515, 140
- Savolainen, T., Homan, D. C., Hovatta, T., et al. 2010, *A&A*, 512, A24+
- Savolainen, T., Wiik, K., Valtaoja, E., & Tornikoski, M. 2008, in *Astronomical Society of the Pacific Conference Series*, Vol. 386, *Extragalactic Jets: Theory and Observation from Radio to Gamma Ray*, ed. T. A. Rector & D. S. De Young, 451
- Sekido, M., Ichikawa, R., Osaki, H., et al. 2004, in *International VLBI Service for Geodesy and Astrometry 2004 General Meeting Proceedings*, ed. N. R. Vandenberg & K. D. Baver, 258
- Shepherd, M. C. 1997, in *Astronomical Society of the Pacific Conference Series*, Vol. 125, *Astronomical Data Analysis Software and Systems VI*, ed. G. Hunt & H. Payne, 77
- Shepherd, M. C., Pearson, T. J., & Taylor, G. B. 1994, in *Bulletin of the American Astronomical Society*, Vol. 26, *Bulletin of the American Astronomical Society*, 987–989
- Sikora, M., Begelman, M. C., Madejski, G. M., & Lasota, J. 2005, *ApJ*, 625, 72
- Sikora, M., Begelman, M. C., & Rees, M. J. 1994, *ApJ*, 421, 153

- Sikora, M., Błażejowski, M., Moderski, R., & Madejski, G. M. 2002, *ApJ*, 577, 78
- Sligh, V. I. 1963, *Nature*, 199, 682
- Snellen, I. A. G., Lehnert, M. D., Bremer, M. N., & Schilizzi, R. T. 2002, *MNRAS*, 337, 981
- Snellen, I. A. G., Schilizzi, R. T., Bremer, M. N., et al. 1998a, *MNRAS*, 301, 985
- Snellen, I. A. G., Schilizzi, R. T., Bremer, M. N., et al. 1999, *MNRAS*, 307, 149
- Snellen, I. A. G., Schilizzi, R. T., de Bruyn, A. G., et al. 1998b, *A&AS*, 131, 435
- Snellen, I. A. G., Zhang, M., Schilizzi, R. T., et al. 1995, *A&A*, 300, 359
- Sokolovsky, K. & Kovalev, Y. 2008, in *The role of VLBI in the Golden Age for Radio Astronomy*
- Sokolovsky, K. V., Kovalev, Y. Y., Kovalev, Y. A., Nizhelskiy, N. A., & Zhekanis, G. V. 2009, *Astronomische Nachrichten*, 330, 199
- Sokolovsky, K. V., Kovalev, Y. Y., Lobanov, A. P., et al. 2010a, arXiv:1006.3084
- Sokolovsky, K. V., Kovalev, Y. Y., Lobanov, A. P., et al. 2010b, arXiv:1001.2591
- Sokolovsky, K. V., Kovalev, Y. Y., Mimica, P., & Perucho, M. 2010c, *A&A* submitted
- Sokolovsky, K. V., Kovalev, Y. Y., Pushkarev, A. B., & Lobanov, A. P. 2010d, *A&A* submitted
- Soldi, S., Türler, M., Paltani, S., et al. 2008, *A&A*, 486, 411
- Spoelstra, T. A. T., Patnaik, A. R., & Gopal-Krishna. 1985, *A&A*, 152, 38
- Stanghellini, C. 2003, *PASA*, 20, 118
- Stanghellini, C., Baum, S. A., O’Dea, C. P., & Morris, G. B. 1990, *A&A*, 233, 379
- Stanghellini, C., Bondi, M., Dallacasa, D., et al. 1997a, *A&A*, 318, 376
- Stanghellini, C., Dallacasa, D., O’Dea, C. P., et al. 2001, *A&A*, 377, 377
- Stanghellini, C., O’Dea, C. P., Baum, S. A., et al. 1997b, *A&A*, 325, 943
- Stanghellini, C., O’Dea, C. P., Dallacasa, D., et al. 1998, *A&AS*, 131, 303
- Stickel, M., Fried, J. W., & Kuehr, H. 1993, *A&AS*, 98, 393
- Tadhunter, C. N., Morganti, R., di Serego-Alighieri, S., Fosbury, R. A. E., & Danziger, I. J. 1993, *MNRAS*, 263, 999
- Tagliaferri, G., Foschini, L., Ghisellini, G., et al. 2008, *ApJ*, 679, 1029
- Taylor, G. B., Marr, J. M., Pearson, T. J., & Readhead, A. C. S. 2000, *ApJ*, 541, 112
- Taylor, G. B., O’Dea, C. P., Peck, A. B., & Koekemoer, A. M. 1999, *ApJ*, 512, L27
- Taylor, G. B. & Peck, A. B. 2003, *ApJ*, 597, 157

- Taylor, G. B., Readhead, A. C. S., & Pearson, T. J. 1996, *ApJ*, 463, 95
- Taylor, G. B., Vermeulen, R. C., Pearson, T. J., et al. 1994, *ApJS*, 95, 345
- Teräsraanta, H., Wiren, S., & Koivisto, P. 2003, in *Astronomical Society of the Pacific Conference Series*, Vol. 299, *High Energy Blazar Astronomy*, ed. L. O. Takalo & E. Valtaoja, 235
- Thompson, A. R. 1999, in *Astronomical Society of the Pacific Conference Series*, Vol. 180, *Synthesis Imaging in Radio Astronomy II*, ed. G. B. Taylor, C. L. Carilli, & R. A. Perley, 11
- Thompson, D. J., Djorgovski, S., & de Carvalho, R. 1990, *PASP*, 102, 1235
- Tingay, S. J., Edwards, P. G., & Tzioumis, A. K. 2003, *MNRAS*, 346, 327
- Tinti, S., Dallacasa, D., de Zotti, G., Celotti, A., & Stanghellini, C. 2005, *A&A*, 432, 31
- Torniainen, I., Tornikoski, M., Lähteenmäki, A., et al. 2007, *A&A*, 469, 451
- Torniainen, I., Tornikoski, M., Teräsraanta, H., Aller, M. F., & Aller, H. D. 2005, *A&A*, 435, 839
- Tornikoski, M., Jussila, I., Johansson, P., Lainela, M., & Valtaoja, E. 2001, *AJ*, 121, 1306
- Tremblay, S. E., Taylor, G. B., Helmboldt, J. F., Fassnacht, C. D., & Romani, R. W. 2009, *Astronomische Nachrichten*, 330, 206
- Unwin, S. C., Wehrle, A. E., Lobanov, A. P., et al. 1997, *ApJ*, 480, 596
- Unwin, S. C., Wehrle, A. E., Urry, C. M., et al. 1994, *ApJ*, 432, 103
- Urry, C. M. & Padovani, P. 1995, *PASP*, 107, 803
- Valtonen, M. J., Lehto, H. J., Nilsson, K., et al. 2008, *Nature*, 452, 851
- Vercellone, S., D'Ammando, F., Vittorini, V., et al. 2010, *ApJ*, 712, 405
- Verkhodanov, O. V., Trushkin, S. A., Andernach, H., & Cherenkov, V. N. 2005, *Bull. Special Astrophys. Obs.*, 58, 118
- Vermeulen, R. C., Ogle, P. M., Tran, H. D., et al. 1995, *ApJ*, 452, L5+
- Véron-Cetty, M. & Véron, P. 2006, *A&A*, 455, 773
- Véron-Cetty, M. & Véron, P. 2010, *A&A*, 518, A10+
- Villata, M. & Raiteri, C. M. 1999, *A&A*, 347, 30
- Villata, M., Raiteri, C. M., Aller, H. D., et al. 2004, *A&A*, 424, 497
- Villata, M., Raiteri, C. M., Kurtanidze, O. M., et al. 2002, *A&A*, 390, 407
- Villata, M., Raiteri, C. M., Larionov, V. M., et al. 2009, *A&A*, 501, 455
- Virtanen, J. J. P. & Vainio, R. 2005, *ApJ*, 621, 313

- Vollmer, B., Krichbaum, T., Angelakis, E., & Kovalev, Y. 2008a, A&A submitted, 0, 53
- Vollmer, B., Krichbaum, T. P., Angelakis, E., & Kovalev, Y. Y. 2008b, A&A, 489, 49
- Walker, R. C., Dhawan, V., Romney, J. D., Kellermann, K. I., & Vermeulen, R. C. 2000, ApJ, 530, 233
- Wilkinson, P. N., Polatidis, A. G., Readhead, A. C. S., Xu, W., & Pearson, T. J. 1994, ApJ, 432, L87
- Willett, K. W., Stocke, J. T., Darling, J., & Perlman, E. S. 2010, ApJ, 713, 1393
- Wilson, A. S. & Colbert, E. J. M. 1995, ApJ, 438, 62
- Wright, A. & Otrupcek, R. 1990, in PKS Catalog (1990)
- Xiang, L., Dallacasa, D., Cassaro, P., Jiang, D., & Reynolds, C. 2005, A&A, 434, 123
- Xiang, L., Reynolds, C., Strom, R. G., & Dallacasa, D. 2006, A&A, 454, 729
- Yang, J., Gurvits, L. I., Frey, S., & Lobanov, A. P. 2008, arXiv:0811.2926
- Zensus, J. A. 1997, ARA&A, 35, 607
- Zensus, J. A., Cohen, M. H., & Unwin, S. C. 1995, ApJ, 443, 35
- Zensus, J. A., Krichbaum, T. P., & Britzen, S. 2006, arXiv:astro-ph/0610712

Selbständigkeitserklärung

Ich versichere, dass ich die von mir vorgelegte Dissertation selbständig angefertigt, die benutzten Quellen und Hilfsmittel vollständig angegeben und die Stellen der Arbeit – einschließlich Tabellen, Karten und Abbildungen –, die anderen Werken im Wortlaut oder dem Sinn nach entnommen sind, in jedem Einzelfall als Entlehnung kenntlich gemacht habe; dass diese Dissertation noch keiner anderen Fakultät oder Universität zur Prüfung vorgelegen hat; dass sie – abgesehen von unten angegebenen Teilpublikationen – noch nicht veröffentlicht worden ist sowie, dass ich eine solche Veröffentlichung vor Abschluss des Promotionsverfahrens nicht vornehmen werde. Die Bestimmungen der Promotionsordnung sind mir bekannt. Die von mir vorgelegte Dissertation ist von Herrn Prof. Dr. Andreas Eckart betreut worden.

Köln, den 01. Dezember 2010

Teilpublikationen

Sokolovsky, K. V. and Kovalev, Y. Y. and Pushkarev, A. B. and Lobanov, A. P. 2010 *A VLBA survey of the core shift effect in AGN jets I. Evidence for dominating synchrotron opacity* submitted to *Astronomy & Astrophysics*.

Sokolovsky, K. V. and Kovalev, Y. Y. and Mimica, P. and Perucho, M. 2010 *A VLBI-selected sample of Compact Symmetric Object candidates and frequency dependent position of hotspots* submitted to *Astronomy & Astrophysics*.

Abdo, A. A., et al. 2010. *The first Fermi multifrequency campaign on BL Lac: characterizing the low activity state of the eponymous blazar* submitted to *The Astrophysical Journal*.

Abdo, A. A., et al. 2010. *Fermi-LAT observations of Markarian 421: the missing piece of its Spectral Energy Distribution* submitted to *The Astrophysical Journal*.

Abdo, A. A., et al. 2010. *Insights Into the High-energy γ -ray Emission of Markarian 501 from Extensive Multifrequency Observations in the Fermi Era* accepted to *The Astrophysical Journal*.

Abdo, A. A., et al. 2010. *Fermi Large Area Telescope and Multi-wavelength Observations of the Flaring Activity of PKS 1510-089 between 2008 September and 2009 June*. *The Astrophysical Journal* 721, 1425-1447.

- Sokolovsky, K. V., et al. 2010. *Constraints on the gamma-ray emitting region in blazars from multi-frequency VLBI measurements*. Proceedings of the Workshop "Fermi meets Jansky - AGN in Radio and Gamma-Rays", Savolainen, T., Ros, E., Porcas, R.W. & Zensus, J.A. (eds.), MPIfR, Bonn p.167 arXiv:1006.3084.
- Vercellone, S., et al. 2010. *Multiwavelength Observations of 3C 454.3. III. Eighteen Months of Agile Monitoring of the "Crazy Diamond"*. The Astrophysical Journal 712, 405-420.
- Sokolovsky, K. V., Kovalev, Y. Y., Lobanov, A. P., Savolainen, T., Pushkarev, A. B., Kadler, M. 2010. *Constraining the magnetic field in the parsec-scale jets of the brightest Fermi blazars with multifrequency VLBI observations*. 2009 Fermi Symposium, Washington, DC, Nov 2-5; eConf Proceedings C091122; arXiv:1001.2591.
- Sokolovsky, K. V., Kovalev, Y. Y., Kovalev, Y. A., Nizhelskiy, N. A., Zhekanis, G. V. 2009. *A sample of GHz-peaked spectrum sources selected at RATAN-600: Spectral and variability properties*. Proceedings of the Fourth Workshop on Compact Steep Spectrum and GHz-Peaked Spectrum Radio Sources, held in Riccione, Italy, from May 26 to 29, 2008. Editors: K.-H. Mack, D. Dallacasa, and C. P. O'Dea *Astronomische Nachrichten* 330, 199.
- Sokolovsky, K., Kovalev, Y. 2008. *Parsec-scale properties of GHz-Peaked Spectrum sources from 2.3 and 8.6 GHz VLBI surveys*. Published in Proceedings of Science, The 9th European VLBI Network Symposium: The role of VLBI in the Golden Age for Radio Astronomy.
- Kovalev, Y., Pushkarev, A., Lobanov, A., Sokolovsky, K. 2008. *Opacity in parsec-scale jets of active galactic nuclei: VLBA study from 1.4 to 15 GHz*. Published in Proceedings of Science, The 9th European VLBI Network Symposium: The role of VLBI in the Golden Age for Radio Astronomy.

Lebenslauf

Persönliche Daten:

Kirill Sokolovskiy
Geburtsdatum: 1. Oktober, 1985
Geburtsort: Moskau, Russland
Staatsangehörigkeit: Russische Föderation

Anschrift:

Frongasse 12,
53121 Bonn, Germany
Telefon: +49 (228) 525-358
Mobil: +49 (177) 257-59-97
Email: ksokolov@mpifr-bonn.mpg.de

Ausbildung und beruflicher Werdegang:

- 2008 – 2010: Doktorand in der VLBI-Gruppe des Max-Planck-Instituts für Radioastronomie in Bonn unter Betreuung durch Dr. Yuri Kovalev, Prof. Dr. J. Anton Zensus und Prof. Dr. Andreas Eckart. Mitglied der International Max Planck Research School for Astronomy and Astrophysics (IMPRS).
- 2001 – 2008: Student am physikalischen Institut der Moscow Lomonosov State University Abschluss: Diplom (M.Sc.) in Astronomie verteidigt im Dezember 2007
- 2005 – 2008: Laborassistent (Teilzeit), Labor fuer extragalaktische Radioastronomie, Astro Space Center des Lebedev Physical Institute, Russische Akademie der Wissenschaften
- 2004 – 2005: Data-center Systemverwalter, IT-Unternehmen "Stack Group" Moskau
- 1993 – 2001: Grund, Mittel und Oberschule N96, Moskau